

Synthetic Molecular and Colloidal Building Blocks for Biofabrication of Complex Tissues

Von der Fakultät für Mathematik, Informatik und Naturwissenschaften der RWTH Aachen University zur Erlangung des akademischen Grades eines Doktors der Naturwissenschaften genehmigte Dissertation

vorgelegt von

Daniel Günther, M. Sc.

aus

Aachen, Deutschland

Berichter: Universitätsprofessorin Dr.-Ing. Laura De Laporte

Universitätsprofessor Dr. med. Stefan Jockenhövel

Tag der mündlichen Prüfung: 30.06.2025

Diese Dissertation ist auf den Internetseiten der Universitätsbibliothek verfügbar.

Dedicated to my Grandmother

Declaration of Authorship

- I, Daniel Günther declare that this thesis and the work presented in it are my own and has been generated by me as the result of my own original research. I do solemnly swear that:
- 1. This work was done wholly or mainly while in candidature for the doctoral degree at this faculty and university;
- 2. Where any part of this thesis has previously been submitted for a degree or any other qualification at this university or any other institution, this has been clearly stated:
- 3. Where I have consulted the published work of others or myself, this is always clearly attributed;
- 4. Where I have quoted from the work of others or myself, the source is always given. This thesis is entirely my own work, with the exception of such quotations;
- 5. I have acknowledged all major sources of assistance;
- 6. Where the thesis is based on work done by myself jointly with others, I have made clear exactly what was done by others and what I have contributed myself;
- 7. Parts of this work have been published before as:
 - a. D. Günther*, C. Bergerbit*, A. Marsee, S. Vedaraman, A. Pueyo Moliner, C. Bastard, M. Dewerchin, J. L. Gerardo-Nava, G. Eelen, P. Carmeliet, R. Kramann, K. Schneeberger, B. Spee, L. De Laporte. *Biofabrication*, 2025, 17, 025015.
 - b. S. Bulut*, D. Günther*, M. Bund, C. Haats, T. Bissing, C. Bastard, M. Wessling, L. De Laporte, A. Pich. Advanced Healthcare Materials, 2024, 13, 2302957.
 - * Authors contributed equally.

03.04.2025, Daniel Günther

List of publications

- J. L. Gerardo-Nava*, J. Jansen*, D. Günther*, L. Klasen, A. L. Thiebes, B. Niessing, C. Bergerbit, A. A. Meyer, J. Linkhorst, M. Barth, P. Akhyari, J. Stingl, S. Nagel, T. Stiehl, A. Lampert, R. Leube, M. Wessling, F. Santoro, S. Ingebrandt, S. Jockenhoevel, A. Herrmann, H. Fischer, W. Wagner, R. H. Schmitt, F. Kiessling, R. Kramann, L. De Laporte. Transformative Materials to Create 3D Functional Human Tissue Models In Vitro in a Reproducible Manner. Advanced Healthcare Materials 2023, 12, 2301030.
- S. Bulut*, **D. Günther***, M. Bund, C. Haats, T. Bissing, C. Bastard, M. Wessling,
 L. De Laporte, A. Pich. Cellular Architects at Work: Cells Building their Own Microgel Houses. *Advanced Healthcare Materials* 2024, 13, 2302957.
- D. Günther*, C. Bergerbit*, A. Marsee, S. Vedaraman, A. Pueyo Moliner, C. Bastard, M. Dewerchin, J. L. Gerardo-Nava, G. Eelen, P. Carmeliet, R. Kramann, K. Schneeberger, B. Spee, L. De Laporte. Synergizing Bioprinting and 3D Cell Culture to Enhance Tissue Formation in Printed Synthetic Constructs. *Biofabrication* 2025, 17, 025015.
- S.-H. Jung, S. Bulut. L. P. B. Guerzoni, **D. Günther**, S. Braun, L. De Laporte,
 A. Pich. Fabrication of pH-degradable Supramacromolecular Microgels with Tunable Size and Shape via Droplet-based Microfluidics. *Journal of Colloid and Interface Science* 2022, 617, 409-421.
- C. Bastard, D. Günther, J. L. Gerardo-Nava, M. Dewerchin, P. Sprycha, C. Licht, A. Lüken, M. Wessling, L. De Laporte. How Does Temporal and Sequential Delivery of Multiple Growth Factors Affect Vascularization Inside 3D Hydrogels? *Advanced Therapeutics* 2024, 7, 2300091.

^{*} Authors contributed equally.

Author's contributions

- 1. The published article titled "Synergizing Bioprinting and 3D Cell Culture to Enhance Tissue Formation in Synthetic Printed Constructs" in Biofabrication is adapted in Chapter 3 and Chapter 4 with permission from IOP Publishing under the terms of the Creative Commons CC BY 4.0 license. D. Günther and C. Bergerbit contributed equally to this work. Chapter 3 contains the optimization of the bioink for cell growth, the characterization of the bioink properties, and the printing with spheroids. Chapter 4 includes the findings about spheroid reorganization into uniluminal structures. D. Günther planned and conducted all cell experiments, except for those with L929 cells, which were performed by S. Vedaraman. S. Vedaraman submitted the results of these experiments, partly shown in Figure 3.2 of this thesis, as part of her PhD thesis about "3D artificial extracellular matrices for directed in vitro cell growth" that was conducted at DWI - Leibniz Institute for Interactive Materials and RWTH Aachen University. D. Günther further optimized the bioink and characterized its properties. C. Bergerbit optimized the printing process. C. Bergerbit and D. Günther printed constructs with cell spheroids at Utrecht University, which was supported by A. Marsee, A. Pueyo Moliner and L. van Uden. L. van Uden contributed to cell culture of printed constructs with cell spheroids. V. Falter tested the influence of cell-conditioned media on spheroid sprouting as part of her master thesis, which was supervised and planned by D. Günther. D. Günther conducted all staining experiments and analyzed, quantified, and interpreted the results. M. Dewerchin, J. L. Gerardo-Nava, G. Eelen, P. Carmeliet, K. Schneeberger and B. Spee provided significant intellectual contributions to the project. L. De Laporte supervised the project. D. Günther and C. Bergerbit wrote the manuscript, which was reviewed by L. De Laporte. All authors finalized the manuscript.
- 2. In addition to the findings about uniluminal spheroid formation, the lumen formation process and respective influences of the hydrogel and spheroid compositions are analyzed in **Chapter 4**. Moreover, the fusion of luminal spheroids to create tubular structures is investigated. D. Günther developed the idea for the project and planned all cell experiments. D. Günther performed all

cell experiments based on 3.4 w/v% and 6.5 w/v% PEG hydrogels. S.-T. Wu conducted cell experiments using 2.5 w/v% PEG hydrogels as part of her internship, which was supervised and planned by D. Günther. Acoustic alignment experiments were conducted in collaboration with J. Hahn from the Department of Dental Materials and Biomaterials Research (ZWBF) at RWTH Aachen University Hospital. J. Hahn provided the setup for the acoustic alignment of spheroids and developed the idea to create a sandwich model with agarose pre-coating to embed spheroids between two PEG hydrogel layers, while D. Günther provided the cells, materials and media. D. Günther and J. Hahn conducted all acoustic alignment experiments together. D. Günther conducted all staining experiments and analyzed, quantified, and interpreted the results. R. Nasehi and H. Fischer provided significant intellectual contributions to the project. L. De Laporte supervised the project.

- 3. **Chapter 5** presents results from a collaboration with the research group of A. Herrmann at DWI - Leibniz Institute for Interactive Materials to control the degradation of hydrogels on-demand, first by supplementing thrombin through the media and then triggered by Low Intensity Focused Ultrasound (LIFU). The initial idea was developed by L. De Laporte. All experiments were planned by D. Günther. Experiments with media-supplemented thrombin as well as hydrogel characterizations were performed by D. Günther and H. Küttner as part of her internship, which was supervised and planned by D. Günther. D. Günther and H. Küttner quantified and interpreted the data. K. Zhang provided the thrombin and thrombin-cleavable peptide for the experiments. For proof-ofconcept experiments with LIFU-triggered hydrogel degradation, K. Zhang synthesized and provided thrombin and hirudin modified with thiols, which were integrated into the hydrogel system by D. Günther. J. Chen from the Institute for Experimental Molecular Imaging, which is led by Prof. Fabian Kiessling, performed LIFU treatments and K. Zhang quantified the enzyme activity as a result of the LIFU treatment in hydrogels. L. De Laporte and A. Herrmann provided significant intellectual contributions and supervised the project.
- 4. The published article "Cellular Architects at Work: Cells Building their Own Microgel Houses" in Advanced Healthcare Materials is adapted in **Chapter 6** with permission from Wiley-VCH GmbH under a personal license. D. Günther and S. Bulut contributed equally to this work. Parts of this work have been

previously submitted as master theses by M. Bund and C. Haats at RWTH Aachen University, which were supervised and planned by D. Günther and S. Bulut and examined by L. De Laporte and A. Pich. S. Bulut, M. Bund and C. Haats produced the microgels. D. Günther, M. Bund and C. Haats performed all cell experiments, which was supported by S. Bulut. All experiments were conceptualized and planned by D. Günther and S. Bulut. D. Günther quantified all cell data presented in this work and analyzed the results together with S. Bulut. L. De Laporte and A. Pich supervised the project. D. Günther and S. Bulut wrote the manuscript, which was corrected by L. De Laporte and A. Pich. All authors finalized the manuscript.

5. To refine the clarity and readability of short text sequences within this thesis, ChatGPT-4o was partly used without contributing to its intellectual content. All scientific content, analyses, conclusions, and interpretations are my own.

Eidesstattliche Erklärung

Hiermit erkläre ich, Daniel Günther, an Eides statt, dass ich die vorliegende Dissertation selbstständig verfasst und keine anderen als die angegebenen Quellen und Hilfsmittel benutzt habe.

Daniel Günther 03.04.2025, Aachen

Table of Contents

1	Mo	Notivation and Overview of the Thesis1				
	1.1	Introduction	1			
	1.2	Cell Culture	5			
	1.2	.1 Scaffold-free 3D Cell Culture	6			
	1.2	.2 The Extracellular Matrix	8			
	1.2	.3 Hydrogels as Artificial ECM for 3D Cell Cultivation	. 10			
	1.3	Synthetic PEG Hydrogels	. 13			
	1.4	Biofabrication of Complex Tissues	. 18			
	1.4	.1 Development of a Synthetic Bioink	. 19			
	1.4	.2 Need for Vascularization	. 22			
	1.5	Transplantation of Tissue Constructs	. 26			
	1.5	.1 Controlling Degradation in PEG Hydrogels	. 27			
	1.6	Granular Hydrogels and Microporous Annealed Particle Scaffolds	. 30			
	1.7	Summary	. 32			
2	Sta	te of the Art	. 33			
	2.1	Controlling Porosity in Injectable Matrices	. 33			
	2.1	.1 Hydrogel Degradation	. 33			
	2.1	.2 Microporous Annealed Particle Scaffolds	. 37			
	2.2	Methods to Engineer Vascularization on Different Scales	. 41			
	2.2	.1 Self-Assembled Vascular Networks	. 41			
	2.2	.2 Engineered Vascular Networks	. 44			
	2.3	Bioprinting in Tissue Engineering	. 46			
	2.3	.1 Bioprinting Techniques	. 46			
	2.3	.2 Bioprinting Complex Functional Tissues	. 48			
3	-	nergizing Bioprinting and 3D Cell Culture to Enhance Tissue Formatio				
۲	rinted	Synthetic Constructs	. 50			

3	3.1 Ir	ntroduction	50
3	3.2 F	Results and Discussion	54
	3.2.1	Influence of Hydrogel Composition on Printed Construct Stabi	lity54
		Influence of Hydrogel and Spheroid Composition on Suting	-
	3.2.3	Printing Process with Spheroids in PEG Bioink	63
3	3.3 C	Conclusion	66
3	3.4 N	Materials and Methods	67
	3.4.1	Synthesis of Ester-Functionalized Di-Thiol PEG Crosslinkers	67
	3.4.2	Preparation of Hydrogel Precursors and Hydrogel Formation	67
	3.4.3	Rheological Characterization of Hydrogels	68
	3.4.4	Scanning Electron Microscopy of the Hydrogels	68
	3.4.5	Quantification of Hydrogel Softening via Nanoindentation	68
	3.4.6	Evaluation of Hydrogel Swelling	68
	3.4.7	Cell Culture	69
	3.4.8	Cultivation of Cell Spheroids in Hydrogels	69
	3.4.9	Immunofluorescence Staining and Imaging	70
		O Printing of Constructs with PEG Bioink and Sacrificial Gelatin	
	3.4.1	1 Printing and Degradation of Constructs with Different Cross	osslinker
	3.4.13	3 Printing of Constructs with Live Cell Spheroids	71
	3.4.14	4 Statistical Analysis	72
4	Engin	eering Vascular Structures by Fusion of Prevascularized Spher	oids73
4	.1 Ir	ntroduction	73
4	.2 F	Results and Discussion	75
	421	Formation of Uniluminal Spheroids in PEG Hydrogels	75

		4.2.2	Fusion of Prevascularized Spheroids to Create Vascular Channel	∍ls with
		Conti	nuous Lumen	80
	4.	3 (Conclusion	85
	4.	4 N	Materials and Methods	87
		4.4.1	Cell Culture	87
		4.4.2	Preparation of Hydrogel Precursors and Hydrogel Formation	87
		4.4.3	Cultivation of Cell Spheroids in Hydrogels	87
		4.4.4	Acoustic Spheroid Alignment in PEG Hydrogels	88
		4.4.5	Immunofluorescence Staining	88
		4.4.6	Image Processing and Analysis	89
		4.4.7	Statistical Analysis	90
5		On-D	emand Degradation of PEG Hydrogels for Medical Applications	91
	5.	1 I	ntroduction	91
	5.	2 F	Results and Discussion	94
			On-Demand Hydrogel Degradation through Media-Suppler	
		5.2.2	Ultrasound-Mediated Thrombin Activation and Hydrogel Degrad	lation .
				103
	5.	3 (Conclusion	107
	5.	4 N	Materials and Methods	108
		5.4.1	Preparation of Hydrogel Precursors and Hydrogel Formation	108
		5.4.2	Degradation Experiments	108
		5.4.3	Rheological Characterization of Hydrogels	108
		5.4.4	Quantification of Hydrogel Softening via Nanoindentation	109
		5.4.5	Cell Culture	109
		5.4.6	Evaluation of Cell Viability	109
		5.4.7	Cultivation of Cell Spheroids in Hydrogels	110
		5.4.8	Microscopy	110

	5.4.9	LIFU-Triggered Thrombin Activation in PEG Hydrogels	.111
	5.4.10) Statistical Analysis	.111
6	Cellul	ar Architects at Work: Cells Building Their Own Microgel Houses	.112
6	.1 Ir	ntroduction	.112
6	.2 R	Results and Discussion	.114
	6.2.1	Cell-Induced Interlinking of Microgels	.114
	6.2.2	Cues to Guide Cell-Induced Interlinking of Microgels	.115
6	.3 C	Conclusion	.125
6	.4 N	laterials and Methods	.126
	6.4.1	Microfluidic Synthesis of dex-MA Microgels	.126
	6.4.2	Functionalization of dex-MA Microgels	.126
	6.4.3	Cell Culture	.127
	6.4.4	Metabolic Cell Activity Assay	.127
	6.4.5	Live/Dead Staining of MAP Scaffolds	.127
	6.4.6	Immunofluorescence Staining	.128
	6.4.7	Confocal Imaging and Image Analysis	.128
	6.4.8	Rheological Characterization of MAP Scaffolds	.129
	6.4.9	Statistical Analysis	.129
7	Refer	ences	.130
8	List of	f Abbreviations	. 155
9	Ackno	owledgments	.158

1 Motivation and Overview of the Thesis

1.1 Introduction

Severe diseases of critical organs like the heart, liver, or kidneys were once considered incurable, often leading to fatal outcomes. This changed in 1954 when a team of scientists and surgeons, led by Joseph Murray, performed the first successful organ transplantation and initiated a new era in modern medicine. To cure a patient with chronic nephritis, they transplanted the kidney of the patient's identical twin after testing their compatibility using small skin grafts. This pivotal moment in medical history marked a new hope for treating organ failure, that remains up to today oftentimes the only treatment option for patients with severe organ diseases. However, the success of transplantations was limited by the need for identical human leukocyte antigen (HLA) types between organ donor and recipient, as it is the case for identical twins, to prevent transplant rejection. This led to the development of immune-suppressive drugs to avoid an immunemediated rejection of the transplanted organ. These significant steps were essential for further achievements, including the transplantation of various solid organs such as the heart, lungs or liver.² As organ transplantation became the gold standard to treat end-stage organ failures, the worldwide demand for donor organs has steadily increased, resulting in an increasing organ donor-supply gap with only 10% of the global transplant demand currently being met.^{3, 4} To overcome this general organ shortage crisis with 15-30% of patients annually dying while waiting for an organ in Europe⁵, resolutions to increase the availability, ethical access and oversight of transplantation have been approved by the World Health Assembly. In addition, Spain successfully operates an opt-out system, which declares that everyone is an organ donor by default to boost donation. However, developing a global strategy with organ donation and transplantation being the norm is challenging as it comes up against cultural, ethical, religious, and personal concerns.⁴ As an alternative to transplanting human organs, animal-to-human xenotransplantation is investigated to fill the need for organ transplants. Since 2022, two hearts, two kidneys and a liver, that were raised in genetically modified pigs, were transplanted into human. However, the organs either failed or had to be

removed within 8 weeks after transplantation.⁶ While promising, this emphasizes the need for autologous transplants.

Tissue engineering displays a disruptive alternative to the general concept of transplanting donor organs and was first introduced by Joseph P. Vacanti and Robert Langer in the 1980s. Here, cells that are isolated from the human body are combined with an artificial matrix to create a three-dimensional (3D) biological substitute that can be transplanted to restore, maintain or improve the function of a diseased tissue or organ (Figure 1.1).8 By utilizing patient-derived cells, autologous tissue constructs can be grown ex vivo for transplantation without the need for a lifetime treatment with immunosuppressive drugs and to close the donor-supply gap effectively. At the same time, the fabrication of human in vitro tissues has the potential to revolutionize the pharmaceutical industry. Currently, the development of new drugs takes 10-15 years, costs 1-2 billion dollars, and mainly relies on preclinical animal testing. As the physiology, disease progression, and reaction to infections between humans and animals differs greatly, translation of data from preclinical animal tests into humans is difficult. 9 This is one of the main reason why 90% of preclinically promising drugs fail when tested in humans in clinical trials. 10 Reliable human tissue models could help to overcome this limitation in preclinical drug development and make it more efficient by reducing costs and the development time. This is further acknowledged by the Food and Drug Administration (FDA) modernization act 2.0 from 2022, which emphasizes the use of cell-based in vitro as well as in silico model systems to replace animal tests for drug discovery. 11

In addition to the development of new drugs and therapies, the creation of adequate tissue models could advance precision medicine. As diseases, like cancer, are often heterogeneous and individuals respond differently to different treatments, personalized therapies are decisive for an effective cure. 12 Thus, the development of *in vitro* disease models using patient cells could help to improve disease diagnosis and prevention as well as to screen and identify effective therapeutics in a standardized manner, while reducing the costs, redundant treatments and side effects of current treatments. 13

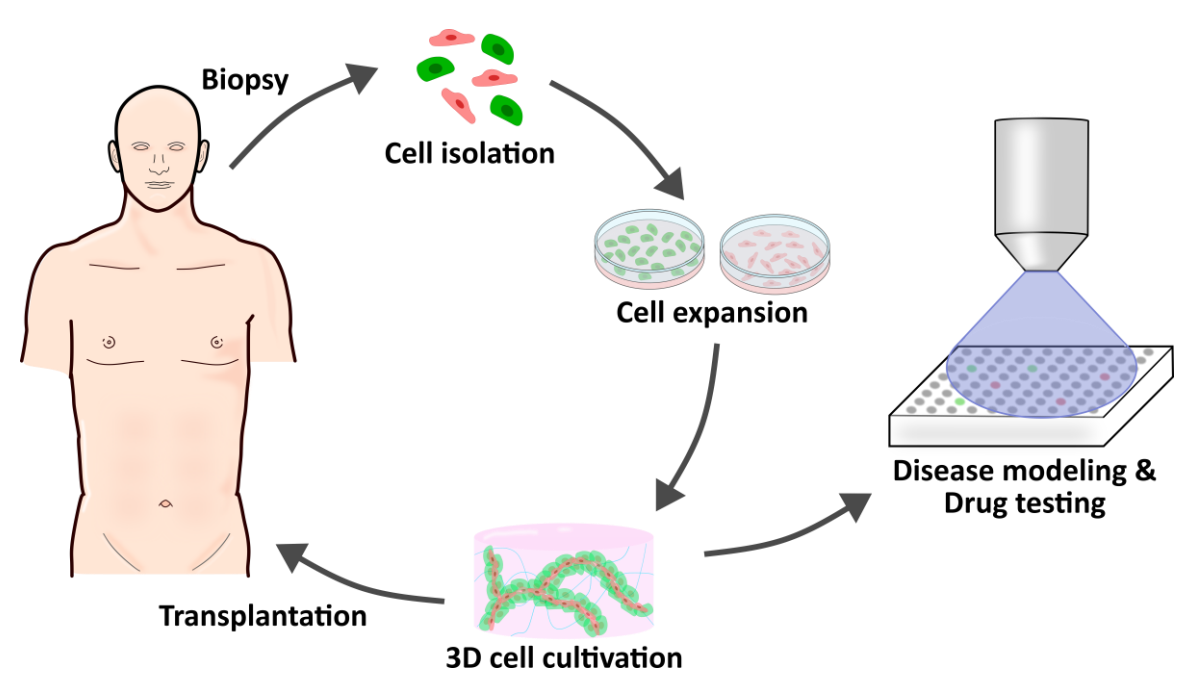


Figure 1.1: Principle of Tissue Engineering.

In 2000, Time Magazine declared tissue engineering as the most promising job field, highlighting the enormous potential it held to revolutionize medicine. 14 At that time, tremendous advances had been made since the concept of tissue engineering was first introduced, including milestones like the engineering and transplantation of an ear¹⁵, skin grafts¹⁶, and cartilage.¹⁷ Fueled by these successes, researchers and the public alike expected that we would by now have the capability to engineer whole, solid organs for transplantation. However, these high hopes have not yet been realized, as the field encountered critical challenges that slowed progress. 18 The main challenge in tissue engineering lies in the fabrication of larger and more complex tissue constructs. Although initial successes have been achieved in simpler tissues with low metabolic demands, replicating these successes in more complex tissues remains a significant hurdle. 19 A critical factor in creating larger tissue constructs is the development of a functional vascular network. In vivo, almost all tissues are vascularized to enable the cellular supply with oxygen and nutrients while removing metabolic waste products, which is why the formation of a functional vascular network in vitro represents one of the main bottle necks and is oftentimes considered as the 'Holy Grail' of tissue engineering.^{20, 21} Addressing this challenge has been a central motivation for me and became the focal point of my research in the group of Prof. Dr.-Ing. Laura De Laporte, which consists of four major research projects (Figure 1.2). Throughout

this thesis, I worked on the EU project OrganTrans, which aimed to develop patient-specific liver tissue in collaboration with 8 partners from industry and academia including Dr. Bart Spee's research group at Utrecht University and Prof. Peter Carmeliet's research group at KU Leuven. To bioprint larger liver tissue constructs, I contributed to the development of a novel synthetic bioink and investigated the growth of prevascularized cell spheroids within the printed constructs for vascularization. In addition, I optimized these prevascularized spheroids to reorganize into luminal structures that can fuse to build perfusable vascular channels. Moreover, I established an on-demand degradation mechanism in collaboration with the research group of Prof. Andreas Herrmann, which can be triggered with ultrasound to precisely control material degradation and the growth of cell spheroids in vitro and potentially in vivo. Finally, I established the creation of cell-microgel assemblies as an alternative to conventional 3D cell cultivation methods based on bulk hydrogels in collaboration with the research group of Prof. Andrij Pich, which has now become a key technique used in our research group. In the following chapters, I will describe the context of my projects, present these projects in detail, highlight their potential contributions to important challenges in the field of tissue engineering, and compare them to the current state of the art.

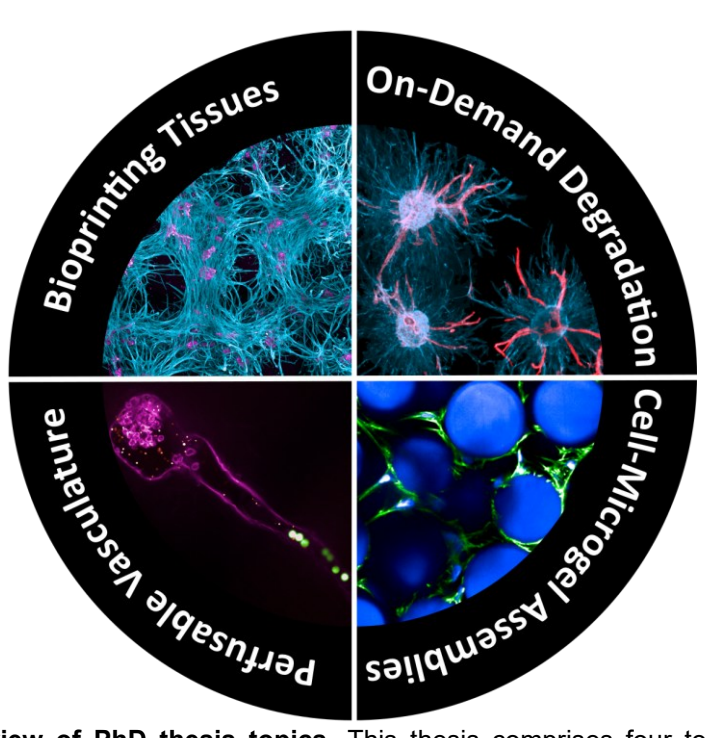


Figure 1.2: Overview of PhD thesis topics. This thesis comprises four topics, including the bioprinting of vascularized tissues (Chapter 3), the formation of perfusable vascular structures (Chapter 4), an on-demand degradation system that can be triggered with ultrasound (Chapter 5), and the cell-induced fabrication of cell-microgel assemblies (Chapter 6).

1.2 Cell Culture

Tissues are depending on their respective functions composed of multiple different cell types. Every cell type has thereby specific requirements that need to be considered when they are isolated from the tissue and should be cultured in vitro. While various hematopoietic cell lines like macrophages, lymphocytes or erythrocytes, are naturally found in the blood stream and do not adhere to surfaces, the majority of cell types isolated from tissues are naturally adherent and require attachment to a surface to grow.²² In this thesis, I have worked with naturally adherent cell types including human endothelial cells, fibroblasts, mesenchymal stem cells, and pericytes which are typically cultured two-dimensionally (2D) as monolayers on polystyrene surfaces in cell culture flasks or petri dishes.²³ Besides the substrate, it is essential to provide cells with an environment that supports their viability and proliferation. This includes physiological temperatures, humidity, CO₂ and O₂ levels, which are regulated by the cultivation in the incubator, as well as nutrients and growth factors supplied through the cell culture media. While the physical parameters in cell culture are stable and mimic the natural environment of the human body (37 °C, 5% CO₂), the chemical composition of the cell culture media differs depending on cellular requirements.²⁴ Endothelial cells, being highly specialized, need various growth factors, including vascular endothelial growth factor (VEGF), epidermal growth factor (EGF), basal fibroblasts growth factor (bFGF) and insulin-like growth factors (IGF) to be able to grow and build vascular structures.²⁵ Thus, I used commercially available, specialized endothelial cell media that are supplemented with these growth factors in all my experiments whenever endothelial cells are included as described in Chapters 3, 4 and 5.

In the pharmaceutical industry, 2D cell culture is widely used for high-throughput screenings of drugs and toxic compounds. They allow researchers to study the standard physiology and biochemistry of cells in a reproducible and cost-effective manner, filling the gap between biochemical assays and animal models.^{26, 27} Furthermore, 2D cell culture systems can be used to investigate the migration and invasiveness of cells under controlled conditions, including the presence or absence of a chemotactic gradient, which are crucial for multiple processes including wound healing or tumor mestastasis.²⁸ However, 2D cell culture models lack the complexity of native tissues and inaccurately represent *in vivo* cells. Cells

in 2D cultures are only in contact with other cells in their periphery, leading to fewer cell junctions and only partial polarity. As a consequence, all cells receive the same amount of nutrients, growth factors and oxygen with the absence of gradients, which makes the cell environment non-physiologically uniform. Therefore, drugs can easily penetrate the cells to induce apoptosis, which makes them appear less resistant to drugs than they would be in native tissues.²⁹ This leads to high drug failure rates, with up to 95% of agents showing promising anticancer activity in preclinical *in vitro* tests but ultimately failing in clinical trials.^{26, 30}

1.2.1 Scaffold-free 3D Cell Culture

Besides their cellular variety, tissues are characterized by their complex 3D structure that is crucial for the respective tissue function. Thus, recreating the three-dimensionality of native tissues in vitro is one of the main requirements to mimic the cells' natural microenvironment. The simplest form of 3D cell culture are thereby scaffold-free techniques where cell attachment to a surface is prevented. This way, cells are forced to aggregate and self-assemble to form multicellular spheroids, which can resemble the architecture, gene expression patterns, physiological responses of tissues, as well as drug resistance mechanisms of diseases like cancer.31 Thus, spheroids are widely used in regenerative medicine as well as in vitro diseases and tissue models for drug screening. 32, 33 During the process of spheroid formation, cells in suspension build loose aggregates by interactions between integrins on the cell membrane surface and arginine-glycineaspartate (RGD) motifs found in proteins of the extracellular matrix secreted by neighboring cells. As a result of the initial cell aggregation, the expression of cadherins is upregulated, which accumulate on the cell membrane. Direct cell-cell contacts are formed via cadherin bindings as well as other adhesion proteins like connexins and pannexins that transform the loose aggregates into solid cell spheroids.34

Multiple techniques for spheroid formation have been developed that can be divided in matrix-free and matrix-based methods.³⁴ These methods utilize physical forces, like gravity or centrifugation, non-adhesive biomaterials, and microstructured surfaces.³⁵ The hanging drop method is the most common form of spheroid formation and uses gravity to accumulate and aggregate cells at the air-

liquid interface of a hanging drop (Figure 1.3 A). In this thesis, I have fabricated spheroids by forming hanging droplets with a volume of 30 µL containing 1000-5000 cells that were cultured in petri dishes. While the hanging drop technique produces uniformly sized spheroids without the need for additional professional equipment, it is labor-intensive and time consuming with a low throughput³⁶, which is a disadvantage when biofabricating larger, spheroid-laden constructs, which is one of the goals of this thesis. In contrast, ultra-low attachment well plates with a microstructured surface in the shape of an inverted pyramid allow to increase the throughput of spheroid production.³³ Thus, I have utilized the Sphericalplate 5D[®] in these cases, which was provided by Kugelmeiers Ltd. as part of the OrganTrans collaboration and allows to produce 750 uniform and size-controlled spheroids in a 24-well plate format (Figure 1.3 B).³⁷ During my research, I formed spheroids consisting of human umbilical vein endothelial cells (HUVECs) in co-culture with normal human dermal fibroblasts (NHDFs) as supporting cells, which is presented in Chapters 3, 4 and 5. The resulting spheroids show an even distribution of HUVECs, confirmed by CD31 immunostaining, and NHDFs (Figure 1.3 C). Spheroids are, depending on their size, characterized by different layers of quiescent and proliferating cells as a result of nutrient and oxygen gradients that are decreasing from the spheroid surface to the core.^{38, 39} While the presence of such gradients mimics the physiologic cell environment, it at the same time limits the spheroid size. Depending on the cellular oxygen consumption rate, spheroids with sizes > 150 µm commonly develop a necrotic core as a result of limited oxygen diffusion.⁴⁰ Such hypoxic conditions are commonly found in tumors, which is why spheroid models are established to recapitulate the tumor microenvironment⁴¹, but are not representative for non-tumor tissues. Thus, simple spheroid systems are unsuitable for the development of more complex and larger tissue models. Typical spheroid cultivation methods are further limited in cell-matrix interactions due to the lack a surrounding matrix, which is a key component of the natural cellular environment. Without the extracellular matrix, cells are deprived of essential biochemical and mechanical signals that influence their function and organization.³⁴ In the following subchapters, we will explore the role of the extracellular matrix in cellular behavior and the significance of providing artificial matrices to advance 3D cell culture systems and create more complex in vitro tissue models.

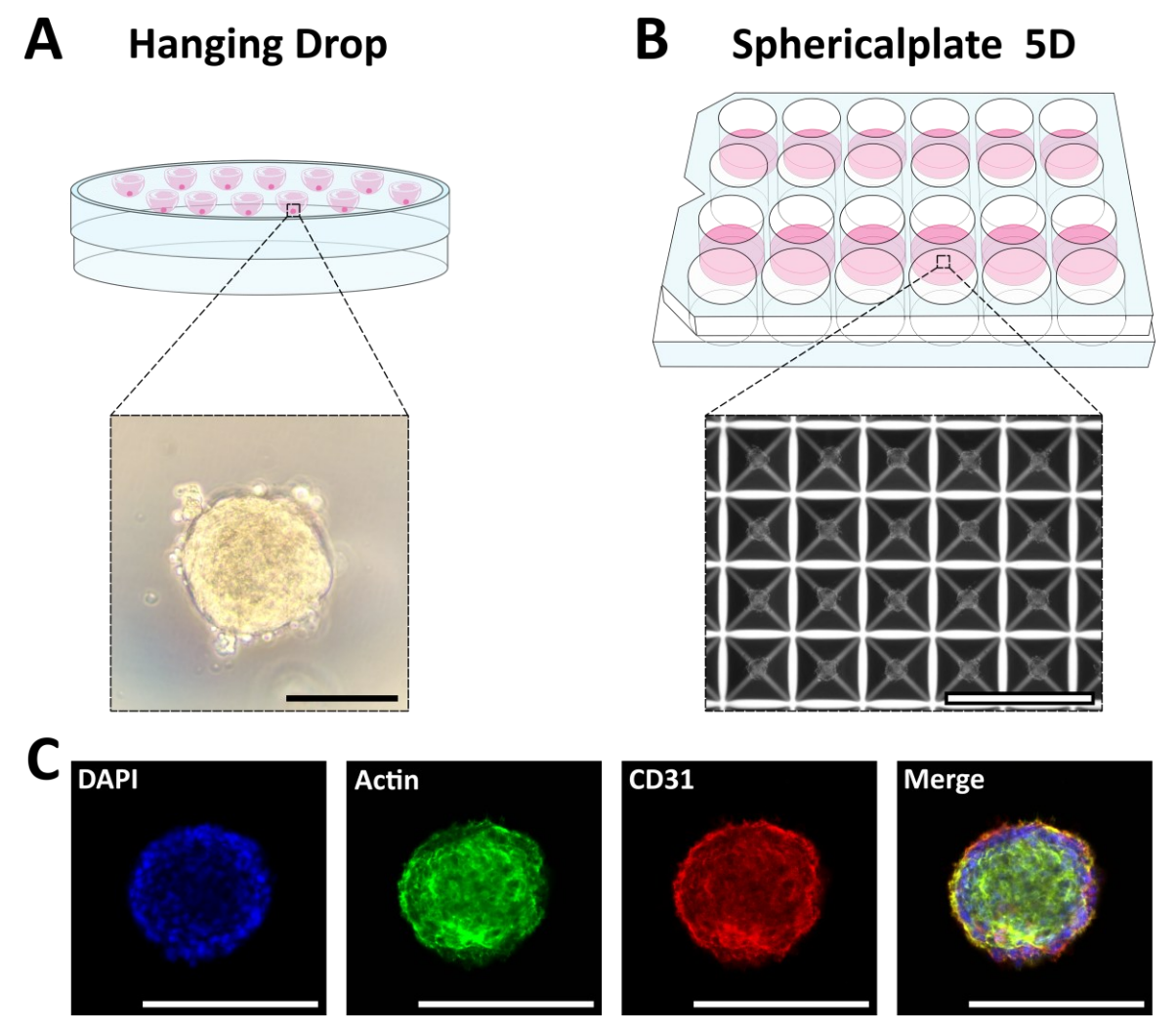


Figure 1.3: Spheroid formation methods. Spheroids are formed in hanging drops (**A**) or using the ultra-low attachment well plate Sphericalplate $5D^{\circledcirc}$ (**B**). **C**) Confocal images of a spheroid consisting of HUVECs and NHDFs in a 3:1 ratio and 1000 cells in total. The spheroid is stained for nuclei (blue), actin (green) and CD31 (red). Scale bars: A) 100 μ m, B) 1 mm, C) 200 μ m.

1.2.2 The Extracellular Matrix

Every cell produces and interacts with a surrounding extracellular matrix (ECM), which is the non-cellular component found in all tissues. The ECM in general consists of water, polysaccharides and around 300 different proteins, which are called the core matrisome. While the macromolecules of the ECM can be classified into collagens, elastin, microfibrillar proteins, proteoglycans like hyaluronan, and noncollagenous glycoproteins, its specific composition varies between different tissue types. These molecules essentially provide a physical scaffold for cells to attach, migrate and orchestrate important biochemical functions, which influence cell proliferation, differentiation, and survival. 43

The ECM comprises two structurally distinct types, called the interstitial ECM and the basement membrane. The interstitial ECM is a porous network consisting of fibrillar proteins, which are produced by fibroblasts, that is found in connective tissue types and the parenchyma of all organs. ^{44, 45} The basement membrane is a thin ECM layer that surrounds most animal tissues and lies beneath epithelial and endothelial cells. It thereby creates an interface between these polarized cell types and the underlying connective tissue, which is essential for the glomerular filtration in the kidneys as well as the function of the blood-brain barrier. ^{44, 46} The main type of ECM found in blood vessels is the basement membrane, which underlies the innermost layer of endothelial cells and surrounds perivascular cells as well as smooth muscle cells in the outer blood vessel layers. ⁴⁷ Thereby, the basement membrane contributes to the mechanical properties of the vessel and influences, depending on its composition, the vessel elasticity, vascular permeability and detection as well as responsiveness to fluid mechanical shear stress. ^{47, 48}

The interaction of cells with the surrounding ECM is depending on the recognition of ECM motifs by the cells and represents the basis for the development, maintenance and functions of tissues in our bodies. The majority of proteins found in the ECM, including fibronectin, vitronectin, collagen, and fibrinogen, contain the tripeptide RGD in their sequence. This sequence serves as a cell recognition site for integrins, a family of cellular transmembrane proteins, that bind to the RGD peptide. Within the cell, integrins are associated with proteins like talin and kindlin and are anchored to the actin filament of the cytoskeleton. This way, they can transmit bidirectional signals across the cell membrane to control cell adhesion to the ECM via inside-out signaling as well as regulating cellular processes as a response to signals from the surrounding microenvironment. ⁵⁰

To be able to contribute to changes during development and to maintain tissue homeostasis, the ECM is a highly dynamic structure, which undergoes constant remodeling processes. Changes in the ECM composition influence the physical and mechanical properties, such as pore size, stiffness, viscoelasticity, and topography. These properties regulate important cell behaviors including cell migration, which is crucial during development, immune defence, wound healing, and diseases.^{51, 52} The ECM remodeling process mainly involves the degradation of the ECM, which is executed by different families of proteases. These proteases

are mainly membrane-bound or soluble matrix metalloproteinases (MMPs) that are secreted by cells as zymogens and are subsequently activated in the extracellular space by proteolytic degradation. So far, 23 different MMPs have been identified, which are able to degrade all proteins of the ECM. To prevent uncontrolled degradation, the activity of MMPs is inhibited by metalloproteinase inhibitors (TIMPs). This way, the overall proteolytic activity is balanced by the ratio of MMPs to TIMPs.⁵³

1.2.3 Hydrogels as Artificial ECM for 3D Cell Cultivation

Tissue engineering aims to build tissues by mimicking the natural interaction of cells with their surrounding ECM and recapitulate essential ECM functions in vitro. Numerous materials have been investigated in their capability to capture these ECM characteristics, which are combined with different scaffold-based culture systems to provide a suitable environment for cells to grow. The majority of these culture systems comprise solid scaffolds as well as aqueous-based hydrogels that serve as artificial extracellular matrices.⁵⁴ Solid scaffolds have been extensively used in the past and are characterized by a high degree of porosity that allows for infiltration of cells that are seeded on top of a pre-prepared scaffold.⁵⁵ The formation of big pores within the scaffold can be achieved by various techniques like solvent casting, porogen leaching, freeze-drying or phase inversion as well as combinations thereof.⁵⁶ In addition, fibrous scaffolds are formed by creating a mesh of fibers that are for example formed by electrospinning.⁵⁷ While these methods allow to control the pore size, shape, and interconnectivity, which have been shown to influence cell fate⁵⁸, the requirement to form the scaffold before cell seeding impedes a homogeneous distribution of the cells throughout the scaffold.55 In addition, the formation of larger pores in a range of 100-600 µm promotes cell attachment and growth in 2D along the pore walls, which prevents the formation of a 3D cellular network.⁵⁹

Hydrogels, on the other hand, are water-swollen, nanoporous polymer networks. Nowadays, they represent the most promising platform for 3D cell culture as they resemble the mechanics of soft tissues, mimic essential characteristics of the ECM, and support cell adhesion as well as protein sequestration.^{60, 61} Hydrogels are formed in a bottom-up process from polymer chains that crosslink and form a

network via covalent bonds or non-covalent interactions. The type of crosslinking thereby influences the mechanical properties of the resulting hydrogel, including the stiffness and pore size, which can be further tuned by changes of the polymer concentration and crosslinking density.⁶² The polymers used for hydrogel formation can be derived from natural or synthetic sources as well as semi-synthetic combinations thereof (**Figure 1.4**).⁶³

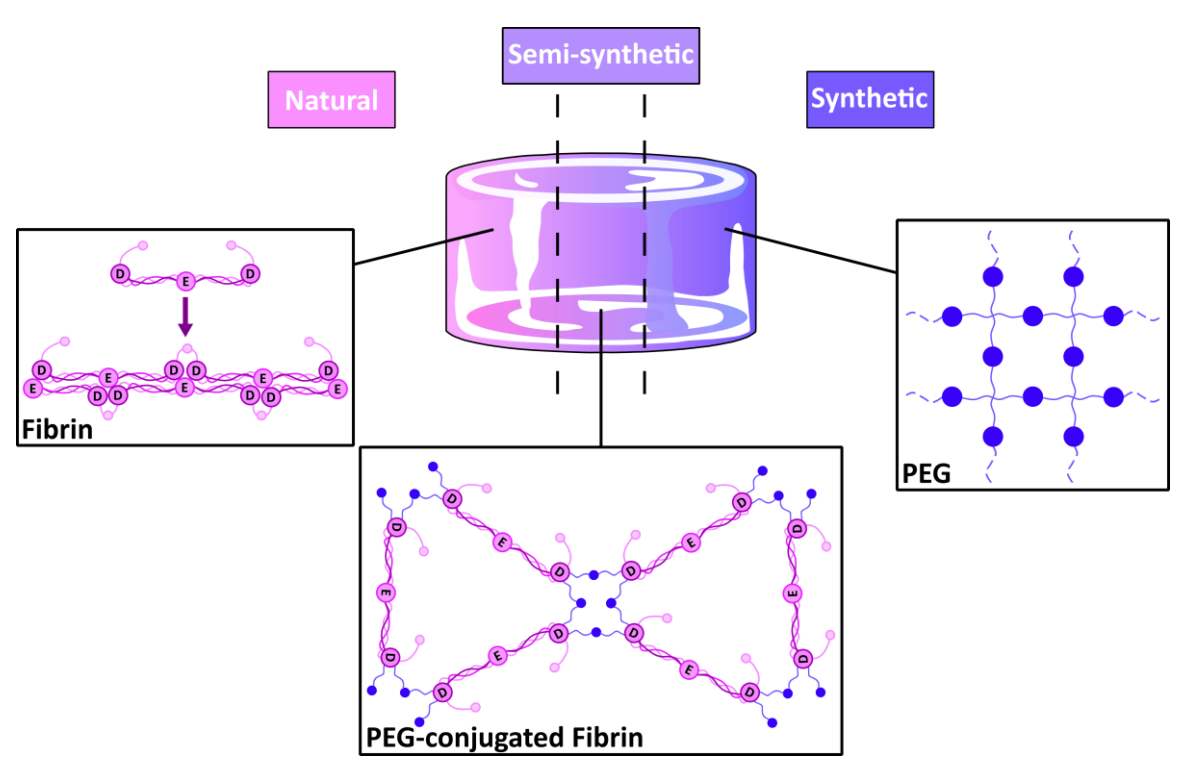


Figure 1.4: Overview of different hydrogel sources. Hydrogels are made of polymers that can be derived from natural, semi-synthetic or synthetic materials.

Natural hydrogels are typically made of polymers that are derived from animals or plants. The majority of these polymers comprise proteins like fibrin, collagen or its derivative gelatin as well as polysaccharides such as cellulose, alginate, hyaluronic acid or dextran. In addition to single polymer hydrogels, decellularized ECMs, derived from human or animal tissues after removal of cellular components, serve as scaffold for tissue engineering. In comparison, decellularized ECMs offer a greater scaffold complexity due to the presence of multiple ECM macromolecules in their native architecture but require more extensive preparation. In general, natural hydrogels are characterized by their inherent biocompatibility and degradability, making them ideal candidates for biomedical applications and tissue engineering. Protein-based hydrogels are thereby becoming increasingly

attractive as they combine these inherent properties with the viscoelasticity of the natural ECM by exhibiting elastic and viscous behavior. The viscoelasticity of these hydrogels is a result of their partial non-covalent crosslinking as well as physical polymer entanglement or protein unfolding and refolding.⁶⁶ Moreover, proteins contain multiple functional groups, such as amines thiols or carboxyl groups that enable further modifications. These functional groups can be reacted with synthetic crosslinkers to create semi-synthetic hydrogels that exhibit increased stability, while retaining their natural biocompatibility, functionality and degradability.⁶⁷ This addresses the limitations of natural hydrogels, characterized by their low stability and mechanical strength.⁶⁸ However, the use of natural polymers can introduce variability in the properties of both natural and semi-synthetic hydrogels as a result of batch-to-batch differences and poorly defined composition, given their origin from native tissues. 69 This makes it difficult to further tune their properties and could limit the reproducibility, data reliability, and upscaling potential of such biomaterials. 70, 71 For this reason, synthetic materials are used as alternatives to natural materials, which are often commercially available, characterized by their excellent potential for modifications, and controllability of their structure and properties.⁷² Multiple synthetic materials have been investigated in their potential to create hydrogels for biomedical applications. Since they are often bioinert, hydrogels based on synthetic polymers need to be biofunctionalized.⁷³ To be able to support cell growth, cells need to be able to adhere to the polymer network. This can be achieved by introducing cell-adhesive proteins like fibronectin or vitronectin that are recognized by cellular integrins.⁷⁴ Since such full-length proteins are however isolated from natural tissues, they are also prone to batch-to-batch variations. Thus, short peptides that contain the integrin recognition site RGD, which can be synthesized in a reproducible manner, are used to create fully synthetic hydrogels that are cell-compatible.75 In addition to promoting cell adhesion, synthetic polymer networks need to be rendered degradable as their pores are otherwise too small to be able to support cell migration and growth. This can be achieved by introducing for example hydrolytically degradable moieties. Thereby, water molecules react with ester, amide or ether groups, which results in a polymer chain scission, polymer mass loss, and hydrogel swelling.⁷⁶ While hydrolysis results in generic hydrogel degradation, more precise mechanisms have been adapted from the natural ECM and involve the enzymatic degradation on celldemand based on MMPs.⁷⁷ In addition, dynamic synthetic hydrogels can be designed by incorporating reversible hydrogen bondings into the polymer network. This way, the viscoelasticity of tissues can be recapitulated in synthetic hydrogels and cell growth promoted in a degradation-independent manner.⁷⁸

1.3 Synthetic PEG Hydrogels

Among the synthetic and hydrophilic polymers used for the formation of hydrogels, polyethylene glycol (PEG) is one of the most widely utilized and stands out by a unique combination of properties. Like other synthetic polymers, PEG is characterized by its tunability and can be tailored to specific applications by changes of the molecular weight and chemical structure, which can be linear or branched and directly influence the mechanical properties as well as scaffold architecture.⁷⁹ In addition, the basic PEG structure consists of a PEG diol with two hydroxyl end groups, which can be modified with the same or two different functional groups, including methyloxyl, carboxyl, amine, thiol, azide, vinyl sulfone, azide, acetylene or acrylates, to create symmetrically or asymmetrically functionalized PEG molecules. This makes PEG a versatile building block for different chemical reactions that are utilized for hydrogel formation or further modifications.80 A major limitation of many synthetic polymers for their use with cells is their toxicity. In contrast, PEG is characterized by its excellent biocompatibility and therefore generally recognized as safe by the FDA and the European Medical Agency (EMA).81 Overall, these properties and the combination thereof make PEG the perfect candidate for applications in tissue engineering, biomolecule release or regenerative medicine (Figure 1.5).82

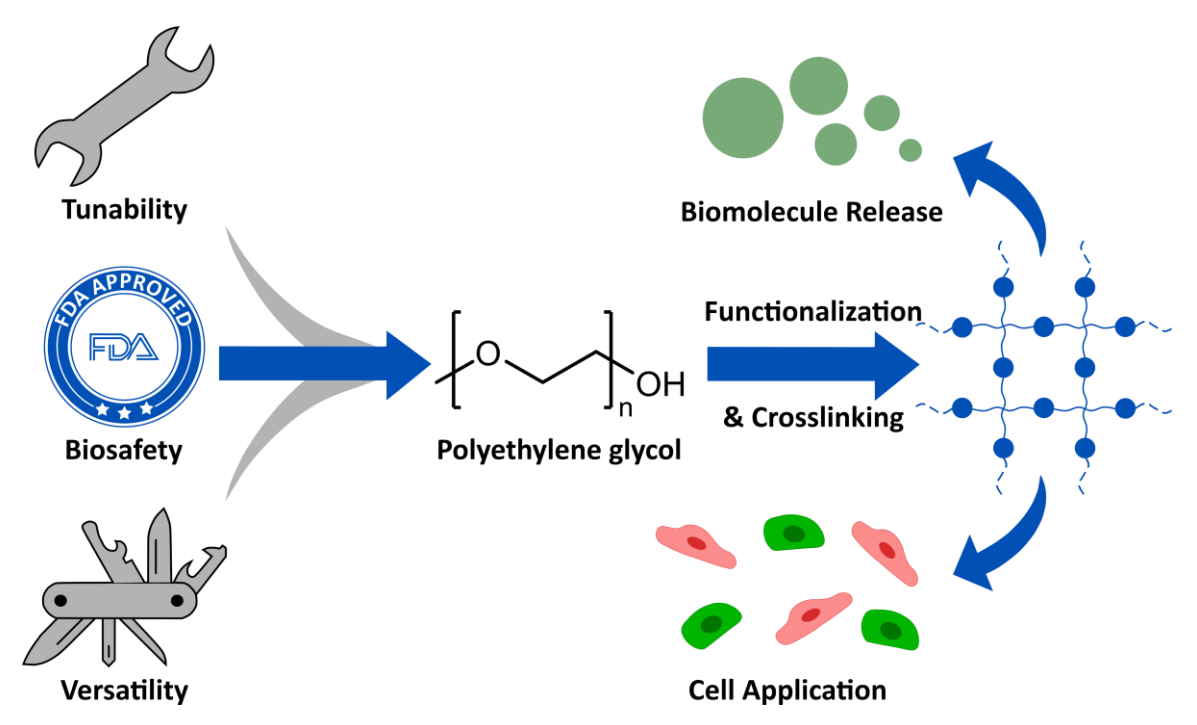


Figure 1.5: Properties and biomedical applications of polyethylene glycol (PEG). PEG is characterized by its tunability, versatility to be modified with a variety of functional groups as well as biosafety that is approved by the FDA for clinical use. This makes PEG an ideal candidate to create hydrogels for biomedical applications such as biomolecule release or cell applications.

Depending on the modification of PEG with functional groups, multiple different crosslinking and hydrogel formation mechanisms have been investigated over the years. The most widely used crosslinking methods include chain-growth and stepgrowth polymerization mechanisms.⁸² During chain-growth polymerization, commonly radicals are generated from photoinitiators upon UV light exposure. Free radicals then initiate the polymerization by transforming monomers like PEGacrylate into an active radical species. This radical species can then react with additional PEG-acrylate molecules to form a polymer network in a process called free-radical polymerization, which ends when two growing polymer chains form a stable bond or the radical is quenched otherwise.⁸³ While such reactions have been used in tissue engineering applications before⁸⁴, the exposure to UV light and radicals can be harmful for cells.⁸⁵ In comparison, step-growth polymerization mechanism are mild reactions and happen under ambient conditions when two multifunctional monomers with mutually reactive functional groups are mixed together. In contrast to chain-growth polymerization, which is characterized by the rapid growth of individual polymer chains, causing defects in the polymer network, the polymer networks are more homogeneous as a result of step-growth polymerization and build up gradually.82 The most commonly utilized step-growth polymerization mechanism to form PEG hydrogels is the thiol-Michael addition. Here, the thiol reacts as a nucleophilic Michael donor with an electron-deficient carbon-carbon double bond, which represents the Michael acceptor, in a highly specific "click" reaction (Figure 1.6 A). Thereby, the carbon-carbon double bond is electron-deficient due to the presence of electron-withdrawing carbonyl groups and is thus available for the nucleophile conjugation (Figure 1.6 B).86 The kinetics of the reaction depend on how strong the electron-withdrawing group is and the partial positive charge it creates on the carbon-carbon double bond where the nucleophile attacks. Therefore, the reactivity is lower for methacrylates and acrylates, which only have a single electron-withdrawing carbonyl group, whereas it is faster for vinyl sulfone and maleimides, characterized by two carbonyl groups (Figure 1.6 C).86,87 This way, the gelation time can be adjusted from seconds (maleimides) to minutes (vinyl sulfone – methacrylates). In addition, the reactivity can be influenced by the pH. A higher pH thereby leads to a higher concentration of thiolates, which react as strong nucleophiles with the electron-deficient carboncarbon double bond of the Michael acceptor (Figure 1.6 D).88 Lastly, the thiol-Michael addition can be accelerated by increasing the temperature. According to the Arrhenius equation, the reaction rate increases with increasing temperatures due to a higher kinetic energy of molecules, which allows them to overcome the activation energy barrier of the reaction.89

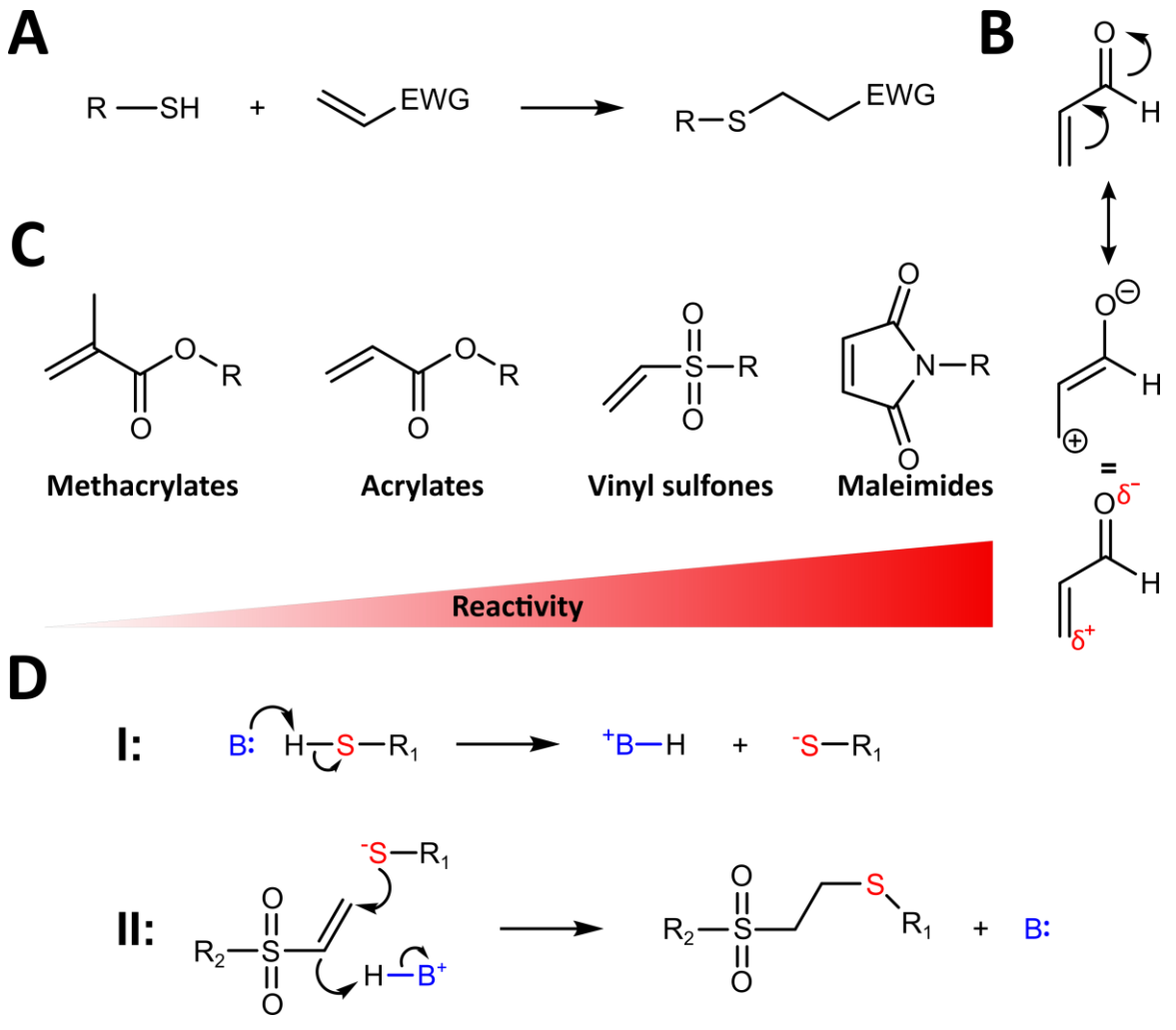


Figure 1.6: Crosslinking mechanism via thiol-Michael addition. Reaction of a thiol with an electron-deficient carbon-carbon double bond (A), which has due to the presence of an electron-withdrawing group (EWG) a partial positive charge (B). The reaction kinetic depends on the strength of the EWG to create such a partial positive charge (C) and can be further catalyzed by the presence of bases to form thiolates, which react with the electron-deficient carbon-carbon double bond of the Michael acceptor in a second step (D).

Throughout this thesis, I have worked with a PEG-based hydrogel that crosslinks via thiol-Michael addition of a four-arm PEG vinyl sulfone (PEG-VS) with linear dithiol crosslinkers. The reagents were dissolved in cell culture media and mixed in equimolar functional concentrations under physiologic conditions, which allowed for a controlled crosslinking of the hydrogel within 5-30 minutes, depending on the polymer concentration. PEG is bioinert and therefore has to be biofunctionalized to promote cell growth as mentioned in the context of synthetic materials before. To facilitate cell growth in general, peptides containing the MMP-sensitive sequence GPQG↓IWGQ were integrated into the polymer network.⁷⁷ These peptides function as crosslinkers by featuring two terminal cysteines with thiol

groups in their side chains, which enable thiol-Michael addition with PEG-VS. In addition, the peptide with the sequence GRGDSPC was incorporated into the polymer network to facilitate cell adhesion (**Figure 1.7**). This hydrogel system provided the basis for the work described in the **Chapters 3, 4 and 5**.

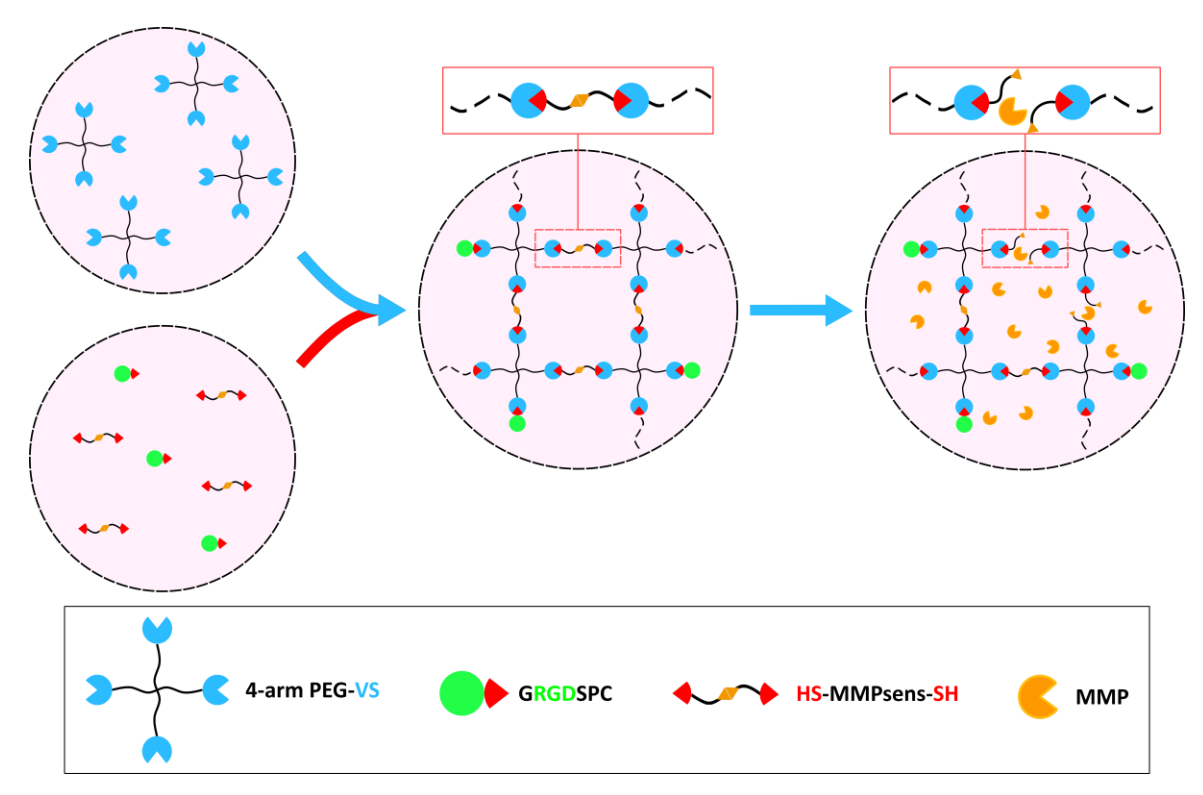


Figure 1.7: Crosslinking of PEG hydrogels via thiol-Michael addition. A polymer network is formed by mixing of a four-arm PEG-VS di-thiol peptide crosslinker that is sensitive for MMPs (HS-MMPsens-SH). Additionally, a peptide containing the integrin recognition site RGD with a terminal cysteine is bound to the polymer network to promote cell adhesion.

1.4 Biofabrication of Complex Tissues

Native tissues are versatile and unique in their function, which is a result of their cellular composition and spatial organization that differs between different tissue types and organs. 90 Thereby, tissues vary in their complexity and can range from simple, bidimensional to tubular structures with a small number of cell types, as well as hollow and complex bulk organs including multiple different cell types.⁹¹ Hydrogels are nowadays well-established in order to provide an artificial extracellular matrix that can support cell growth in vitro. However, the cellular and structural complexity of the respective tissue has to be recapitulated by combining tissue-specific cell types with structural cues to create functional tissue models. 92 While models of simple tissues, such as the skin, are already on the market⁹³, it still remains a challenge to create models of more complex organs. For example, multiple tissues are characterized by their anisotropic structures, which cannot be recapitulated by conventional bulk hydrogels that are isotropic by default. 92 Thus, our research group has developed the Anisogel technology to introduce directionality and align cells within hydrogels. This way, more relevant models of nerve tissues and platforms to facilitate their regeneration in vivo are created.94 However, microtissues with a native-like microenvironment are unable to capture the full functionality of complex organs. 95 Instead, they require cellular organization on a macroscopic scale to create tissues with physiologically relevant size and architecture that can serve as artificial organs for drug screening or transplantation. 96 Biofabrication combines the principles of engineering, biology, and material science and is defined as 'the automated generation of biologically functional products with structural organization from living cells, bioactive molecules, biomaterials, cell aggregates such as microtissues, or hybrid cellmaterial constructs, through bioprinting or bioassembly and subsequent tissue maturation processes'.97 Especially bioprinting, originally developed as an additive manufacturing technology, has emerged as a promising biofabrication technique due to its precise spatial control over material and cell deposition layer-by-layer that has now been widely applied in tissue engineering.98 This way, it allows to pattern cells and materials at a high resolution to mimic the cellular microenvironment that can be upscaled for manufacturing and production to recapitulate the biological complexity of native tissues in large constructs.99

Materials used as bioinks must meet specific criteria in order to be printable. Extrusion-based bioprinting, the most commonly used bioprinting technique, requires materials that exhibit steady flow until deposition and rapid stabilization upon delivery to create constructs with a well-defined architecture. Moreover, the bioink formulation and the printing process must be optimized to protect the cells from high shear stresses and maintain viability of cells in high densities within the bioink. These requirements have been successfully met by natural biomaterials, such as gelatin methacrylate (GelMA), which crosslinks upon exposure to light or cooling and is characterized by its innate biofunctionality as well as – compatibility. 99 Thus, natural bioinks are now widely established in the field while synthetic alternatives are scarce, despite their potential advantages in tunability and reproducibility.

1.4.1 Development of a Synthetic Bioink

The PEG hydrogel that I have been working with during this thesis is liquid upon mixing of the precursors and characterized by the transformation into a 3D solid network in a process called sol-gel transition upon thiol-Michael addition. Thus, this hydrogel is considered as an injectable material. Injectable materials present a promising alternative to cell delivery for tissue engineering as they allow for the minimally-invasive injection of cells with the liquid precursor mixture into the body where the material locally transforms into a hydrogel. 100, 101 At the same time, injectable materials are also extrudable due to their flow properties and therefore theoretically compatible with bioprinting. However, they lack post-extrusion stability, which makes it impossible to form defined structures. This limitation can be addressed by printing liquid matrix bioinks alongside stable template bioinks that provide structural integrity during the printing process in an approach called void-free 3D bioprinting. 102 This approach makes it possible to print materials that are widely considered unprintable and has been used in Chapter 3 to create synthetic printed constructs from a slowly crosslinking PEG-based bioink in combination with sacrificial template bioinks. Once the PEG-based matrix bioink is crosslinked, the sacrificial bioink can be removed, allowing for the formation of a stable construct with perfusable channels (Figure 1.8 A). Additionally, bioprinting requires hydrogels with specific physico-chemical properties to create stable constructs while supporting cellular functionality. For shape fidelity, hydrogels must possess sufficient stiffness to maintain their structure after deposition. However, this requirement hinders cellular activity, which require space and thus a softer matrix to grow. These contradicting requirements result in a biofabrication window with a narrow range of material properties that allow hydrogels to meet both the structural and biological demands. 103 This limits the number of available bioinks, which are almost exclusively based on natural polymers, characterized by their excellent printability and cell support as described above. To develop a synthetic bioink that meets the requirements for bioprinting, I addressed the increased stiffness needed to ensure shape fidelity by adjusting the hydrogel degradability to rapidly create more space for cells to grow. Combining MMP-sensitive crosslinkers (HS-MMPsens-SH) with hydrolytically degradable, ester-functionalized crosslinkers (HS-Esters-SH) in an 80:20 ratio accelerated hydrogel softening and thereby improved the growth of encapsulated spheroids consisting of HUVECs and NHDFs (Figure 1.8 B). Finally, we combined the printing method with the optimized hydrogel to print stable constructs that allowed for extensive growth of the encapsulated spheroids (Figure 1.8 C). As the cells grow within the printed construct, they contribute to stabilizing the construct and thereby compensate for the softening due to crosslinker degradation.¹⁰⁴ Thus, the combination of initially stiff bioinks with rapid degradation could present a promising approach to address the narrow biofabrication window and the limited number of available bioinks.

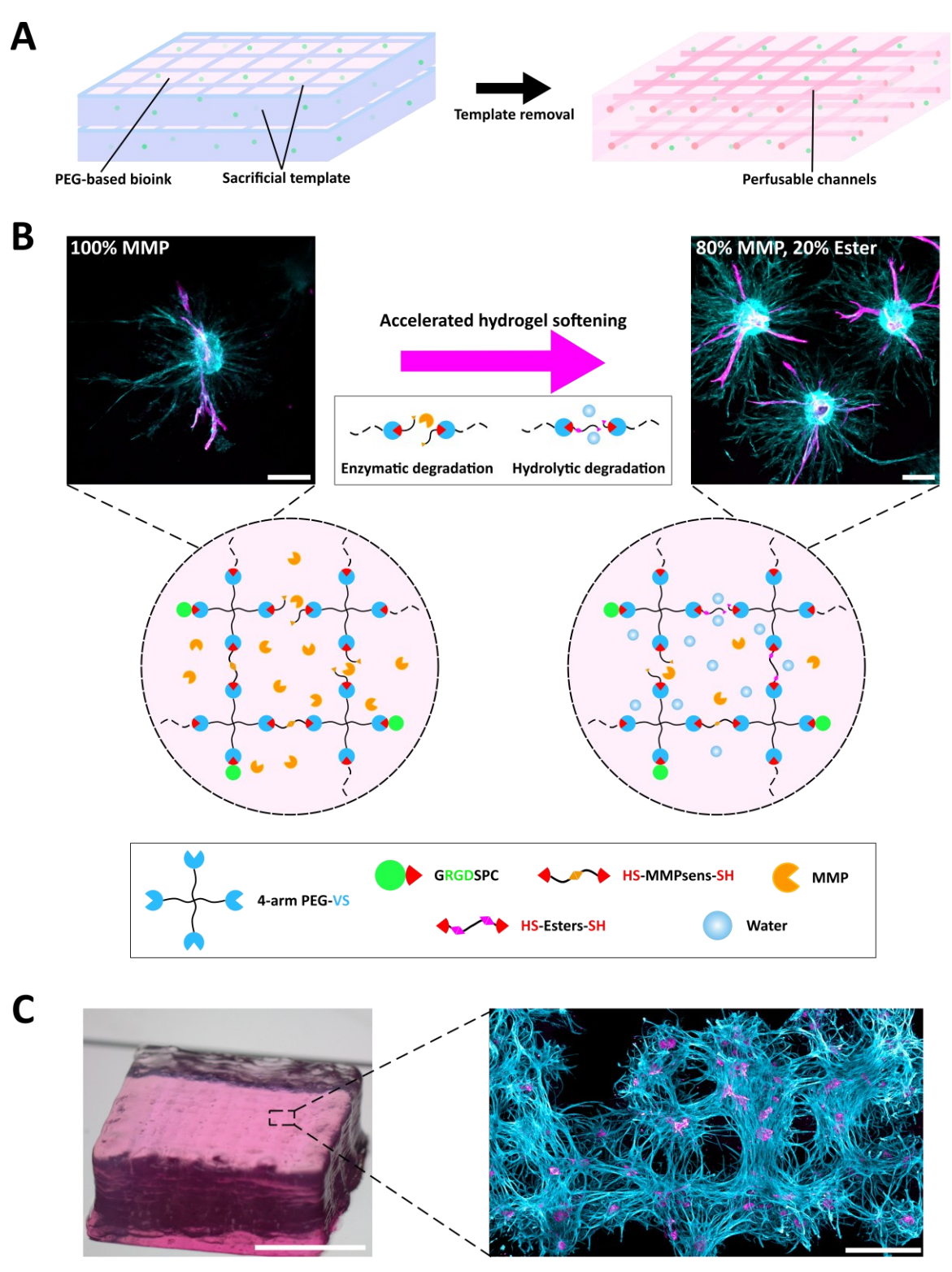


Figure 1.8: Hydrogel optimization for bioprinting. A) Void-free bioprinting of a slowly crosslinking PEG-based bioink with a sacrificial template bioink that can be removed to create perfusable channels. B) The degradation of this PEG-based bioink is optimized by combining 80% MMP-sensitive/20% ester-functionalized crosslinkers to improve the growth of spheroids consisting of HUVECs and NHDFs in a 3:1 ratio. Scale bars: 200 μ m. C) Bioprinting of this optimized bioink allows for the formation of printed construct that support extensive spheroid growth. Scale bars: 5 mm, 1 mm.

1.4.2 Need for Vascularization

The formation of complex and large tissue models that are suitable for transplantation requires cells to organize into dense structures that capture the functionality of their native counterpart. At the same time, these cells need to be supplied with oxygen and nutrients while metabolic waste products are removed. Otherwise, the tissue thickness is limited to 100-200 µm. In native tissues, this is addressed by the presence of an extensive vascular system, consisting of a 100 000 km network of arteries, capillaries and veins that ensures the cells' supply and guarantee their viability. Thereby, the arterial network transports nutrient-and oxygen-rich blood, which is distributed to all tissues through capillaries with a maximum distance of approximately 200 µm between each other, while low-nutrient and -oxygen blood is circulated back to the heart and lungs through the venous networks.

Vascular structures are forming in two different processes, called vasculogenesis and angiogenesis. Vasculogenesis thereby describes the de novo formation of blood vessels as one of the first functional structures during embryogenesis due to their critical importance to the developing embryo. Thereby, mesodermal progenitor cells aggregate to form blood islands, which then, triggered by growth factors like VEGF, differentiate into angioblasts and hematopoietic precursor cells. 109 Multiple blood islands subsequently fuse and build a primary capillary plexus, while the angioblasts differentiate into endothelial cells along the inner lumen of capillary plexus. 110 This structure builds the foundation to establish a functional circulatory network after its remodeling and maturation, followed by the recruitment of mural cells, which form the outer blood vessel wall. In parallel, the hematopoietic precursor cells differentiate into circulating blood cells in a process called hematopoiesis.¹¹¹ Once a functional vascular network is established, new blood vessels are formed from existing ones during angiogenesis. Triggered by hypoxic conditions and the production of nitric oxide, the sprouting blood vessel dilates resulting in an increased vascular permeability and the extravasation of plasma proteins, which provide a temporary scaffold for migrating endothelial cells. 112, 113 In addition, the interendothelial cell contacts are loosened and supporting pericytes detach, leading to blood vessel destabilization. A leading endothelial tip cell is formed that migrates out of the original blood vessel, guided

by an angiogenic signal such as a VEGF gradient. To sense the surrounding environment, the tip cell is equipped with filopodia. Neighboring endothelial cells of the tip cell transform into stalk cells that follow the tip cell's lead while proliferating, elongating, and forming a lumen. At the same time, the stalk cells release chemokines, which recruit pericytes to stabilize the forming neovessel. Once tip cells of two neighboring branches meet, they fuse to build a continuous lumen and the formed vessel is stabilized by the deposition of a basement membrane and the re-establishment of cell junctions.¹¹⁴

Tissue engineering aims to recapitulate the natural processes of vascular structure formation *in vitro* by combining relevant cell types, including endothelial and mural cells, with a supportive scaffold. However, like other cell types derived from soft tissues, endothelial cells are sensitive to the stiffness of their environment, which conflicts with the material requirements for bioprinting as described in Chapter 1.4.1 above. This is why in **Chapter 3**, I cultured spheroids consisting of 1 HUVECs/3 NHDFs, which in comparison to single cells are characterized by a high number of cell-cell contacts, locally increased concentrations of secreted MMPs and growth factors to promote cell growth, in our developed bioink. These spheroids are characterized by the growth of endothelial sprouts as a first step towards the formation of microvascular structures within printed constructs (**Figure 1.9 A**).

Despite having distinct functions and different sizes, ranging from microvessels and fine capillaries with 20 µm to large vessels, i.e. the aorta with 3.2 cm in diameter, the general structure of blood vessels is similar.^{117, 118} All vessel types consist of an innermost, single layer of endothelial cells, called the tunica intima. This endothelium is in direct contact with the blood and represents a cell barrier that regulates the trafficking of cells and nutrients, the permeability of the blood vessel as well as the blood fluidity. Moreover, the endothelium is a highly dynamic and heterogeneous structure, capable of adapting to pathophysiological stimuli and the specific needs of the underlying tissue.¹¹⁹ For example, endothelial cells of the blood-brain barrier exhibit very limited permeability to macromolecules due to the presence of unique tight junctions¹²⁰, whereas blood vessels in tissues like the liver, which require extensive exchange between the blood and their surrounding environment, have an endothelium with significantly higher

permeability. 121 The endothelium is depending on the blood vessel type further surrounded by outer layers of mural cells. These are called tunica media and tunica externa, while the description of an additional layer called tunica adventitia is suggested (Figure 1.9 B). 122 Thereby, the tunica media is visually the most prominent layer in large arteries as it consists of smooth muscle cells that help to withstand high pressure while retaining vessel elasticity. In addition, the tunical externa and adventitia represent the outermost layers that consist of compact and loose connective tissue, which contains a mixture of stem cells, fibroblasts, myofibroblasts and pericytes. 122, 123 During this thesis, I found that changing the ratios of HUVECs and NHDFs from 1:3 to 3:1 in spheroids results in the formation of a central lumen when cultured in PEG hydrogels. Similar to native blood vessels, the lumen is covered by an inner layer of endothelial cells as shown by CD31 immunostaining, which are surrounded by fibroblasts, resembling the connective tissue layers (Figure 1.9 C). This way, spheroids reorganize into uniluminal structures that resemble the crosssection of simplified blood vessels. This phenomenon was further investigated in Chapter 4 were I could show that the probability of lumen formation and the size of the lumen can be influenced by the stiffness of the surrounding hydrogels. Increasing the stiffness thereby lowered the probability of lumen formation and resulted overall in smaller lumens. In addition, the size of the spheroids has an impact on the probability of lumen formation and can be varied to create lumens with different sizes.

Since a spheroidal luminal structure is not yet functional, I sought for ways to create tubular structures with a continuous lumen to function as simplified blood vessels *in vitro*. I observed that when culturing spheroids in softer 2.5 w/v% as well as 3.4 w/v% PEG hydrogels, they could fuse with neighboring spheroids in close proximity to form a continuous lumen. In this case, the fusion process relies on chance and the density-dependent proximity of neighboring spheroids. In collaboration with the research group of Prof. Dr.-Ing. Fischer, we used acoustic patterning to align the spheroids in a more controlled manner, aiming to bring them into closer proximity and thereby guide their fusion. This way, oriented tubular structures were formed (**Figure 1.9 D**). The continuity of the lumen could be further proven by the addition of fluorescent beads, which infiltrated the lumens. This work showed that prevascularized spheroids that reorganize into uniluminal structures

can possibly serve as fundamental building blocks to recreate vascular structures *in vitro* and thereby ensure the nutrient and oxygen supply of complex tissue models.

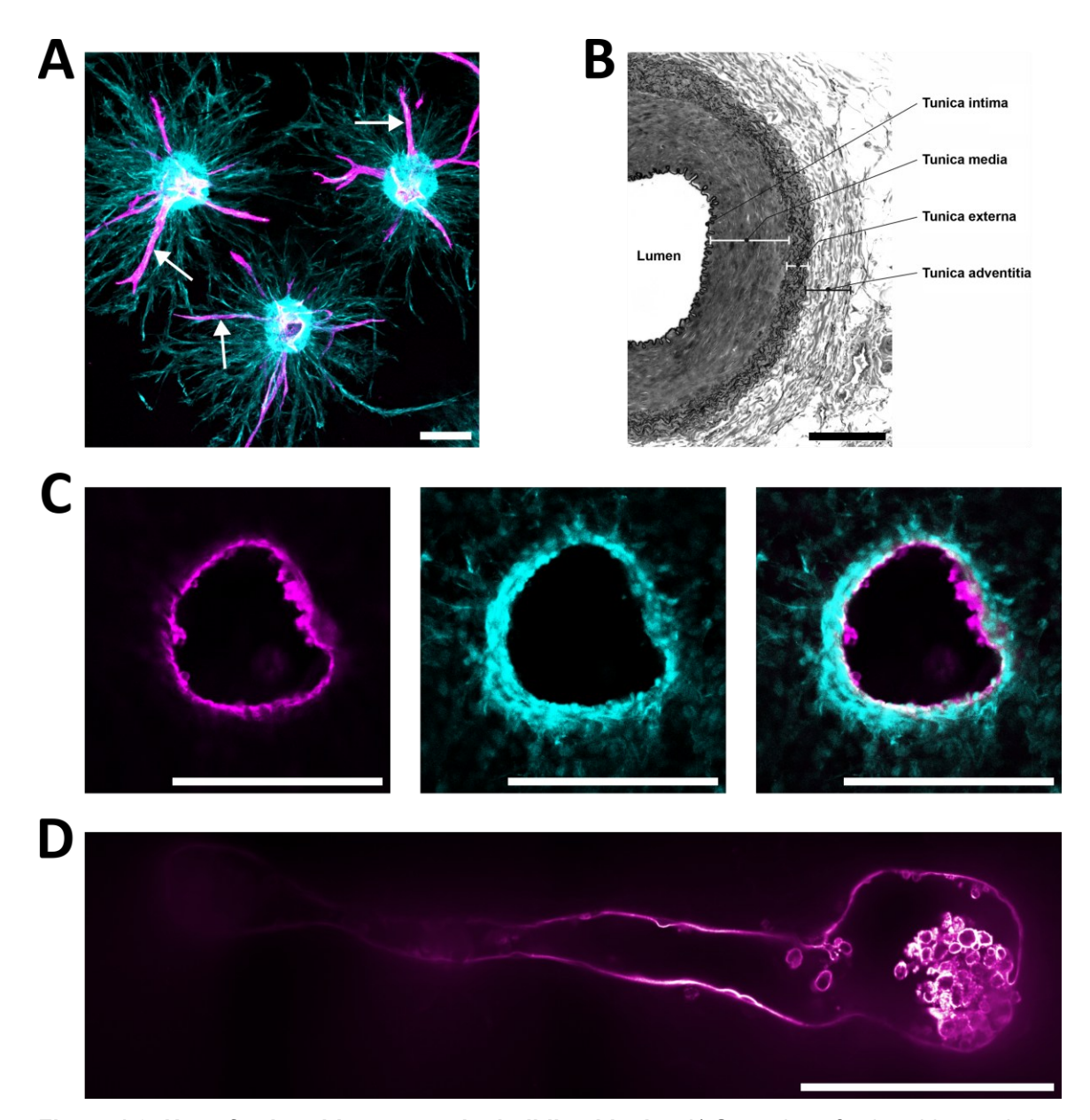


Figure 1.9: Use of spheroids as vascular building blocks. A) Sprouting of spheroids consisting of HUVECs and NHDFs in a 1:3 ratio in PEG hydrogels. Arrows highlight sprouts formed by endothelial cells. Samples are stained for F-actin (cyan) and CD31 (magenta). Scale bar: 200 μm. B) Histological crosssection of a canine artery showing the distinct layers of the blood vessel stained with trichrome. Scale bar: 200 μm. Copyright 2016, Wiley-VCH GmbH. Reproduced with permission. C) Lumen formation of spheroids consisting of HUVECs and NHDFs in a 3:1 ratio in PEG hydrogels. Samples are stained for F-actin (cyan) and CD31 (magenta). Scale bars: 200 μm. D) Fusion of neighboring spheroids into tubular structures with a continuous lumen. Samples are stained for CD31 (magenta). Scale bar: 200 μm.

1.5 Transplantation of Tissue Constructs

When transplanting engineered tissue construct, additional parameters have to be considered. The immune system is constantly screening the body for potentially harmful compounds including pathogens and foreign materials. While the use of autologous cells in tissue engineering can reduce the risk of an immune response upon transplantation, the materials used to fabricate these constructs represent a foreign body to the immune system that can be detected as a potential threat. This way, the artificial organ can trigger an unwanted foreign body response and activate an inflammatory cascade of events, starting with the recruitment of innate and adaptive immune cells. 124 At the same time, the implantation causes a forced tissue injury, which induces a physical trauma that leads to the formation of an edema and the enrichment of plasma proteins at the implant site. A variety of plasma proteins then adsorbs to the surface of the artificial organ to mark it as a foreign body. Once the immune cells recognize and confirm the implanted material as a foreign body, they initiate an inflammation reaction within minutes to hours as a response to tissue injury. 125 While neutrophils are the first responders to a foreign body, macrophages are mainly involved in the foreign body response to biomaterials. 126 They try to degrade the implant by phagocytosis or release of degrading enzymes as well as reactive oxygen species, which can impair the stability of the implant. 127 In case the macrophages cannot degrade the implant, the inflammatory reaction transforms to a chronic fibrotic stage during which the implant is encapsulated in fibrous tissue. This way, a fibrotic capsule is formed that shields the implant from the surrounding tissue and can ultimately lead to its failure and rejection. 128

As previously mentioned, natural materials are characterized by their excellent biocompatibility. However, since they are often derived from animals, they carry antigens that are foreign to the human immune system and thus come with the risk of rejection upon transplantation. ¹²⁹ In addition, products from biological sources can be contaminated due to impurities with the risk of disease transfer. ⁷¹ While the use of animal-derived materials is well-established in medical devices, this risk is further acknowledged by the FDA, which therefore provides guidance to control animal tissue sources as well as recommendations and methods to remove pathogens from the final product. ¹³⁰ In this context, the bioinert properties of PEG

are of advantage as PEG-based transplants can minimize the risk of foreign body responses and transplant rejection by creating a biologically silent environment. 81 Additionally, the transplanted tissue must not only be not recognized as a foreign body by the immune system but needs to be integrated into the host environment and vascularized by blood vessels. 131 Here, the versatility and tunability of PEG allow for specific biofunctionalizations to promote tissue infiltration and the integration of the transplant into the host environment. For example, the modification of PEG hydrogels with VEGF improves vascularization upon transplantation in the subcutaneous space. 132 These advantages underline the significance of developing suitable PEG-based hydrogels and bioinks to engineer complex tissues *in vitro* that can be in the next step successfully transplanted.

1.5.1 Controlling Degradation in PEG Hydrogels

After successful transplantation and integration of the tissue substitute into the host environment, additional requirements have to be addressed to facilitate the transplant to restore, maintain, improve or replace the function of the specific tissue type. The *in vivo* environment differs vastly from the *in vitro* situation as the artificial tissue is transferred from a controlled to a dynamic and heterogeneous environment that can be hardly regulated. Yet, is it important to create a transplant that matches the mechanical properties of the targeted tissue and application, while it is degrading into non-toxic compounds over time that can be metabolized and cleared from the body. 133 Thereby, the degradation rate of the implanted material is crucial and has to match the healing process and tissue formation in order to ensure its functionality and viability. If the material degrades faster than the surrounding tissue regenerates, the encapsulated cells will be isolated from the native ECM and the formed tissue ends up being defective. 124 However, if the material stays too long at the site of transplantation, it could negatively affect the tissue regeneration process and may lead to encapsulation of the transplant, poor transplant integration, scar tissue formation and immune responses. 124, 134, 135 While the rate of degradation can be partly controlled by the crosslinking density or integration of degradation sites with different sensitivities, adjusting the crosslinking density also influences the stiffness of the hydrogel, which may impact its mechanical compatibility with the tissue environment. 134 Moreover, tailoring the sensitivity of degradation sites to match the in vivo environment remains challenging due to its mentioned dynamic nature and complexity, making a precise prediction difficult. This is why I worked on a proof-of-concept project in collaboration with the research group of Prof. Andreas Herrmann to create a degradation system that is independent of external factors and can be controlled on-demand, which is presented in Chapter 5. Hereby, I integrated thrombin cleavable peptides that are functionalized with thiols (HS-TCP-SH) and were provided by Kuan Zhang from Prof. Andreas Herrmann's research group into our hydrogel system. These can be degraded in a second step by thrombin that is externally added through the cell culture media. This way, it is possible to significantly soften the PEG hydrogel on-demand. Combining HS-MMPsens-SH with HS-TCP-SH in a 70:30 ratio thereby results in improved cell growth and migration from spheroids encapsulated into the hydrogel (Figure 1.10 A). As part of this study, I have demonstrated that the hydrogel degradation and cell growth can be further influenced by adjusting the crosslinker ratios, thrombin concentration, and timing of thrombin exposure. While this system has proven effective for use in vitro, controlling the local degradation of thrombin-cleavable crosslinks in vivo for example by injection of thrombin is difficult. Therefore, we sought to conjugate a biocatalytic system consisting of thrombin and hirudin into the polymer network that can be activated with low intensity focused ultrasound (LIFU). In contrast to other non-invasive methods like light, heat or magnetic fields, ultrasound can deeply penetrate into human tissues to induce local effects with low signal attenuation. 136 While high intensity ultrasound in general can damage and ablate tissues due to heating, pressure changes and cavitation, LIFU can be safely applied to sensitive tissues such as the brain without adverse effects. 137 For this purpose, Kuan Zhang produced thrombin and hirudin modified with thiols that I integrated into the hydrogel network by covalently coupling this biocatalytic system to the four-arm PEG-VS via thiol-Michael addition. Upon exposure to LIFU, the non-covalent interaction between thrombin and hirudin is interrupted which activates thrombin to cleave the surrounding thrombin-cleavable crosslinkers (Figure 1.10 B). The activation of thrombin is thereby reversible as hirudin binds to thrombin and inhibits its activity again as the LIFU exposure stops. This allows for precise control over thrombin activity and hydrogel degradation, which can be further combined with the ultrasound-triggered release of biomolecules to promote tissue regeneration. 138

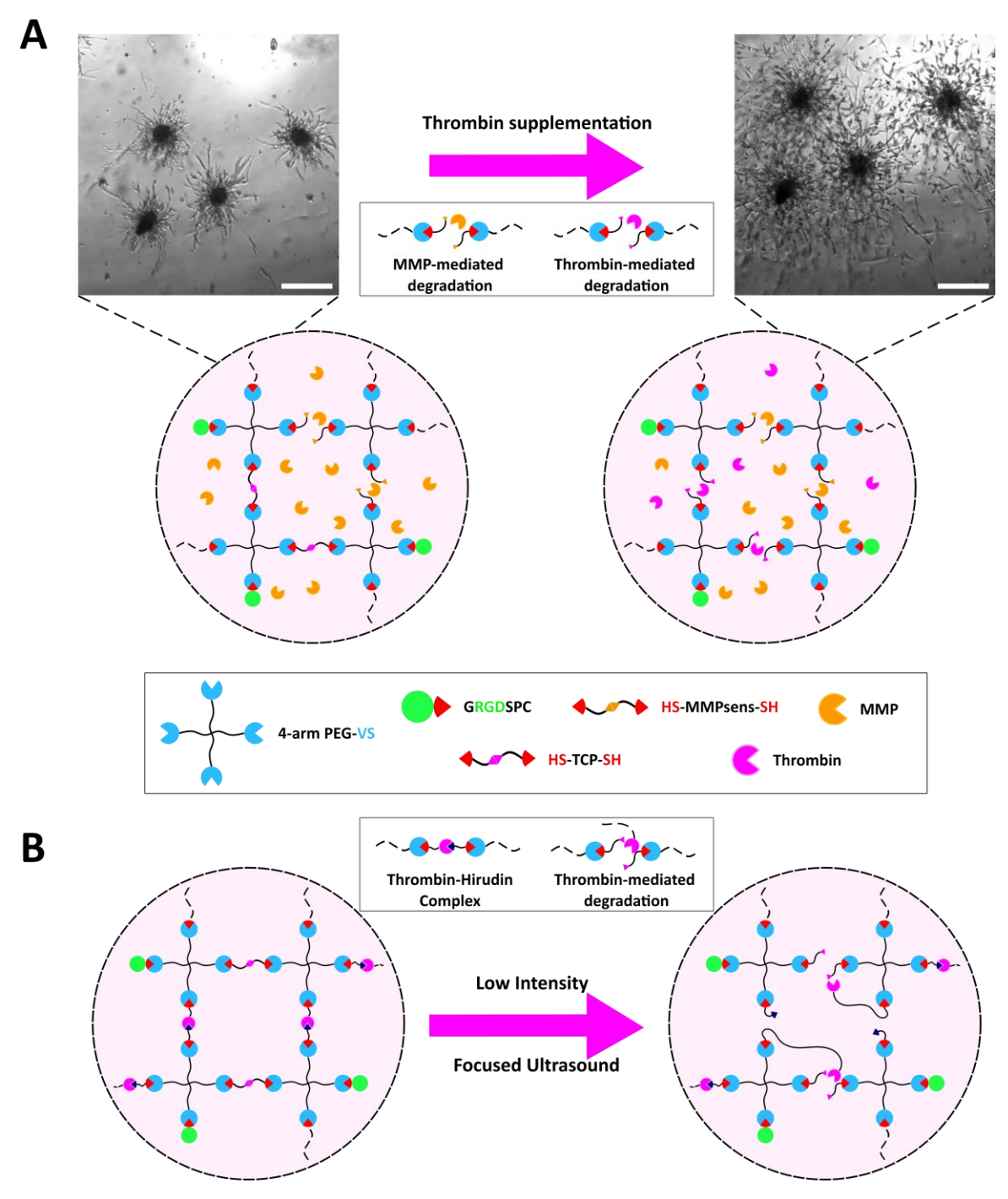


Figure 1.10: Thrombin-mediated on-demand degradation of PEG hydrogels. Thrombin-sensitive PEG hydrogels are formed by the introduction of a thrombin-cleavable crosslinker (HS-TCP-SH) that can be degraded by the supplementation of thrombin through the media to improve cell growth (A). Scale bars: $200 \ \mu m$. Thrombin and its inhibitor hirudin, both modified with thiols, can be integrated into the hydrogel network to activate thrombin upon ultrasound exposure (B).

1.6 Granular Hydrogels and Microporous Annealed Particle Scaffolds

While hydrogels are a well-established platform for 3D cell culture, their nanoporous polymer network, with pore sizes typically an order of magnitude smaller than cells, presents a significant limitation to the formation of complex tissues. Due to the size mismatch between the hydrogel's pores and cells, the cells have to "work hard" to degrade the material and thereby create space to migrate, proliferate and grow. 139 Although external degradation mechanisms can be applied to create additional space for cell growth, hydrogels often result in constructs with minimal cell fractions, limited cell-cell interactions and excessive amounts of synthetic material dominating the constructs. 140 In contrast, native tissues are characterized by the abundancy of cell-cell interactions, necessary for tissue function and homeostasis. 141 Thus, granular hydrogels become more and more relevant, which are characterized by a higher degree of porosity and space for cells to grow and interact. 142 One class of granular hydrogels is called microporous annealed particle (MAP) scaffold and consists of microgels in various shapes that are interconnected via physical or chemical crosslinks. Similar to porous solid scaffolds described in Chapter 1.2.3, the cells infiltrate MAP scaffolds from the outside and migrate through the interstitial space between neighboring microgels without the need for material degradation. This makes MAP scaffolds a powerful tool for regenerative medicine as they for example improve wound healing by providing structural support to the surrounding, regenerating tissue. 143 However, in vitro this method leads to an inhomogeneous cell distribution and a cellular gradient with most cells accumulating on the surface of the MAP scaffold and only a few infiltrating its core. To address this issue, I collaborated with Selin Bulut from Prof. Andrij Pich's research group at DWI and developed cell-induced interlinked MAP scaffolds with a homogeneous cell distribution as described in Chapter 6. Instead of sequentially annealing the microgels in a first step and adding the cells to the formed MAP scaffolds in a second step, this method describes a one-step procedure where the cells are mixed with cell-adhesive microgels. Thereby, the cells can adhere to multiple microgels at the same time and glue them together (Figure 1.11). In addition, the scaffold formation is solely based on cellular selforganization, which is fundamental for the development of functional and organized structures in living systems.¹⁴⁴ While these processes are independent from external factors, we can actively influence them during the construct assembly by adjusting parameters such as the cell/microgel ratio, the microgel stiffness or the well geometry. This allows us to create constructs with different shapes. Tissue engineering leverages these cell-driven processes to build complex tissues from stem cells that differentiate and self-organize through cell-cell and cell-matrix into so called organoids, which replicate key aspects of specific organ architectures and functions.¹⁴⁵ However, the reliance on cellular self-organization presents a significant challenge as it limits reproducibility and maturity of organoids.¹⁴⁶ By enabling control over this process, our approach holds the potential to address this challenge and facilitate the reproducible formation of next-generation organoids.

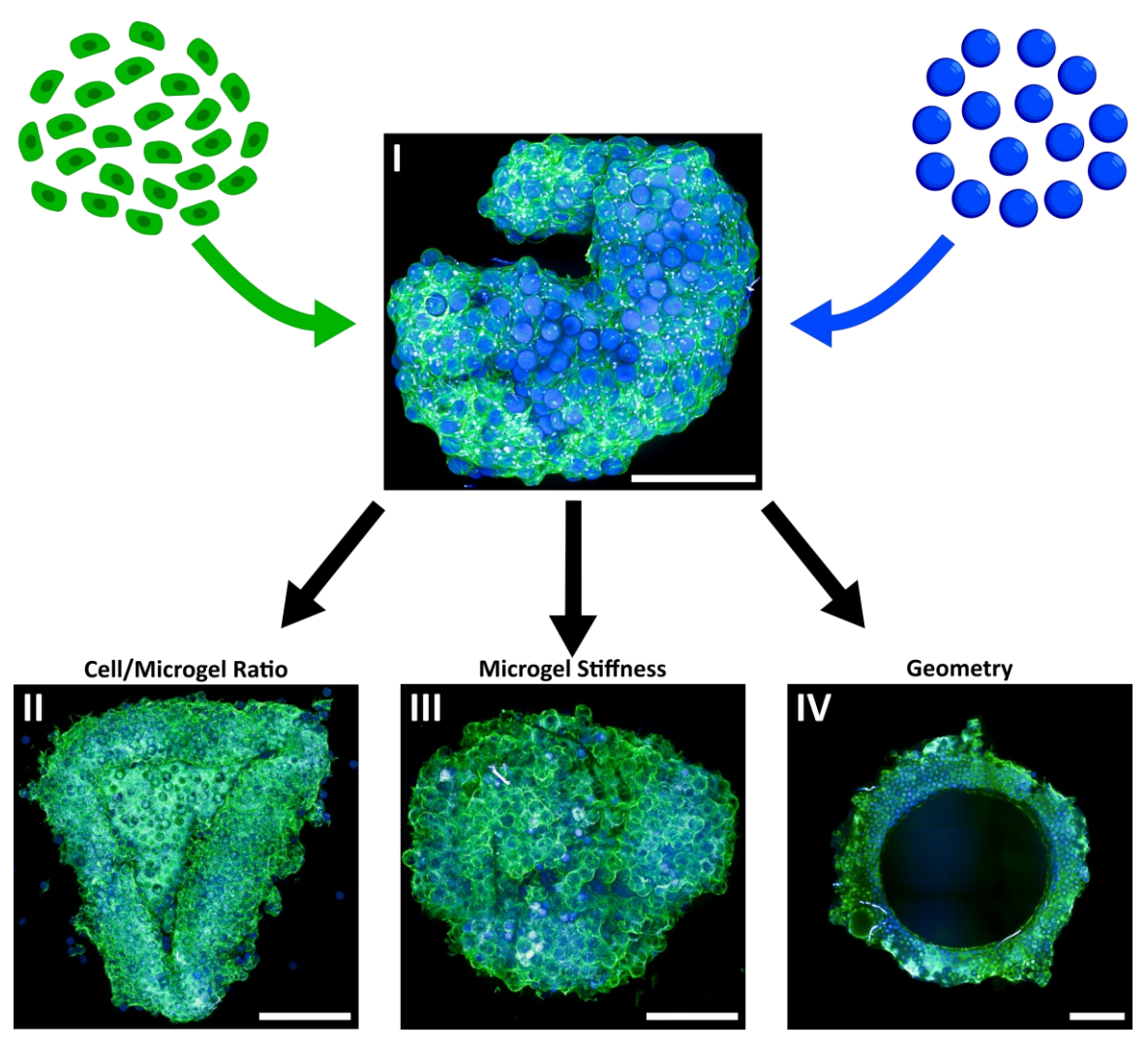


Figure 1.11: Formation of cell-induced interlinked MAP scaffolds. Cell-induced interlinked MAP scaffolds are formed via cellular self-organization upon mixing of normal human dermal fibroblasts (green) with cell-adhesive microgels (blue). The self-organization process can be influenced by adjusting the cell/microgel ratio, the microgel stiffness or the well geometry, resulting in the formation of scaffolds with different shapes. Scale bars: 500 µm (I), 1 mm (II, III, IV).

1.7 Summary

In this thesis, I explore different strategies to create complex tissues by optimizing materials that are compatible with biofabrication techniques to support cell growth, while investigating the formation of vascular structures, essential for ensuring the long-term viability of the engineered constructs. After discussing the motivation of my work to create complex tissues and their potential use in clinical transplantation as well as in vitro model systems, Chapter 2 gives an overview of the current state of the art in that field. This includes methods to control the porosity of artificial matrices, strategies to create vascular structures on different scales, and different bioprinting techniques used for the fabrication of complex tissues. In Chapter 3, I describe the optimization of a PEG-based bioink to support the growth of prevascularized spheroids, which are sensitive to the stiffness of the surrounding matrix and preferably grow in soft hydrogels. By combining hydrolytic and enzymatic degradation mechanisms, I compensate for the initial high stiffness required to ensure the shape fidelity of bioprinted constructs, while enabling extensive cellular network formation. This approach bridges the gap between the mechanical demands of bioprinting and the biological needs of 3D cell culture, enabling rapid material softening to create space for cell growth. In Chapter 4, I demonstrate that these spheroids can reorganize into uniluminal structures resembling the inherent structure of simplified blood vessel at a 3 HUVECs/1 NHDF ratio and depending on the spheroid size and hydrogel stiffness. Additionally, such spheroids can fuse with neighboring spheroids to create tubular structures with a continuous lumen. For better control over hydrogel degradation, which is particularly challenging to regulate in vivo after transplantation, the establishment of an on-demand hydrogel degradation mechanism is presented in **Chapter 5**. The integration of thrombin-cleavable crosslinkers into PEG hydrogels allows for controlled degradation via thrombin that is supplemented to the media or integrated into the polymer network as part of a biocatalytic system that can be activated with ultrasound. While media-supplemented thrombin has proven effective to promote cell growth in vitro, the ultrasound-triggered degradation is particularly promising for in vivo application. Finally, Chapter 6 describes the formation of cell/microgel assemblies without the need for material degradation. While this process is fully driven by cellular self-organization, it can be influenced by external guiding cues.

2 State of the Art

After outlining the motivation and objectives of this thesis, the following chapter provides an overview of contributions from other research groups as well as the current state of the art in the field of tissue engineering and biofabrication that are relevant for my own work. I present key advancements and methods to control porosity in injectable artificial matrices, essential to facilitate cell growth, as well as strategies to engineer vascularization on different scales to sustain tissues long-term *in vitro*. Finally, I discuss bioprinting techniques that build up on materials, which support cell growth as well as vascularization strategies to create complex functional tissues. By examining these existing strategies, this chapter establishes the foundation to understand how this thesis builds upon and contributes to the field and its associated challenges.

2.1 Controlling Porosity in Injectable Matrices

2.1.1 Hydrogel Degradation

The degradation of hydrogels, used as artificial matrices for cell culture, is one of the most important parameter to consider in order to promote the growth of cells that are encapsulated in the hydrogel or their infiltration from outside. As discussed in Chapter 1, I utilized multiple degradation mechanisms throughout this thesis to facilitate cell growth in synthetic polyethylene glycol (PEG) hydrogels, including hydrolytic, enzymatic and externally triggered, on-demand degradation (Figure **2.1**). Hydrolytic degradation thereby represents the simplest and least controllable form of degradation that is used for a broad range of biomedical applications. For example, Zustiak and Leach developed a hydrolytically degradable PEG hydrogel that crosslinks via thiol-Michael addition of PEG vinyl sulfone (PEG-VS) with an ester-functionalized di-thiol PEG crosslinker. 147 They showed that the degradation rate can be influenced by varying the molecular weight of the crosslinker, which can be utilized for the controlled release and delivery of drugs and provides a suitable environment for fibroblast culture. 147 In a more sophisticated setup with juvenile bovine chondrocytes cultured in photopolymerizable PEG hydrogels, Neumann et al. demonstrated that hydrolytic degradation of introduced ester bonds can promote the cellular deposition of a cartilaginous tissue matrix. 148 The

extracellular matrix (ECM), secreted by the chondrocytes with cartilage-specific deposition of collagen type II and aggrecan, thereby resulted in an 8-fold increase of the compressive tissue modulus over a period of 28 days and resembled the native ECM in structure and organization. 148 In addition, hydrolytic degradation mechanisms resulting in the rapid softening of synthetic hydrogel matrices has been shown to influence the fate of encapsulated stem cells. Gjorevski et al. found that intestinal stem cells cultured in a stiff PEG hydrogel are characterized by significantly enhanced expansion, which is directed by a yes-associated protein (YAP)-dependent mechanism. 149 However, the differentiation and reorganization of single cells into intestinal organoids requires a softer matrix. Therefore, the authors incorporated hydrolytically degradable moieties to create mechanically dynamic PEG hydrogels. This way, an initially stiff hydrogel that softens over time can support both intestinal stem cell expansion as well as organoid formation. 149 This work was a major inspiration for the design of my hydrogel system that softens over time to meet the requirements for both bioprinting and 3D cell culture by combining hydrolytic and enzymatic degradation mechanisms. While natural ECMderived biomaterials are inherently susceptible to enzymatic degradation mechanisms by different classes of MMPs, Lutolf et al. designed peptides with a sequence that is sensitive for MMPs and can be incorporated into synthetic hydrogels.⁷⁷ This way, cell growth in synthetic hydrogels can be promoted by mimicking the MMP-mediated invasion of the natural ECM. The sensitivity and kinetic parameters of the introduced MMP substrate with the sequence GPQG\IWGQ, which laid the foundation for the degradability of PEG hydrogels used in this thesis, can be altered by the addition of charged amino acids.⁷⁷ In addition to modifications of the specific peptide sequence, Patterson and Hubbell screened additional peptide sequences susceptible to MMP-mediated degradation with the aim to develop material formulations with a more rapid response to enzymatic remodeling. 150 They characterized 17 MMP substrates with different sensitivities for MMP-1 and MMP-2, enabling the degradability of hydrogels to be fine-tuned according to specific applications. At the same time, hydrogels can be tailored to match the MMP expression profile of different cell types, such as the dominant expression of MMP-2 by endothelial cells and MMP-1 in case of fibroblasts. 150 In our research group, synthetic PEG hydrogels susceptible to MMPs

lay the foundation for the Anisogel. Here, ultrasoft hydrogels with a storage modulus of 10 Pa support the growth of encapsulated dorsal root ganglia and orient neurite extension by addition of magnetically aligned rod-shaped microgels. ^{151, 152} This highlights the effectiveness of synthetic MMP-sensitive hydrogels to support the growth of complex neuronal structures and demonstrates their potential as a powerful tissue engineering platform.

While MMP-mediated degradation represents a cell-derived remodeling mechanism, it is inherently reliant on cellular activity and lacks external control. Therefore, degradation strategies have been developed that can be triggered by external factors on-demand. For example, Zhang et al. developed mechanoresponsive hydrogels that display on-demand stiffening or softening by transforming mechanical forces into chemical processes. 153 For that purpose, they incorporated a biocatalytic system consisting of thrombin and its inhibitor hirudin into PEG hydrogels. Upon stretching of the hydrogel, the non-covalent inhibitory interaction between thrombin and hirudin is reversibly interrupted, which switches the enzymatic activity of thrombin on. Self-softening behavior of the hydrogels was facilitated by the integration of thrombin-cleavable crosslinkers into the hydrogel that are cleaved by the activated thrombin. 153 This idea was fundamental for the collaboration with Kuan Zhang from Prof. Andreas Herrmann's research group to facilitate on-demand degradation of PEG hydrogels with low intensity focused ultrasound using the same biocatalytic system as presented in Chapter 5 of this thesis. In addition, the authors present self-stiffening behavior of the hydrogels by adding fibrinogen to the hydrogel mix, which can be polymerized to form fibrin fibers catalyzed by thrombin. 153 Light represents another external trigger that is commonly used for polymerization and degradation mechanisms. Narayan et al. developed an elastin-like protein hydrogel with a light-responsive domain that can undergo multiple cycles of reversible sol-gel and gel-sol transition.¹⁵⁴ Thereby, light with a wavelength of 400 nm triggers the assembly of monomeric domains into tetrameric structures that disassemble again upon exposure to light with a wavelength of 500 nm. At the same time, the resulting hydrogel supports the viability and proliferation of encapsulated cells that can be released on-demand, making it a promising cell delivery system. *In vivo* studies further demonstrate that the sol-gel transition can be initiated with light after subcutaneous injection, while

the hydrogel degrades substantially within 72 h.154 In addition to controlling mechanical hydrogel properties in vivo with light, such systems are also used to study the influences of biophysical cues on mechanosensitive cells in vitro. The stiffness of muscles is known to increase during aging and in case of diseases like fibrosis. At the same time, muscle stem cells are sensitive to the stiffness of their surrounding environment and lose their potential to regenerate during aging and diseases. 155 In this context, Madl et al. suggested that muscle stem cells develop a mechanical memory of their biophysical microenvironment during their activation that determines their fate. 155 To prove their hypothesis, they cultured muscle stem cells on dynamic hydrogels that, triggered by light, can stiffen or soften on-demand. When the cells are cultured on stiff hydrogels for 72 h, they stopped to expand and differentiated prematurely, resulting in a quiescent-like state, which could not be reversed by subsequent softening of the hydrogel substrate. In contrast, cultivation for 72 h on a soft hydrogel was sufficient to preserve the expansion potential of the stem cells, making the cells resilient to subsequent hydrogel stiffening. 155 These studies demonstrate that regulating hydrogel degradation is essential for guiding in vitro tissue formation, the design of precise drug delivery systems, achieving controlled tissue regeneration in vivo, and developing platforms to study how changes of mechanical properties affect cellular fate in a controlled environment.

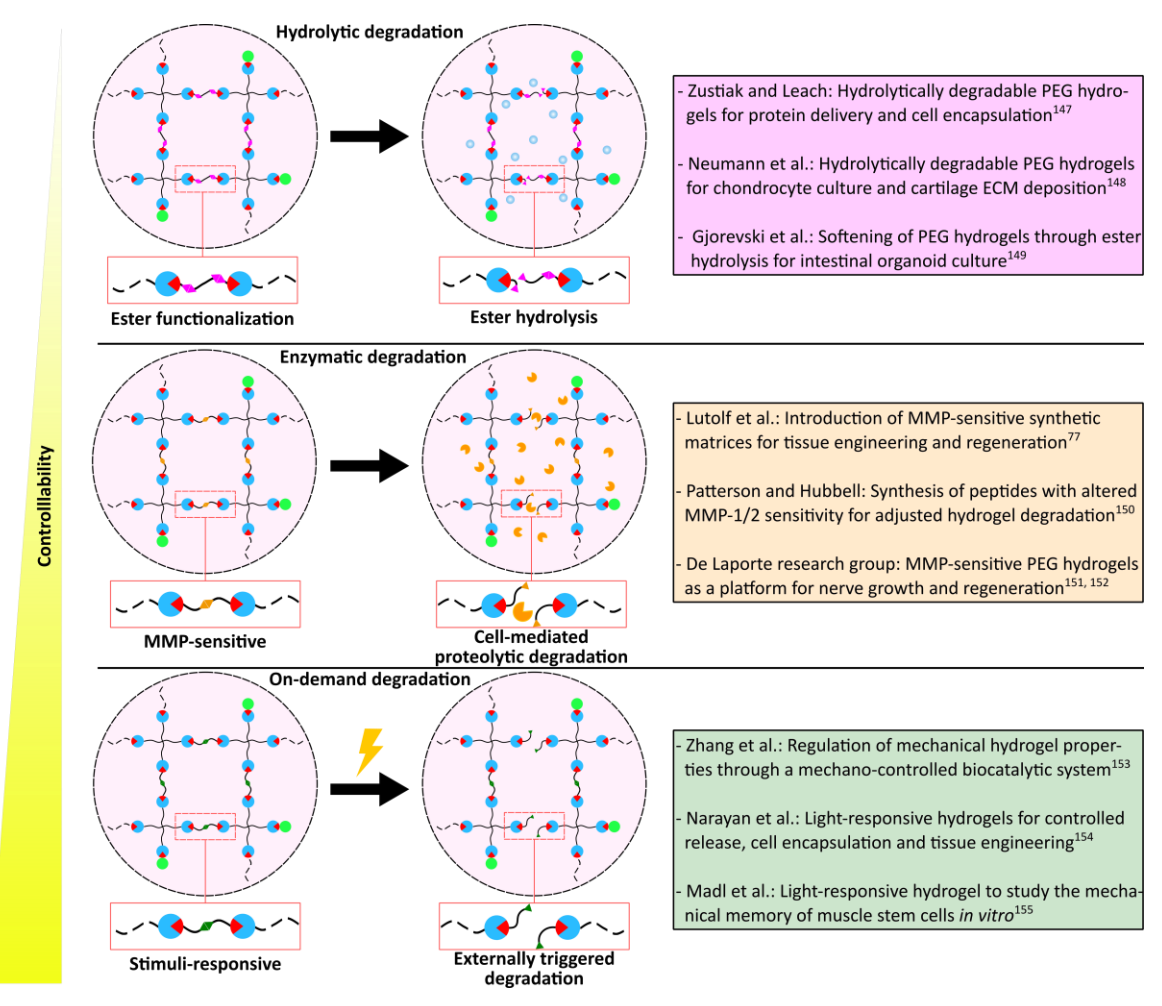


Figure 2.1: Overview of state of the art hydrolytic, enzymatic and externally triggered degradation mechanisms and their use in tissue engineering.

2.1.2 Microporous Annealed Particle Scaffolds

As an alternative to hydrogels, the research group of Prof. Tatiana Segura introduced microporous annealed particle (MAP) scaffolds in 2015, which facilitate cell infiltration without the need for previous material degradation. Griffin *et al.* produced spherical PEG-based microgels that are MMP-sensitive and either functionalized with lysine (K) or glutamine (Q) peptides that served for microgel annealing via non-canonical amide linkage, catalyzed by Factor XIII. This way, MAP scaffolds were formed with pore sizes in the range of 10-35 µm depending on the size of the microgels, which provided enough space for cells to infiltrate and grow within the scaffold (**Figure 2.2**). Moreover, MAP scaffolds are injectable and can be molded into any shape, which make them promising for applications in regenerative medicine. The authors showed that MAP scaffolds can be locally injected and annealed at the site of injury in a murine wound-healing model. MAP

scaffolds thereby accelerated wound closure and supported wound healing with a lower inflammatory immune response in comparison to non-treated controls as well as conventional bulk hydrogels.¹⁴³

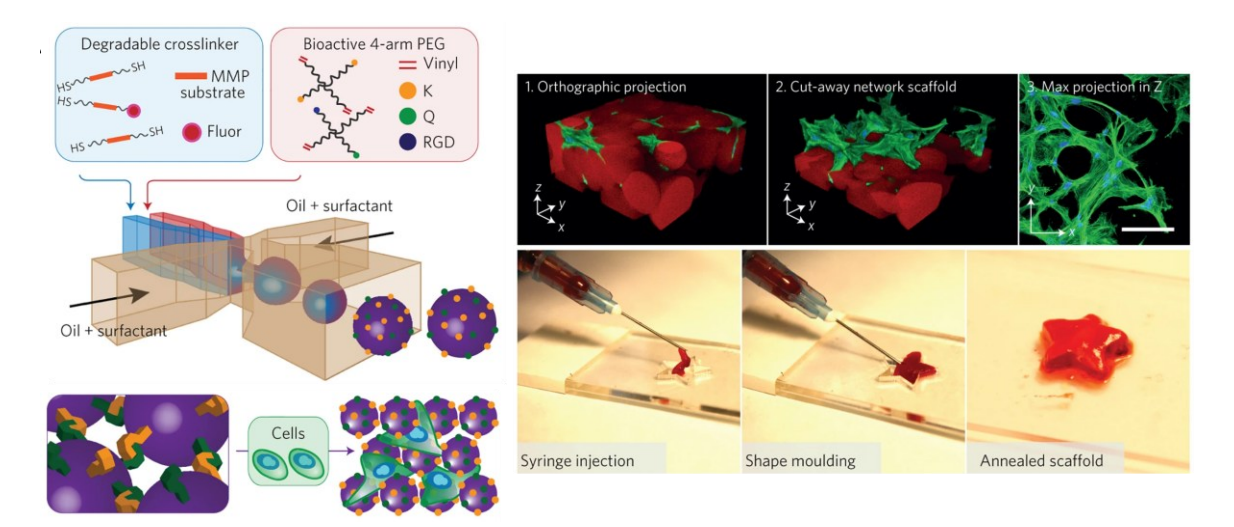


Figure 2.2: MAP scaffolds based on spherical microgels. Microgels functionalized with K and Q peptides are produced via plug-flow microfluidics, crosslinked via thiol-Michael addition, and subsequently interlinked using Factor XIII. The open porous network provides space for cells to proliferate within the MAP scaffolds and build interconnected networks in the interstitial space of the microgels. MAP scaffolds can be injected to form complex shapes that are fixed after microgel annealing. Scale bar: 100 μm. Copyright 2015, Springer Nature. Reproduced with permission.¹⁴³

While MAP scaffolds based on spherical microgels are the current gold standard, opportunities to tune their porosity are limited to the packing density and the diameter of the microgels. Additionally, increasing the particle diameter results in bigger pores but since the aspect ratio of the particle is constant, the void volume fraction of the MAP scaffolds remains the same. 156 Therefore, anisotropic rodshaped microgels are established as alternative building blocks, leading to MAP scaffolds with larger pores compared to those formed with spherical microgels. The pore size, number, and interconnectivity can be further adjusted by modifying the aspect ratio of the microgels. 157 Rommel et al. reported for the first time the formation of such MAP scaffolds. 158 Here, PEG microgels functionalized with primary amine and epoxy groups are produced via continuous on-chip gelation in microfluidics via free-radical polymerization. Amine and epoxy functionalized microgels are then mixed to interlink via amine-epoxy click reaction to build MAP scaffolds with pore sizes in the range of 30 µm to above 150 µm. When functionalized with RGD, these MAP scaffolds support the infiltration and growth of normal human dermal fibroblasts (NHDFs) and human umbilical vein endothelial

cells (HUVECs), which fill the open pores and build elongated prevascular structures (Figure 2.3 A). Additionally, the microgels facilitate diffusion of oxygen and nutrients and thereby serve as artificial "blood vessels" that prevent the formation of a necrotic core within the constructs after the cells fill all the remaining open pores. 158 In another study from our research group, Suturin et al. investigated the influence of rod-shaped microgels with different aspect ratios on the porosity of MAP scaffolds. 159 Microgels with aspect ratios of 5, 10 and 20 are produced via particle replication in nonwetting templates and afterwards interlinked via epoxyamine click chemistry as reported by Rommel et al. (Figure 2.3 B). These MAP scaffolds are characterized by porosities in the range of 65-90% and mean pore sizes of 39-82 µm for microgels with varying aspect ratios of 5 to 20. When fibroblasts are cultured on the MAP scaffolds infiltration of the open pores is observed for all conditions, while it takes longer for the cells to fill up the larger pores, which results initially in a higher fraction of remaining void spaces with increasing aspect ratio of the microgels. In these cases, the cells cover the microgel surfaces before they start to fill up the remaining open pores to form systems that are characterized by a smaller amount of synthetic material in comparison to the fraction of cells within the scaffold. 159

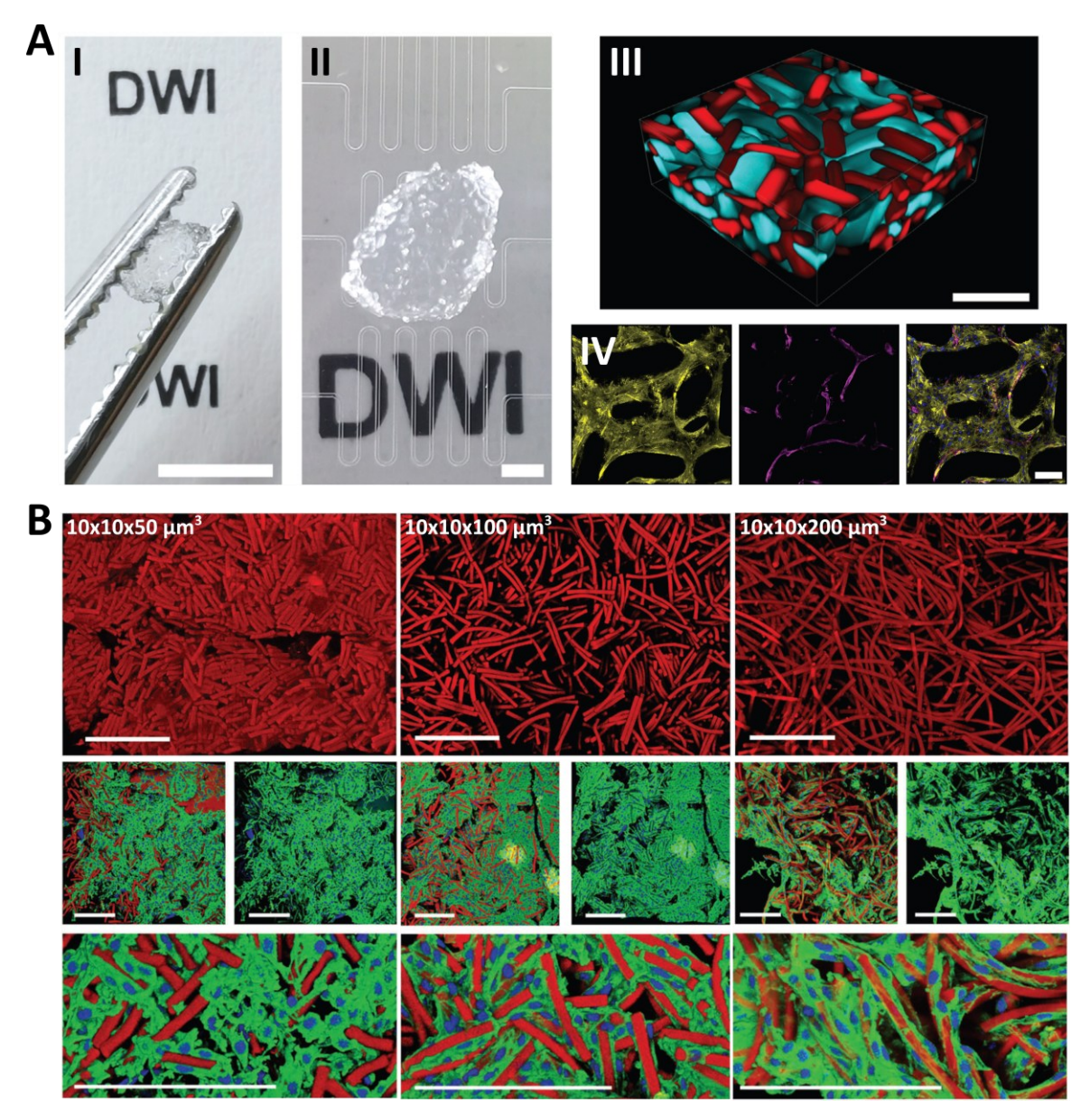


Figure 2.3: MAP scaffolds based on rod-shaped microgels. A) I, II) Interlinked MAP scaffold based on rod-shaped microgels produced via plug-flow on-chip gelation microfluidics. III) Epoxyfunctionalized microgel rods (red) are mixed with the same number of amine-functionalized microgel rods (cyan) for their interlinking. IV) NHDFs are cultured for 5 days inside the scaffolds before HUVECs and additional NHDFs (1:3 ratio) are added for 14 more days. Samples are stained for nuclei (blue), F-actin (yellow) and CD31 (magenta). Scale bars: I) 5 mm; II) 1 mm; III) 500 μm; IV) 100 μm. Copyright 2022, Wiley-VCH GmbH. Reproduced with permission. B) Formation of MAP scaffolds based on rod-shaped microgels with aspect ratios of 5, 10 and 20. L929 cells are cultured on the scaffolds for 7 days and infiltrate the pores. Microgels are shown in red, F-actin in green and nuclei in blue. Scale bars: 200 μm. Copyright 2022, Wiley-VCH GmbH. Reproduced with permission. 159

2.2 Methods to Engineer Vascularization on Different Scales

With the aim to create tissues in the lab, the need to integrate vascular structures and to ensure the cell supply with nutrients and oxygen came. Research groups all around the world are working on different strategies to create functional vasculature, ranging from microvascular networks that mimic the blood capillaries to larger structures that resemble the arteries and veins. The following sections will explore some of the strategies to achieve vascularization on different scales, starting with cellular self-assembled vascular networks.

2.2.1 Self-Assembled Vascular Networks

2.2.1.1 Single Cell Culture

When endothelial cells are co-cultured with supportive mural cells in a suitable matrix and are supplied with the right growth factors, they spontaneously organize into vascular networks. 160 Bastard et al. further studied the influences of different pro-angiogenic growth factors as well as their timing of delivery on vascular structure formation based on HUVECs co-cultured with NHDFs, mesenchymal stem cells or pericytes in soft PEG hydrogels. 161 Besides the commonly supplemented growth factors like vascular endothethial growth factor (VEGF), they identified that the sequential delivery of Angiopoietin-1 (Ang-1) and platelet-derived growth factor (PDGF) after 4 days, followed by the supplementation of Angiopoietin-2 (Ang-2) after 6 days promoted the formation of vascular structures best. This was observed for co-cultures of HUVECs with NHDFs or mesenchymal stem cells in a 1:3 ratio over a period of 7 days in total (**Figure 2.4 A**). 161 Levenberg et al. reported for the first time the engineering of vascularized skeletal muscle tissue for transplantation by culturing endothelial cells with murine myoblasts on poly-(L-lactic acid) (PLLA)/polylactic glycolic acid (PLGA) scaffolds. 115 Due to the big pores in the range of 225-500 µm, the cells infiltrated the scaffolds and the endothelial cells organized into tubular structures while the myoblasts differentiated to build myotubes. 115 The Levenberg research group further advanced this technology to create mature vessel networks that facilitate graft-host anastomosis upon transplantation of engineered tissues: Ben-Shaul et al.

demonstrated that the co-culture of HUVECs with NHDFs in fibrin hydrogels combined with PLLA/PLGA sponges supported the formation of mature vessel-like networks within 14 days of cultivation. Additionally, they showed that the level of vessel maturity influences the success of graft integration and perfusion upon implantation into a mouse dorsal skinfold window. Thereby, the implantation of prematurely vascularized grafts that were cultured for 1 day *in vitro* did not properly support host vessel penetration and anastomosis. In contrast, grafts that were cultured for 14 days before implantation showed extensive host vessel penetration, anastomosis and functionality as fluorescent dextran, injected into the mouse tail, was detected perfusing both the host blood vasculature and the engineered vessels without blood clot formation (**Figure 2.4 B**).

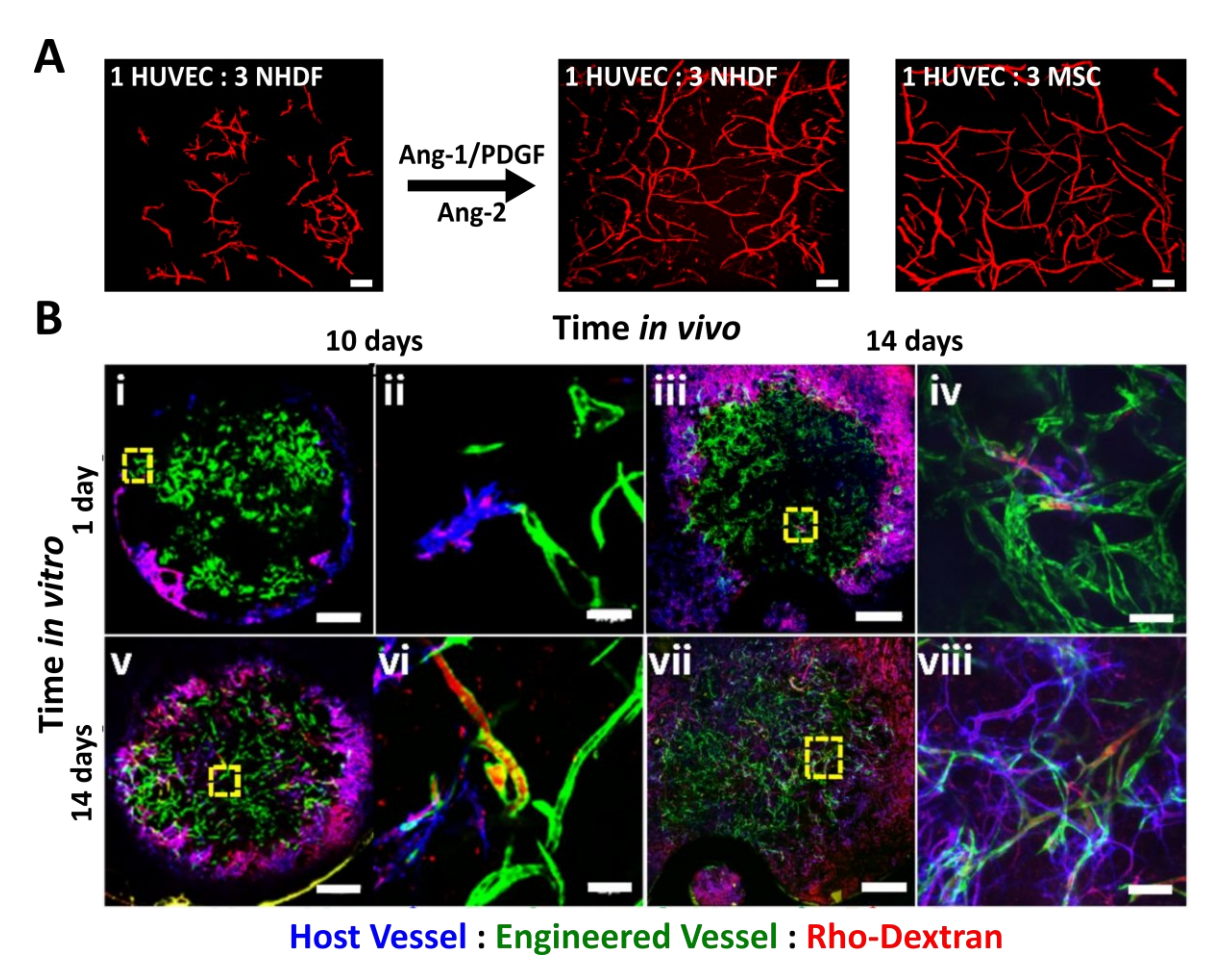


Figure 2.4: Formation of microvascular structures *in vitro.* A) Co-culture of HUVECs and NHDFs or mesenchymal stem cells (MSC) in a 1:3 ratio in PEG hydrogels for 14 days with or without the supplementation of an optimized growth factor cocktail consisting of Ang-1 and PDGF added after 4 days and Ang-2 added after 6 days of culture. Samples are stained for CD31. Scale bars: 100 μm. Copyright 2023, Wiley-VCH GmbH. Reproduced with permission. He in Host-graft vasculature 10 and 14 days after implantation of prevascularized constructs into mouse dorsal skinfold window. The grafts were cultured for 1 or 14 days before implantation. Vessel perfusion is visualized with injected rhodamine-conjugated dextran (Rho-dextran, red). GFP-HUVECs are green, host vessels are blue (mCD31-AF647 injected). Scale bars: 1000 μm. Copyright 2019, National Academy of Sciences. Reproduced with permission.

2.2.1.2 Prevascularized Spheroids

Originally, prevascularized spheroids have been utilized to better understand and recapitulate processes of vascular biology. Gentile *et al.* cultured spheroids consisting of mouse allantoic tissue in hanging drops that reorganized into an outer layer of smooth muscle cells and an inner layer of endothelial cells that enclose a central lumen when treated with VEGF.¹⁶³ These spheroids resembled blood vessels in their basic functions as they could demonstrate physiologically relevant vasodilatory and contractile responses. Based on these findings, Fleming *et al.* further investigated the assembly of blood vessels by fusing uniluminal spheroids.¹⁶⁴ Using the same uniluminal vascular spheroids as described by Gentile *et al.*, they showed that spheroids can fuse with neighboring spheroids to create larger diameter spheroids with a central lumen. The herein presented vascular fusion principle could explain how large diameter blood vessels may be formed from the fusion of adjacent small diameter blood vessels, which is typical for the formation of the descending aorta.¹⁶⁴

De Moor et al. utilized prevascularized spheroids to address the vascularization challenge in tissue engineering and described them as useful building blocks to create larger vascularized 3D tissues. 165 Spheroids combining HUVECs with fibroblasts and/or mesenchymal stem cells were produced and cultured in a highthroughput non-adhesive agarose microwell system in different ratios. Thereby, a 1:9 ratio of HUVECs to fibroblasts, mesenchymal stem cells or a combination of both resulted in stable spheroids with a high cell viability. In case of spheroids containing HUVECs, mesenchymal stem cells and fibroblasts, the formation of capillary-like networks with a significant larger number of lumens was observed within 10 days of culture. These networks were preserved when spheroids were encapsulated in Matrigel and fused to create larger tissue constructs (Figure 2.5 **A**). 165 In a follow-up study, De Moor *et al.* loaded these spheroids into a gelatin methacrylate-based bioink to bioprint constructs of clinically relevant size. 166 Depending on the UV exposure to induce photo-crosslinking of the bioink, they demonstrated a high viability of the spheroids as well as capillary network formation in the spheroids and their fusion (Figure 2.5 B).

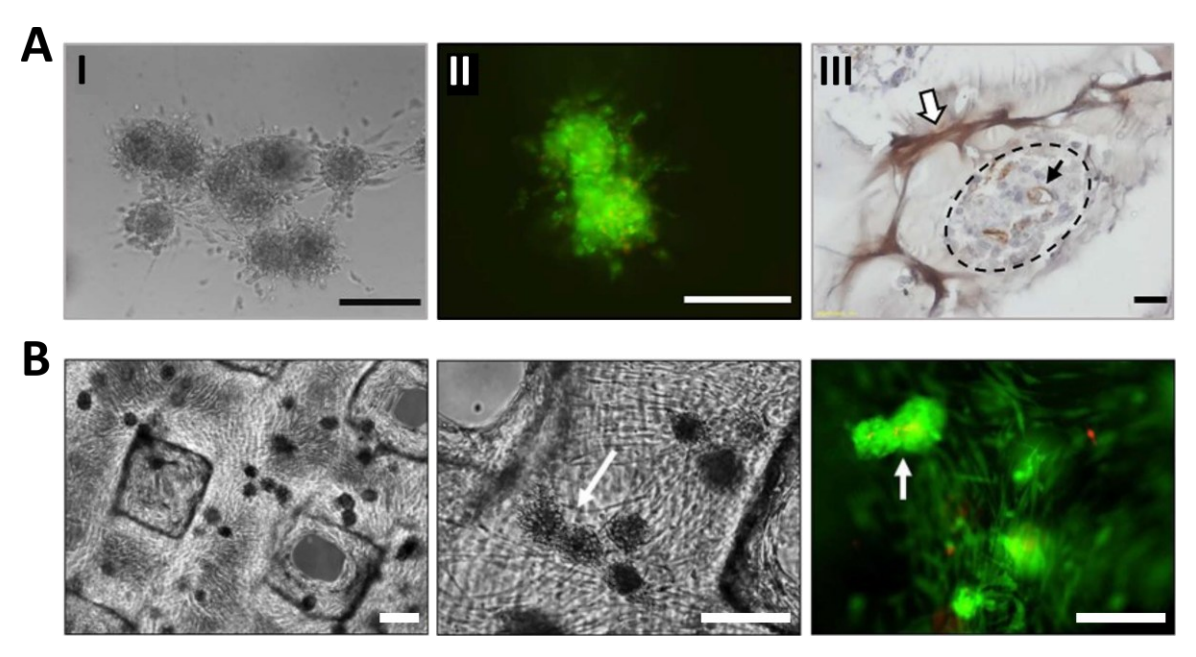


Figure 2.5: Use of spheroids as vascular building blocks. A) Fusion, viability (II) and vascular network formation (III) of spheroids in Matrigel after 96 h in culture. Scale bars: I) 200 μm, II) 100 μm, III) 20 μm. Copyright 2018, IOP Publishing. Reproduced with permission. All rights reserved. ¹⁶⁵ B) Fusion (indicated by white arrows) and viability of spheroids in 3D bioprinted constructs after 6 days in culture. Scale bars: 200 μm. Copyright 2021, IOP Publishing. Reproduced with permission. All rights reserved. ¹⁶⁶

2.2.2 Engineered Vascular Networks

The formation of larger diameter vascular structures commonly relies on biofabrication techniques like bioprinting with sacrificial materials to create perfusable channels. Ouyang et al. reported for the first time the concept of voidfree 3D bioprinting in which a sacrificial gelatin bioink is deposited layer-by-layer alongside a slowly crosslinking matrix bioink via extrusion bioprinting, which inspired our work presented in Chapter 3.102 Thereby, the printed gelatin bioink stabilizes the crosslinking matrix bioink and can be removed thereafter to create a 3D network of interconnected tubular channels. Additionally, preloading endothelial cells into the gelatin bioink allows for in situ endothelialization of the inner channel surface upon liquefaction and release of the gelatin phase. Compared to post seeding methods, this results in an even distribution of endothelial cells throughout the channels that form a confluent monolayer within 8 days of cultivation (Figure **2.6 A**). Finally, the authors demonstrated that these channels are perfusable. They designed multiple perfusion patterns and showed that the cells form a uniform layer across the length of the channels while remaining viable for 12 days of perfusion culture. 102

A similar system was used by De Lorenzi and Hansen et al. to create a perfusable tumor angiogenesis model. 167 Here, they printed strands of gelatin mixed with endothelial cells inside of a bioreactor chamber that was filled with a fibrin-collagen hydrogel blend which contained a multicellular spheroid consisting of cancer and stromal cells. After hydrogel gelation, the bioreactor was incubated at 37 °C to liquefy the gelatin and coat the resulting channels with the encapsulated endothelial cells to create vascular channels. Promoted by the secretion of proangiogenic factors by the tumor cells, vascular sprouts were growing from the initial channels and infiltrated the tumor mass. Dynamic cultivation of the bioreactors for up to 3 weeks resulted in the formation of open lumens within the capillary network. The anastomosis of the self-assembled vascular network and the printed endothelium as well as the continuity of the vascular network lumens was proven by the perfusion with red blood cells, which were able to flow through the capillaries with up to 25 µm in diameter (Figure 2.6 B). 167 These studies demonstrate how bioprinting facilitates the formation of vascular networks by enabling precise spatial organization of endothelial cells into channels.

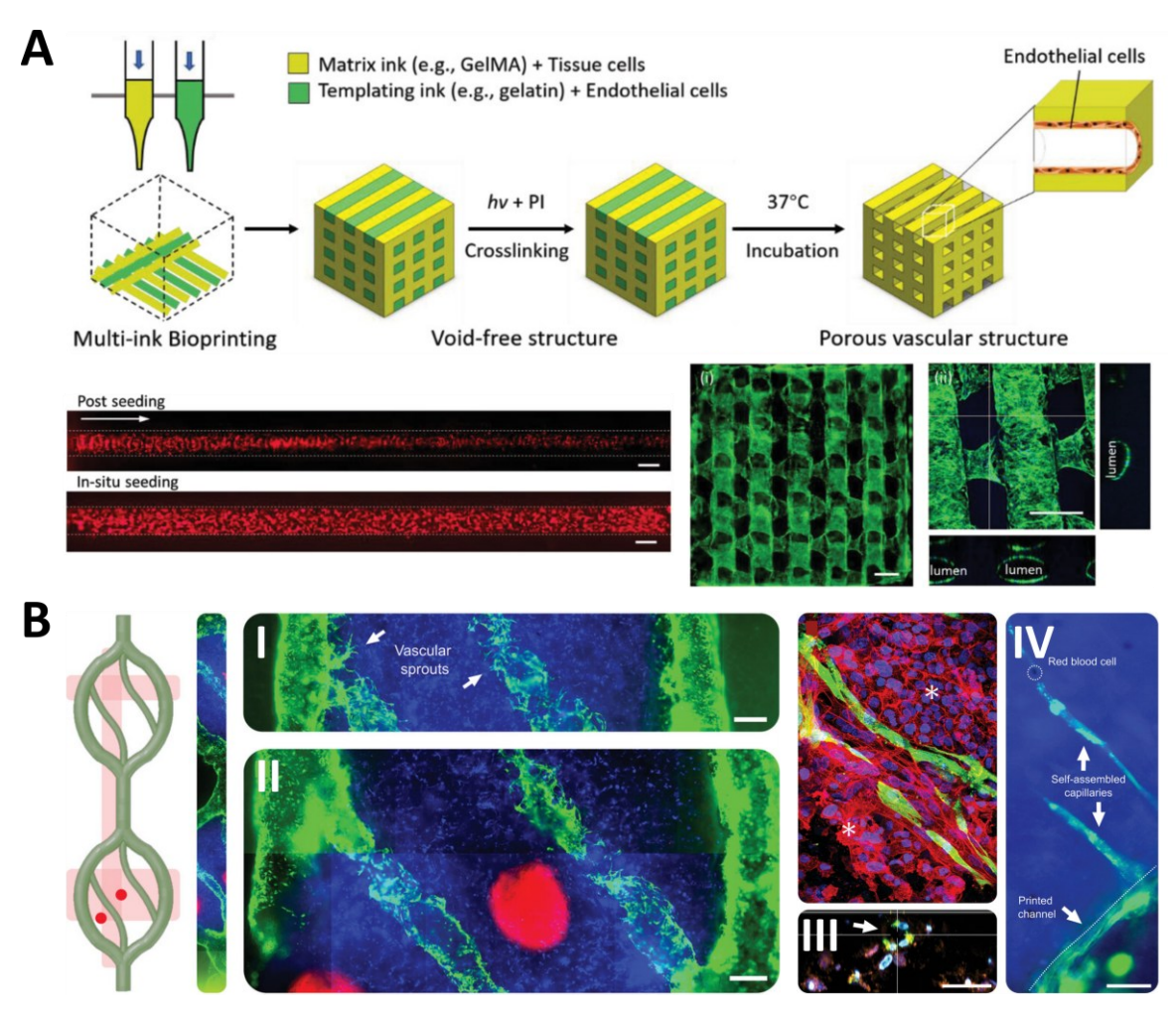


Figure 2.6: Bioprinting of perfusable vascular channels. A) Void-free bioprinting of a matrix bioink (yellow) printed alongside a sacrificial gelatin bioink (green) that is removed by incubation at 37 °C upon photo-crosslinking of the matrix bioink. Preloading of the gelatin bioink with endothelial cells allows for efficient *in situ* endothelialization of the resulting channels and the formation of a tubular vascular network inside 3D bioprinted constructs. Scale bars: 500 μm. Copyright 2020, Wiley-VCH GmbH. Reproduced with permission. B) Design of a bioprinted vascular structure with GFP-HUVECs (green), comprising two sequential hexagon-shaped channels and two small S-shaped inner branches, and placement of a tumor spheroid (DiD-labeled, red). At day 14 of dynamic cultivation, the formation of vascular sprouts is observed, which have a lumen and penetrate the tumor spheroids (indicated by asterisks). The functionality of the capillary network was assessed by the perfusion with red blood cells, which flow through the self-assembled capillaries. Scale bars: I), II) 500 μm; III) 25 μm; IV) 50 μm. Copyright 2023, Wiley-VCH GmbH. Reproduced with permission. 167

2.3 Bioprinting in Tissue Engineering

2.3.1 Bioprinting Techniques

Besides the commonly used extrusion-based bioprinting, which was applied in the presented studies so far as well as in my work shown in Chapter 3, alternative bioprinting techniques have been developed over the years (**Figure 2.7**). Similar to the concept of extrusion bioprinting, inkjet bioprinting describes the deposition

of bioink droplets through a nozzle. Compared to the deposition of a continuous filament, this method allows to precisely shoot bioink droplets in the picoliter volume range, triggered by an actuator without contact to the substrate. 168 Daly et al. used this advantage of inkjet bioprinting to deposit mesenchymal stem cells and chondrocytes into 3D printed polycaprolactone microchambers. 169 These microchambers are hydrophobic and thus cause cellular condensation, which results in cellular aggregation and fusion while additionally confining and directing the growth of the formed aggregates. By printing spatially organized polycaprolactone implants with microchambers to create osteochondral templates, the authors were able to orient cell growth in a way that resembles the zonal organization of stratified cartilage. 169 However, as nozzle-based approaches, extrusion and inkjet bioprinting can result in clogging and are limited in printing speed as well as bioink viscosity. Additionally, the bioink extrusion through the nozzle creates shear stresses that can harm the cells and affect their viability. 170 Thus, nozzle-free bioprinting alternatives, such as laser-assisted bioprinting are developed. Here, a laser is pulsed onto a metal or polymer film that absorbs the laser light and converts it into heat. The generated heat vaporizes portions of the bioink layer found on the donor substrate, which results in the transfer of bioink droplets onto the receiving substrate.¹⁷¹ As a proof-of-concept for this technique, Hall et al. utilized laser-induced forward transfer (LIFT), a form of laser-assisted bioprinting, to print high densities of multicellular spheroids consisting of human periosteum-derived cells with high precision. The spheroids were characterized by a high viability and the capacity to undergo chondrogenic differentiation. 172

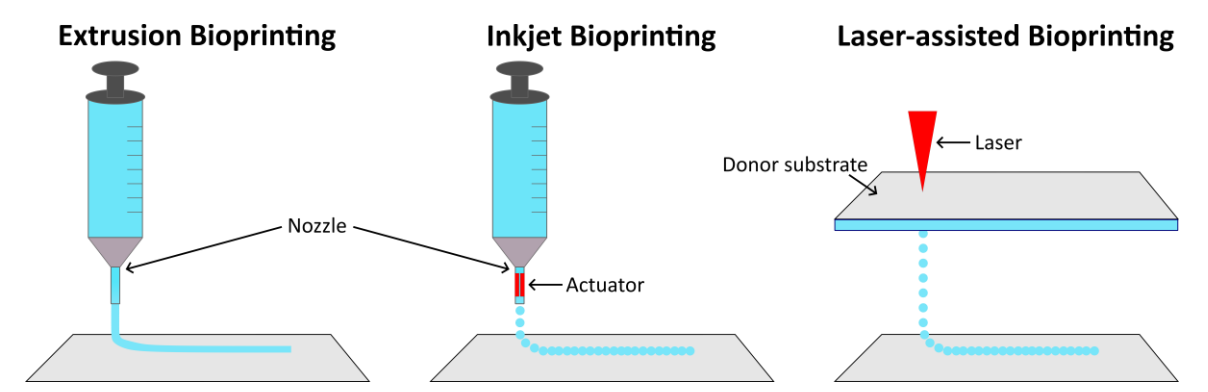


Figure 2.7: Overview of different printing techniques. Extrusion and inkjet bioprinting are methods that involve the deposition of the bioink through a nozzle. While a continuous filament is extruded in case of extrusion bioprinting, an actuator in the nozzle of the printhead creates droplets that are deposited onto a printing substrate. In case of laser-assisted bioprinting, a laser is pulsed on an energy-absorbing donor substrate that vaporizes a portion of the bioink layer to create a bubble that shoots a bioink droplet onto the receiving substrate.

2.3.2 Bioprinting Complex Functional Tissues

Beyond vascularization as highlighted in Chapter 2.2.2, bioprinting of multiple cell types and biomaterials offers the potential to biofabricate advanced tissues with increasing complexity and functionality. Ahrens et al. developed functional cardiac tissue with anisotropic organ building blocks (aoBB) that were bioprinted in a hydrogel mixture of gelatin and fibrin. 173 The aoBBs were produced from human induced pluripotent stem cell-derived cardiomyocytes and human fibroblast on a micropillar array. During the extrusion-based printing process, the generated aoBBs aligned along the printing path, which was induced by shear forces and evident from the orientation of individual aOBBs to the sarcomeric structure of the generated tissue. Additionally, the authors developed elastomeric macro-pillar platform onto which cardiac filaments were printed. The contraction of the printed cardiac tissue thereby caused a deflection of the pillars, which allowed for quantification of the contractile force depending on the degree of pillar deflection. Compared to spheroidal and thus non-aligned controls, the cardiac filaments composed of aoBBs generated a significantly higher contractile force. This was confirmed in calcium imaging experiments, which revealed that the conduction velocity of action potential propagation in aligned cardiac filaments was significantly higher after 4 days compared to controls as well, while in both cases an increase was observed over time due to cellular remodeling (Figure 2.8 A). 173 This demonstrates the importance of combining large-scale models with cellular orientation to create tissues with native-like functionality.

Brassard *et al.* re-invented the concept of extrusion-based bioprinting by depositing a suspension of stem cells and organoids directly into a viscous Matrigel/collagen mixture that supports cellular self-organization. This approach, termed bioprinting-assisted tissue emergence (BATE), enabled the controlled formation of self-organized macro-scale tissues in a more controlled manner by regulating the printing design and cellular density. They demonstrated this concept for connective, epithelial and vascular tissues based on three cell types with known self-organizing capacities. Mesenchymal stem cells reorganized into fibrous connective tissue, while HUVECs created branched vascular tubes with a continuous lumen that can be perfused. Printed intestinal stem cells further self-organized into characteristic crypts and villi with differentiated Paneth cells and

enterocytes (**Figure 2.8 B**).⁹⁶ The concept of BATE served as a significant inspiration for the idea of aligning prevascularized spheroids in order to guide their reorganization process into continuous luminal structures as presented in Chapter 4.

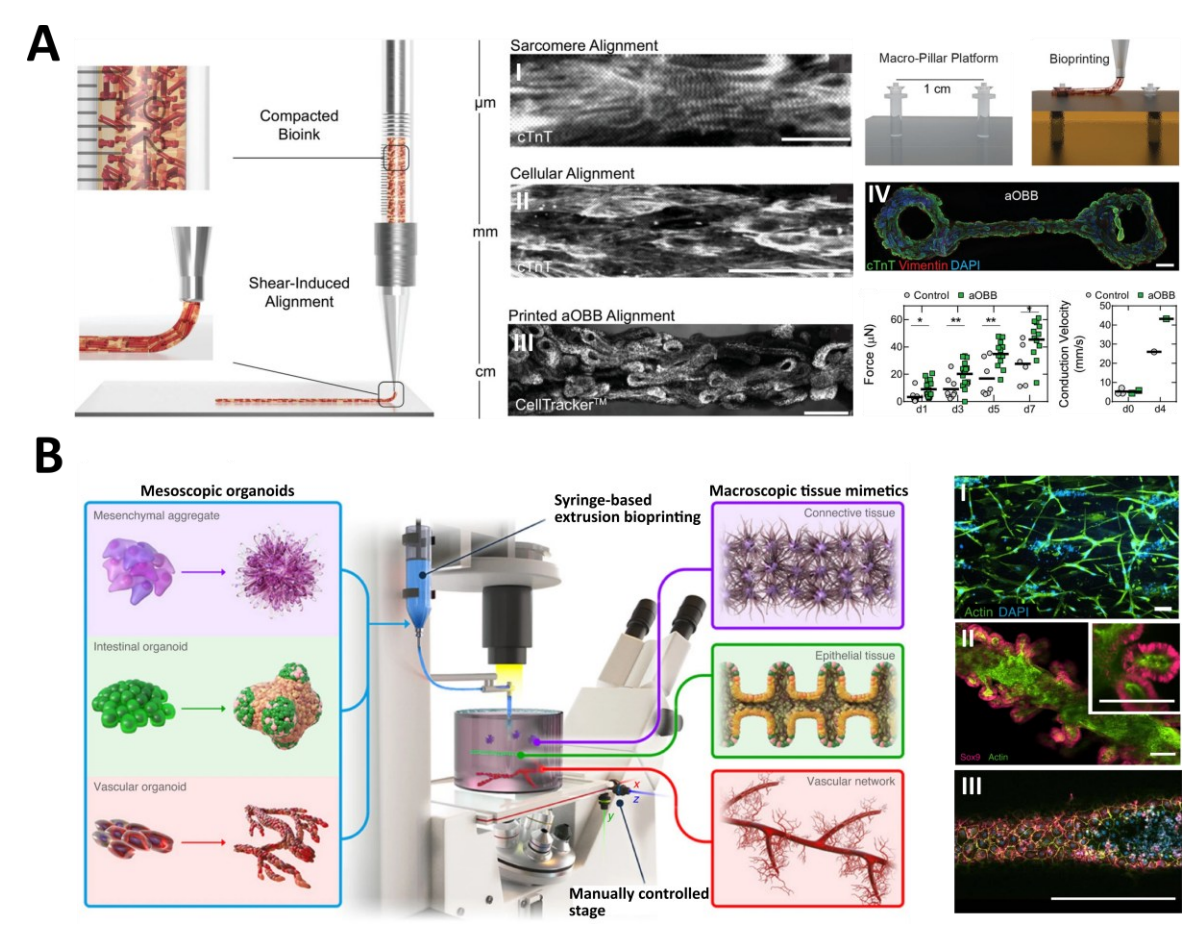


Figure 2.8: Bioprinting of complex functional tissues. A) Bioprinting of aligned cardiac tissue by deposition of anisotropic organ building blocks (aoBBs) that orient within the compacted bioink due to the shear forces during the printing process. The alignment is visible on multiple scales as the aoBBs are aligned within the bioprinted tissue, the individual cells are aligned within the aoBBs and the sarcomeres are aligned within each cell. Cardiac filaments consisting of aOBBs as well spheroid-based controls are printed on a macro-pillar platform. Deflection of the pillars due to cardiac contraction shows that the force generated by cardiac filaments consisting of aoBBs is higher compared to controls, which is also evident for the conduction velocity determined by calcium imaging. Scale bars: I) 20 μm; II, IV) 100 μm; III) 2 mm. Copyright 2022, Wiley-VCH GmbH. Reproduced with permission.¹⁷³ B) Illustration of the bioprinting-assisted tissue emergence concept that deposits suspensions of self-organizing stem cells and organoids as building blocks into viscous ECM to create large-scale tissues. This is demonstrated for connective tissue that self-organizes from mesenchymal stem cells (I), intestinal tissue build by intestinal stem cells (II), and vascular channels formed by HUVECs (III). Scale bars: I) 250 μm; II) 100 μm; III) 500 μm. Copyright 2021, Springer Nature. Reproduced with permission.⁹⁶

3 Synergizing Bioprinting and 3D Cell Culture to Enhance Tissue Formation in Printed Synthetic Constructs

Daniel Günther, Cédric Bergerbit, Ary Marsee, Sitara Vedaraman, Alba Pueyo Moliner, Lisa van Uden, Céline Bastard, Vanessa Falter, Guy Eelen, José Gerardo Nava, Mieke Dewerchin, Peter Carmeliet, Rafael Kramann, Kerstin Schneeberger, Bart Spee, Laura De Laporte

3.1 Introduction

Tissue engineering aims for the development of 3D human functional tissues that mimic native tissues and organs. This way, autologous tissues could be designed and grown in the lab using patient-derived (stem) cells to complement and eventually replace donor organs for transplantation, which, up to now, remains the only life-saving treatment option for patients suffering from end-stage organ failure. Moreover, creating 3D human functional tissue models could revolutionize drug and therapy discovery, which is afflicted by the poor validity of current preclinical test procedures based on 2D cell culture and animal testing. At the same time, human-like 'disease in a dish' models based on patient cells would allow for personalized drug testing and help to find the best treatment option to cure specific pathologies. However, and besides its great potential, tissue engineered solutions only play a minor role in regenerative medicine and precision medicine so far. However.

The development of 3D functional human tissues *in vitro* requires providing tissue inherent cell types with a surrounding extracellular matrix that recapitulates the native tissue organization and architecture, while introducing mechanical and biochemical cues that support cell growth. ⁹² 3D bioprinting has thereby emerged as a tool of choice to construct complex, anatomical tissues by depositing cells and biomaterials layer-by-layer as briefly demonstrated on the examples of bioprinted heart tissue as well as connective, intestinal and vascular tissues in the previous Chapter 2.3.2. Commonly, cells are suspended in a hydrogel precursor bioink, consisting of polysaccharides, such as alginate or hyaluronic acid, or animal-derived proteins, such as gelatin or collagen, that is deposited as a continuous

filament or droplets by pressure-driven extrusion from a printer nozzle.¹⁷⁵ Animalderived proteins have the advantage that they mimic essential mechanical and biochemical properties of the native extracellular matrix (ECM) and thereby provide an optimal environment for cells to grow. In combination with a good printability and printing resolution, this allows for the fabrication of complex tissues in vitro. 176 However, the properties of animal-derived materials are often difficult to control and may differ from batch to batch, which affects their reliability and data reproducibility.⁷¹ Although gelatin has been used in multiple clinical trials, e.g. to treat posterior epistaxis¹⁷⁷ or chronic skin ulcers¹⁷⁸, these materials still carry concerns related to potential disease transfers and immunogenic effects, which could increase the risk of graft rejection upon transplantation as well as ethical issues. 179-181 In this context, bioinks based on synthetic polymers that are approved by the Food and Drug Administration (FDA) for clinical use, such as polyethylene glycol (PEG), are investigated as alternative materials for bioprinting as they can reduce the reliance on animal-derived materials. Yet, they represent only ~10% of the currently used bioinks. 182 These types of polymers are characterized by their high batch-to-batch reproducibility, well-defined structures, functionality, and tunability. Over the last years, PEG-based bioinks were extensively used for 3D bioprinting of tissue constructs. The most common use of PEG in bioprinting is via photopolymerization by free-radical polymerization (FRP) of acrylated or methacrylated PEG in combination with a photoinitiator. As PEG is lacking the inherent shear-thinning and thermoresponsive properties of natural polymers, rendering it non-printable by itself, acrylated or methacrylated PEG is often used in combination with natural polymers, such as alginate 183, gelatin 184, or GelMa. 185 In these examples, the natural polymers are mixed within the PEG bioink and become part of the final hydrogel network or are used as temporary filler materials for mechanical support during printing after which they can be washed out. Alternatively, inorganic fillers, such as nanosilicates, have also been used to render PEG bioinks printable. 186 These methods have the drawbacks of requiring a secondary crosslinking process with potentially harmful free radicals and UV light to stabilize the construct, while FRP can suffer from oxygen inhibition. 187

Alternative to photopolymerization, mild radical-free thiol-Michael addition between a thiol (SH) and an activated alkene, such as vinyl sulfone (VS), has also been used for extrusion bioprinting of a PEG bioink.¹⁸⁴ Here, the authors counteracted the inherent non-printability of PEG by pre-crosslinking the hydrogel directly in a micro-capillary nozzle and utilizing small molecular weight gelatin fragments to aid the extrusion process. While the printing resolution and cell viability achieved were high, the printing process is sequential and cannot be applied to continuously print large-scale constructs in an automated fashion.

In contrast to animal-derived bioinks that are inherently degradable and bioactive, synthetic materials like PEG are bioinert. Thus, they must be functionalized bottomup with degradable moieties and integrin-binding sites, like RGD-based oligopeptides, to facilitate cell adhesion and growth, which at the same time allows for precise control of the individual hydrogel properties. To render synthetic hydrogels degradable in vitro and in vivo, they are commonly crosslinked with MMP-sensitive peptides and are thereby degradable on cell demand.77, 151 Additionally, hydrolytic degradation has been utilized to soften PEG hydrogels by integrating ester groups into the polymer network, which, as briefly mentioned in Chapter 2.1.1, facilitates the expansion of intestinal stem cells and organoid culture. 149 However, the cytocompatibility of printed, synthetic constructs is usually demonstrated with less sophisticated cell lines, such as L929¹⁸⁴ or NIH 3T3 mouse fibroblasts¹⁸⁸, instead of primary human cell types, which are ultimately needed to create functional, physiologically relevant tissues in vitro. On the one hand, previous studies with synthetic bioinks have not adequately demonstrated the ability to support the formation of cellular constructs as a first step towards tissue formation. On the other hand, it has been shown that cells originating from soft tissues, such as endothelial cells in co-culture with supporting cells, are able to grow pre-vascular structures in soft PEG hydrogels (100-300 Pa), whereas the endothelial network formation is diminished as the hydrogel stiffness increases. 116, ¹⁶¹ While microvascular structures formed by endothelial cells are key requirements to ensure sufficient oxygen and nutrient supply of the tissue, their sensitivity to hydrogel stiffness and the requirement of a soft matrix opposes with the need for stiff materials, in the range of kPa, to ensure shape fidelity of the printed constructs. 189, 190 This contradiction is a significant reason for the limited number of available synthetic bioinks that have the right balance between functionality and printability.

This work aims to bridge the gap between bioprinting and 3D cell culture by inducing tissue formation based on cell spheroids consisting of human umbilical vein endothelial cells (HUVECs) and normal human dermal fibroblasts (NHDFs) in PEG-based 3D printed constructs for the first time. We designed a synthetic bioink for extrusion bioprinting that crosslinks via thiol-Michael addition of a four-arm PEG-VS and two types of di-thiol crosslinkers that are either MMP-sensitive (HS-MMPsens-SH) or functionalized with ester groups (HS-Esters-SH) and thereby hydrolytically degradable. By adjusting the ratio of HS-MMPsens-SH to HS-Esters-SH, the rate of cell-laden hydrogel degradation can be tuned. This allows us to print stable constructs based on an initially stiffer hydrogel that rapidly softens over time to create more space for the cell spheroids to grow. The use of a 3D bioprinter equipped with a novel dynamic mixing tool, developed by REGENHU during our collaborative EU project OrganTrans, allows for in situ mixing of the PEG bioink precursor molecules at low viscosity directly during printing at the correct stoichiometric ratio, along with a flush of the mixer after printing to prevent nozzle clogging. To overcome the non-shear thinning behavior of a PEG solution, the bioink loaded with spheroids is co-bioprinted with sacrificial template materials to create cubic constructs that are perfusable after template removal (Figure 3.1).

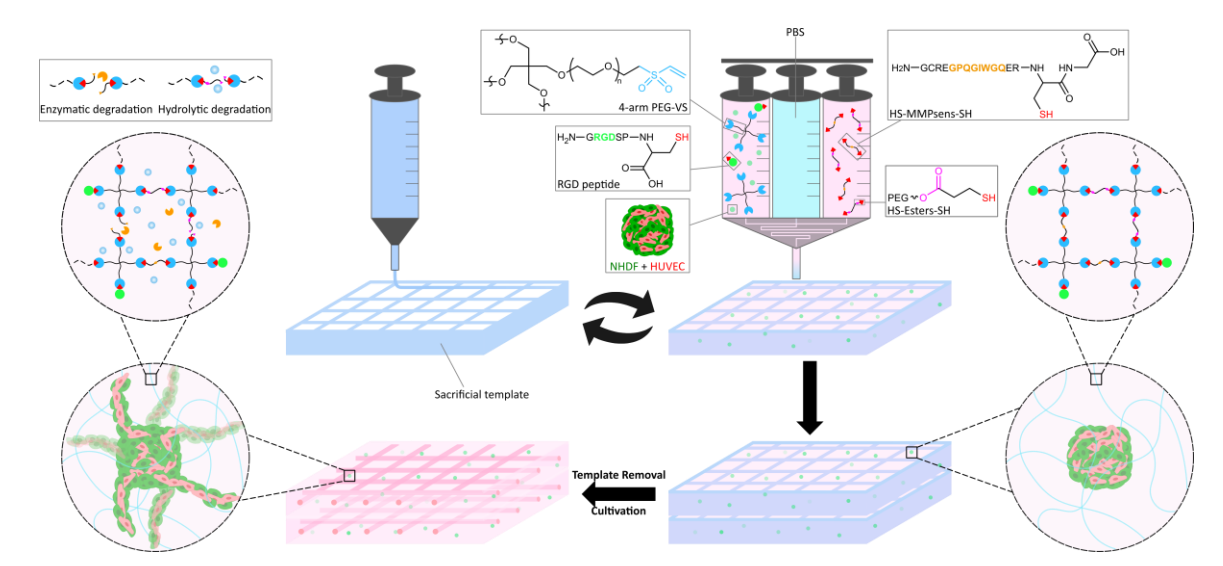


Figure 3.1: Printing of perfusable PEG-based constructs containing prevascularized spheroids. A PEG-based bioink is printed side by side with sacrificial cellulose nanofibril and gelatin template inks that keep the shape of the construct during crosslinking of the PEG precursor molecules. Moreover, they allow for the formation of perfusable channels after their removal. To facilitate the growth of prevascularized spheroids consisting of NHDFs and HUVECs within printed constructs, the PEG-based bioink consists of four-arm PEG-VS and two di-thiol crosslinkers that are MMP-sensitive (orange; HS-MMPsens-SH) or functionalized with ester groups (pink; HS-Esters-SH) as well as a RGD oligopeptide (green).

3.2 Results and Discussion

3.2.1 Influence of Hydrogel Composition on Printed Construct Stability

The shape fidelity of printed constructs depends on the polymer concentration and crosslinking density of the respective bioink, while cells require a soft matrix to grow in. This defines the gap between bioprinting and 3D cell culture in the frame of this work. For further demonstration of this gap, we initially culture L929 cells in hydrogels with PEG concentrations ranging between 3.4-7 w/v%. Thereby, cells are able to grow in 3.4 w/v% PEG hydrogels, which have been used to support the growth of mesenchymal stem cells in a previous study¹⁹¹, but remain round in stiffer hydrogels (**Figure 3.2**).

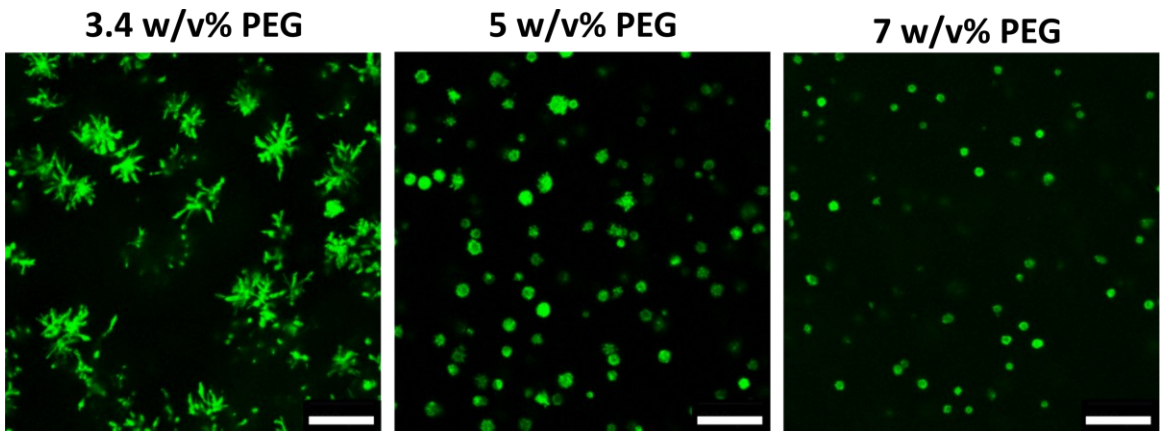


Figure 3.2: Influence of hydrogel stiffness on cell growth. L929 mouse fibroblasts (500 cells/ μ L) are cultured in MMP-sensitive PEG hydrogels with different PEG concentrations ranging from 3.4-7 w/v% and 30 μ M RGD. After 7 days, confocal images of cells stained for F-actin (green) are recorded. Scale bars: 200 μ m.

For comparison, constructs are printed based on the cell-optimized 3.4 w/v% PEG bioink as well as a stiffer 6.5 w/v% PEG bioink. Both bioinks are liquid upon mixing of the hydrogel precursors with initial complex viscosities < 0.05 Pa·s and crosslink within two minutes after mixing, shown by sharp increases of the complex viscosity and storage moduli. Thereby, 3.4 w/v% PEG hydrogels have a stiffness of 850 Pa while 6.5 w/v% PEG hydrogels have a stiffness of 3120 Pa after 30 min at 37 °C (Figure 3.3 A-C). Scanning electron microscopy (SEM) images of the formed hydrogels at both polymer concentrations show a denser network for the 6.5 w/v% PEG hydrogels compared to the 3.4 w/v% PEG hydrogel, correlating with the higher stiffness observed for the 6.5 w/v% PEG hydrogel (Figure 3.3 D). The use

of the 6.5 w/v% PEG bioink is adapted from a previous bioprinting study that also crosslinked four-arm PEG-VS with a linear di-thiol crosslinker via Michael-type addition. 184 In this study, low molecular weight gelatin fragments were mixed inside the PEG bioink to improve the extrudability and shape fidelity of the printed filament. In addition, the reported bioink, containing PEG and gelatin fragments, is premixed as a single stock solution and aspirated through a capillary nozzle where it crosslinks for 5 min at 37 °C before extrusion. While this process affords filaments with great shape fidelity, the sequential nature of the process limits it to the printing of filaments whose length is equal to that of the capillary. The printing of additional filaments requires the use of several pre-loaded capillaries with manual interchanging, overall limiting the maximum size of the printed constructs. As all the hydrogel precursors are mixed prior to printing, the stock solution has a lifespan of only several minutes before it starts clogging in the capillary. Using our novel mixing chip and nozzle, developed by REGENHU, it is possible to continuously create stable constructs for both tested PEG concentrations when alternating lines of the PEG bioink and a sacrificial gelatin template are printed (Figure 3.3 E, F). Due to its reversible thermal gelation properties, gelatin is used here as sacrificial template and co-printed with the bioink on a cooled print bed (15 °C) to serve as a temporary mold for the liquid PEG bioink while it is crosslinking within minutes after mixing and printing. As mentioned in Chapter 2.2.2, this method of void-free bioprinting introduced by Ouyang et al. expands the scope of potential bioinks for extrusion bioprinting by enabling the printing of liquid, slowly crosslinking bioinks, while allowing for precise layer stacking up to centimeter-size constructs. 102 After removal of the gelatin template during incubation at 37 °C, the formation of hollow tubular networks throughout the constructs is obtained for both tested PEG concentrations that can be perfused with a red dye. Yet, while 6.5 w/v% PEG constructs are stable after gelatin removal, the 3.4 w/v% PEG constructs do not retain their initial shape and collapse (Figure **3.3 G**). These results show that stiffer bioinks have to be printed to form stable constructs that can be handled post-printing.

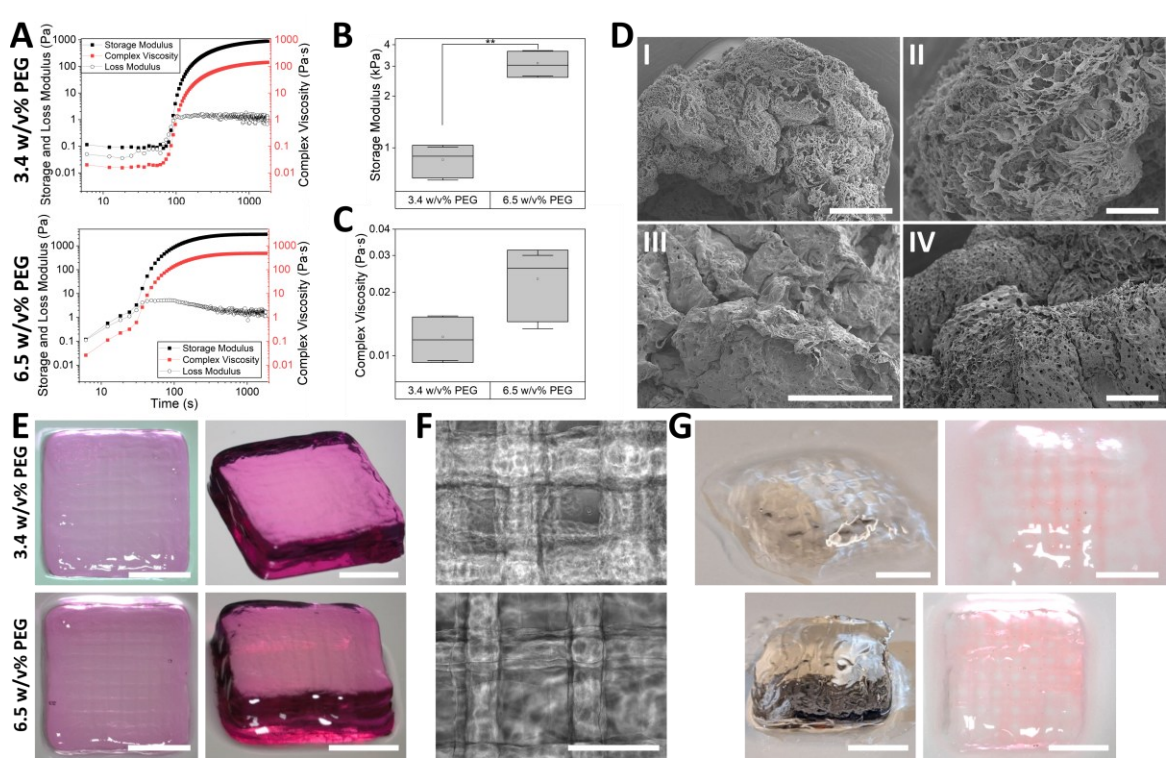


Figure 3.3: Mechanical properties, printability and shape fidelity depending on PEG concentration. A) Storage and loss moduli as well as complex viscosity of 3.4 and 6.5 w/v% PEG precursor solutions and formed hydrogels as a function of time. A representative measurement is shown for each condition with similar results observed across three independent replicates (n = 3). Storage modulus (B) and complex viscosity at t = 0 s (C) of 3.4 and 6.5 w/v% PEG hydrogels at 37 °C. Box plots present mean \pm SD with n = 3 per condition (error bar = min-max values, hollow square = mean value, horizontal line = median). P values are calculated using one-way ANOVA with post-hoc Tukey test, *p < 0.05, **p < 0.01, ***p < 0.001. D) Scanning electron microscope (SEM) images of 3.4 (I, II) and 6.5 w/v% (III, IV) PEG hydrogels. Scale bars: I, III) 1 mm; II, IV) 250 µm. Macroscopic (E) and microscopic (F) images of printed constructs (13 layers) with 3.4 and 6.5 w/v% PEG and gelatin strands after printing. Scale bars: 5 mm (E) and 1 mm (F). G) Macroscopic images of printed constructs with 3.4 and 6.5 w/v% PEG after overnight incubation at 37 °C that are dyed with red ink to visualize open channels within the constructs. Scale bars: 5 mm.

Attempting to grow vascular networks, HUVECs and NHDFs are co-cultured in PEG hydrogels that are fully crosslinked via bis-cysteine peptides with the commonly used MMP-sensitive sequence $GPQG\downarrow IWGQ^{77}$ to render the gels degradable on cell demand. In manually pipetted hydrogels modified with 0.6 mM RGD, extensive network formation is observed when the cells are cultured in 2 w/v% PEG hydrogels ($G'\sim 300~Pa^{151}$), while only a few elongated structures are observed in 2.5 w/v% PEG hydrogels ($G'\sim 550~Pa^{151}$) (**Figure 3.4 A**). To compensate for the increased stiffness, we sought to adjust the degradation rate of PEG hydrogels by combining the MMP-sensitive peptide crosslinker (HS-MMPsens-SH) with a second, ester functionalized PEG crosslinker (HS-Esters-SH) that hydrolytically degrades over time. Proof-of-concept experiments indeed

show that this crosslinker combination facilitates cell growth by creating more space for the cells to grow. A ratio of 70% HS-MMPsens-SH/30% HS-Esters-SH in the 2.5 w/v% PEG hydrogels facilitates cellular network formation that is similar to the extent of cell growth in softer 2 w/v% PEG hydrogels (**Figure 3.4 B**).

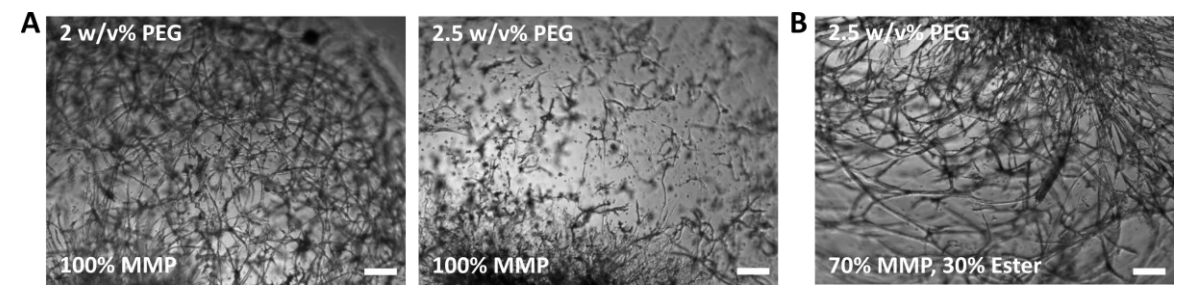


Figure 3.4: Growth of HUVECs and NHDFs encapsulated as single cells in soft PEG hydrogels. HUVECs and NHDFs are co-cultured in a 1:1 ratio with 5,700 cells/ μ l in 2 and 2.5 w/v% PEG hydrogels with 100% HS-MMPsens-SH (A) or 70% HS-MMPsens-SH/30% HS-Esters-SH (B). Brightfield images are recorded after 14 days of culture. Scale bars: 200 μ m.

Anticipating that tuning the hydrogel degradation would then be eminently necessary for the stiffer 6.5 w/v% PEG hydrogels that show superior shape retention properties after bioprinting compared to their softer counterparts, the influence of different crosslinker ratios on the mechanical properties as well as hydrogel softening over time is investigated (Figure 3.5). Thereby, the fraction of HS-Esters-SH is limited to 30% as the hydrogels start to fully degrade over a time span of 4 days when a higher fraction of HS-Esters-SH is used. The storage moduli of the 6.5 w/v% PEG hydrogels are in the range of 3 kPa for all tested conditions. By increasing the HS-Esters-SH fraction from 0 to 30%, the hydrogel stiffness only slightly decreases without significant variations (Figure 3.5 A). The influence of the HS-Esters-SH fraction on hydrogel softening is monitored via nanoindentation over a period of 14 days when incubated in PBS at pH 7.4 and 37 °C (**Figure 3.5 B**). While fully ester-degradable hydrogels completely degrade within 7 days, the stiffness of 100% MMP-degradable hydrogels fluctuates in a range of 90-112% of their initial stiffness. For variable fractions of HS-Esters-SH, hydrogels lose about 35% of their initial stiffness in conditions with 10% HS-Esters-SH, 48% with 20% HS-Esters-SH, and 66% with 30% HS-Esters-SH after 14 days. This trend inversely correlates with the swelling behavior of the hydrogels as hydrogels with 20-30% HS-Esters-SH both gain about 330% of their initial weight (Figure 3.5 C). Moreover, the swelling experiments reveal that hydrogels with increasing HS-

Esters-SH fraction swell more within the first 30 min after hydrogel crosslinking and subsequent incubation in PBS. For example, fully ester-degradable hydrogels gain about 240%, while 100% MMP-degradable hydrogels gain about 155% of their initial weight in that period. As this difference cannot be attributed to ester hydrolysis yet, it may be caused by the different chemical structure of the crosslinkers. Compared to the linear backbone of HS-Esters-SH, HS-MMPsens-SH is an oligopeptide consisting of amino acids with additional side chains, which could restrict hydrogel swelling due to peptide-peptide chain interactions. Moreover, as both crosslinkers are designed to have the same molecular weight of about 1.7 kDa, HS-MMPsens-SH is shorter than HS-Esters-SH in uncoiled state due to the presence of more bulky amino acids, leading to a limited swelling potential. To study the influence of ester degradation on shape fidelity, large centimeter-size constructs with different HS-MMPsens-SH/HS-Esters-SH ratios are printed (Figure 3.5 D). Before degradation, all constructs printed with HS-Esters-SH fractions varying between 0-30% have similar dimensions, are indistinguishable from each other, and able to support their own weight. After hydrolytic degradation in PBS adjusted to pH 9 at 37 °C, complete degradation of the 100% HS-Esters-SH construct is observed, while the 100% HS-MMPsens-SH construct keeps its cubic shape and does not collapse. Increasing the fraction of HS-Esters-SH results in constructs that show increasing level of swelling and collapse, as shown by a widening of the base compared to the top of the construct and a twisting effect. This causes 30% HS-Esters-SH constructs to collapse, similar to the softer 3.4 w/v% printed constructs after removal of the sacrificial template (Figure 3.5 D, dashed square box). As both these constructs are very fragile and difficult to handle, the 10% and 20% HS-Esters-SH conditions are chosen to achieve the right balance between construct shape fidelity and hydrogel softening for further studies with cell-laden hydrogels.

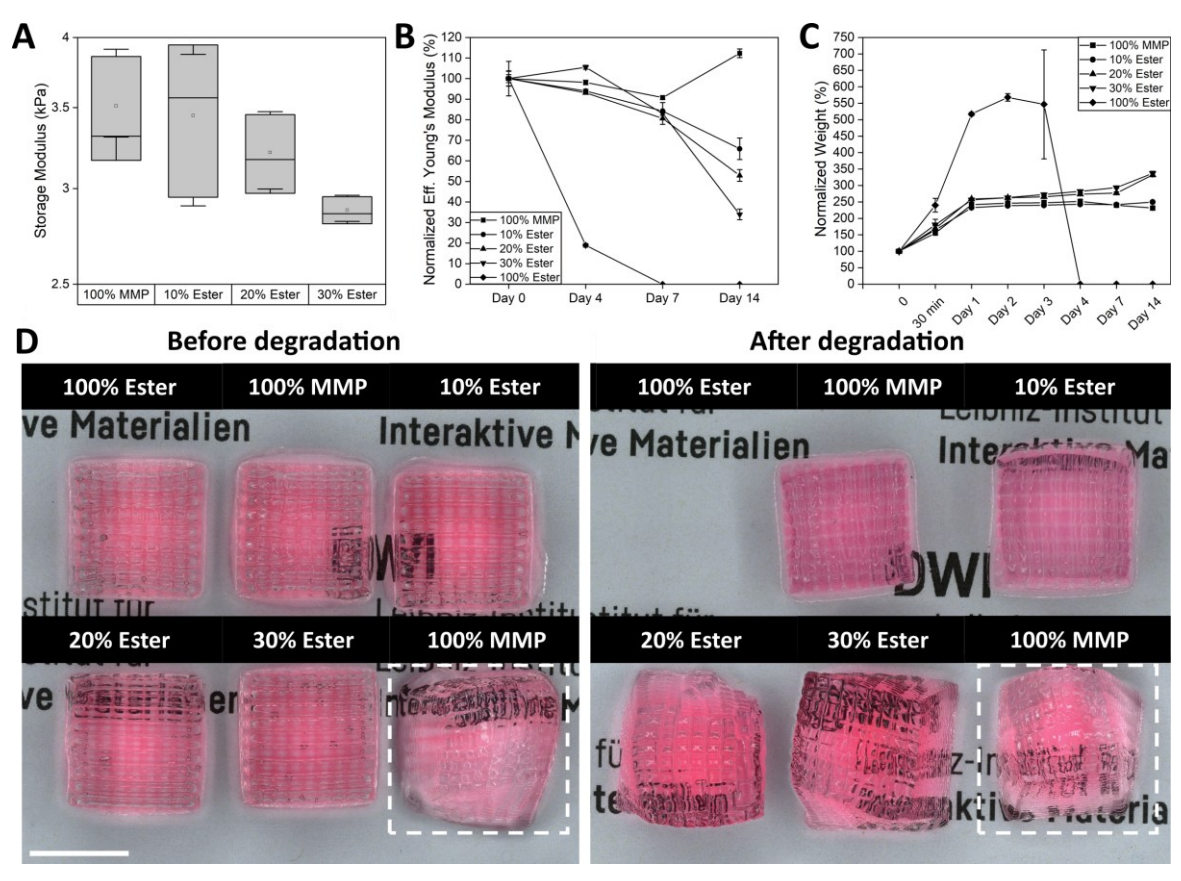


Figure 3.5: Influence of ester degradation on hydrogel softening and shape fidelity of printed constructs. A) Storage modulus of 6.5 w/v% PEG hydrogels with different ratios of HS-MMPsens-SH (MMP)/HS-Esters-SH (Ester). Box plots present mean \pm SD with n = 3 per condition (error bar = min-max values, hollow square = mean value, horizontal line = median). P values are calculated using one-way ANOVA with post-hoc Tukey test, *p < 0.05, **p < 0.01, ***p < 0.001. B) Normalized Effective Young's moduli of 6.5 w/v% PEG hydrogels with different ratios of HS-MMPsens-SH/HS-Esters-SH monitored over a period of 14 days via nanoindentation. Data is presented as mean \pm SD with n = 75 per condition. C) Swelling of 6.5 w/v% PEG hydrogels with different ratios of HS-MMPsens-SH/HS-Esters-SH, quantified as normalized hydrogel weight to the initial weight after hydrogel formation. Data is presented as mean \pm SD with n = 3 per condition. D) Shape fidelity of printed constructs (25 layers) before and after hydrolytic degradation depending on HS-MMPsens-SH/HS-Esters-SH ratio. Dashed square boxes show constructs made with 3.4 w/v% PEG. Scale bar: 1 cm.

3.2.2 Influence of Hydrogel and Spheroid Composition on Spheroid Sprouting

Following up on initial experiments to grow vascular networks, HUVECs and NHDFs are co-cultured in stiffer hydrogels to close the stiffness gap between the requirements for 3D cell culture and bioprinting. However, limited cell growth is observed in 3.4 w/v% PEG hydrogels with adjusted crosslinker ratios. Nevertheless, elongated structures of both cell types are forming in areas with densely crowded cells, likely due to locally higher levels of MMPs and growth factors secreted by the cells (**Figure 3.6**).

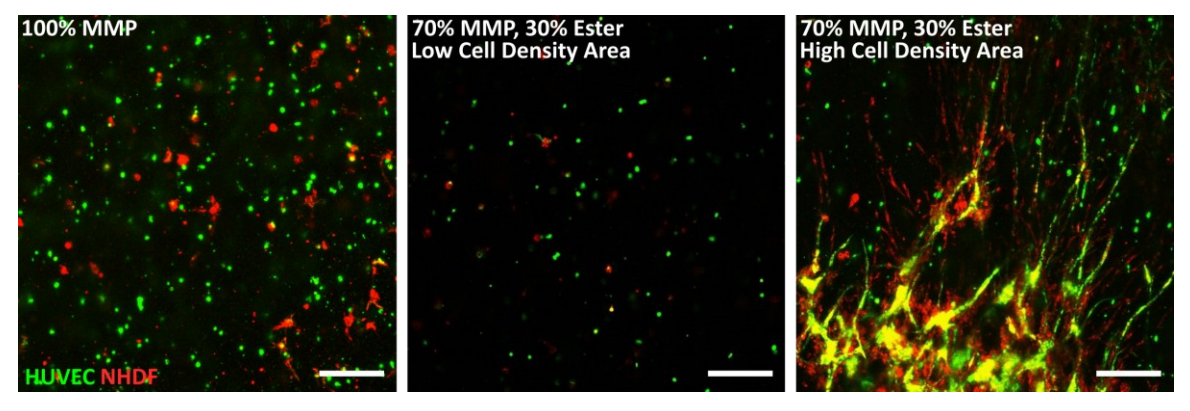


Figure 3.6: Growth of HUVECs and NHDFs encapsulated as single cells in 3.4 w/v% PEG hydrogels. HUVECs (green) and NHDFs (red) that are pre-stained with Vybrant DiO (green) and Dil (red) are cultured in a 1:1 ratio with 5,700 cells/μL in 3.4 w/v% PEG hydrogels with 100% HS-MMPsens-SH (MMP) as well as 70% HS-MMPsens-SH/30% HS-Esters-SH (Ester). Confocal images are recorded after 14 days of culture. Scale bars: 200 μm.

Given this observation, spheroids are used instead to start from local high cell concentrations. The spheroids are formed via hanging drop cultivation and tested to improve cell growth in the stiffer, 6.5 w/v% PEG hydrogels used for 3D bioprinting. Cultivation of spheroids consisting of 1000 cells/spheroid at a 1 HUVEC/3 NHDFs ratio, which was optimized to support the formation of vascular structures in ultrasoft PEG hydrogels¹⁶¹, results in cellular outgrowth from the spheroids with endothelial sprout formation as indicated by CD31 staining (**Figure 3.7 A**). While endothelial sprouting is observed in all tested conditions ranging from 0-20% HS-Esters-SH, the overall spheroid sprouting and sprout density is significantly enhanced by increasing the fraction of HS-Esters-SH, which is shown by elevated cell infiltration and longer sprout lengths (**Figure 3.7 B**). As hypothesized, accelerated hydrogel softening via ester degradation improves the

growth of spheroids within 6.5 w/v% PEG hydrogels. For this reason, 6.5 w/v% PEG hydrogels with a crosslinker combination of 20% HS-Esters-SH and 80% HS-MMPsens-SH are used for further experiments.

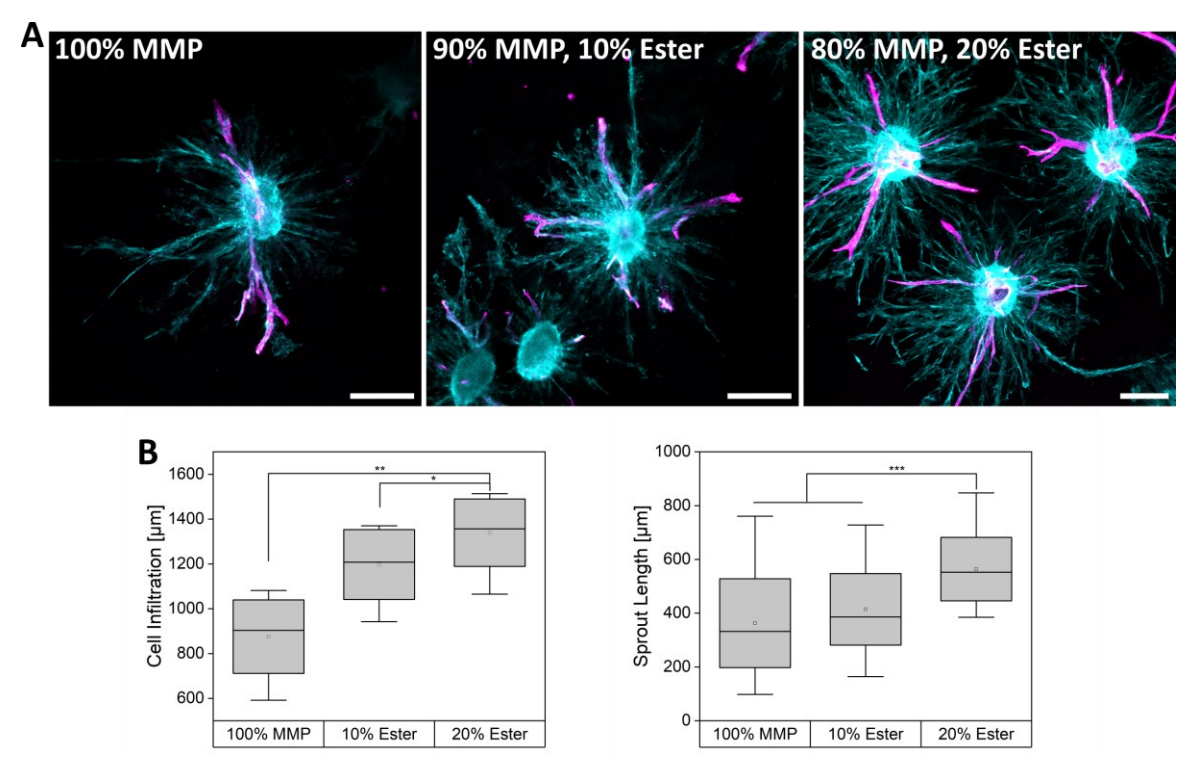


Figure 3.7: Influence of PEG hydrogel softening by ester degradation on spheroid sprouting. Spheroids consisting of 1 HUVECs/3 NHDFs are cultured in 6.5 w/v% PEG hydrogels with different HS-MMPsens-SH (MMP)/HS-Esters-SH (Ester) ratios. A) Confocal images of spheroids stained for F-actin (cyan) and CD31 (magenta) after 14 days in culture. Scale bars: 200 µm. B) Quantification of average cell infiltration (n = 6) and sprout length (n \geq 27) of spheroids depending on the fraction of HS-Esters-SH. Box plots present mean \pm SD (error bar = min-max values, hollow square = mean value, horizontal line = median). P values are calculated using one-way ANOVA with post-hoc Tukey test, *p < 0.05, **p < 0.01, ***p < 0.001.

In addition to the influence of the hydrogel composition, the influence of the spheroid composition on spheroid sprouting is investigated by varying the HUVEC/NHDF ratio in a range of 1:10 to 10:1. In native tissues, the endothelial to mural cell ratios is commonly between 1:1 and 10:1. Pheroids consisting of 1 HUVEC/10 NHDFs hardly sprout and are characterized by large spheroid cores. When the HUVEC fraction is increased, the cores become smaller while the overall sprouting is improved (**Figure 3.8 A**). Both, cell infiltration and sprout length gradually increase inside the hydrogel with larger HUVEC fractions (**Figure 3.8 B**). Moreover, endothelial outgrowth from the spheroids is observed with multicellular endothelial sprouts forming in all tested conditions except for 10 HUVECs/1 NHDF. In this case, the cell sprouts only consist of fibroblasts while HUVECs migrate as

single cells. Previous studies have demonstrated that 3D cell migration is depending on the matrix degradability and degradation rate, where a fast matrix degradation can trigger the switch from collective to single cell migration. Since we use the same crosslinker ratio for all conditions (20% HS-Esters-SH/80% HS-MMPsens-SH) in these experiments, this indicates that the matrix degradation may be accelerated in conditions with larger HUVEC fraction.

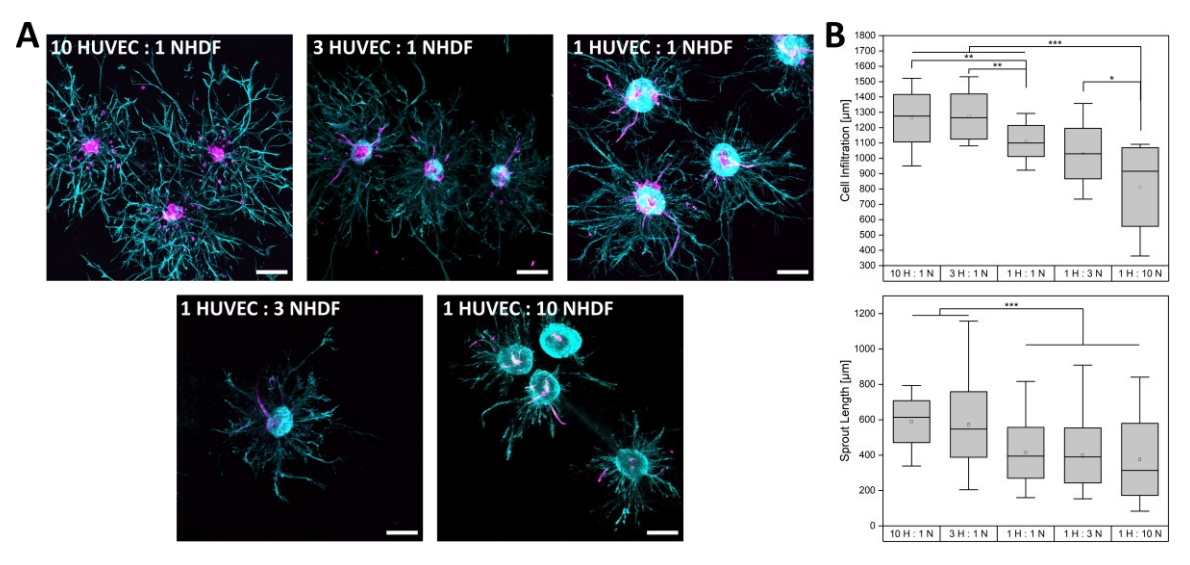


Figure 3.8: Influence of cell ratios on spheroid sprouting. Spheroids consisting of HUVECs (H) and NHDFs (N) in ratios ranging from 10:1 to 1:10 are cultured in 6.5 w/v% PEG hydrogels with 80% HS-MMPsens-SH/20% HS-Esters-SH. A) Confocal images of spheroids stained for F-actin (cyan) and CD31 (magenta) after 14 days of culture. Scale bars: 200 μ m. B) Quantification of the cell infiltration (n = 12) and sprout length (n \geq 58) depending on the cell ratio. Box plots present mean \pm SD (error bar = min-max values, hollow square = mean value, horizontal line = median). P values are calculated using one-way ANOVA with post-hoc Tukey test, *p < 0.05, **p < 0.01, ***p < 0.001.

To test this hypothesis and the influence of HUVECs on overall cell sprouting, spheroids consisting of NHDFs only are cultured with HUVEC-conditioned media. Compared to controls that are cultivated with NHDF-conditioned as well as unconditioned endothelial cell growth medium 2 (EGM-2), the spheroids show superior sprouting when cultured with the HUVEC-conditioned media (**Figure 3.9**). While *in vitro* vascular structure formation is typically optimized by adjusting the type and ratio of supporting cells to maximize endothelial sprouting ¹⁶¹, this observation highlights a mutually supportive cellular interaction. This suggests that (growth) factors secreted by HUVECs promote NHDF invasiveness, which is known to happen for tumor cells. ¹⁹⁴ In addition to the presence of ester groups to accelerate hydrogel degradation, adjusting the cell ratio thus represents another

strategy to promote cellular invasiveness and improve overall cell growth in less favorable cellular environments.

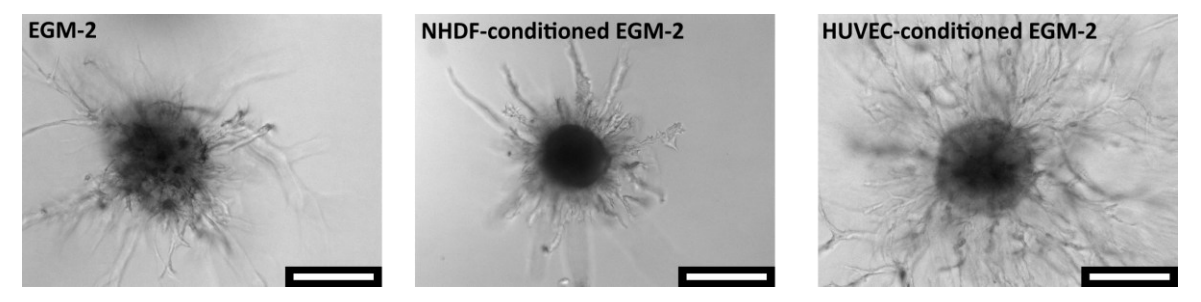


Figure 3.9: Effect of HUVEC-conditioned media on NHDF growth. Spheroids consisting of 1000 NHDFs/spheroid are cultured in 6.5 w/v% PEG hydrogels with 80% HS-MMPsens-SH/20% HS-Esters-SH. The spheroids are cultured with unconditioned EGM-2 media or EGM-2 media that is conditioned by previous cultivation of NHDFs (middle) or HUVECs (right). Brightfield images are recorded after 6 days of culture. Scale bars: 200 μm .

3.2.3 Printing Process with Spheroids in PEG Bioink

Bioprinting of larger constructs with spheroids introduces new challenges compared to the previous experiments where 15 μ L hydrogel droplets are manually prepared. As the number of spheroids needs to be sufficiently high in the much larger volume of bioink (360 μ L of PEG bioink per printed construct) to support the connection and fusion of spheroids and tissue formation, uniform spheroids (3 HUVECs/1 NHDF) with sizes of 124 ± 25 μ m (n = 400) are now produced in ultra-low attachment well plates that allow for the formation of > 20 000 spheroids within 24 h per well (**Figure 3.10**).

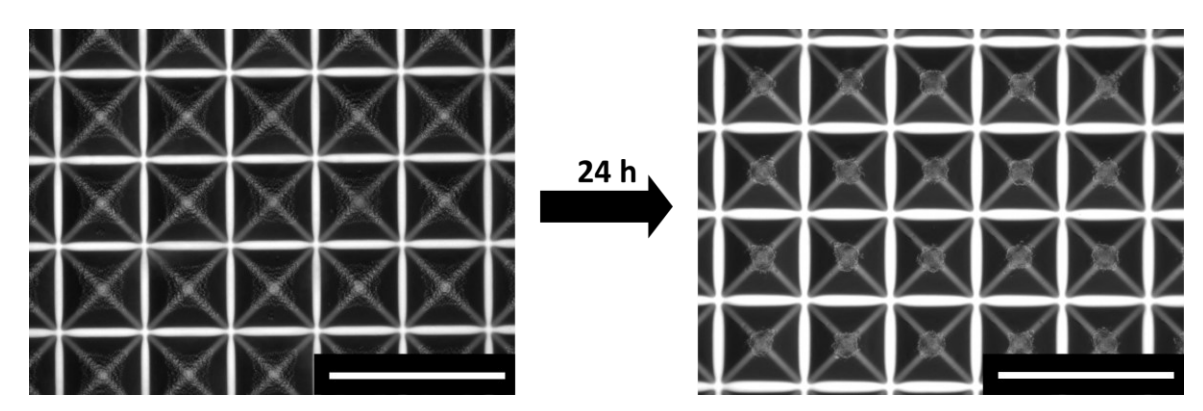


Figure 3.10: Spheroid formation on Sphericalplate 5D[®]. Formation of uniform spheroids on the Sphericalplate 5D[®] with a 3 HUVECs/1 NHDF ratio and 1000 cells/spheroid after 24 h of incubation at 37 °C and 5% CO₂. Scale bars: 1 mm.

The printed spheroid density is 6000 spheroids/mL of PEG bioink, compared to 500 spheroids/mL in case of PEG hydrogel droplets. So far, slowly crosslinking bioinks remain poorly suited for cell-laden biofabrication applications due to their inability to prevent gravity-induced sedimentation of the cells in both, the ink reservoir and the printed constructs while the bioink is still liquid. While the hydrogel droplets can be manually flipped after casting to sufficiently prevent spheroid sedimentation, spheroids have been observed to accumulate at the bottom plane of the printed constructs during bioprinting (Figure 3.11 A). To overcome this challenge and prevent spheroid sedimentation, OptiprepTM is added to the bioink as a density enhancer. OptiprepTM is commonly used as density gradient medium for isolation and purification of cells¹⁹⁵ or organelles¹⁹⁶ and has also been employed to prevent cell sedimentation during microfluidics. 197 An optimized concentration of 20 v/v% OptiprepTM efficiently prevents spheroid sedimentation in the bioink without significantly affecting the hydrogel stiffness (Figure 3.11 B). This way, it is possible to print constructs with evenly distributed spheroids throughout the whole construct (Figure 3.11 C). Moreover, the viability of spheroids within the constructs directly after printing and after 7 days of culture is assessed (Figure 3.11 D). At both time points, the cell viability ranges between 75-90%, which indicates that the shear stress during bioprinting as well as the cultivation of high spheroid densities over 7 days does not adversely affect the cell viability. Confocal images of cellular constructs stained for F-actin and CD31 show extensive growth and fusion of the spheroids as well as sprout anastomosis (Figure 3.11 E). Thereby, the network formation between the spheroids resembles the initial printing pattern. Since cells commonly grow along the path of lowest resistance, the cells growth through the hydrogel towards the channels left behind after gelatin removal and spread along their inner lumen. Due to the increased spheroid density compared to the previously prepared hydrogel droplets, the spheroids interconnect, which is important to create larger tissue constructs based on spheroid building blocks. These results pave the way for future implantation as the constructs are still handleable for transplantation, contain open channels that can be infiltrated by the host vasculature, and are primed for integration with the host tissue due to formed cellular networks during in vitro pre-cultivation.

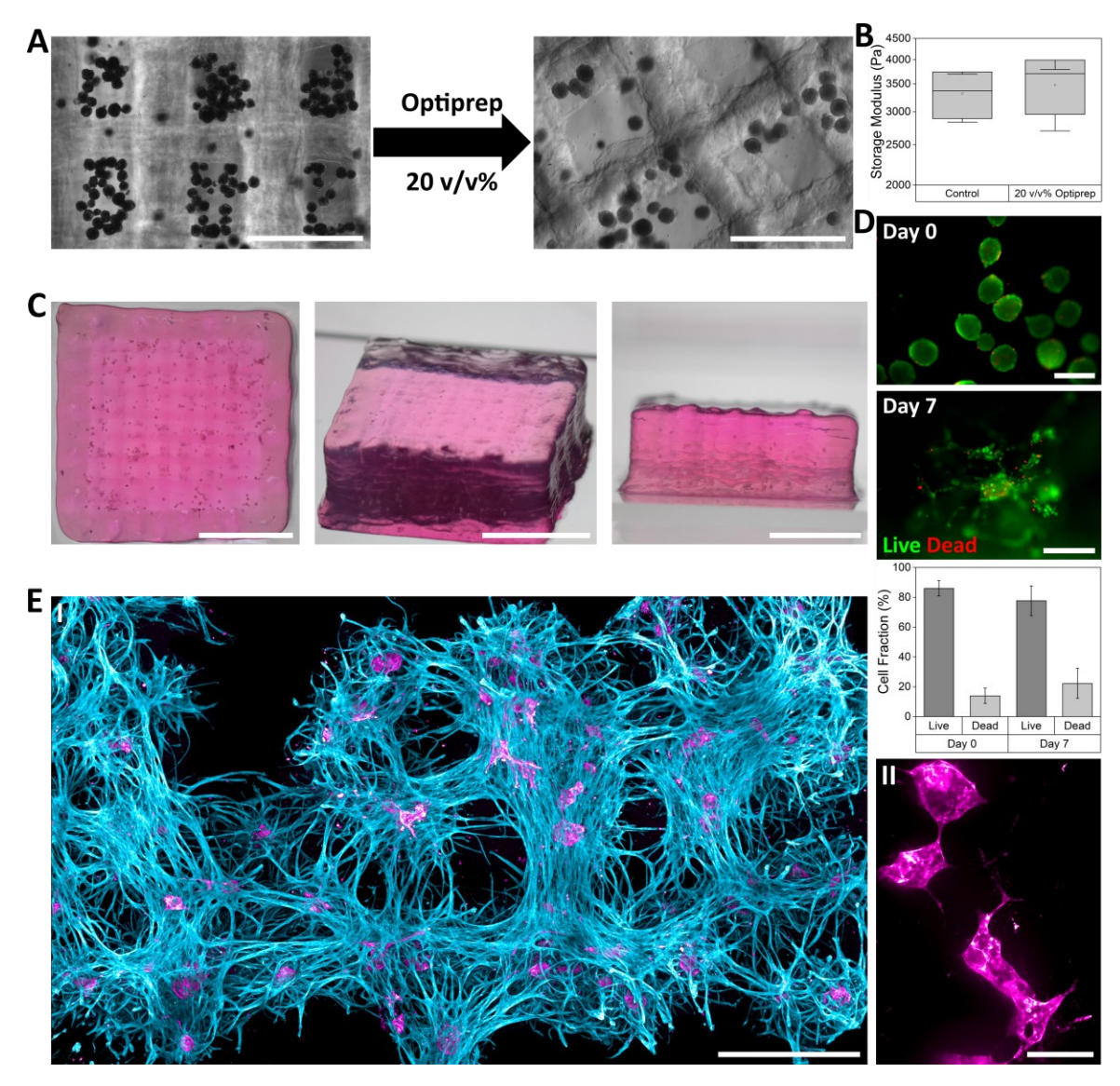


Figure 3.11: Printing of constructs with spheroids. A) Brightfield images of spheroids in printed 6.5 w/v% PEG constructs with 20 v/v% OptiprepTM to avoid spheroid sedimentation. Scale bars: 1 mm. B) Storage modulus of 6.5 w/v% PEG hydrogels with 80% HS-MMPsens-SH/20% HS-Esters-SH as well as with or without 20 w/v% OptiprepTM. Box plots present mean ± SD with n = 4 per condition (error bar = min-max values, hollow square = mean value, horizontal line = median). P values are calculated using one-way ANOVA with post-hoc Tukey test, *p < 0.05, **p < 0.01, ***p < 0.001. C) Macroscopic images of printed 6.5 w/v% PEG constructs with 20 v/v% OptiprepTM and distributed spheroids before removal of the sacrificial template. Scale bars = 5 mm. D) Viability of spheroids within printed constructs on day 0 and day 7 after printing. Scale bars: 200 μm. E) Network formation of spheroids within printed constructs (I) including the fusion of spheroids (II), stained for F-actin (cyan) and CD31 (magenta). Scale bars: I) 1 mm; II) 200 μm.

3.3 Conclusion

In contrast to commonly used animal-derived bioinks, our work demonstrates the development of a PEG-based bioink to bioprint 3D perfusable constructs with high shape fidelity that support the growth and fusion of spheroids consisting of both HUVECs and NHDFs. On the one hand, 3D cell growth and cell-cell interactions inside bulk synthetic hydrogels usually demand an environment that provides sufficient space for cells to grow, which is commonly achieved by a low polymer concentration resulting in soft hydrogels. However, these gels have poor shape retention and are difficult to handle. On the other hand, bioprinting necessitates structural fidelity to achieve precise architecture, which is provided by stiffer hydrogels. This presents a challenge in reconciling these divergent requirements, which has not been sufficiently addressed in previous works on synthetic bioinks. To overcome this limitation, we utilize ester hydrolysis to accelerate the softening of initially stiffer hydrogel constructs and to locally promote the creation of more space for cells to grow, while keeping the shape of the construct. The bioprinting of very low viscosity PEG-based bioinks with dispersed spheroids is achieved by co-printing sacrificial template materials and mixing Optiprep™ inside the bioink to acquire stable millimeter-scale 3D perfusable constructs and prevent spheroid sedimentation, respectively. This technique enables that with the optimized HUVEC/NHDF ratio of 3:1, a high overall cell invasiveness is achieved. This way, we show that 3D cell culture and bioprinting based on FDA-approved, PEG-based bioinks can be synergized to fabricate large tissue constructs and may lay the foundation for future applications of engineered tissues in the clinic.

3.4 Materials and Methods

3.4.1 Synthesis of Ester-Functionalized Di-Thiol PEG Crosslinkers

An ester-functionalized di-thiol PEG crosslinker (HS-Esters-SH) is prepared according to the literature. PEG Briefly, 1500 Da linear difunctional PEG-OH (5 g, 6.67 mmol of OH groups, Sigma-Aldrich), 3-mercaptopropionic acid (2.12 g, 20 mmol, Sigma-Aldrich) and p-toluenesulfonic acid (32 mg, 0.025 eq., Sigma-Aldrich) are added to cyclohexane (100 mL, VWR Chemicals) in a round bottom flask equipped with a Dean Stark apparatus. The mixture is heated to 100 °C under vigorous stirring for 24 h, during which the Dean Stark is emptied twice. After cooling to room temperature (RT), dichloromethane (50 mL) is added and the clear solution is washed with NaHCO₃ sat. solution (2x15 mL), brine (15 mL) and dried over MgSO₄. The solid is removed by filtration and the solution is concentrated until a viscous oil is obtained. The resulting oil is precipitated by dropwise addition in excess cold (-20 °C) diethyl ether and the final product is isolated as a white powder (isolated yield = 70%). ¹H NMR (CDCl₃, 400 MHz): δ (ppm) = 4.26 (4H, m, -CH₂CH₂OC(O)-), 3.64 (133H, br), (CH₂CH₂O)_n), 2.77 (4H, m, -CH₂CH₂SH), 2.68 (4H, m, -CH₂CH₂SH), 1.68 (2H, t, SH).

3.4.2 Preparation of Hydrogel Precursors and Hydrogel Formation

Four-arm PEG-VS (20 kDa, Creative PEGWorks) and di-thiol crosslinkers are dissolved in Dulbecco's modified Eagle medium (DMEM, Gibco) that is supplemented with 10% fetal calf serum (FCS, Biowest) and 1% antibiotic-antimycotic (ABM, Gibco). PEG-VS and crosslinker solutions are mixed in equimolar ratios and incubated at 37 °C for 30 min to form hydrogels via Michael-type addition. To render the hydrogels enzymatically and hydrolytically degradable, two different crosslinkers are combined: MMP-sensitive peptide with terminal cysteines (HS-MMPsens-SH, GCREGPQGIWGQERCG, 1774 Da, GenScript) that can be cleaved on cell-demand and an ester-functionalized HS-Esters-SH (1.7 kDa).

3.4.3 Rheological Characterization of Hydrogels

For rheological measurements, a Discovery HR 3 hybrid rheometer with a 20 mm cone-plate (2°) geometry is used. Hydrogel mixtures with a volume of 74 μ L are pipetted on the rheometer plate which is heated to 37 °C. Time-dependent measurements are performed for 30 min at a frequency of 1 Hz, an oscillation strain of 1% and a gap size of 51 μ m with triplicates per condition.

3.4.4 Scanning Electron Microscopy of the Hydrogels

3.4 and 6.5 w/v% PEG hydrogels are prepared. After crosslinking, the hydrogels are incubated in water to reach equilibrium swelling and subsequently lyophilized. Lyophilized samples are sputtered with platinum and microscopy imaging is performed with a Hitachi SU 5000 Field Emission Scanning Electron Microscope.

3.4.5 Quantification of Hydrogel Softening via Nanoindentation

Flat disk-shaped hydrogels with a volume of 45 μ L are formed in printed pluronic rings that have a radius of 4 mm and a height of 1.2 mm. After crosslinking of the hydrogels, the pluronic is removed by washing with cold PBS. The hydrogels are incubated in PBS + 1% ABM at 37 °C. To determine the hydrogel softening over a period of 14 days, the high-throughput mechanical screening platform Pavone (Optics11 Life) is used. Indentation measurements are performed at different time points using a cantilever-based probe with a spherical tip radius of 53 μ m and a stiffness of 0.21 N/m. The indentation-depth is 8 μ m. Per hydrogel, an automated matrix scan is configured to obtain the mechanical properties of a 5×5 grid. All measurements are performed at RT with triplicates per condition.

3.4.6 Evaluation of Hydrogel Swelling

Flat, disk-shaped hydrogels with a volume of 45 μ L are formed in printed pluronic rings. After crosslinking of the hydrogels, the pluronic is removed by washing with cold PBS. The hydrogels are incubated in PBS + 1% ABM at 37 °C. To determine

the hydrogel swelling, individual hydrogels are weighed at different time points over a period of 14 days. Triplicates are prepared per condition.

3.4.7 Cell Culture

Human umbilical vein endothelial cells (HUVECs, Lonza) are cultured in tissue culture flasks with endothelial cell growth medium 2 (EGM-2, Promocell) supplemented with 1% antibiotic-antimycotic (ABM, Gibco) up to passage 6. Normal human dermal fibroblasts (NHDFs, Promocell) are cultured in tissue culture flasks with DMEM supplemented with 10% FCS and 1% ABM up to passage 8. Both cell types are cultured at 37 °C with 5% CO₂ according to standards protocols.

3.4.8 Cultivation of Cell Spheroids in Hydrogels

Cell spheroids consisting of 1000 cells/spheroid are formed in hanging drops. Briefly, HUVECs and NHDFs are suspended in DMEM with 10% FCS and 1% ABM in different ratios. Cell suspensions are then mixed with 20% Methocel (1.2 w/v% methyl cellulose (4000 cP, Sigma) in DMEM) and 30 μ L droplets are formed on petri dishes that are incubated overnight at 37 °C and 5% CO₂ to allow for spheroid formation. Afterwards, spheroids are harvested and mixed with hydrogel components at a concentration of 0.5 spheroids/ μ L. To promote cell growth, PEG-VS is pre-incubated with GRGDSPC (690.7 Da, CPC Scientific) at a final concentration of 0.6 mM before crosslinkers are added in different ratios to render the hydrogels hydrolytically and enzymatically degradable. Finally, 15 μ L hydrogel droplets are casted on 8-well ibidi slides and allowed to crosslink for 30 min before adding 300 μ L EGM-2 and cultivation at 37 °C and 5% CO₂ with medium changes every 2-3 days. To investigate the influence of HUVEC- or NHDF-conditioned media on NHDF spheroid sprouting, EGM-2 is conditioned by incubation with HUVECs or NHDFs for 24 h before spheroid cultivation.

3.4.9 Immunofluorescence Staining and Imaging

After 14 days of culture, the cell culture media is removed from the hydrogel samples, followed by washing with PBS for 30 min and fixing with 4% paraformaldehyde solution (PFA, AppliChem) for 50 min at RT. After washing twice with PBS, the samples are incubated with 0.1% Triton X-100 (Sigma Aldrich) solution in PBS for 20 min for cell membrane permeabilization, followed by three more PBS washing steps. Afterwards, the samples are blocked by incubating with 4% bovine serum albumin (BSA, SEQENS) solution in PBS for 4 h. This is followed by incubation with a monoclonal mouse anti-human CD31/PECAM-1 antibody (Bio-Techne, 1:200) in 1% BSA in PBS solution overnight at 4 °C. After washing with PBS thrice, 30 min each, the samples are incubated with Alexa Fluor 555 goat anti-mouse antibody (Invitrogen, 1:200) and Phalloidin-iFluor 405 (abcam, 1:1000) in PBS for 4 h at RT. After washing twice with PBS, the samples are stored in PBS at 4 °C. Alternatively, cells are pre-stained with carbocyanine dyes DiO and Dil (VybrantTM Cell-Labeling Solutions, Molecular Probes) by adding 5 µL cell labeling solution per mL of cell suspension with a concentration of 1·10⁶ cells/mL, followed by incubation at 37 °C. Afterwards, the cell suspensions are washed three times with serum-free DMEM before cell encapsulation in PEG hydrogels. The samples are imaged using a Leica SP8 Tandem Confocal microscope using an air objective of 10×/0.3 NA. Z-stacks of up to 500 µm thickness were obtained for each sample. For excitation at 405 nm and 561 nm, the microscope is equipped with a diode 405 and DPSS 561 laser. HyD detectors with CS2 UV Optics 1 filters are used to detect the resulting emission. Tile scan images of spheroid growth in printed constructs are additionally recorded using an Opera Phenix Plus High-Content Screening System with a 10×/0.3 NA air objective.

3.4.10 Printing of Constructs with PEG Bioink and Sacrificial Gelatin Scaffold

Constructs are printed using a R-GEN 200 3D bioprinter (REGENHU, Switzerland) mounted with a volumetric printhead for sacrificial material (gelatin in DMEM at 7.5 w/v%) dispensing and a dynamic formulation printhead equipped with a cartridge containing the PEG-VS solution at 20 w/v% in DMEM (cartridge 1), a

cartridge containing the HS-MMPsens-SH and HS-Esters-SH crosslinker solution at 3 w/v% in DMEM (cartridge 2), a cartridge containing DMEM (cartridge 3), and a cartridge containing sterile Milli-Q water (cartridge 4) used for flushing. The ratios of cartridge 1, 2, and 3 are adjusted to print either a 3.4 w/v% or a 6.5 w/v% construct according to the same design and printing parameters. Cartridges 1 and 2 are maintained at 15 °C, the cartridge containing the sacrificial material is maintained at 27 °C, and the print bed is maintained at 15 °C during the entire printing process. The sacrificial material is printed at a speed of 12 mm/s with a G23 nozzle. The bioink is printed at a speed of 10 mm/s with a G22 nozzle. The construct is designed using the integrated SHAPER software (REGENHU, Switzerland). Briefly, a layer of sacrificial template is printed first. The bioink is then extruded in between the struts of the sacrificial scaffold. The process is repeated for 13 or 25 layers of 200 µm each with alternating layers of channels in the horizontal and vertical direction to achieve a final height of 2.5 or 5 mm. After printing, the construct is left to crosslink at RT for at least another 30 min. The sacrificial material is then removed by incubation at 37 °C.

3.4.11 Printing and Degradation of Constructs with Different Crosslinker Ratios

Constructs are printed as previously described. The ratios of HS-MMPsens-SH and HS-Esters-SH crosslinkers are directly adjusted in cartridge 2 at the desired ratio. After printing and scaffold removal, the constructs are imaged using a Keyence VHX-7000 digital microscope and the channel interconnectivity is verified by perfusing red food dye. For accelerated hydrolytic crosslinker degradation, the constructs were incubated in PBS adjusted to pH 9 for 3 days at 37 °C. The constructs are then imaged again.

3.4.13 Printing of Constructs with Live Cell Spheroids

Cell spheroids consisting of 1000 cells/spheroid are formed using the Sphericalplate 5D® in 6-well format (Kugelmeiers Ltd, Erlenbach). Per well, which contains 3364 microwells for spheroid formation, 1.5 mL of HUVEC and 0.5 mL of

NHDF suspensions in EGM-2, each with a concentration of 1 682 000 cells/mL, are added and centrifuged at 150 g for 3 min at RT to force the cells into the microwells. After 24 h of incubation at 37 °C and 5% CO₂, spheroids are harvested by repetitive pipetting and suspended in PEG-VS solution in DMEM (with 20 v/v% OptiprepTM) to a concentration of 20,184 spheroids/mL, which is subsequently used for bioprinting. 3D bioprinting is adapted for printing with live spheroids and otherwise performed as described previously. Briefly, all cartridges, nozzles and tubings are sterilized with gamma radiation. Gelatin is sterilized by exposure to UV light for 1 h. The 3D bioprinter is sterilized prior to use using the built-in germicide UV lamp for 1 h. All stock solutions and cartridge filling are performed in a laminar Cartridge 1 is filled with a suspension of spheroids (20 184 spheroids/mL) in 20 w/v% PEG-VS in DMEM with 20 v/v% Optiprep[™] and a solution of GRGDSPC (21.91 mg/mL) in DMEM with 20 v/v% Optiprep[™] in a 9:1 volume ratio. Cartridge 2 is filled with a solution of HS-MMPsens-SH crosslinker (3 w/v%) and HS-Esters-SH crosslinker (3 w/v%) in DMEM with 20 v/v% OptiprepTM in an 8:2 volume ratio. Cartridge 3 is filled with DMEM with 20 v/v% OptiprepTM. To achieve the final hydrogel composition, cartridges 1, 2, and 3 are mixed in a 29.2:31.8:39.0 ratio in the dynamic dispensing tool. After printing, the constructs are allowed to further crosslink at RT for 30 min. Gelatin is removed by incubating (37 °C, 5% CO₂) the construct and subsequent washes with DMEM. Constructs are then incubated (37 °C, 5% CO₂) for 7 days. Spheroid viability is evaluated by sacrificing one construct after printing (day 0) and after 7 days by LIVE/DEAD assay and quantified by determining the mean gray value of live and dead cells.

3.4.14 Statistical Analysis

Each experiment is performed with $n \ge 3$. Statistical analysis of the data is conducted in OriginPro 2020 using a one-way ANOVA. Pair comparisons are performed using Tukey's method, where p-values below 0.05 are considered as significant differences (*p < 0.05; **p < 0.01; ***p < 0.001).

4 Engineering Vascular Structures by Fusion of Prevascularized Spheroids

Daniel Günther, Johannes Hahn, Si-Ting Wu, Ramin Nasehi, Mieke Dewerchin, Horst Fischer, Laura De Laporte

4.1 Introduction

In Chapter 3, prevascularized spheroids consisting of HUVECs and NHDFs were introduced as building blocks for bioprinting. These spheroids can fuse with neighboring spheroids into larger structures, which is an important requirement to grow large and dense tissue constructs in the future. Yet, the implementation of a vascular network is essential to ensure the sustained supply of nutrients and oxygen to the cells within the fabricated constructs. While the presented spheroids supported endothelial sprouting in PEG-based bioinks as a first step towards the formation of vascular structures, the sprouts did not exhibit a central lumen, which is characteristic for functional vasculature. Rather than relying on endothelial sprouting for lumen formation, previous studies have demonstrated that spheroids can reorganize into multi-luminal structures, utilizing the spheroids themselves as vascular building blocks. In prevascularized spheroids that are cultured in Matrigel or gelatin hydrogels and contain HUVECs, fibroblasts, and mesenchymal stem cells in a ratio of 1:4.5:4.5, HUVECs can form multiple capillary-like structures within the spheroid core, which may connect upon spheroid fusion. 165, 166 While these studies show the potential of prevascularized spheroids for vascular tissue engineering by demonstrating the formation of multiple small lumens and the fusion of limited numbers of spheroids, it remains uncertain whether this approach can support the formation of functional, long-scale vascular structures with a continuous lumen. Alternatively, engineered vascular structures with a continuous lumen can be fabricated using sacrificial bioinks that support in situ endothelialization 102, 167 or by pre-forming channels coated with endothelial cells. 193, 199 These approaches facilitate the formation of artificial blood vessels and sprouting of luminal capillaries originating from the engineered vessel, but they are labor-intensive, time-consuming, and therefore difficult to scale. Thus, we investigate in this work if our prevascularized spheroids could autonomously reorganize into luminal structures with the potential to fuse and build continuous vascular channels. Since this process would entirely rely on cellular selforganization, it could offer a scalable strategy to fabricate vascular structures in larger tissue constructs and could be integrated into high-throughput applications. Based on our investigation of the influence of spheroid composition on cellular sprouting by varying the HUVEC/NHDF ratio in Chapter 3, we observed in higher magnification images that spheroids with a 3 HUVECs/1 NHDF ratio reorganize into uniluminal structures when cultured in 6.5 w/v% PEG hydrogels. This phenomenon is not observed for other spheroid compositions (Figure 4.1 A). We hypothesize that, while spheroids with the mentioned 1 HUVEC/9 supporting cells form multi-luminal structures, a higher fraction of HUVECs results in the fusion of multiple small lumens into one bigger central lumen. In addition, we investigate how the spheroid size and matrix stiffness influence the lumen formation. Finally, we show that neighboring spheroids can fuse to create continuous lumens, which is further manipulated by acoustic alignment to direct the organization of tubular vascular structures (Figure 4.1 B).

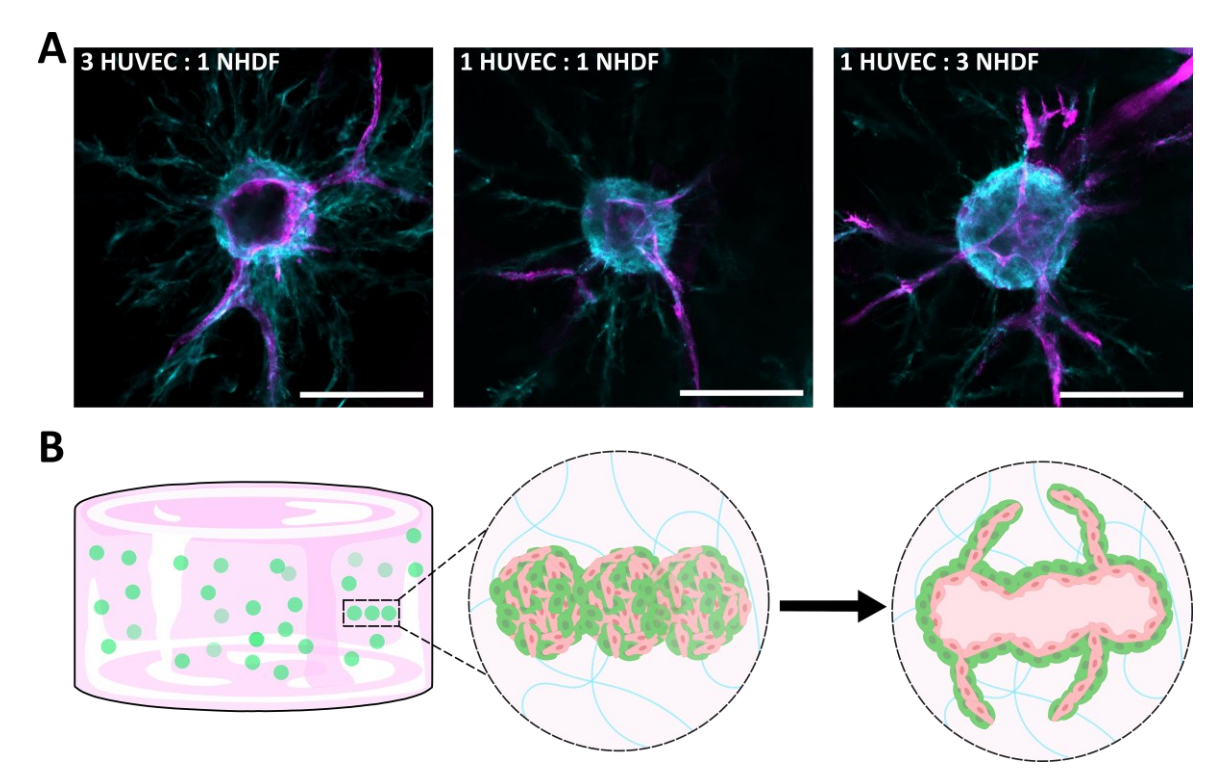


Figure 4.1: Influence of cell ratios on spheroid reorganization and fusion into tubular vascular structures. A) Confocal images of spheroid with HUVEC/NHDF ratios from 3:1 to 1:3 cultured in 6.5 w/v% PEG hydrogels. The samples are stained for F-actin (cyan) and CD31 (magenta) after 14 days in culture. Scale bars: 200 μm. B) Schematic of spheroids reorganizing and fusing to create vascular-like structures with a continuous lumen that is lined by endothelial cells (red) and surrounded by layers of fibroblasts (green).

4.2 Results and Discussion

4.2.1 Formation of Uniluminal Spheroids in PEG Hydrogels

When spheroids consisting of 3 HUVECs/1 NHDF and 1000 cells/spheroid are cultured in PEG hydrogels, HUVECs are initially evenly distributed throughout the solid spheroids (**Figure 4.2 A**). Within 14 days of cultivation, the spheroids substantially reorganize into hollow structures with a central lumen that resemble the structure of simplified blood vessels. Similar to the tunica intima, which is the inner layer of endothelial cells in blood vessels, the HUVECs within the hollow spheroids are lining the inner lumen and build a continuous monolayer as shown in 3D reconstruction images of CD31 immunostained samples. The HUVEC monolayer is thereby surrounded by layers of fibroblasts, which resemble the connective tissue layers of blood vessels (**Figure 4.2 B**).

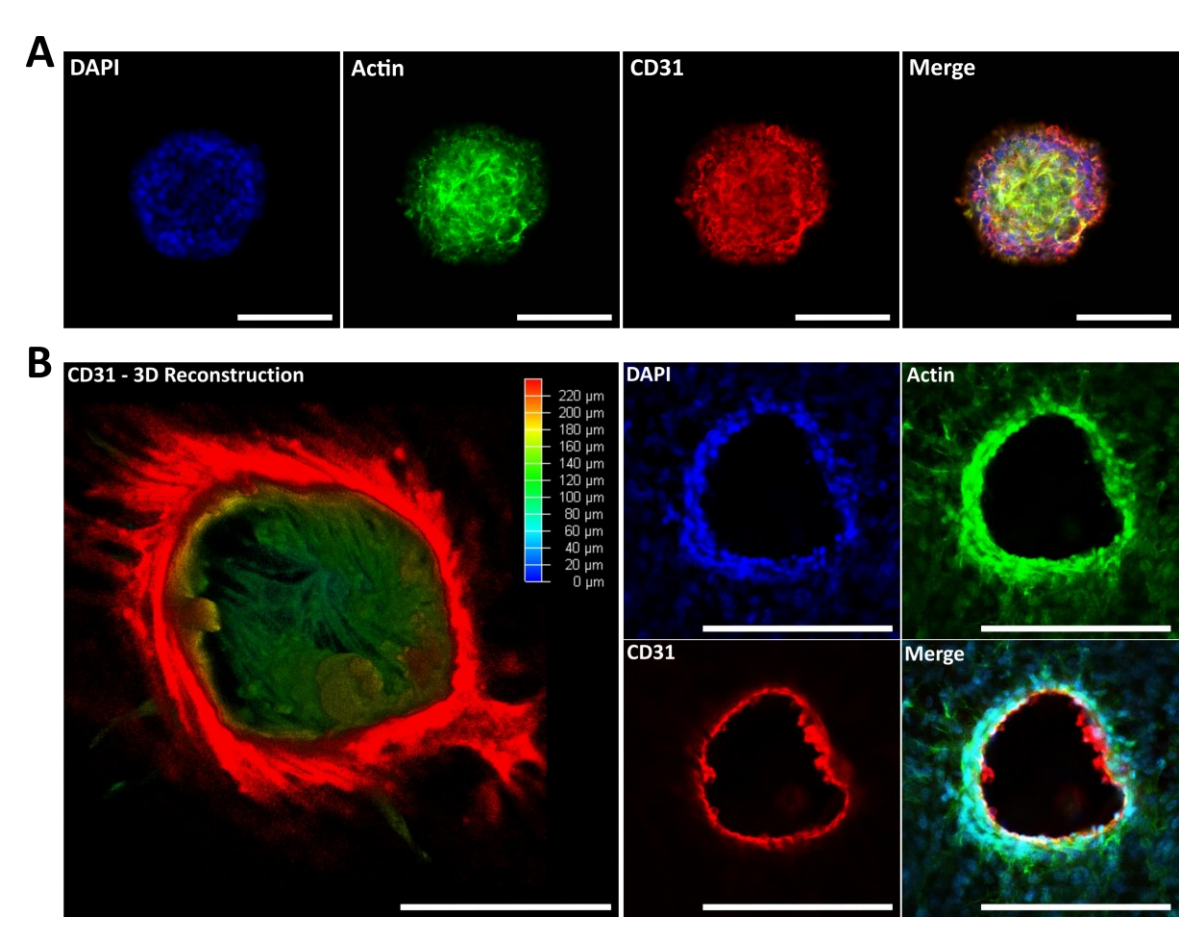


Figure 4.2: Uniluminal spheroid formation in PEG hydrogels. A) Confocal images of spheroids consisting of 1000 cells/spheroid with a 3 HUVECs/1 NHDF ratio fixed immediately after hydrogel encapsulation. B) 3D reconstruction of spheroid lumen stained for CD31, including sections stained for nuclei (blue), F-actin (green) and CD31 (red). Scale bars: 200 µm.

To further understand the process of spheroid lumen formation, the influence of the hydrogel stiffness is tested by cultivating spheroids in 2.5, 3.4 and 6.5 w/v% PEG hydrogels. Additionally, the spheroid size is varied by cultivation of spheroid with a 3 HUVECs/1 NHDF ratio and 333, 1000 and 3000 cells/spheroid in the hydrogels. The reorganization of spheroids into luminal structures with the characteristic inner layer of endothelial cells is observed for all conditions except for spheroids consisting of 333 cells spheroid that are cultured in 6.5 w/v% PEG hydrogels (Figure 4.3 A). Thereby, both the spheroid size and the hydrogel stiffness influence the probability of lumen formation as well as the lumen diameter and area after 14 days of culture (Figure 4.3 B). While all spheroids form lumens in 2.5 w/v% PEG hydrogels, the fraction of lumen-forming spheroids as well as the lumen diameter and area decrease for all tested spheroid sizes as the hydrogel stiffness increases, which was quantified based on confocal images. In case of 2.5 w/v% PEG hydrogels, the spheroid lumen diameter and area vary between $173 \pm 32 \,\mu\text{m}$ and $15 \, 434 \pm 6587 \,\mu\text{m}^2$ for 333 cells/spheroid and 223 ± 35 $\,\mu\text{m}$ for 3000 cells/spheroid. In 3.4 w/v% PEG hydrogels, spheroids consisting of 333 cells form lumens with a diameter of 59 \pm 9 μ m and an area of 2626 \pm 1069 μ m², while 3000 cells/spheroid are characterized by lumen diameters of 145 \pm 8 μ m and areas of 12 994 ± 1296 µm². The biggest lumens in 6.5 w/v% PEG hydrogels are formed by spheroids consisting of 3000 cells with a lumen diameter 138 ± 33 µm and an area of 11 316 ± 6353 µm². As expected, the size of the lumen consistently increases with increasing number of cells per spheroid, which allows to control the size of the lumen and thereby the diameter of engineered capillaries for different purposes. Yet, the reorganization of spheroids to create a central lumen requires space and therefore cells to migrate out of the spheroid core and into the surrounding hydrogel matrix. As discussed in Chapter 3, the growth of spheroids is restricted in stiffer hydrogels, which therefore limits spheroids to reorganize into uniluminal structures, resulting in a decreased fraction of lumenized spheroids and the size of their lumens with increasing hydrogel stiffness. In contrast to the lumen size, the probability of lumen formation does not continuously increase with increasing number of cells per spheroid. In case of 3.4 w/v% PEG hydrogels, 94% of spheroids consisting of 1000 cells form lumens, whereas 52% and 48% of spheroids consisting of 333 and 3000 cells/spheroid form lumens, respectively. Therefore, the growth of spheroids is monitored over a period of 14 days.

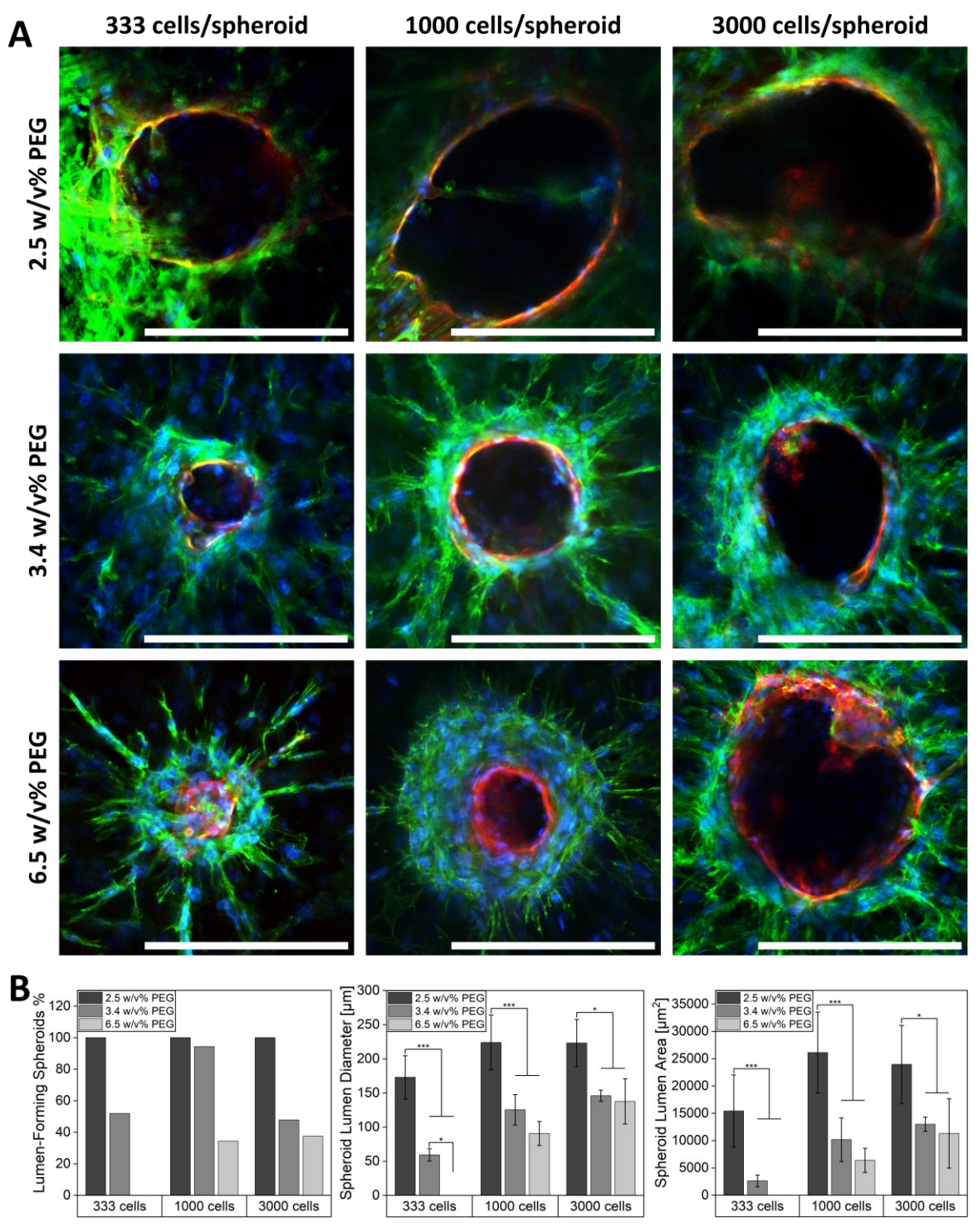


Figure 4.3: Influence of spheroid size and hydrogel stiffness on spheroid lumen formation. A) Confocal images of spheroids consisting of 333, 1000 and 3000 cells/spheroid with a cell ratio of 3 HUVECs/1 NHDF cultured in 2.5, 3.4 and 6.5 w/v% PEG hydrogels for 14 days. The samples are stained for nuclei (blue), F-actin (green) and CD31 (red). B) Quantification of lumen-forming spheroids and spheroid lumen diameter as well as spheroid lumen area depending on the spheroid size and hydrogel stiffness. Data of spheroid lumen diameter and area is presented as mean \pm SD with $n \ge 3$ for each condition. P values are calculated using one-way ANOVA with post-hoc Tukey test, *p < 0.05, **p < 0.01, ***p < 0.001.

Smaller spheroids consisting of 333 cells as well as 1000 cells start to form long sprouts after 1 day of culture, whereas bigger spheroids with 3000 cells only start to sprout slowly and are partly fused as the number of cells exceeded the capacity of the microwells used for spheroid formation, causing them to escape and merge with spheroids in neighboring microwells (Figure 4.4 A). After 7 days, lumens are forming in conditions with 333 cells/spheroid as well as 1000 cells/spheroids, which is not observed for the bigger spheroids consisting of 3000 cells. As the number of cells per spheroid increases, they become more compact due to stronger cell-cell contacts and the deposition of more ECM, leading to a denser pericellular environment, which has been shown to influence their sensitivity in drug screenings. 200, 201 This potentially limits their ability reorganize into uniluminal structures as well. Only after 14 days, some of the spheroids form lumens that are visible in brightfield images while other develop a dark core, characteristic for cell death. This is likely the result of oxygen deprivation of cells at the core. At the same time, hypoxic conditions are known to stimulate angiogenesis and thereby lumen formation.²⁰² As the oxygen gradient increases with increasing spheroid size, this could explain why lumen formation is most frequent in spheroids with 1000 cells. Smaller spheroids may lack a sufficient oxygen gradient to promote lumen formation, while larger spheroids experience excessive hypoxia, which can instead promote necrosis. In case of 2.5 w/v% PEG hydrogels, which support lumen formation of all spheroid sizes, confocal images show that spheroids consisting of 1000 cells form central lumens that are characterized by the typical inner layer of endothelial cells already after 1 day of culture (Figure 4.4 B). These lumens have a diameter of 92 \pm 8 μ m and an area of 4542 \pm 1314 μ m². Over time, the size of the lumens increase and reach a diameter of 215±54 µm and an area of 25 839 ± 10 920 μm² after 7 days, which stagnates during further cultivation for up to 14 days (Figure 4.4 C). Instead, continued cultivation results in excessive cell growth within the hydrogel without significantly affecting the size of the lumens. This shows that a prolonged cultivation that extends 7 days does not contribute to the formation of bigger lumens.

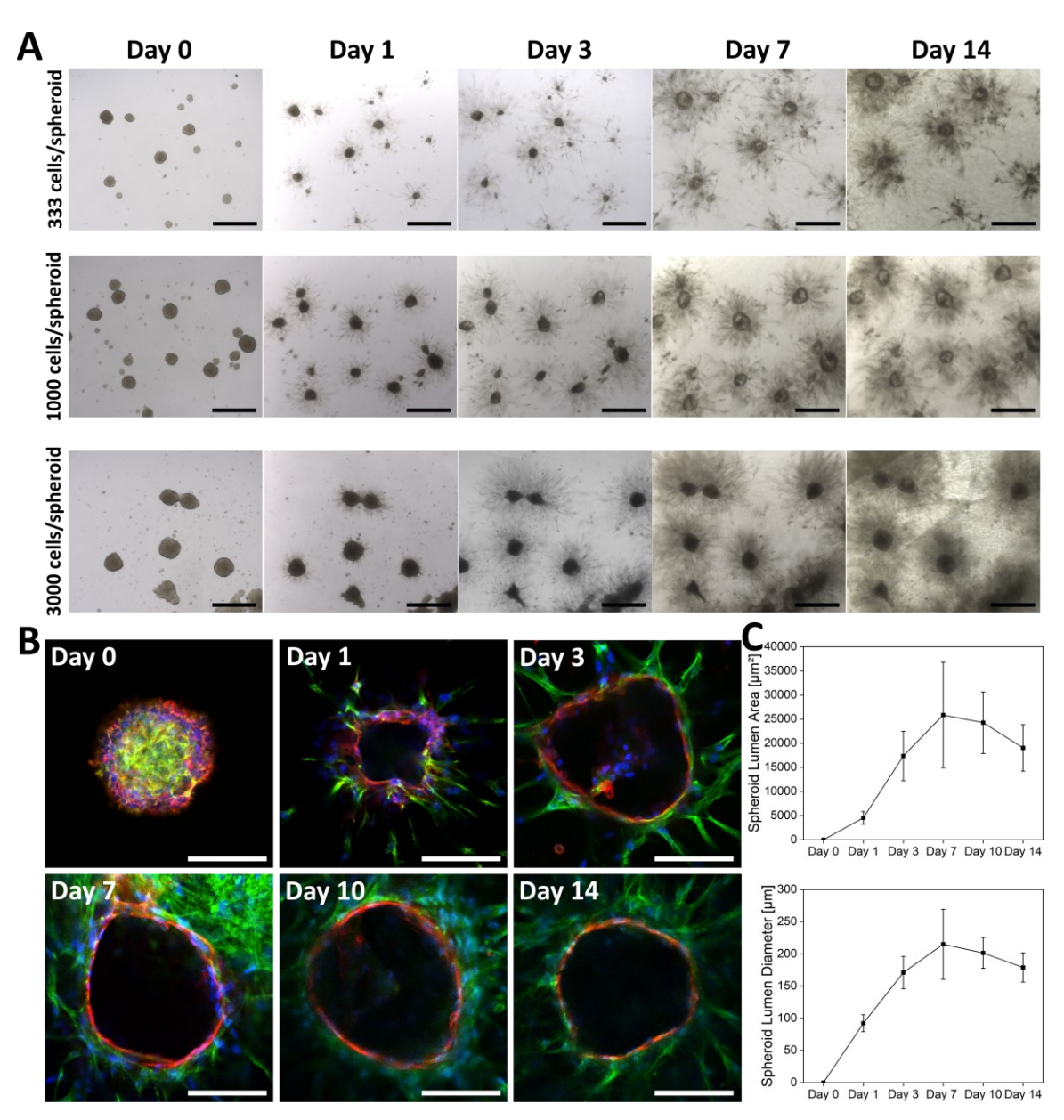


Figure 4.4: Monitoring spheroid reorganization over time. A) Cultivation of spheroids consisting of 333, 1000 and 3000 cells with a cell ratio of 3 HUVECs/1 NHDF in 3.4 w/v% PEG hydrogels. Brightfield mages are recorded after 0, 1, 3, 7 and 14 days. Arrows indicate lumenized spheroids Scale bars: $500 \ \mu m$. B) Confocal images of spheroids consisting of 1000 cells with a cell ratio of 3 HUVECs/1 NHDF in 2.5 w/v% PEG hydrogels recorded after 0, 1, 3, 7 and 14 days of culture. The samples are stained for nuclei (blue), F-actin (green) and CD31 (red). C) Quantification of lumen diameter and surface area depending on the duration of spheroid culture in 2.5 w/v% PEG hydrogels.

4.2.2 Fusion of Prevascularized Spheroids to Create Vascular Channels with Continuous Lumen

While the lumen formation of spheroids is essential for the functionality of artificial blood vessels, the formation of tubular structures requires the fusion of multiple spheroids and the generation of continuous lumens as a result of their fusion. During single spheroid experiments with various cell numbers per spheroid as well as different hydrogel stiffnesses, the fusion of neighboring spheroids into larger cell structures is observed (Figure 4.5 A). In all cases of spheroid fusion, endothelial cells form continuous structures between the neighboring spheroids, which is an important step to create a vascular network. As for single spheroid experiments, the formation of a continuous lumen between the spheroids and its width thereby depend on the hydrogel stiffness and the number of cells per spheroid. In 3.4 w/v% PEG hydrogels, uniluminal spheroids fuse with neighboring spheroids to form a continuous lumen. While spheroids with 1000 cells/spheroid form a narrow lumenized connection that is lined by endothelial cells, fusing spheroids with 3000 cells/spheroid form a vascular-like lumen at full spheroid width. In contrast, the lower probability of lumen formation in 6.5 w/v% PEG hydrogels, causes that not all fusing spheroids develop a continuous lumen as observed in the condition with 1000 cells/spheroid. These spheroids are characterized by the reorganization into a solid core of endothelial cells that fuse with neighboring spheroids without lumen formation. When spheroids in 6.5 w/v% PEG hydrogels do reorganize into uniluminal structures, as observed in the condition with 3000 cells/spheroid, the fusion of neighboring spheroids results in a narrow, continuous lumen that is less efficiently formed compared to spheroids of the same size in 3.4 w/v% PEG hydrogels. This could indicate that the fusion process is hampered as the stiffness of the surrounding hydrogel increases. On the other hand, spheroids consisting of 3000 cells partly fused already during their formation within microwells with adjacent spheroids. As a result, these spheroids no longer need to undergo fusion within the hydrogel to form elongated tubular structures. This way, larger spheroids consisting of 3000 cells form mm-long tubular structures within softer 2.5 w/v% PEG hydrogels. These are characterized by a continuous layer of endothelial cells that fully encloses the formed tubes as shown in 3D reconstruction images of CD31-positive structures (Figure 4.5 B). This is likely due to the combination of pre-fusion during spheroid formation and the softer hydrogels providing a more supportive environment for both continued spheroid fusion as well as lumen formation.

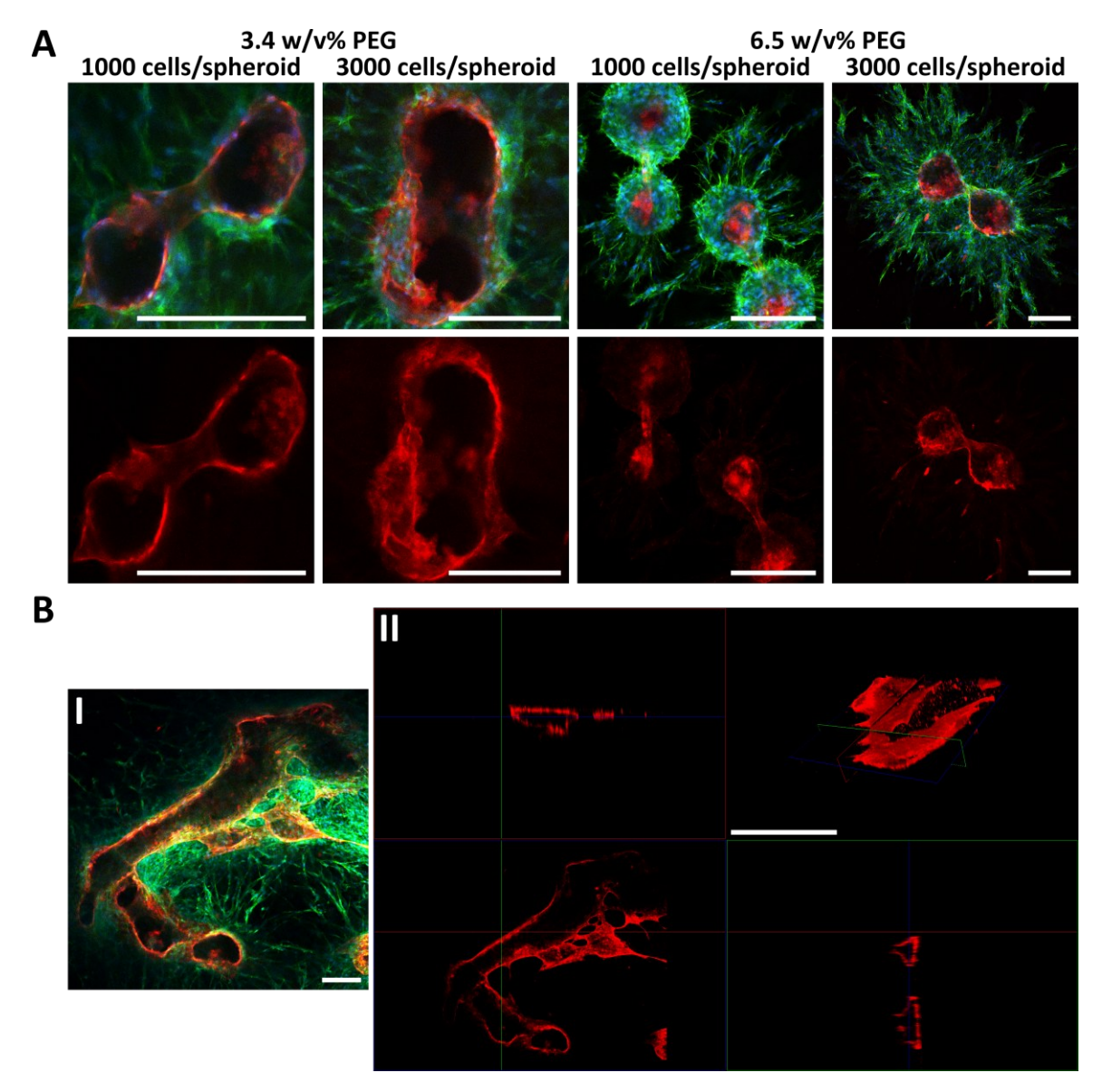


Figure 4.5: Fusion of neighboring spheroids. A) Confocal images of neighboring spheroids consisting of 1000 or 3000 cells with a cell ratio of 3 HUVECs/1 NHDF that are fusing after 14 days of culture in 3.4 or 6.5 w/v% PEG hydrogels. The samples are stained for nuclei (blue), F-actin (green) and CD31 (red). Scale bars: 200 μ m. B) Fusion of neighboring spheroids consisting of 3000 cells after 14 days of culture in 2.5 w/v% PEG hydrogels. 3D Reconstruction of CD31-positive structures (II) show that the lumen is continuous and enclosed by endothelial cells. Scale bars: I) 200 μ m; II) 1 mm.

The fusion efficiency of neighboring spheroids also depends on their proximity. Previous studies have demonstrated that depending on the spacing between spheroids, they either form cellular bridges from interacting sprouts at distances of 200 µm and more or they fuse when the spheroid distance is 100 µm or lower.²⁰³ In the experiments so far, the distance between adjacent spheroids depend on the spheroid density and distribution within the hydrogel, resulting in irregular spheroid fusion. Thus, to be able to control the distance between spheroids and thereby their fusion, acoustic alignment is utilized to organize spheroids into single lines, aiming to create continuous vascular channels. Here, 400 µL of PEG hydrogel mixture containing 3750 spheroids/mL are filled into well plates with silicon chambers that are placed in a mold filled with water and two opposite transducers. The transducers convert electrical power into an acoustic standing wave. During the gelation of the hydrogel, the spheroids accumulate at the pressure nodes of the standing wave and sediment, which results in the formation of spheroid lines. The density and proximity of neighboring spheroids can be controlled by adjusting both the amplitude as well as the frequency of the acoustic wave. As the hydrogel crosslinks, the spheroids are fixed in their position for further cultivation (Figure 4.6).

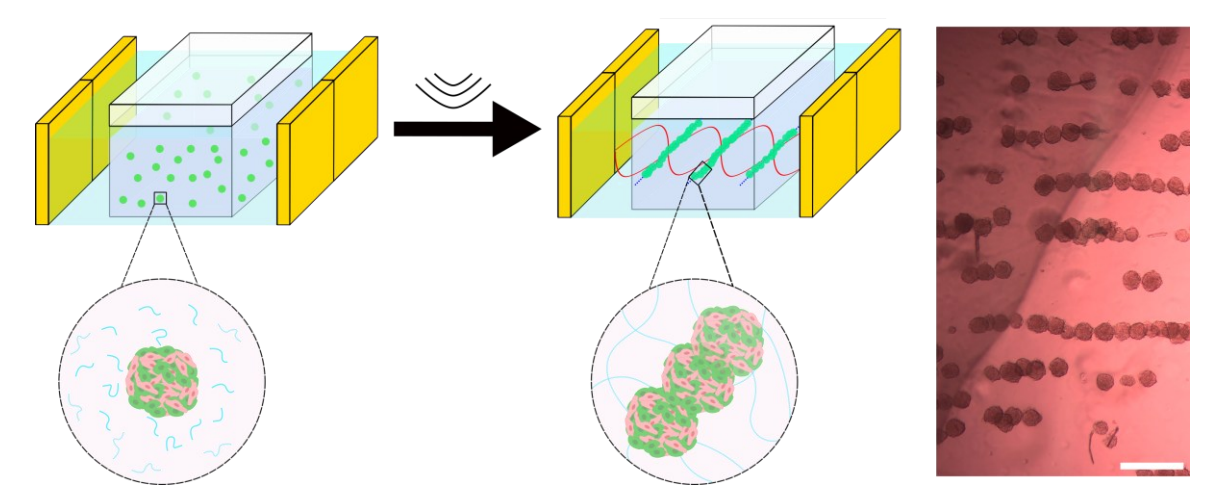


Figure 4.6: Schematic of acoustic spheroid alignment. A silicon chamber filled with the PEG hydrogel mixture and spheroids is placed in a water bath with two opposing transducers (yellow). During the gelation of the hydrogel, two transducers (yellow) transform electrical power into acoustic power that creates a standing wave (red). Spheroids (green) within the hydrogel mix accumulate at the pressure nodes while they sediment to the bottom of the well and form a line. Scale bar: 500 μm.

When spheroids consisting of 1000 cells and a 3 HUVECs/1 NHDF ratio are cultured in 3.4 w/v% PEG hydrogels for 14 days after acoustic spheroid alignment, the cells form a confluent layer on the hydrogel surface. This includes patches of endothelial cells that form networks observed on the edges of the hydrogel. Spheroids are visible as CD31-positive structures with a central lumen that is open to the bottom of the hydrogel and embedded within the layer of cells (Figure 4.7 A I). While most of the spheroids are arranged in lines, multiple single spheroids are randomly distributed within the hydrogel, which indicates inefficient spheroid alignment probably due to air bubbles within the surrounding water that hindered wave propagation due to scattering.²⁰⁴ In the hydrogel, neighboring spheroids are able to fuse as part of spheroid lines that are characterized by endothelial cell anastomosis in-between spheroids, while NHDFs are sprouting and form cellular bridges with further distant spheroids (Figure 4.7 A II). Higher magnification images reveal that multiple neighboring spheroids undergo fusion and form a continuous tubular structure with a length of approximately 600 µm. Surrounding the central lumen, HUVECs form a cohesive layer with uniform morphology, which indicates that the spheroids are fully integrated into the created channel (Figure **4.7** A III). As the spheroids are open to the bottom of the hydrogel, they can be perfused with fluorescent beads of 1 and 15 µm. Both bead sizes enter the formed lumen and are found at the interface of fusing spheroids, which proves both the presence of lumens as well as the continuity of the lumens between multiple neighboring spheroids (Figure 4.7 B). These results represent an important first step towards the formation of functional and perfusable vascular structures made of spheroid building blocks. However, in order to be functional the vasculature is required to be fully enclosed by endothelial cells to fulfill its barrier function. Therefore, the sedimentation of the spheroids must be prevented, which otherwise results in the formation of a lumen that is open to the bottom of the hydrogel. For this purpose, a sandwich model is developed by pre-coating the well for acoustic alignment with a layer of agarose. After spheroid alignment and crosslinking of the hydrogel, the agarose layer is removed with a scalpel and replaced with a second PEG hydrogel to embed the spheroid layer between two PEG hydrogels, resulting in a stable construct (Figure 4.8 A).

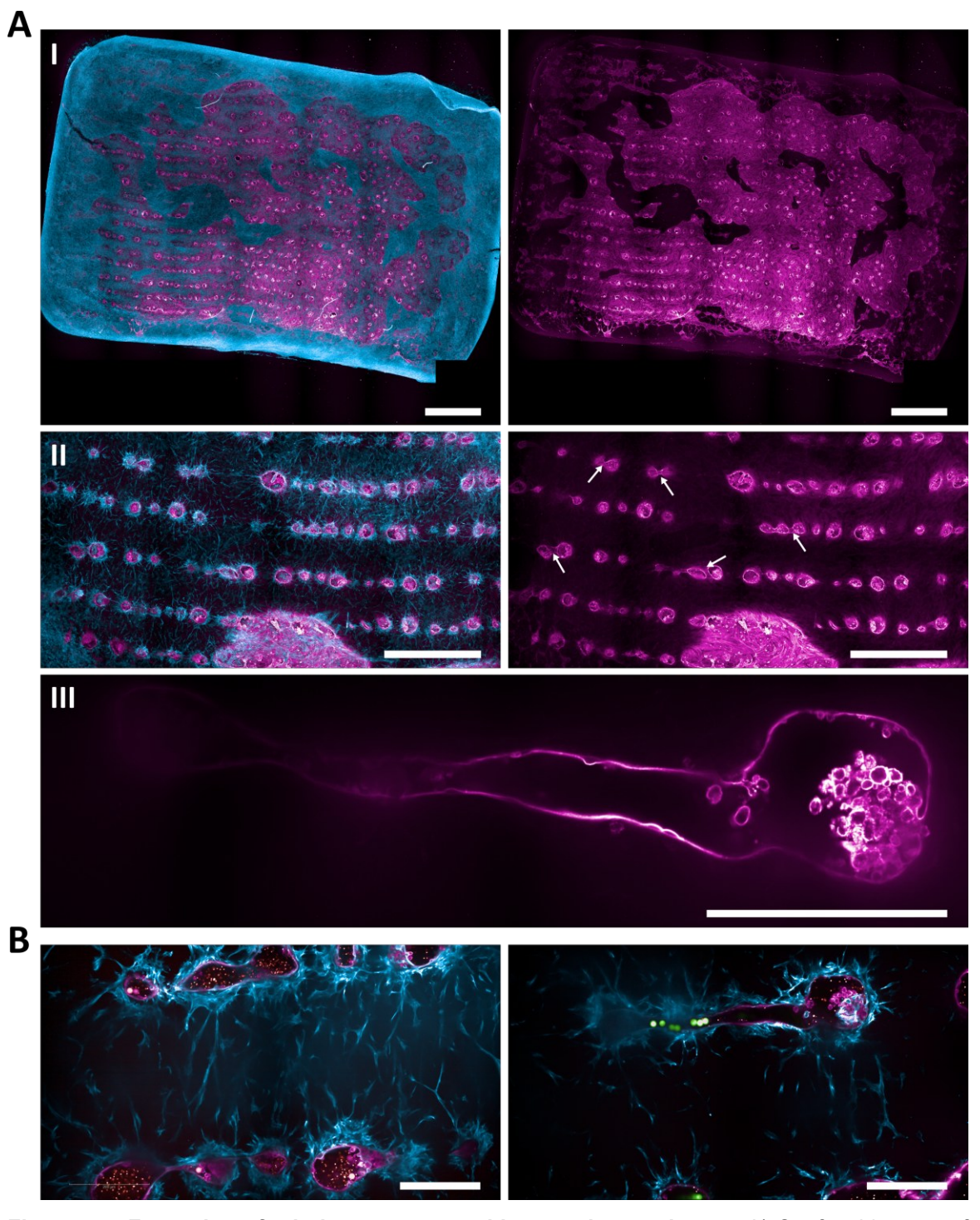


Figure 4.7: Formation of tubular structures with a continuous lumen. A) Confocal images of spheroids consisting of 1000 cells with a ratio of 3 HUVECs/1 NHDF that are organized into lines by acoustic alignment and cultured in 3.4 w/v% PEG hydrogels for 14 days. White arrows indicate fusing spheroids. Samples are stained for F-actin (cyan) and CD31 (magenta). Scale bars: I) 2 mm; II) 1 mm; III) 200 μ m. B) Visualization of continuous lumen formation by perfusion fusion with fluorescent beads of 1 μ m (red) and 15 μ m (green) diameter. Scale bars: 200 μ m.

After 14 days of cultivation, the cells infiltrate the bottom PEG hydrogel, revealing that the two hydrogel layers form a seamless connection as the cells would otherwise grow at the hydrogel interface, which represents the path of least resistance for cell growth. However, spheroid lumen formation and fusion within the top hydrogel layer is hardly visible as the imaging through the bottom hydrogel layer and the infiltrating cells reduces image clarity (**Figure 4.8 B**). Thus, the hydrogel is cut vertically in a 90° angle to the spheroid layer into two pieces that are imaged from the side. The spheroids are reorganizing into uniluminal structures and are fully enclosed by endothelial cells without any disruptions or openings (**Figure 4.8 C**). This suggests that this method can effectively maintain spheroid integrity due to the structural confinement provided by the top and bottom hydrogel layers.

4.3 Conclusion

Engineering functional vascular structures remains one of the main bottlenecks when it comes to the development of large-scale tissue constructs that can sustain long-term culture. Prevascularized spheroids are gaining interest as building blocks to overcome this limitation of tissue engineering due to their ability to reorganize into luminal structures and fuse into vascular channels. In contrast to previous works demonstrating the fusion of spheroids forming multiple small lumens with limited capacity to create a continuous vascular tree, this study shows that spheroids can reorganize into uniluminal structures that fuse into continuous channels as evidenced by perfusion with fluorescent beads. Lumen formation depends on an increased fraction of HUVECs, occurring only in conditions with a 3 HUVECs/1 NHDF ratio, and is influenced by the spheroid size and stiffness of the surrounding hydrogel. While an increasing stiffness restricts spheroid reorganization, varying spheroid sizes and moderate stiffness levels enable control over the lumen diameter for different purposes. By confining such spheroids in a hydrogel that supports their structural reorganization and ensuring their close proximity, as achieved through acoustic spheroid alignment, this approach enables the formation of continuous vascular channels that are lined by endothelial cells. These findings demonstrate the potential of this strategy to contribute to the development of functional vascular networks in engineered tissues in the future.

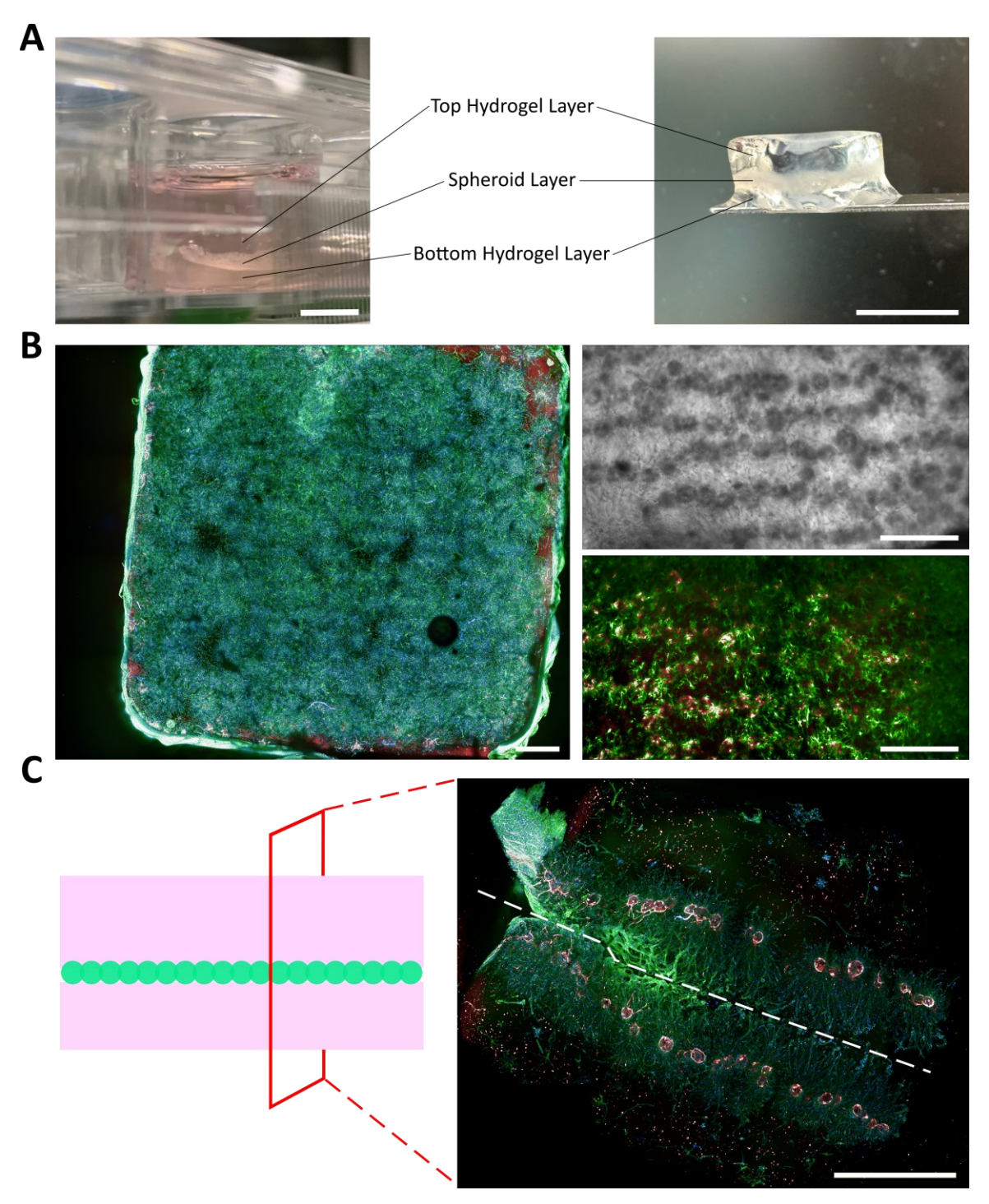


Figure 4.8: Sandwich model for the formation of enclosed tubular structures. A) A layer of aligned spheroids is enclosed between two hydrogel layers. After acoustic alignment and gelation of the first hydrogel, a second hydrogel layer is added to fully embed the spheroids within a hydrogel matrix. Scale bars: 5 mm. B) Confocal images of spheroids cultured in sandwich model with 3.4 w/v% PEG hydrogels after 14 days of culture through the bottom hydrogel layer with infiltrating cells. Scale bars: 1 mm. C) Visualization of spheroid crosssection after cutting the hydrogel in half at a 90° angle to the spheroid layer and confocal imaging from the side. Both halves are shown and a dotted white lines indicates their separation in the picture. The samples are stained for nuclei (blue), F-actin (green) and CD31 (red). Scale bar: 2 mm.

4.4 Materials and Methods

4.4.1 Cell Culture

Human umbilical vein endothelial cells (HUVECs, Lonza) are cultured in tissue culture flasks with endothelial cell growth medium 2 (EGM-2, Promocell) supplemented with 1% antibiotic-antimycotic (ABM, Gibco) up to passage 6. Normal human dermal fibroblasts (NHDFs, Promocell) are cultured in tissue culture flasks with Dulbecco's modified Eagle medium (DMEM, Gibco) supplemented with 10% fetal calf serum (FCS, Biowest) and 1% ABM up to passage 8. Both cell types are cultured at 37 °C with 5% CO₂ according to standards protocols.

4.4.2 Preparation of Hydrogel Precursors and Hydrogel Formation

Four-arm PEG-VS (20 kDa, Creative PEGWorks) and di-thiol crosslinkers are dissolved in DMEM that is supplemented with 10% FCS and 1% ABM. To promote cell growth, PEG-VS is pre-incubated with GRGDSPC (690.7 Da, CPC Scientific) at a final concentration of 0.6 mM before HS-MMPsens-SH (GCREGPQGIWGQERCG, 1774 Da, GenScript) is added for hydrogel crosslinking via thiol-Michael addition. PEG-VS and thiol-functionalized components are mixed in equimolar ratios and incubated at 37 °C for 30 min to form hydrogels via thiol-Michael addition.

4.4.3 Cultivation of Cell Spheroids in Hydrogels

Cell spheroids consisting of 333, 1000 and 3000 cells/spheroid and a 3 HUVECs/1 NHDF ratio are formed using the Sphericalplate $5D^{\$}$ (Kugelmeiers Ltd, Erlenbach) in 24-well format, which contain 750 microwells for spheroid formation. Both, HUVECs and NHDFs are suspended in EGM-2 to a concentration of 2250 000 cells/mL. For the formation of spheroids with 333 cells/spheroid, 83.25 µL of HUVEC, 27.75 µL of NHDF suspensions and 989 µL EGM-2 are mixed and added to the Sphericalplate $5D^{\$}$. For the formation of spheroids with 1000 cells/spheroid, 250 µL of HUVEC, 83.33 µL of NHDF suspension and 666.67 µL EGM-2 are mixed and added to the Sphericalplate $5D^{\$}$. For the formation of spheroids with 3000 cells/spheroid, 750 µL of HUVEC and 250 µL of

NHDF suspension are mixed and added to the Sphericalplate 5D®. Immediately after plating, the plate is swirled in a figure 8 to evenly distribute the cells in the wells. After 24 h of incubation at 37 °C and 5% CO₂, spheroids are harvested by pipetting and mixed with hydrogel components at a concentration of around 2 spheroids/µL. Finally, 15 µL hydrogel droplets are casted on 8-well ibidi slides and allowed to crosslink for 30 min before adding 300 µL EGM-2 and cultivation at 37 °C and 5% CO₂ with medium changes every 2-3 days.

4.4.4 Acoustic Spheroid Alignment in PEG Hydrogels

The setup for the acoustic alignment is developed and provided by Johannes Hahn from the Department of Dental Materials and Biomaterials Research led by Prof. Dr.-Ing. Horst Fischer at the RWTH Aachen University Hospital. 400 µL of hydrogel mixture containing 1500 spheroids are added to a well of an 8-well ibidi slide with removable silicone chamber. The ibidi slide is placed in a bigger chamber that contains two transducers and is filled with degassed water. For the acoustic alignment, a frequency of 2.061 MHz and an amplitude of 20.000 Vpp are applied. After 30 min at RT, the hydrogels are crosslinked and the alignment of the spheroids is confirmed. The hydrogels are transferred with a sterile spatula to the well of a 24-well plate that is filled with EGM-2 and subsequently incubated at 37 °C and 5% CO₂ with medium changes every 2-3 days.

4.4.5 Immunofluorescence Staining

The cell culture media is removed from the hydrogel samples, followed by washing with PBS for 30 min and fixing with 4% paraformaldehyde solution (PFA, AppliChem) for 50 min at room RT. After washing twice with PBS, the samples are incubated with 0.1% Triton X-100 (Sigma Aldrich) solution in PBS for 20 min for cell membrane permeabilization, followed by three more PBS washing steps. Afterwards, the samples are blocked by incubating with 4% bovine serum albumin (BSA, SEQENS) solution in PBS for 4 h. This is followed by incubation with a monoclonal mouse anti-human CD31/PECAM-1 antibody (Bio-Techne, 1:500) in 1% BSA in PBS solution overnight at 4 °C. After washing thrice with PBS, 30 min

each, the samples are incubated with Alexa Fluor 647 goat anti-mouse antibody (Invitrogen, 1:500) and Phalloidin-iFluor 488 (abcam, 1:1000) in PBS for 4 h at RT. Alternatively, samples that are not in the following stained with DAPI to observe the nuclei, they are incubated with Alexa Fluor 555 goat anti-mouse (Invitrogen, 1:500) and Phalloidin-iFluor 405 (abcam, 1:1000) for 4 h at RT. After washing twice with PBS, the samples are stored at 4 °C or incubated for 30 min with DAPI (1:200) to stain the nuclei, followed by three more washing steps with PBS before the samples are stored at 4 °C or imaged. To prove the presence and continuity of lumens formed by fusing spheroids, the samples are incubated with fluorescent polystyrene beads (Bangs Laboratories, Inc.) of 1 μ m (660/690 nm) and 15 μ m (480/520 nm) diameter that are diluted in PBS.

4.4.6 Image Processing and Analysis

Brightfield images of spheroids cultured in PEG hydrogels are recorded using an Echo Revolution microscope equipped with a 4× objective. The fraction of lumenforming spheroids is determined by counting the spheroids forming a central lumen, visible as a low-contrast region compared to the denser spheroid edges, which is normalized to the total number of spheroids.

Immunofluorescence-stained samples are imaged using a Leica SP8 Tandem Confocal microscope equipped with an air objective of 10×/0.3 N.A using lasers for excitation at 405, 488, 561 and 633 nm. HyD and PMT detectors are used to detect the resulting emission. Higher magnification images of spheroids are recorded using the 10× air objective with a 4× zoom. The confocal images of uniluminal spheroids are analyzed with ImageJ. To quantify the size of the lumens that are lined by endothelial cells, the diameter and surface area are measured in the CD31 fluorescence channel at the widest crosssection. Tile scan images of spheroid lines formed via acoustic alignment are additionally recorded before and after perfusion with fluorescent beads using an Opera Phenix Plus High-Content Screening System with 5×/0.16 NA and 10×/0.3 NA air objectives as well as a 20×/1.0 NA and 40×/1.1 NA water immersion objectives.

4.4.7 Statistical Analysis

Each experiment, except for acoustic alignment experiments, is performed with $n \ge 3$. Statistical analysis of the data is conducted in OriginPro 2024 using a one-way ANOVA. Pair comparisons are performed using Tukey's method, where p-values below 0.05 are considered as significant differences (*p < 0.05; **p < 0.01; ***p < 0.001).

5 On-Demand Degradation of PEG Hydrogels for Medical Applications

Daniel Günther, Hannah Küttner, Kuan Zhang, Junlin Chen, Andreas Herrmann, Laura De Laporte

5.1 Introduction

Tissues are highly dynamic structures that undergo constant remodeling processes due to cell migration and proliferation and their continually changing interactions with their surrounding extracellular matrix (ECM) and neighboring cells.²⁰⁵ Thereby, cells produce matrix metalloproteinases (MMPs), a family of Zn²⁺-dependent proteinases that degrade and remodel multiple components of the ECM to enable cell migration by disrupting ECM barriers, cleaving of proteins associated with cell-cell and cell-matrix interactions or the release and activation of ECM-bound growth factors, chemokines, and cytokines, which is involved in wound healing, angiogenesis and development. 206-208 The activity of MMPs is tightly regulated by the presence of tissue inhibitors of metalloproteinases (TIMPs). A dysregulation of the balance between MMPs and TIMPs results either in excessive ECM degradation or deposition that can cause many pathological conditions, including atherosclerosis, scar tissue formation, fibrosis, and cancer.²⁰⁹ ²¹⁰ Tissue engineering recapitulates these processes to facilitate degradation of synthetic hydrogels consisting of nanoporous polymer networks by incorporation of MMP-sensitive moieties.⁷⁷ This way, cells that are encapsulates in the hydrogels are able to create space within the hydrogel by secreting MMPs, which enables them to migrate, proliferate and ultimately form tissues. Yet, similar to the balance of MMPs and TIMPs in vivo, the degradation of the hydrogel matrix must be regulated to match the growth rate of cells to ensure proper tissue formation. At the same time, the rate of degradation controls cell behavior determining the multicellularity of cell migration as well as the differentiation of stem cells. 193, 211 Due to the defined in vitro environment with stable external factors like temperature and pH, the degradation rate of a hydrogel can be well controlled. This is why I relied on MMP-mediated hydrogel degradation in Chapters 3 and 4, which can be further combined with passive ester hydrolysis to accelerate hydrogel softening and compensate for higher hydrogel stiffnesses as shown in Chapter 3. However,

after transplantation of a tissue substitute that is initially matured in vitro, the environment drastically changes with more complex and dynamic influences. During a potential foreign body response, biomaterial-adherent macrophages produce a variety of MMPs in their attempt to degrade the foreign body, which further depends on its composition.²¹² Native cells of the surrounding tissue additionally secrete multiple types of MMPs, while the rate of MMP secretion varies between different cell types and sources.^{213, 214} Moreover, the degradation rate varies between patients and transplantation sites, making the degradation less predictable and reproducible. 124, 215 This overall results in differing responses and biomaterial degradation rates in vivo and in vitro, which has been demonstrated for MMP-sensitive polyethylene glycol (PEG) hydrogels.²¹⁶ Thus, mechanisms that are independent of factors found in the in vivo environment and can be triggered on-demand could present a promising approach to enhance the control over degradation in transplanted tissue constructs. As described previously in Chapter 2, multiple on-demand degradation mechanisms so far involve light or mechanical forces as external triggers. 153-155 However, the application of these triggers in vivo after transplantation remains challenging as light is characterized by strong scattering, which limits its tissue penetration depth, while the mechanical stretching of the material does not allow for minimally-invasive therapy.²¹⁷ In contrast, ultrasound presents a non-invasive alternative that enables controlled tissue penetration by varying its frequency and intensity. Its additional potential for biomedical applications has recently been demonstrated by the introduction of ultrasound for controlled drug activation through mechanochemical bond scission as well as the release of drugs from microgels as drug carriers in the newly established field of sonopharmacology. 218, 219 Building up on the mechanical force of ultrasound, an on-demand degradation system, triggered by low intensity focused ultrasound (LIFU), is presented in this work. Thereby, a thrombincleavable, thiol-functionalized crosslinker (HS-TCP-SH) replaces the previously used ester-functionalized crosslinker. At first, it is shown that the formed hydrogels can then be degraded on-demand by supplementing thrombin through the media. By adjusting the concentration of thrombin, timing of thrombin supplementation as well as the ratio of HS-TCP-SH to MMP-sensitive crosslinker (HS-MMPsens-SH), the softening of the hydrogels can be controlled, which influences the growth of encapsulated spheroids.

For LIFU-triggered degradation, the non-covalent inhibitory interaction between thrombin and hirudin is exploited as previously demonstrated by Zhang *et al.*, which can be mechanically interrupted to induce the catalytic activity of thrombin. This biocatalytic system is integrated into the PEG hydrogel network by modifying both enzymes with thiols for thiol-Michael addition with four-arm PEG vinyl sulfone (PEG-VS). Upon LIFU exposure, thrombin is reversibly activated and therefore able to degrade the surrounding thrombin-cleavable crosslinks (**Figure 5.1**).

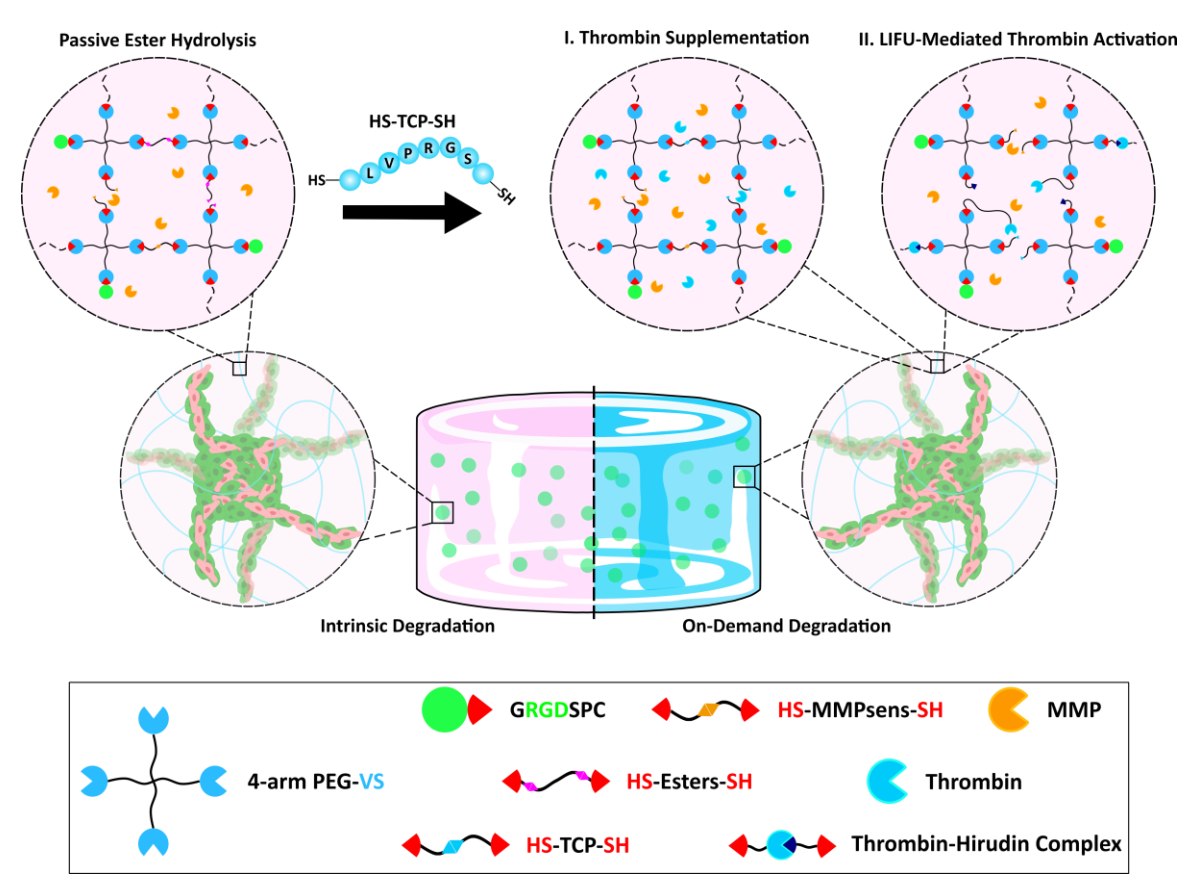


Figure 5.1: Transition from hydrolytic to on-demand hydrogel degradation. To enhance control over hydrogel degradation, ester-functionalized crosslinks (HS-Esters-SH), which passively degrade over time, are replaced with thrombin-cleavable crosslinks (HS-TCP-SH). These can be degraded on-demand either by supplementing thrombin through the media or by integrating a biocatalytic system consisting of thrombin and its inhibitor hirudin into the hydrogel network, which can be activated using low intensity focused ultrasound (LIFU).

5.2 Results and Discussion

5.2.1 On-Demand Hydrogel Degradation through Media-Supplemented Thrombin

5.2.1.1 Characterization of Thrombin-Sensitive Hydrogels and Their Degradation

To verify the on-demand degradation of thrombin-sensitive hydrogels with thrombin under cell culture conditions and monitor the time required for degradation, 6.5 w/v% PEG hydrogels with 100% HS-TCP-SH are formed and incubated with 20, 10 or 5 nM thrombin diluted in cell culture media (**Figure 5.2**). After 60 min of incubation, gels in all conditions are smaller than after hydrogel formation and become smaller with increasing thrombin concentration. In conditions with 20 nM thrombin, all gels are gone within 90 min, while it takes about 120 min and 240 min for hydrogels to fully degrade with 10 nM and 5 nM thrombin, respectively.

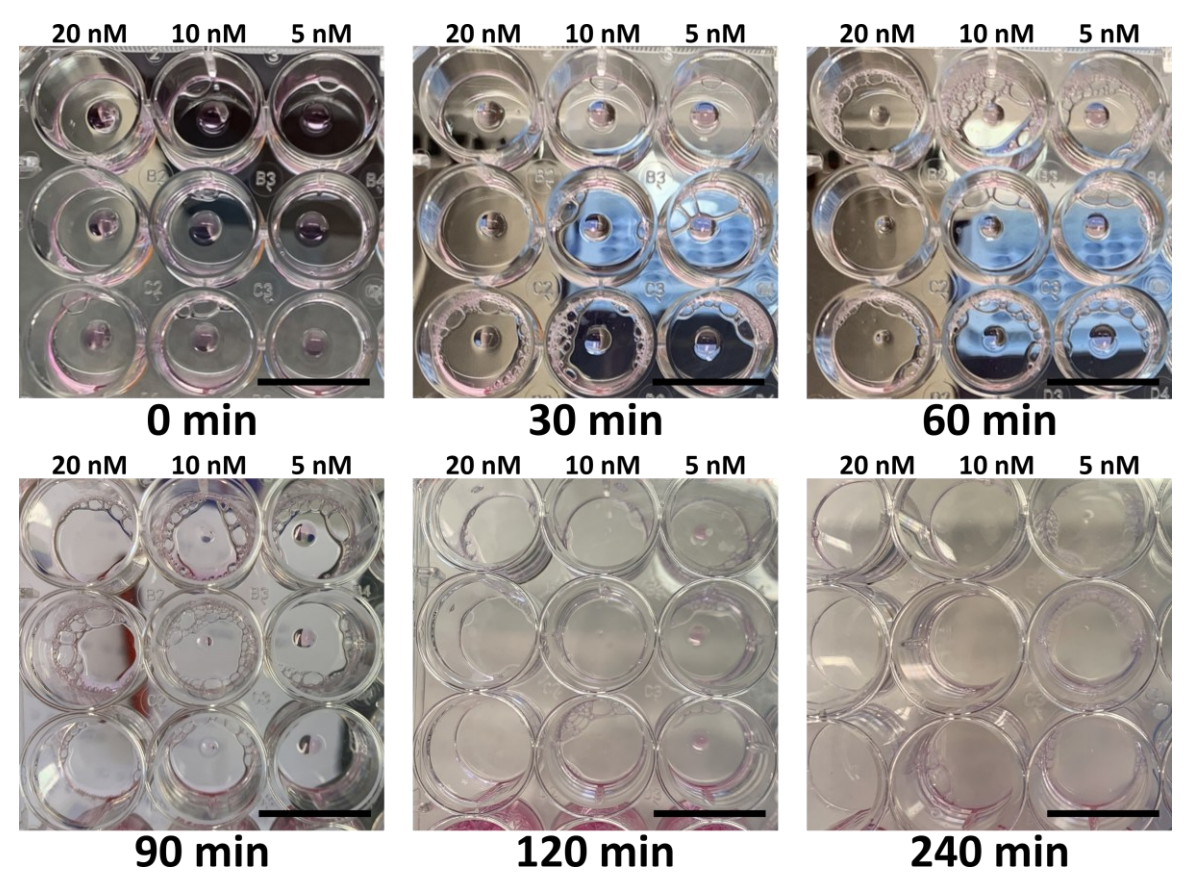


Figure 5.2: Thrombin concentration-dependent hydrogel degradation over time. 6.5 w/v% PEG hydrogels made with 100% HS-TCP-SH are incubated with DMEM supplemented with 20, 10 or 5 nM thrombin. Images of the gels are recorded every 30 min over a period of 240 min. Scale bars: 15 mm.

As the degradation of fully thrombin-sensitive hydrogels with thrombin in low concentrations is too fast to support cell growth, HS-TCP-SH is combined with HS-MMPsens-SH in different ratios for cell applications. The stiffness of 6.5 w/v% PEG hydrogels decreases significantly as the fraction of HS-TCP-SH is increased (Figure 5.3 A). PEG hydrogels formed with 100% HS-MMPsens-SH have a storage modulus of approximately 3900 ± 200 Pa, which reduces to 2200 ± 800 Pa in case of PEG hydrogels formed with 100% HS-TCP-SH. Yet, the gelation times are similar as in both cases the gelation starts within 60 s (Figure 5.3 B). This could be a result of differences in the peptide sequences besides the respective degradation sites and their length. HS-MMPsens-SH (1774 Da) is slightly longer than HS-TCP (1431 Da) and could result in additional network entanglement that contributes to the overall stiffness. Additionally, the presence of positive charges from arginine in the sequence of HS-MMPsens-SH decreases the p K_a of the thiol, promoting the formation of more reactive thiolates.²²⁰ While lysines residues in the sequence of HS-TCP-SH also contain positively charged amine groups, their shorter side chains and localized positive charges are potentially less effective at stabilizing thiolates compared to the delocalized positive charge of arginine's guanidinium group, which benefits from a longer side chain. Moreover, electrostatic interactions between guanidinium groups and negatively charged glutamic acid found in HS-MMPsens-SH could further reinforce the hydrogel, while HS-TCP-SH mostly contains uncharged glycines with a single hydrogen atom as its side chain.

Nanoindentation measurements of 6.5 w/v% PEG hydrogels with different HS-MMPsens-SH/HS-TCP-SH ratios confirm the trend of decreasing hydrogel stiffness with increasing HS-TCP-SH fraction (**Figure 5.3 C**). Moreover, the hydrogels are incubated overnight with 20 nM thrombin to degrade the thrombin-cleavable crosslinks, resulting in significant hydrogel softening. As expected, the measured Young's modulus gradually decreases with increasing HS-TCP-SH fraction due to crosslink degradation, while it remains constant for gels made with 100% HS-MMPsens-SH. The Young's modulus of hydrogels containing 10% HS-TCP-SH reduces by 33% after thrombin treatment, whereas 30% HS-TCP-SH hydrogels lose almost 80% of their initial stiffness. This demonstrates that the adjustment of the crosslinker ratio allows for enhanced control over hydrogel softening.

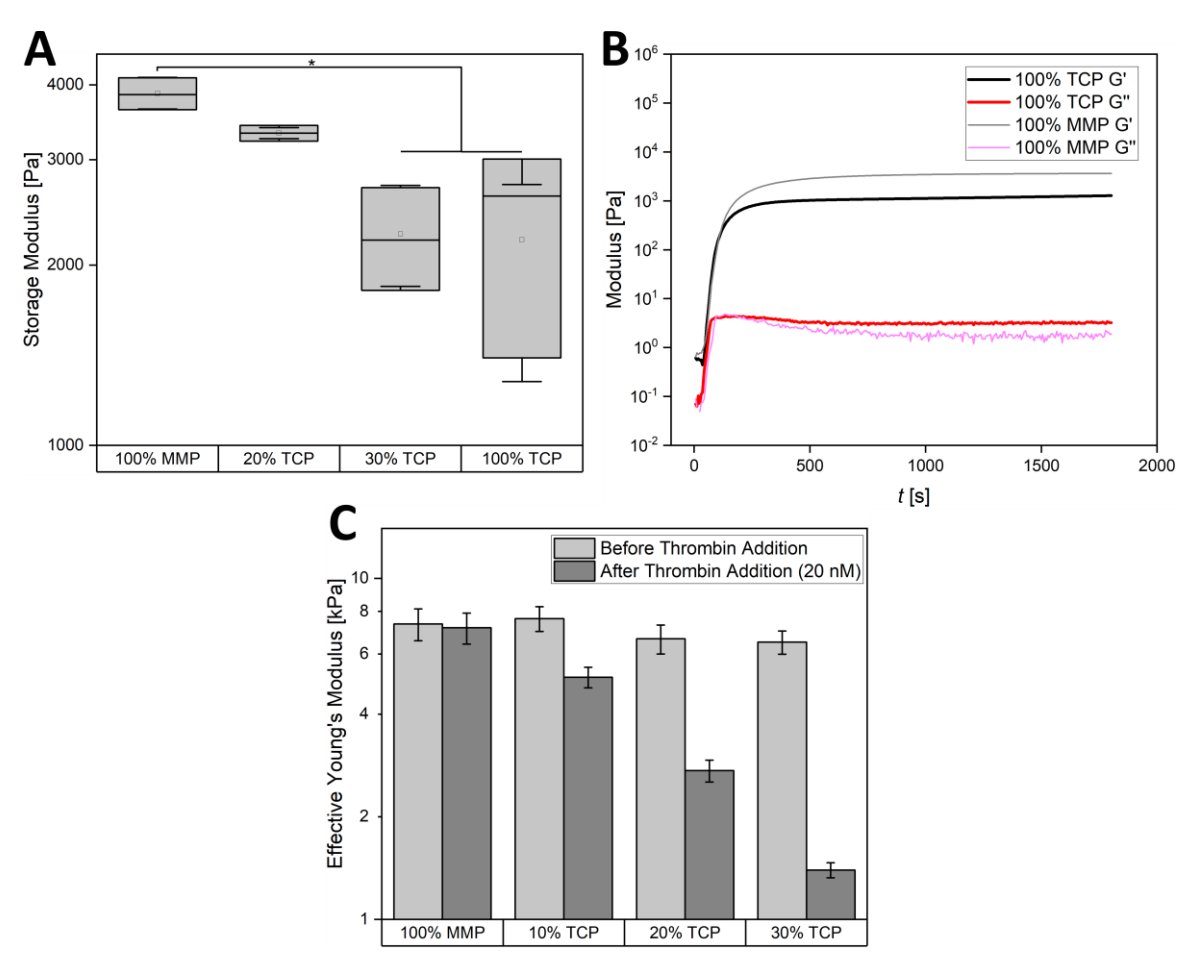


Figure 5.3: Mechanical hydrogel properties and softening depending on HS-MMPsens-SH/HS-TCP-SH ratio. A) Storage modulus of 6.5 w/v% PEG hydrogels with different ratios of HS-MMPsens-SH (MMP)/HS-TCP-SH (TCP). Box plots present mean \pm SD with n = 3 per condition (error bar = min-max values, hollow square = mean value, horizontal line = median). P values are calculated using one-way ANOVA with post-hoc Tukey test, *p < 0.05, **p < 0.01, ***p < 0.001. B) Storage and loss moduli of 6.5 w/v% PEG precursor solutions and formed hydrogels with 100% HS-MMPsens-SH or 100% HS-TCP-SH as a function of time. C) Effective Young's moduli of 6.5 w/v% PEG hydrogels with different ratios of HS-MMPsens-SH/HS-TCP-SH monitored before and after treatment with 20 nM thrombin overnight via nanoindentation. Data is presented as mean \pm SD with n = 75 per condition.

5.2.1.2 Thrombin-Mediated Hydrogel Degradation for Improved Cell Growth

While thrombin is part of the natural blood coagulation cascade, it is also reported to affect the cell viability by inducing cell apoptosis in a dose-dependent manner, whereas low concentrations promote cell proliferation.^{221, 222} Thus, we test the influence of thrombin in concentrations used for the previous degradation experiments on the viability of human umbilical vein endothelial cells (HUVECs) and normal human dermal fibroblasts (NHDFs) after incubation for 24 h. For all tested conditions, the viability is in a range of 80-99%, which is generally considered healthy (**Figure 5.4**). However, a decrease in cell viability is observed for both tested cell types with increasing thrombin concentration. Thereby, around

82% of HUVECs treated with 20 nM thrombin are viable, which is significantly lower compared to all other conditions, characterized by a viability of > 90%. This further demonstrates that HUVECs are more susceptible to thrombin-mediated cell death than NHDFs. Thrombin is described to cause profound changes in endothelial cell biology and leads to an increased endothelial permeability by altering cell junctions. Thrombin also promotes the expression of connective tissue growth factor, which acts as a fibroblast mitogen and stimulates their proliferation. This could indicate that endothelial cells are more sensitive to thrombin-induced apoptosis than fibroblasts. Yet, given the generally high cell viability, thrombin in concentrations up to 20 nM is considered suitable for further cell experiments.

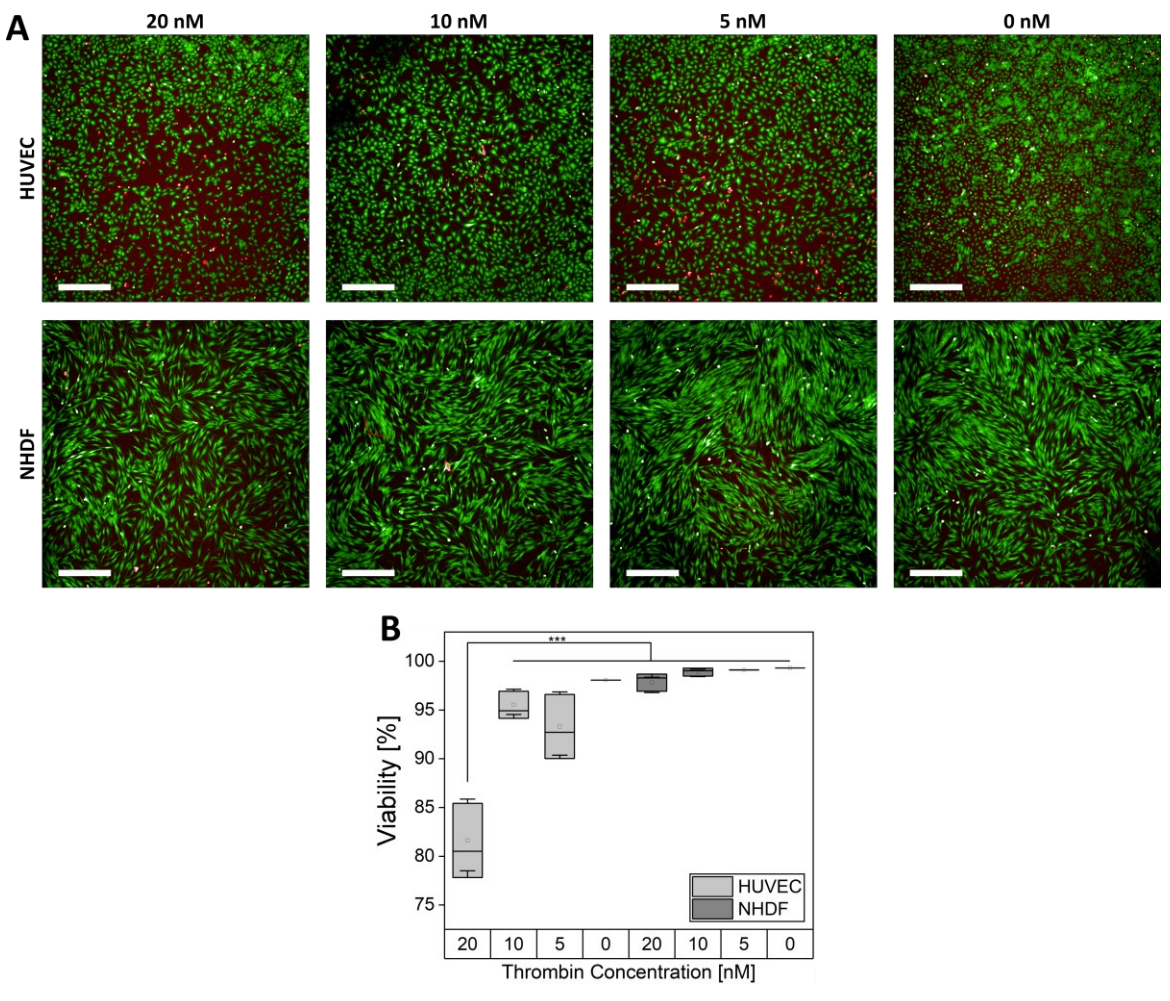


Figure 5.4: Influence of thrombin on cell viability. A) Live/Dead staining of HUVECs and NHDFs that are cultured for 24 h with 20, 10 or 5 nM thrombin solutions in cell culture media. Controls (0 nM) are not treated with thrombin. Live cells are shown in green and dead cells are red. Scale bars: $500 \, \mu m$. B) Quantification of cell viability as the ratio of living to the total number of cells. Box plots present mean \pm SD with n = 3 per condition (error bar = min-max values, hollow square = mean value, horizontal line = median). P values are calculated using one-way ANOVA with post-hoc Tukey test, *p < 0.05, **p < 0.01, ***p < 0.001.

To investigate the influence of thrombin-induced hydrogel softening on cell growth, spheroids consisting of HUVECs and NHDFs in a 1:3 ratio and 1000 cells/spheroid are cultured in 6.5 w/v% PEG hydrogels with different ratios of HS-MMPsens-SH/HS-TCP-SH containing up to 50% HS-TCP-SH. Until day 4, spheroids are cultured with regular endothelial cell growth medium 2 (EGM-2) and show similar growth in all conditions (Figure 5.5 A). On day 4, 20 nM thrombin are added per condition to degrade the thrombin-cleavable crosslinks, which causes gels with 40% and 50% HS-TCP-SH to fully degrade. Compared to untreated controls, the spheroid sprouting improved in all tested conditions as well as with increasing fraction of HS-TCP-SH, characterized by enhanced cell infiltration (Figure 5.5 B). While this can be mainly attributed to degradation of thrombin-cleavable crosslinks, enhanced cell infiltration in hydrogels made with 100% HS-MMPsens-SH suggests that thrombin additionally promotes cell growth. As mentioned previously, thrombin in low concentrations stimulates cell proliferation and acts as a fibroblast mitogen, which could explain the improved spheroid sprouting in this case. 221, 224 Additionally, the cell infiltration increases in controls with increasing HS-TCP-SH fraction. As this way the fraction of crosslinks that the cells are unable to degrade increases, which should limit cell growth, this seems counterintuitive. Yet, the stiffness of the hydrogels decreases with increasing HS-TCP-SH fraction, which promotes cell growth despite a reduced degradability on cell-demand.

The thrombin treatment further influences the sprout morphology depending on the HS-MMPsens-SH/HS-TCP-SH ratio. While shorter, multicellular sprouts are formed in conditions with 0% and 10% HS-TCP-SH, the sprouts are less defined with predominant single cell migration in conditions with 20% and 30% HS-TCP-SH. The multicellularity of cell growth thereby depends on the degradability of the surrounding matrix where high degradation rates trigger a switch between collective to single cell migration by enabling cells to break cell-cell junctions during accelerated migration. ¹⁹³ Increasing the fraction of HS-TCP-SH therefore leads to progressively more pronounced softening of the hydrogels, which in turn drives the transition from collective to single cell migration due to loss of structural support.

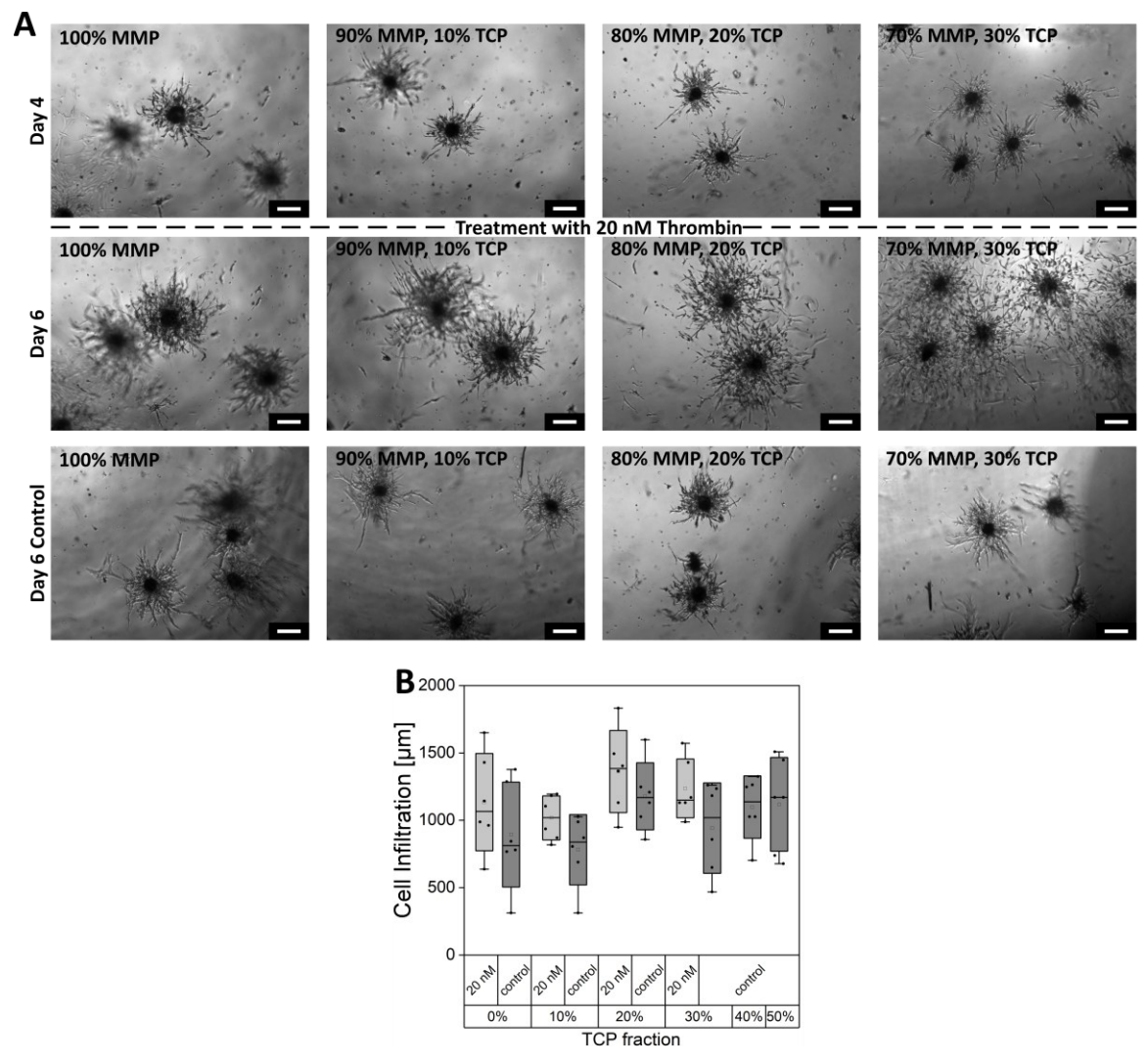


Figure 5.5: Influence of PEG hydrogel softening by on-demand TCP degradation on spheroid sprouting. Spheroids consisting of 1000 cells with a 1 HUVEC/3 NHDF ratio are cultured in 6.5 w/v% PEG hydrogels with different ratios of HS-MMPsens-SH (MMP)/HS-TCP-SH (TCP) for 6 days. After 4 days, the gels are treated with 20 nM thrombin. Controls are not treated with thrombin. A) Brightfield images are recorded after 4 (before thrombin addition) and 6 days of culture. Scale bars: 200 μ m. B) Quantification of average cell infiltration of spheroids into the hydrogel depending on the HS-TCP-SH fraction. Box plot presents mean \pm SD with n = 6 per condition (error bar = minmax values, hollow square = mean value, horizontal line = median). P values are calculated using one-way ANOVA with post-hoc Tukey test, *p < 0.05, **p < 0.01, ***p < 0.001.

To investigate the influence of the HS-TCP-SH degradation rate, spheroids are cultured in 6.5 w/v% PEG hydrogels with 70% HS-MMPsens-SH/30% HS-TCP-SH that are treated with thrombin concentrations of 20, 10, 5 and 1 nM after 4 days of culture. Controls are incubated with unconditioned media. Similar to the previous experiment, the treatment with 20 nM leads to extensive cell growth, which is dominated by single cell migration after 6 days of culture (**Figure 5.6 A**). In conditions treated with 10 nM and 5 nM thrombin the same cell behavior is observed, resulting in similar cell infiltration rates for these conditions (**Figure 5.6**

B). Although decreasing the thrombin concentration from 20 to 5 nM prolongs the degradation time as shown before from 90 to 240 min, this slower degradation is still too fast compared to the rate of cell growth. Consequently, the cells are not influenced by the different degradation rates. In contrast, spheroids that are treated with 1 nM thrombin as well as controls are characterized by more defined sprouts without single cell migration. Additionally, these conditions show comparable cell infiltration rates that are significantly lower than those in conditions with higher thrombin concentrations. These results indicate that 1 nM thrombin is not sufficient to degrade the thrombin-cleavable crosslinks within the given culture time in order to promote cell growth.

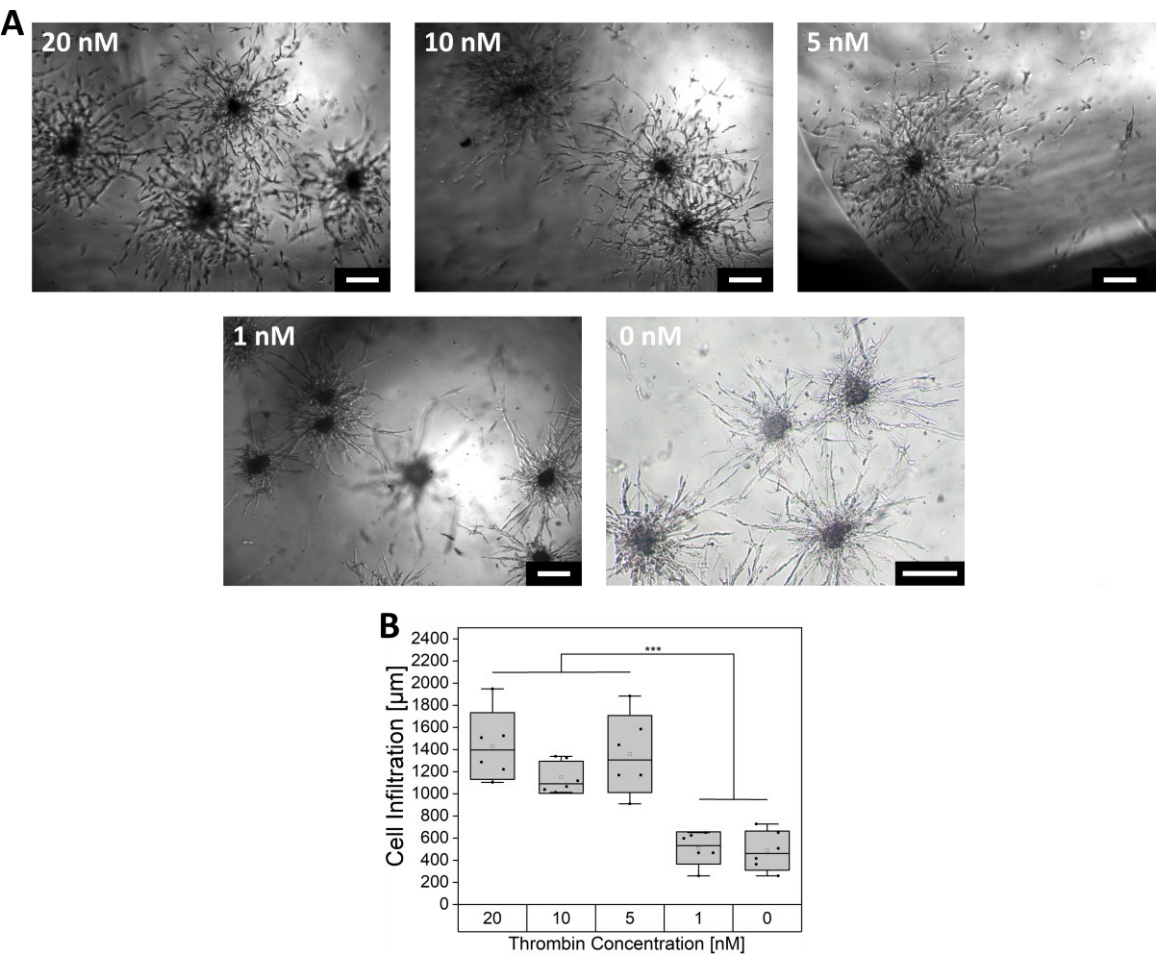


Figure 5.6: Influence of thrombin concentration on spheroid sprouting. Spheroids consisting of 1000 cells with a 1 HUVEC/3 NHDF ratio are cultured in 6.5 w/v% PEG hydrogels with a crosslinker ratio of 70% HS-MMPsens-SH/30% HS-TCP-SH for 6 days. After 4 days, the gels are treated with 20, 10, 5 or 1 nM thrombin. Controls (0 nM) are not treated with thrombin. A) Brightfield images are recorded after 6 days of culture. Scale bars: 200 μ m. B) Quantification of the average cell infiltration of spheroids into the hydrogel depending on the HS-TCP-SH fraction. Box plot presents mean \pm SD with n = 6 per condition (error bar = min-max values, hollow square = mean value, horizontal line = median). P values are calculated using one-way ANOVA with post-hoc Tukey test, *p < 0.05, **p < 0.01, ***p < 0.001.

Additionally, the influence of the timing of thrombin addition on spheroid sprouting in 6.5 w/v% PEG hydrogels with a ratio of 70% HS-MMPsens-SH/30% HS-TCP-SH is investigated. Since 5 nM thrombin is sufficient to enhance spheroid sprouting similarly to the treatment with 20 nM thrombin, the samples in this experiment are treated with 5 nM thrombin between day 0 and day 5 of culture and their growth is assessed after 6 days of culture. Thereby, the spheroid sprouting and cell infiltration increase the earlier thrombin is added (**Figure 5.7**). This is likely because the earlier the hydrogel softens as a result of thrombin-mediated degradation, the longer the cells have more space to grow in a more favorable environment.

Besides extensive sprouting, early thrombin treatment on day 0 or day 1 leads to extensive multicellular sprouting, while single cells are observed when thrombin is added at later time points (Figure 5.7 A). The spheroids in conditions with delayed thrombin addition start to form sprouts before thrombin treatment. As a result of thrombin-mediated hydrogel softening, these sprouts rapidly lose their structural support mitigated by the hydrogel, which might result in their disintegration into single cells. Since spheroids that are treated with thrombin on day 0 or day 1 do not form sprouts previous to the hydrogel softening, no single cells are observed in these conditions. At the same time, the hydrogel softening promotes the growth of new multicellular sprouts, which explains why the fraction of single cell decreases the earlier the thrombin is added. This demonstrates a mismatch between rapid hydrogel degradation and cell growth, which could be regulated by adjusting the HS-MMPsens-SH/HS-TCP-SH ratio as well as further decreasing the thrombin concentration within a range of 1-5 nM. Yet, the results show that the ondemand degradation system offers a platform to create a responsive, dynamic environment that effectively facilitates controlled cell infiltration and sprouting.

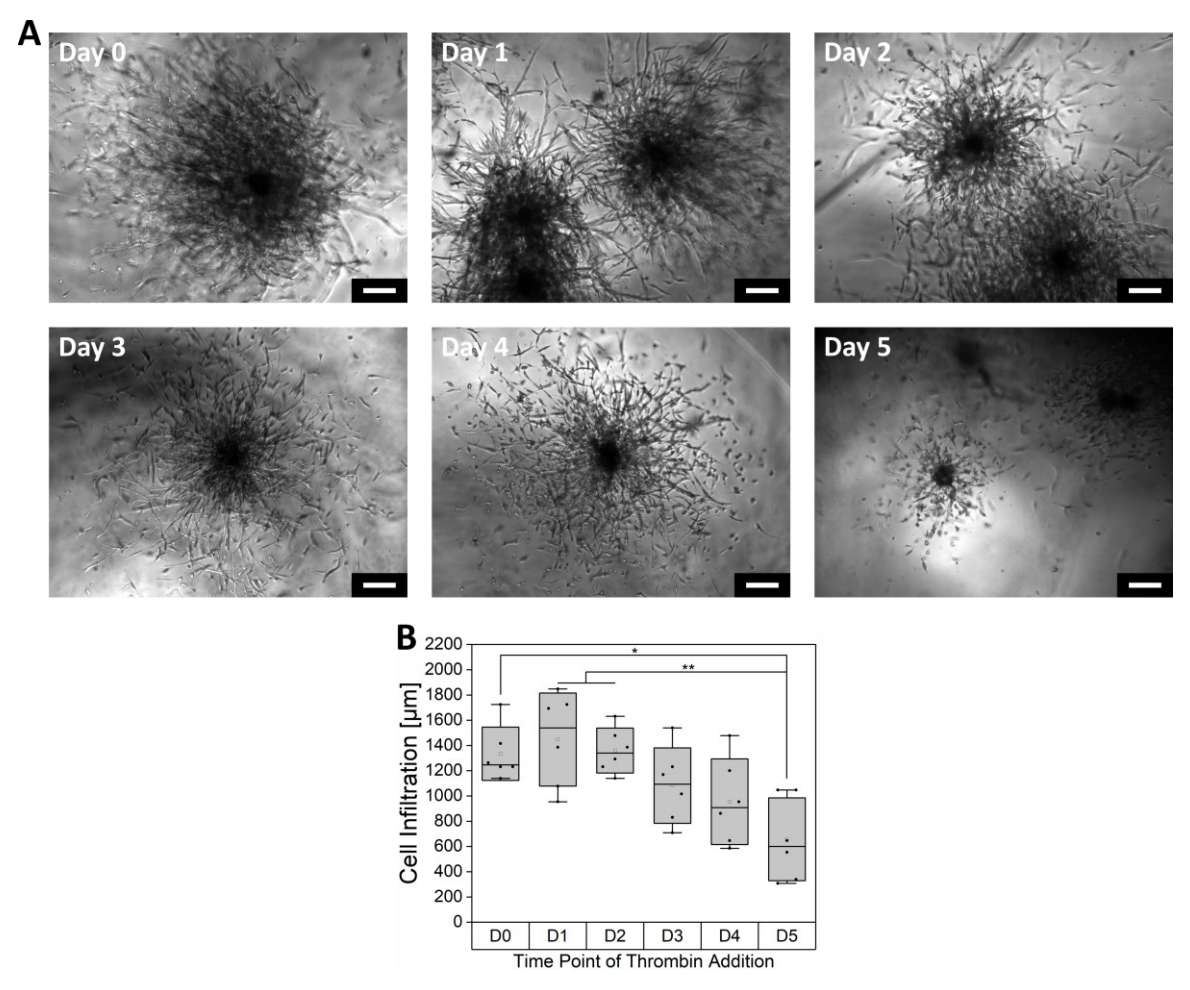


Figure 5.7: Influence of temporal thrombin treatment on spheroid sprouting. Spheroids consisting of 1000 cells with a 1 HUVEC/3 NHDF ratio are cultured in 6.5 w/v% PEG hydrogels with a crosslinker ratio of 70% HS-MMPsens-SH/30% HS-TCP-SH for 6 days. At different time points between day 0 (D0) to day 5 (D5), the gels are treated with 5 nM thrombin for the remaining period of cultivation. A) Brightfield images are recorded after 6 days of culture. Scale bars: 200 µm. B) Quantification of average cell infiltration of spheroids into the hydrogel depending on the HS-TCP-SH fraction. Box plot presents mean \pm SD with n = 6 per condition (error bar = min-max values, hollow square = mean value, horizontal line = median). P values are calculated using one-way ANOVA with post-hoc Tukey test, *p < 0.05, **p < 0.01, ***p < 0.001.

5.2.2 Ultrasound-Mediated Thrombin Activation and Hydrogel Degradation

The development of an on-demand degradation system based on thrombin that can be activated by LIFU requires the efficient inhibition of thrombin with hirudin, the effective yet controlled disruption of the thrombin/hirudin interaction by LIFU, and the covalent integration of the biocatalytic system into the PEG hydrogel network. While thrombin and hirudin interact through non-covalent bonds, their modifications with thiols allows for thiol-Michael addition with four-arm PEG-VS to integrate the enzymes into the hydrogel network. Before they are integrated into the hydrogel network, thrombin and hirudin are mixed in a 1:1.5 ratio to ensure the efficient inhibition of thrombin's catalytic activity and prevent degradation of the HS-TCP-SH previous to hydrogel crosslinking. To evaluate if LIFU can sufficiently disrupt the inhibitory interaction between thrombin and hirudin within the hydrogel to potentially degrade the thrombin-sensitive crosslinks, the gels are incubated with the fluorogenic thrombin substrate Fluoro-s. Upon disruption of the inhibitory interaction, the substrate is cleaved by thrombin to create a fluorescent molecule that allows to quantify thrombin's enzymatic activity (Figure 5.8 A). As the substrate conversion as well as the hydrogel degradation rate depend on the amount of activated thrombin, different concentrations of thrombin and hirudin are tested. Additionally, it is assumed that thrombin is activated only locally and only during LIFU exposure. Therefore, the thrombin concentration is increased to 2-10 µM compared to the lower concentration of 20 nM used in previous experiments with media-supplemented thrombin, where it freely diffuses throughout the hydrogel and degrades it over an extended incubation period. For thrombin activation, the samples are exposed to LIFU with a frequency of 1 Hz and an intensity of 4.25 MPa for 5 min. This treatment results in a fluorescent signal in all tested conditions, indicating that the LIFU is sufficiently strong to disrupt the inhibitory interaction between thrombin and hirudin. The fluorescence intensity gradually increases with increasing concentrations of thrombin and hirudin, suggesting that increasing the concentration of thrombin and hirudin allows for elevated enzymatic activity upon LIFU exposure to regulate the rate of hydrogel degradation (Figure 5.8 B).

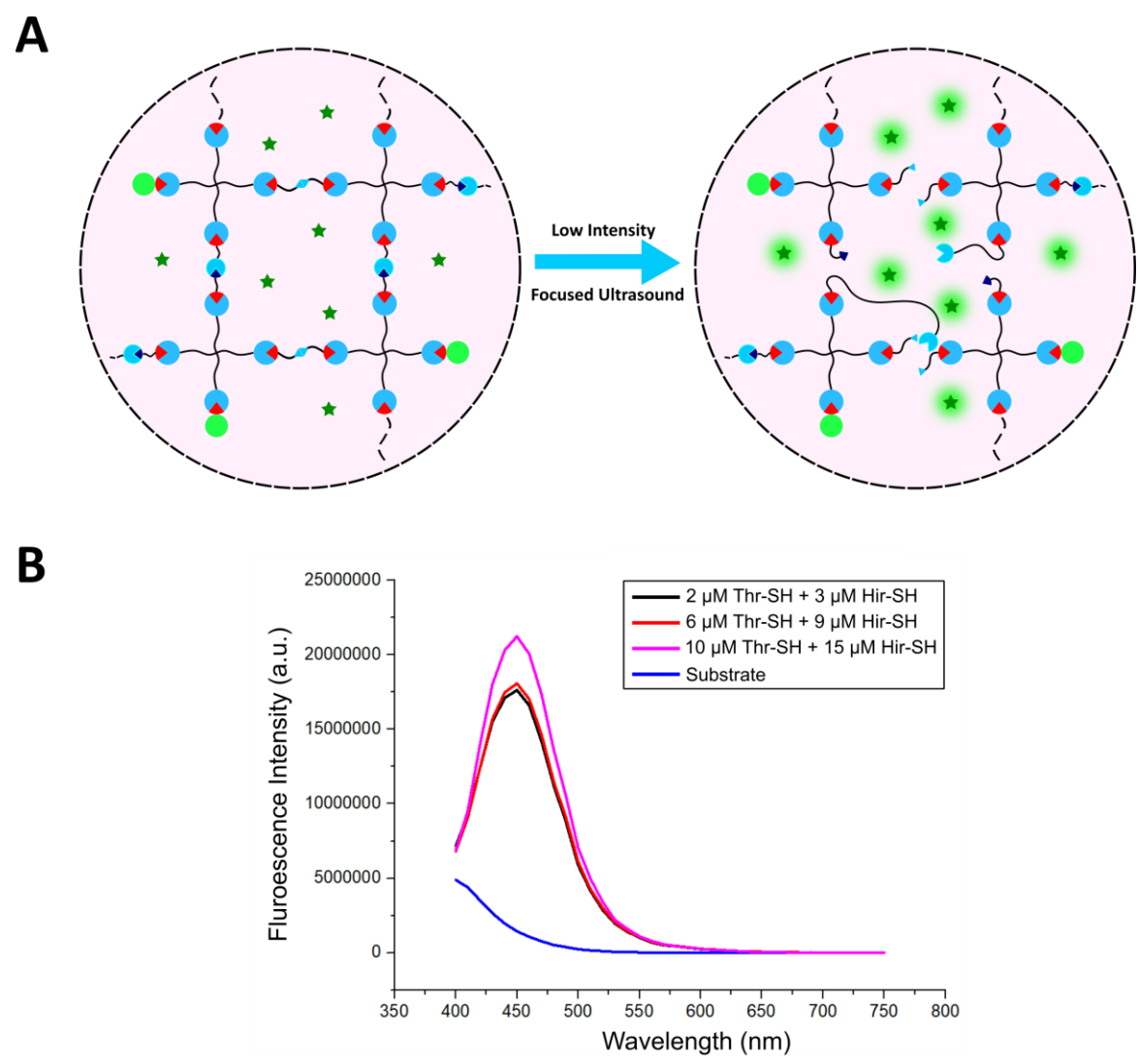


Figure 5.8: Activation of thrombin via low intensity focused ultrasound (LIFU). A) Schematic illustration of thrombin activation by LIFU, resulting in the conversion of a fluorogenic substrate (green stars) into a fluorescent product, which allows for quantification of the thrombin activity. Thiol-functionalized thrombin and hirudin are integrated into the polymer network of a PEG hydrogel, which is crosslinked with HS-TCP-SH. B) Fluorescence emission spectrum of the fluorogenic substrate conversion depending on the concentration of thiol-functionalized thrombin (Thr-SH) and hirudin (Hir-SH) that are integrated into 6.5 w/v% PEG hydrogels. Hydrogels are exposed for 5 min to LIFU at a frequency of 1 MHz and an intensity of 4.25 MPa.

As the covalent integration of thrombin and hirudin into the hydrogel network would require high enzyme concentrations to achieve hydrogel degradation that is thereby locally restricted, the feasibility to integrate a biocatalytic system consisting of thiol-functionalized hirudin with unmodified thrombin into the hydrogel is investigated (Figure 5.9 A). This way, thrombin that is non-covalently bound to hirudin but not covalently to PEG-VS could be released from the hydrogel network upon LIFU exposure to diffuse freely through the hydrogel and degrade it more efficiently without local restriction. Additionally, the enzyme concentrations are increased to 30 µM thrombin and 45 µM hirudin, which are the highest possible concentrations to add based on the respective stock concentrations, and the LIFU exposure times are varied between 20, 10 and 5 min. However, after LIFU exposure, the thrombin-sensitive PEG hydrogels in conditions with unmodified thrombin remain mainly unaffected, while hydrogels containing thiol-functionalized thrombin show signs of degradation (Figure 5.9 B). With increasing LIFU exposure time, the hydrogels appear more swollen and are larger compared to conditions with unmodified thrombin. Moreover, they are more difficult to handle and partly disintegrate upon transfer from a 96-well plate to a microscopy slide for imaging. The differences in hydrogel degradation indicate that the activation of thrombin is more efficient when it is covalently bound to PEG-VS, which is confirmed by measurements of the thrombin activity with Fluoro-s (Figure 5.9 C). Interestingly, fluorescence intensities below 5.107 are detected at a wavelength of 450 nm in conditions with unmodified thrombin, whereas they exceed 2·108 in conditions with thiol-functionalized thrombin. Although prolonged LIFU exposure increases fluorescence intensities in both cases, indicating extended and potentially enhanced thrombin activation, the higher activity of thiol-functionalized thrombin is evident. When the biocatalytic system consisting of thiol-functionalized thrombin and hirudin is covalently bound to the hydrogel network, the exposure to LIFU causes localized shear forces that effectively separate thrombin and hirudin from each other to activate thrombin's catalytic activity. In contrast, unmodified thrombin is only non-covalently associated with hirudin, giving thrombin greater freedom of movement and reducing the impact of mechanical forces during LIFU treatment.

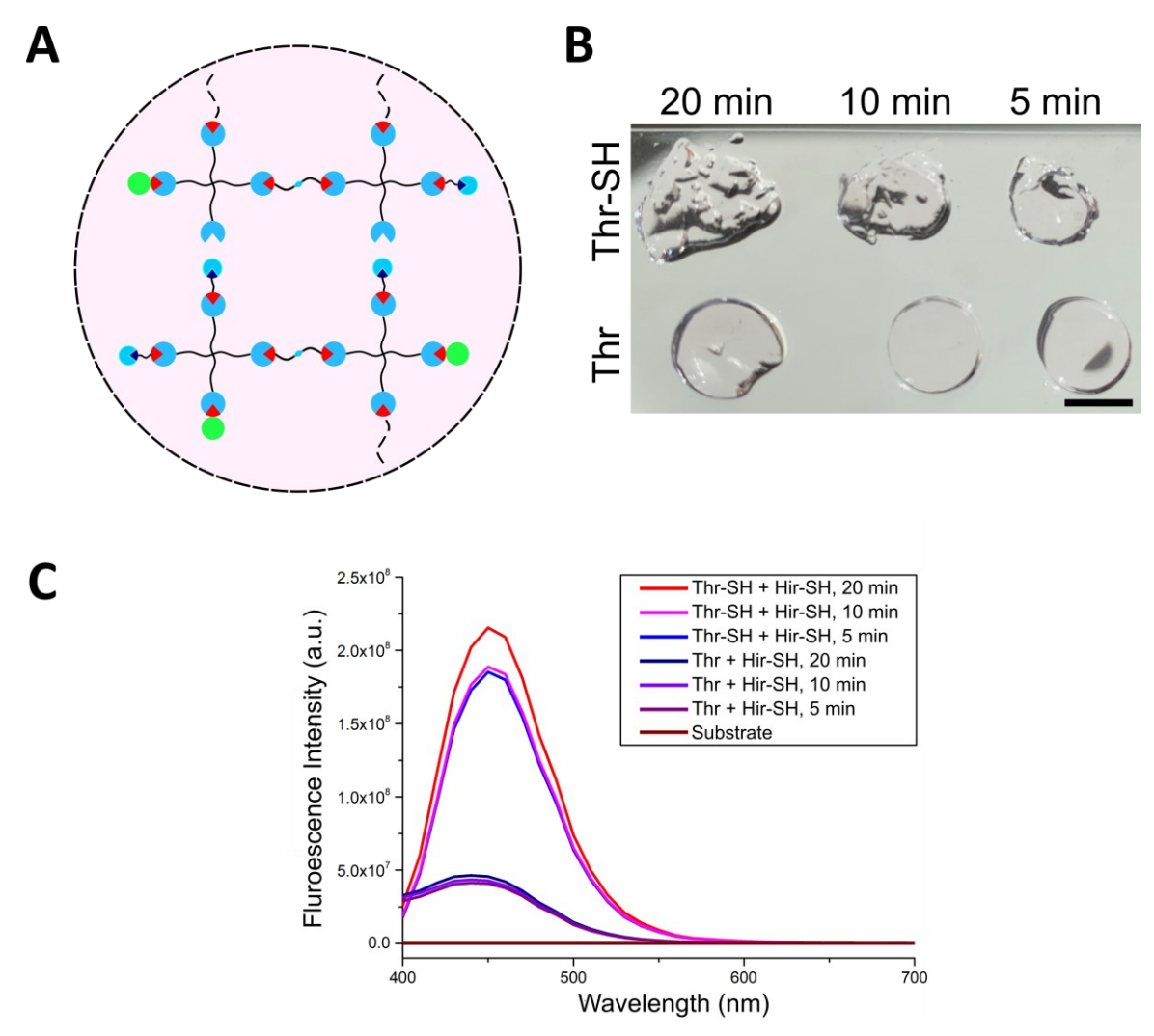


Figure 5.9: Influence of thiol functionalization on thrombin activation. A) Schematic illustration of the integration of thiol-functionalized hirudin and non-functionalized thrombin into PEG hydrogels crosslinked with HS-TCP-SH. B) Images of 6.5 w/v% PEG hydrogels with 100% HS-TCP-SH, containing 30 μ M non-functionalized (Thr) or thiol-functionalized (Thr-SH) thrombin as well as 45 μ M thiol-functionalized hirudin (Hir-SH), after LIFU exposure for 5, 10 or 20 min at an intensity of 4.25 MPa and a frequency of 1 MHz. Scale bar: 5 mm. C) Fluorescence emission spectra indicate the thrombin activity within these PEG hydrogels based on fluorogenic substrate conversion depending on the thiol functionalization and LIFU exposure time.

5.3 Conclusion

While tissue engineering primarily relies on natural or synthetic hydrogels that support tissue formation through MMP-mediated degradation mechanisms in vitro, predicting and controlling their degradation in the more complex in vivo environment with dynamic and individual influences is challenging. This work introduces a precisely controlled alternative that allows for on-demand degradation by integrating thrombin-sensitive crosslinks into PEG hydrogels. Independent of other external factors, these hydrogels can be efficiently degraded by thrombin to promote the growth of encapsulated cell spheroids. By combining HS-TCP-SH with HS-MMPsens-SH, the overall softening of the hydrogel and thereby the cell behavior can be controlled as extensive hydrogel softening leads to single cell migration instead of multicellular sprouting. The adjustment of the thrombin concentration and the time point of thrombin treatment further allow to influence the degradation rate and the onset of degradation. While the tested thrombin concentrations lead to rapid degradation and therefore similar cell behavior, an earlier thrombin treatment induces extensive multicellular sprouting, whereas formed sprouts lose their structural support to disintegrate into single cells upon delayed thrombin addition. To be able to control the degradation of such hydrogels in vivo, thrombin and its inhibitor hirudin are integrated as a biocatalytic system into the hydrogel network. The non-covalent inhibitory interaction between thrombin and hirudin can be interrupted by LIFU exposure to activate thrombin's catalytic activity and degrade the surrounding thrombin-sensitive crosslinks. As demonstrated based on a fluorometric assay, the overall enzyme activity can be increased by increasing the thrombin concentration as well as LIFU exposure time and requires both enzymes to be covalently bound to the hydrogel network to generate local shear forces that separate thrombin and hirudin from each other. Since ultrasound is characterized by a high degree of tissue penetration, this approach enables the highly controlled and reversible thrombin activation to facilitate regulated hydrogel degradation with the potential for non-invasive in vivo application.

5.4 Materials and Methods

5.4.1 Preparation of Hydrogel Precursors and Hydrogel Formation

Solutions of 20 w/v% four-arm PEG-VS (20 kDa, Creative PEGWorks) and 3 w/v% di-thiol crosslinkers are prepared in Dulbecco's modified Eagle medium (DMEM, Gibco) that is supplemented with 10% Fetal Calf Serum (FCS, Biowest), 1% Antibiotic-Antimycotic (ABM, Gibco). In cell experiments, PEG-VS is pre-incubated with GRGDSPC (690.7 Da, CPC Scientific) at a final concentration of 0.6 mM to promote cell growth and 16 v/v% OptiprepTM is added to prevent spheroid sedimentation. To allow for degradation, two different types of crosslinkers are used: MMP-sensitive peptide with terminal cysteines (HS-MMPsens-SH, GCREGPQGIWGQERCG, 1774 Da, GenScript) that can be cleaved on cell-demand and a thrombin-cleavable peptide with terminal cysteines (HS-TCP-SH, CKGGGLVPRGSGGGKC, 1431 Da, provided by Kuan Zhang). PEG-VS and thiol-functionalized components are mixed in equimolar ratios and incubated at 37 °C for 30 min to form 6.5 w/v% PEG hydrogels via thiol-Michael addition.

5.4.2 Degradation Experiments

Degradation experiments are performed using 6.5 w/v% with 100% HS-TCP-SH. 15 µL hydrogel droplets are pipetted on a 24-well plate. After crosslinking, the hydrogels are incubated with 20, 10 and 5 nM thrombin solutions in DMEM supplemented with 10% FCS and 1% ABM at 37 °C. The degradation of the hydrogels is observed visually and images are recorded every 30 min to determine the rate of hydrogel degradation depending on the thrombin concentration. The experiment is carried out in triplicates per condition.

5.4.3 Rheological Characterization of Hydrogels

For rheological measurements, a Discovery HR 3 hybrid rheometer with a 20 mm cone-plate (2°) geometry is used. 6.5 w/v% PEG hydrogel mixtures with a volume of 74 μ L are pipetted on the rheometer plate which is heated to 37 °C. Due to the absence of cells, GRGDSPC and OptiprepTM are not added. Time-dependent

measurements are performed for 30 min at a frequency of 1 Hz, an oscillation strain of 0.1% and a gap size of 51 µm with triplicates per condition.

5.4.4 Quantification of Hydrogel Softening via Nanoindentation

Flat disk-shaped hydrogels with fractions of 0-30% HS-TCP-SH in combination with HS-MMPsens-SH and with a volume of 45 μ L are formed in printed pluronic rings that have a radius of 4 mm and a height of 1.2 mm. After crosslinking of the hydrogels at 37 °C, the pluronic is removed by washing with cold PBS. The hydrogels are incubated in PBS + 1% ABM overnight at 37 °C. To determine the hydrogel softening before and after thrombin treatment, the high-throughput mechanical screening platform Pavone (Optics11 Life) is used. Indentation measurements are performed using a cantilever-based probe with a spherical tip radius of 44 μ m and a stiffness of 0.43 N/m. The cantilever is moved as a piezo speed of 15 μ m/s to reach an indentation-depth of 8 μ m. Per hydrogel, an automated matrix scan is configured to obtain the mechanical properties of a 5×5 grid. All measurements are performed at RT with duplicates per condition.

5.4.5 Cell Culture

Human umbilical vein endothelial cells (HUVECs, Lonza) are cultured in tissue culture flasks with endothelial cell growth medium 2 (EGM-2, Promocell) supplemented with 1% ABM up to passage 6. Normal human dermal fibroblasts (NHDFs, Promocell) are cultured in tissue culture flasks with DMEM supplemented with 10% FCS and 1% ABM up to passage 8. Both cell types are cultured at 37 °C with 5% CO₂ according to standards protocols.

5.4.6 Evaluation of Cell Viability

To investigate the influence of thrombin on cell viability, HUVECs and NHDFs are incubated with thrombin concentrations of 20, 10 and 5 nM for 25 h, followed by live/dead staining using a LIVE/DEAD Cell Imaging Kit (Invitrogen). Cells are incubated with live (488/515 nm)/dead (570/602 nm) reagent, diluted in DMEM

supplemented with 10% FCS and 1% ABM to create a 1x working solution, for 15 min at RT. The experiment is performed with triplicates per condition, including a positive and negative control that are incubated with unconditioned media or 70 v/v% ethanol respectively. Images of the cells are recorded using a PerkinElmer Opera Phenix Plus confocal microscope with a 10×/NA 0.3 air objective or a 20×/NA 1.0 water immersion objective.

5.4.7 Cultivation of Cell Spheroids in Hydrogels

Cell spheroids consisting of 1000 cells/spheroid are formed in hanging drops. Briefly, HUVECs and NHDFs are suspended in DMEM with 10% FCS and 1% ABM in a 1:3 ratio. Cell suspensions are then mixed with 20% Methocel (1.2 w/v% methyl cellulose (4,000 cP, Sigma) in DMEM) and 30 µL droplets are formed on petri dishes that are incubated upside down overnight at 37 °C and 5% CO₂ to allow for spheroid formation. Afterwards, spheroids are harvested by flushing with 5 mL DMME per plate and collected in centrifuges tubes. After centrifugation at 100 rcf for 5 min, the spheroids are resuspended in DMEM supplemented with 10% FCS, 1% ABM, and 16 v/v% OptiprepTM and mixed with hydrogel components to reach a concentration of 0.5 spheroids/µL. Finally, 15 µL hydrogel droplets are casted on 8-well ibidi slides and allowed to crosslink for 30 min before adding 350 µL EGM-2 and cultivation at 37 °C and 5% CO₂ with medium changes every 2-3 days. For on-demand degradation, thrombin in EGM-2 is added in concentrations at different time points.

5.4.8 Microscopy

Brightfield images of spheroids cultured in PEG hydrogels are recorded using a Zeiss Axio Observer.Z1 light microscope equipped with a 4× objective. Images are recorded before thrombin addition and on the following days after thrombin addition until the end of the experiment to monitor spheroid sprouting. Additionally, the cell infiltration into the hydrogel was determined by recording z-stacks of 6 spheroids per condition at 10× magnification.

5.4.9 LIFU-Triggered Thrombin Activation in PEG Hydrogels

For LIFU-triggered thrombin activation, thrombin and hirudin modified with thiols are synthesized and provided by Kuan Zhang. These are mixed in a molar thrombin/hirudin ratio of 1:1.5, ensuring the effective inhibition of thrombin's catalytic activity, and subsequently integrated as a biocatalytic system into thrombin-sensitive 6.5 w/v% PEG. Hydrogel droplets with a volume of 50 µL are casted into lumox® 96-well plates. LIFU experiments are performed by Junlin Chen from the Institute for Experimental Molecular Imaging led by Prof. Fabian Kiessling at a frequency of 1 MHz and an intensity of 4.25 MPa. The fluorogenic thrombin substrate Fluoro-s is used to measure the enzyme activity during sonication and it is cleaved by thrombin to produce a fluorescence signal at 450 nm.

5.4.10 Statistical Analysis

Each experiment is performed with $n \ge 2$. Statistical analysis of the data is conducted in OriginPro 2020 using a one-way ANOVA. Pair comparisons are performed using Tukey's method, where p-values below 0.05 are considered as significant differences (*p < 0.05; **p < 0.01; ***p < 0.001).

6 Cellular Architects at Work: Cells Building Their Own Microgel Houses

Daniel Günther, Selin Bulut, Michelle Bund, Christina Haats, Thomas Bissing, Céline Bastard, Matthias Wessling, Laura De Laporte, Andrij Pich

6.1 Introduction

The development of functional human tissue models to offer disruptive solutions for drug discovery and regenerative medicine requires the recapitulation of the native tissue architecture and organization by combining tissue inherent cell types with adequate 3D scaffolds. 92 Hydrogels, which are crosslinked networks of natural or synthetic polymers, have emerged as the most promising platform for 3D cell culture as they can be varied in their mechanics and provide biochemical cues to promote cell adhesion and growth.60 Thereby, polysaccharides, such as dextran, gain more and more interest as they combine the chemical functionality, structural complexity, biocompatibility, and degradability of natural polymers with the possibility for bottom-up functionalization of many synthetic polymers. The hydroxyl groups of the dextran backbone can be used for biofunctionalization in many different tissue engineering applications.²²⁵ Dextran methacrylate (dex-MA) has been demonstrated to be a suitable material to support angiogenesis, where endothelial cells from pre-engineered vasculature invade the surrounding matrix to form new vascular structures. 193 Yet, as extensively discussed in the last chapters, one of the main challenges associated with hydrogels is their small pore size, which requires degradation to create sufficient space for encapsulated cells to grow, while providing cell attachment sites and maintaining the required mechanics to support the cells. Thus, this chapter focusses on the development of novel microporous annealed particle (MAP) scaffolds, which overcome the limitations of conventional, nanoporous hydrogels to improve cell growth and infiltration as introduced by the research group of Tatiana Segura. 143 In most MAP scaffolds, the microgels are chemically interlinked, resulting in pre-determined frameworks that lack the dynamics of native tissues and limit cellular self-organization. In contrast, it is yet known for biological systems, such as cells, to actively organize their constituents away from thermodynamic equilibrium by dissipating energy. To recapitulate the development and dynamics of native tissues, organoids have taken center stage as they represent simplified in vitro model systems of organs. They are often derived from stem cells and self-organize through cell-cell and cell-matrix interactions into structures that resemble the native tissue architecture and function. 145 While organoids have been developed to represent various tissues, including the kidney²²⁶, liver²²⁷, intestine¹⁴⁹, heart²²⁸, brain²²⁹, and respective diseases, they are not yet able to fully match the architecture, complexity, maturity, and function of native tissues and lack reproducibility.²³⁰ For example, miniintestines could be formed by combining perfusable scaffolds that resembled the topology of the gut surface with intestinal stem cells, which otherwise build cystic organoid structures.²³¹ Alternatively, cellular self-organization can be combined with micron-sized particles to interlink the particles and form millimeter-sized scaffolds.²³² While it is possible to construct scaffolds through various methods, it remains a challenge to control scaffold formation based on cellular selforganization. To further understand how cells interlink soft microgels to build millimeter-sized tissue scaffolds and ultimately guide cellular self-organization via external cues, we build cell-induced interlinked scaffolds by combining normal human dermal fibroblasts (NHDFs) and bio-based dextran microgels. Here, the cells build their own microgel houses by using the microgels as bricks that they glue together through cell-cell and cell-material interactions (Figure 6.1). We further investigate influences, such as cell/microgel ratios and the microgel properties, to guide the scaffold formation process. The microgels consist of crosslinked dex-MA, which is known to be biocompatible and inert. The concept of establishing MAP scaffolds through a combination of self-organization and a novel bio-based material possesses several advantages over previous techniques by abolishing the confinement of cells by a pre-defined architectural framework. This method aims to build 3D cellular scaffolds with structural integrity while maintaining their plasticity and dynamic nature, which mimics the formation of macroscopic cellular structures in biological systems. The microgel properties can be varied without hindering cell growth, which is usually limited in conventional 3D hydrogels. Driven by the ability of the fibroblasts to attach to the microgels and migrate, no external energy is needed for the formation of the MAP scaffolds. Thereby, cells themselves create their optimal environment by determining the degree of porosity over cell-cell and cell-matrix interactions.

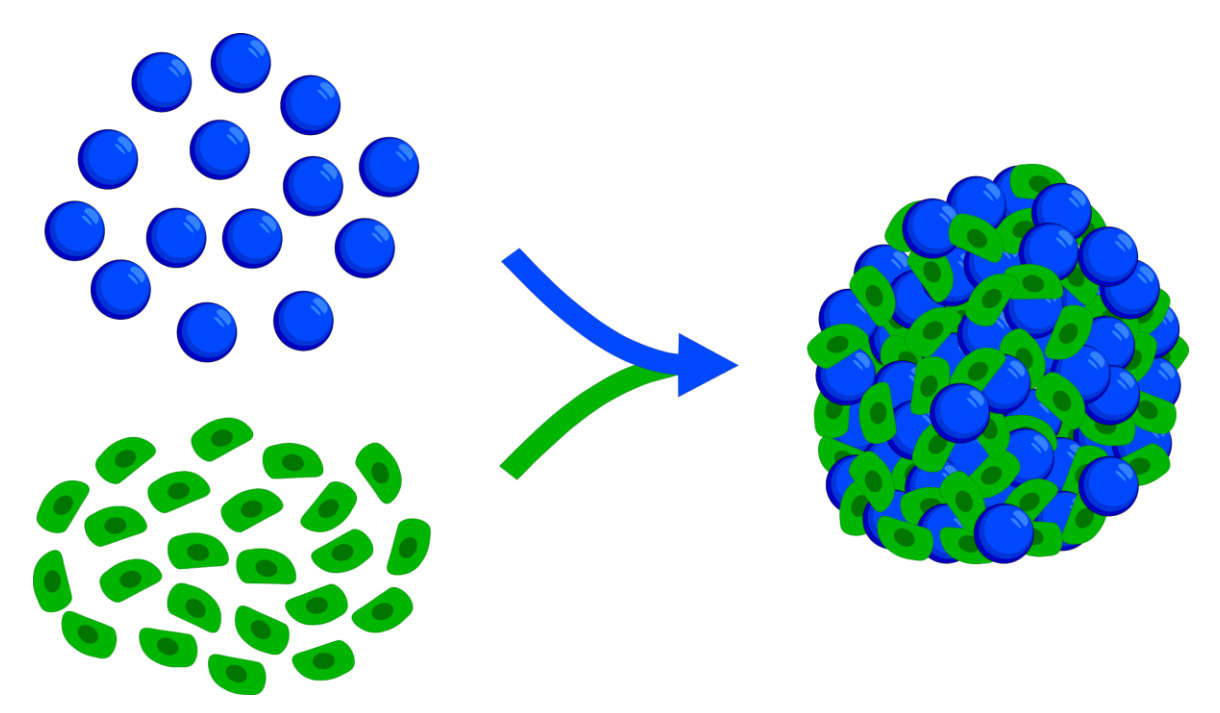


Figure 6.1: Schematic of cell-induced interlinked MAP scaffolds formation. NHDFs are mixed with dex-MA microgels, post-functionalized with GRGDSPC to promote cell attachment, and interlink them to form MAP scaffolds through cellular self-organization.

6.2 Results and Discussion

6.2.1 Cell-Induced Interlinking of Microgels

Spherical, dex-MA microgels are synthesized via droplet-based microfluidics and an off-chip free radical crosslinking reaction, which is initiated by UV-light exposure (λ = 365 nm) using lithium phenyl-2,4,6-trimethylbenzoylphosphinate (LAP) as a photoinitiator according to recent literature.²³³ By adjusting the concentration of dex-MA in microfluidic droplets between 5-20 w/v%, the Young's moduli of the microgels is tuned between 1.32 ± 0.20 kPa to 629.87 ± 114.32 kPa, covering a broad stiffness range.²³³ This makes them a versatile platform for engineering of various tissues with different mechanical properties. To promote cell growth, they need to be cell-adhesive and are thus post-functionalized in a solution of 1 mM GRGDSPC, which is confirmed by RGD immunostaining (**Figure 6.2 A**). However, a weak fluorescent signal is also observed in non-functionalized microgels, which can be attributed to antibody binding to free acrylate groups as well as the porous nature of the microgels, which allows for diffusion of the antibody into the microgel network. Yet, the formation of cell-induced interlinked MAP scaffolds is only

achieved by mixing of RGD-functionalized microgels with NHDFs as the replacement of RGD with L-cysteine prevents scaffold formation (**Figure 6.2 B**).

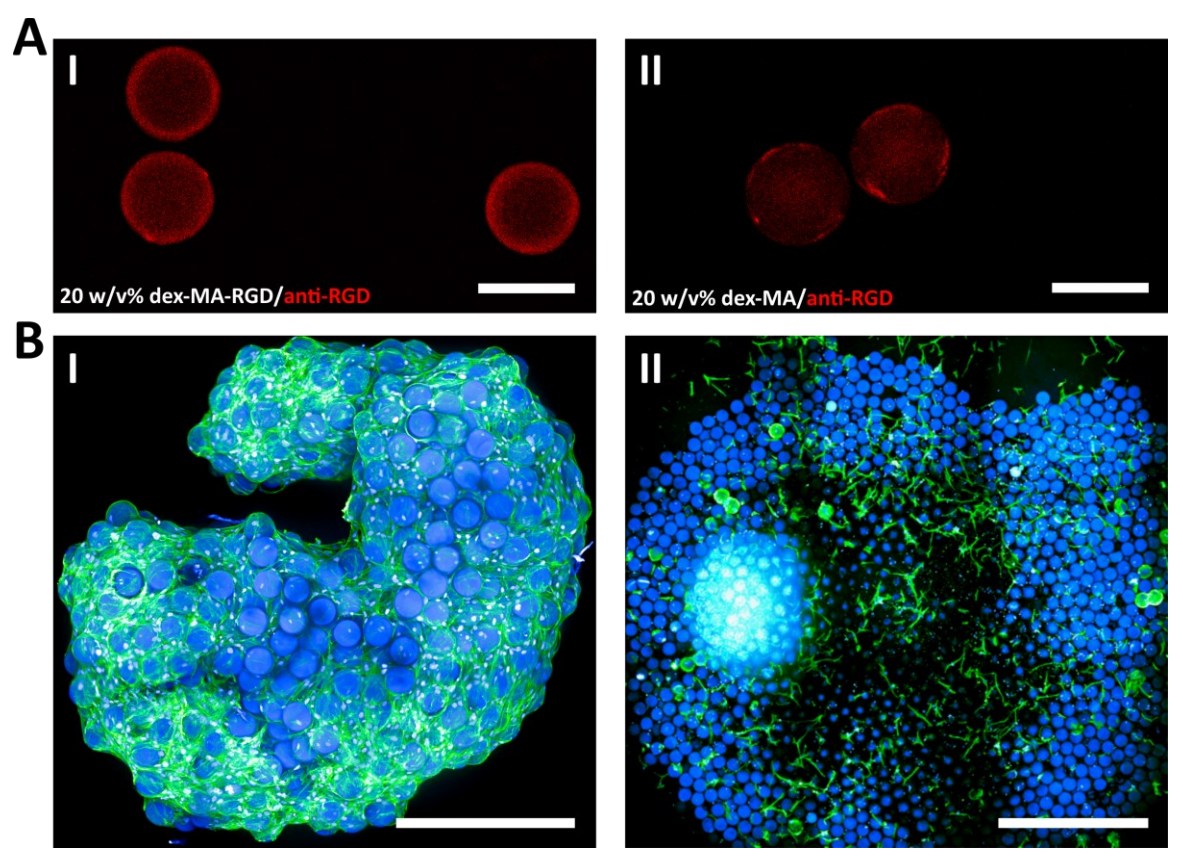


Figure 6.2: Microgel post-functionalization for MAP scaffold formation. A) Confocal images of RGD-functionalized 20 w/v% dex-MA (dex-MA-RGD) microgels (I) and unmodified dex-MA microgels (II) stained with anti-RGD antibody (red). Scale bars: 100 μ m. B) Comparison of MAP scaffold formation with RGD- (I) or L-cysteine- (II) functionalized microgels. Confocal images of NHDFs cultured with 20 w/v% dex-MA microgels that are post-functionalized in a 1 mM RGD or L-cysteine solution. The samples are stained for F-actin (green) and DAPI (blue). Scale bars: I) 500 μ m, II) 1 mm.

6.2.2 Cues to Guide Cell-Induced Interlinking of Microgels

6.2.2.1 Influence of Cell Concentration on MAP Scaffold Formation

Initially, different volumes of cells and microgels are mixed to find the right ratio of cells/microgels for the formation of cell-induced interlinked MAP scaffolds. Thus, 10 or 20 μ L of a microgel suspension with a concentration of 1.5 mg/mL are mixed with 5000, 10 000 or 20 000 NHDFs in a total volume of 60 μ L and cultivated on ibidi well plates. After 7 days of culture, the formation of cell-induced interlinked MAP scaffolds is observed in all conditions (**Figure 6.3**). However, their size and the number of microgels in conditions with fixed microgel volumes varies significantly. The biggest scaffolds are observed in conditions with 10 μ L microgel

suspension and 10 000 NHDFs, while the same number of cells with 20 μ L microgel suspension formed the smallest scaffold. The microgels are sticky and sediment quickly after mixing, which is why during multiple pipetting steps many microgels are lost, resulting in inconsistent microgel numbers per well. Additionally, in conditions that contain less cells relative to the number of microgels, such as 20 μ L of microgel suspension with 5000 NHDFs, scaffolds are only partially formed, while the addition of 20 000 NHDFs with 20 μ L microgel suspension results in compact scaffolds. This indicates that for efficient scaffold formation more cells are needed to interlink the microgels.

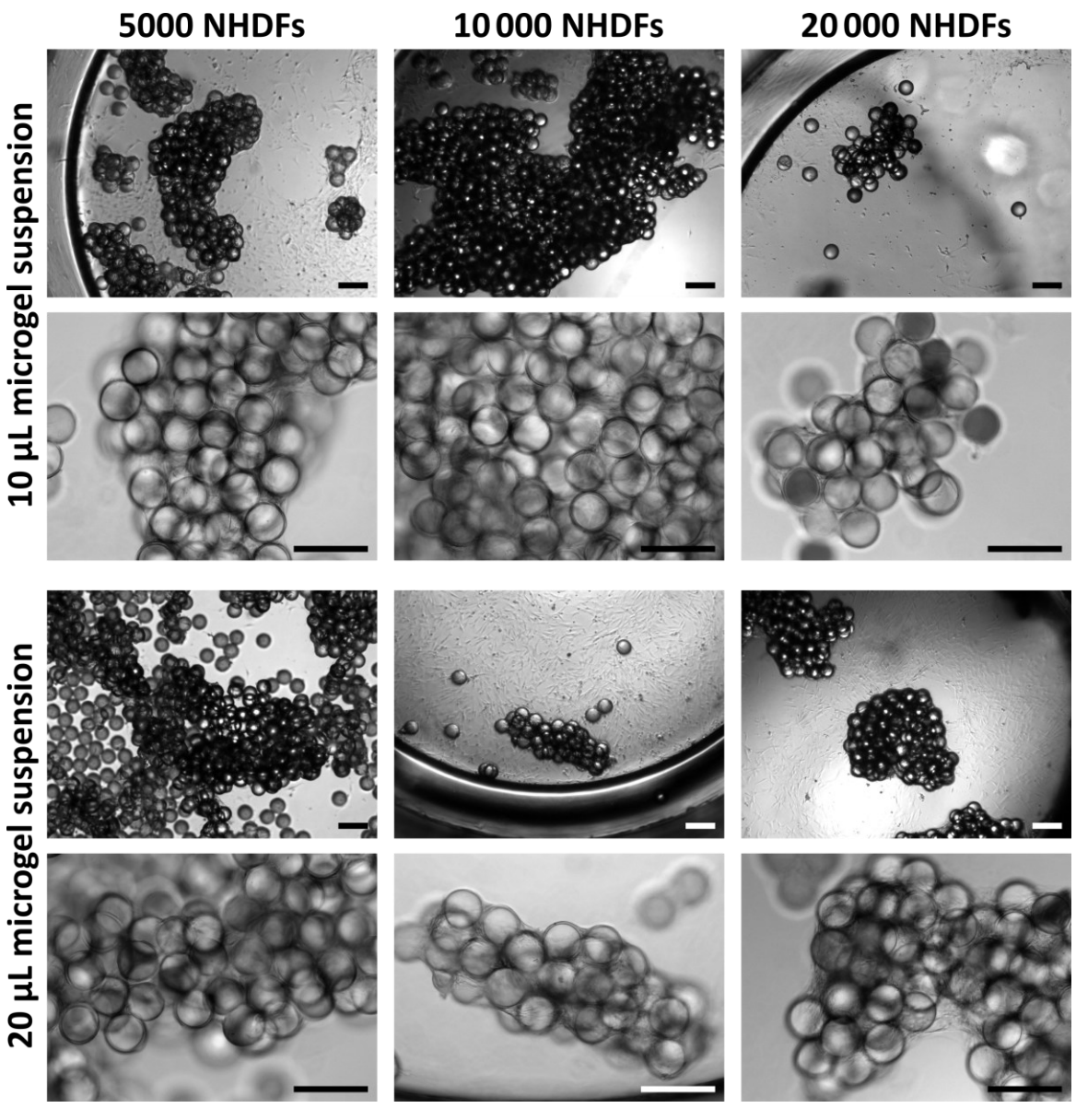


Figure 6.3: Pipetting of microgels and cells in different ratios to form cell-induced interlinked MAP scaffolds. 10 or 20 μ L of a microgel suspension with 1.5 mg/mL are mixed with 5000, 10 000 or 20 000 NHDFs in a total volume of 60 μ L. After 7 days of culture, brightfield images are recorded at 4x and 10x magnification. Scale bars: 200 μ m.

To avoid multiple pipetting steps, batches with a defined concentration of 1.5 mg/mL in a volume of 100 µL are collected in LoBind® tubes that are mixed with 100 µL of cell suspension containing 200 000-500 000 NHDFs that are transferred in a single pipetting step to a well of 96-well plate per sample. In order to prevent cells from attachment to the well surface, the wells are pre-coated with polydimethylsiloxane (PDMS). This way, a low-attachment environment is created that allows the cells to adhere only to other cells as well as cell-adhesive microgels, thereby increasing the scaffold formation efficiency. Cellular self-organization results in the formation of scaffolds within 24 h without the need for chemical interlinking steps (Figure 6.4 A). Hereby, cells from the outer edge start to migrate to the well center while binding to the microgels and interlinking them. Even though the overall shape of the scaffold forms in less than 24 h, cells continuously remodel parts of the scaffold, which demonstrates the highly dynamic properties of these cell-assembled constructs. During the scaffold formation process, the constructs fold inwards, which results in bowl-shaped scaffolds. Additionally, different cell/microgel ratios result in scaffolds with different geometries in a reproducible manner. Increasing the cell number of to 500 000 lead to a triangular structure, whereas lower cell numbers (200 000 and 350 000 NHDFs) results in elongated oval 3D structures (Figure 6.4 B). The triangular shape formation can be explained by the high number of cells, which start to pile up and build a scaffold upwards. As shown in higher magnification images, cells within the MAP scaffolds wrap around the microgels, which is characterized by a spread cell morphology. To form scaffolds, cells interlink the microgels by the formation of elongated protrusions that build bridges between different microgels. The possible driving force for MAP scaffold formation lies in the intrinsic motivation of the cells to form cell-matrix interactions as well as maximize cell-cell contacts for inter-cellular communication. Quantification of the total construct volume, total cell volume, defined by F-actin signal, and surface area of F-actin signal inside the formed scaffolds gives an insight into how large the formed scaffolds are in 3D, the fractional volume occupation by the cells, and the cell-cell interactions. A smaller ratio of surface area to volume of F-actin signal inside the formed scaffold suggests more cell-cell contacts due to the presence of less single cells without formed cell-cell contacts. The data reveal that the final construct volume is larger with increasing amount of initially added cells (Figure 6.4 C). The largest cellular scaffolds are formed with

the highest cell number of 500 000, resulting in a total construct volume (F-actin plus microgel volume) of 1.36 ± 0.52 mm³ and cell volume (F-actin volume) of 0.95 ± 0.39 mm³ with a surface area of F-actin signal of 54 ± 10.8 mm². Scaffolds formed with 350 000 NHDFs have a construct volume of 0.96 ± 0.09 mm³ and cell volume of $0.62 \pm 0.1 \text{ mm}^3$ with a surface area of F-actin signal of $43.1 \pm 6.9 \text{ mm}^2$. The smallest scaffolds are formed with 200 000 NHDFs, leading to a construct volume of 0.42 ± 0.04 mm³ and a cell volume of 0.28 ± 0.02 mm³ with a surface area of F-actin signal of 29 ± 4.7 mm². While the cell volume and surface area of F-actin signal per construct increases with increasing cell numbers, the ratio of Factin surface area/volume slightly decreases, which indicates that the number of cell-cell contacts increases with increasing cell numbers. Additionally, the cell volume fraction ranges consistently between 60-70%. This is a result of cellular self-organization, suggesting that the cells grab the number of microgels they need to build their house. By increasing the number of cells, more microgels are integrated into the scaffolds, even though the amount of added microgels is the same in all tested conditions. This can be seen in Figure 6.4 A, where in case of scaffolds formed with 200 000 NHDFs peripheral microgels are loosely associated and thereby not integrated into the scaffold, while 500 000 NHDFs are able to integrate most microgels into the formed scaffold. This suggests that the added number of microgels offers sufficient support for the high number of cells to build the 3D construct, while the amount of microgels integrated into the scaffold is proportional to the number of added cells, resulting in scaffolds with a consistent cell volume fraction for the tested conditions.

Scaffolds made with 350 000 NHDFs are characterized by an increased aspect ratio of 2.05 ± 0.06 compared to 1.72 ± 0.15 in the case of scaffolds formed from initially 200 000 NHDFs. Larger scaffolds, made with the highest cell number of 500 000, display the smallest aspect ratio of 1.21 ± 0.06 due to their triangular shape. While cells in suspension culture commonly form multicellular, spherical aggregates, these results further suggest that the addition of microgels does not disturb the cellular aggregation process, but rather changes the construct geometry by integration of microgels. 234

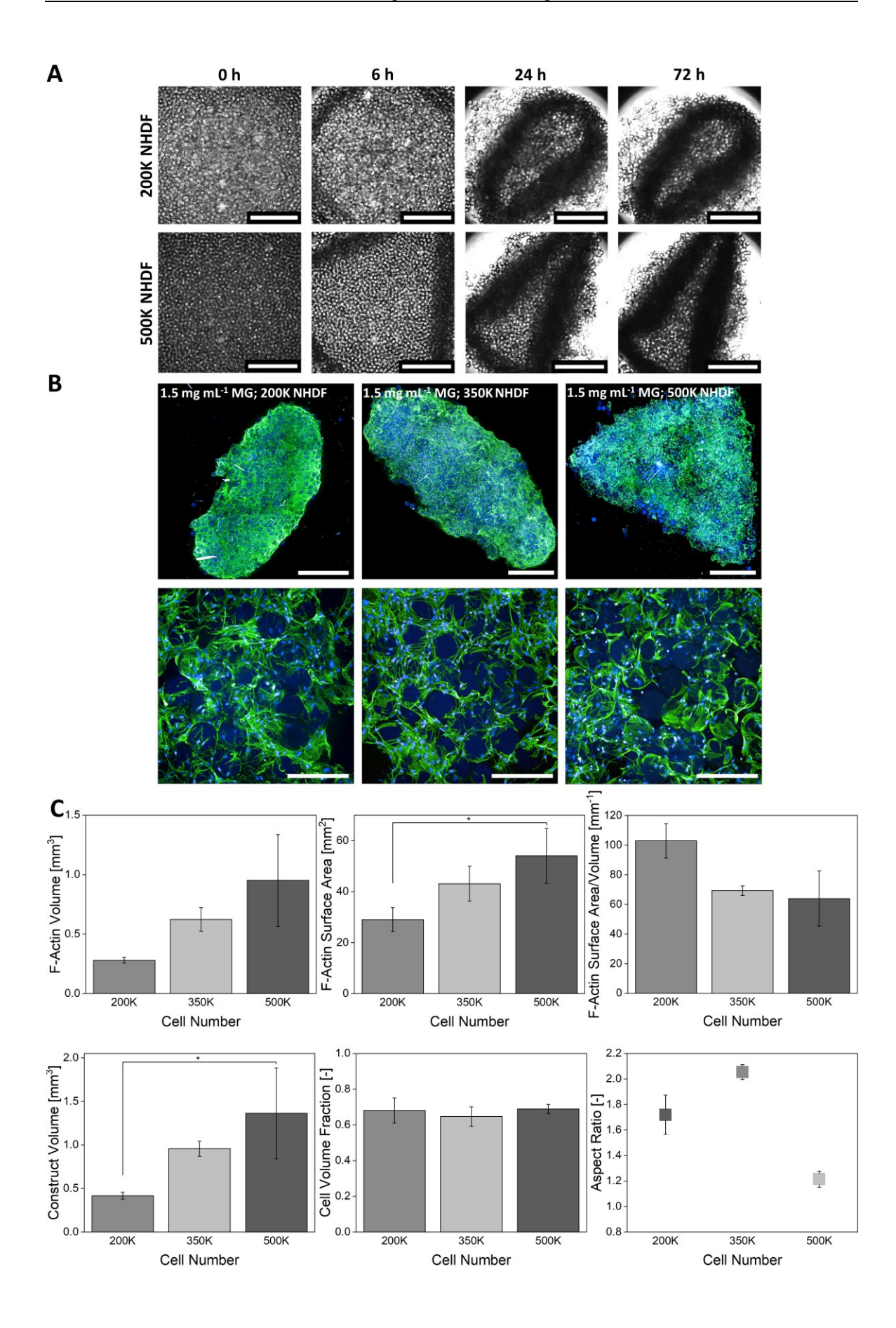


Figure 6.4: Formation of MAP scaffolds. A) Time-lapse images of MAP scaffold formation with a fixed microgel concentration of 1.5 mg/mL and cells numbers of 200 000 and 500 000 recorded at time points t=0, 6, 24, and 72 h. Scale bars: 1 mm. B) Confocal images of MAP scaffolds formed with a fixed microgel (MG) concentration of 1.5 mg/mL and cell numbers of 200 000, 350 000 and 500 000 after 7 days of culture. The samples are stained for F-actin (green) and DAPI (blue). Scale bars: 1 mm and 200 μ m for higher magnification images. C) Quantification of F-actin volume, F-actin surface area, F-actin surface area/volume, construct volume (F-actin plus microgel volume), cell volume fraction, and aspect ratio of the resulting MAP scaffolds depending on the cell number. Data is presented as mean \pm SD with n = 3 for each scaffold type. P values are calculated using one-way ANOVA with post-hoc Tukey test, *p < 0.05, **p < 0.01, ***p < 0.001.

6.2.2.2 Influence of Microgel Stiffness on MAP Scaffold Formation

Since substrate stiffness is a significant factor in cell attachment and spreading and influences cell migration, proliferation, and differentiation²³⁵, the influence of the microgel stiffness on cell-mediated MAP scaffold formation is investigated. Microgels (1.5 mg/mL) with different dex-MA concentrations are cultivated with 500 000 NHDFs for 7 days. Interestingly, the microgels with the lowest effective Young' modulus (5 w/v% dex-MA; 1.32 ± 0.2 kPa) result in round scaffolds with an aspect ratio of 1.08 ± 0.004, while NHDFs cultured with stiffer microgels (10 w/v% dex-MA; 184.15 ± 55.57 kPa) form oval structures with an aspect ratio of 1.56 ± 0.15 (**Figure 6.5 A**). For microgels with 20 w/v% dex-MA and a stiffness of 629.87 ± 114.32 kPa, the characteristic triangular shape is observed with an aspect ratio of 1.21 ± 0.06. Despite the same initial cell number, the cell volume and surface area of the F-actin signal are significantly higher in conditions with 20 w/v% dex-MA microgels compared to conditions with softer microgels (Figure **6.5 B**). In addition, the ratio of F-actin surface area/volume slightly decreases with increasing microgel stiffness, indicating that more cell-cell contacts are formed in constructs made with stiffer microgels. This can be explained by the fact that cell adhesion, spreading, and proliferation are usually enhanced on substrates with a higher Young's modulus in the case of elastic hydrogels. The final scaffold shape is therefore likely associated with the fact that stiffer microgels lead to increased cell adhesion and proliferation, which improves both microgel integration into the scaffold as well as cell-cell interaction. 236 Thus, it is assumed that by decreasing the microgel stiffness, the scaffold formation efficiency is reduced, resulting in smaller, spherical constructs as shown for scaffolds made with 5 w/v% dex-MA microgels.

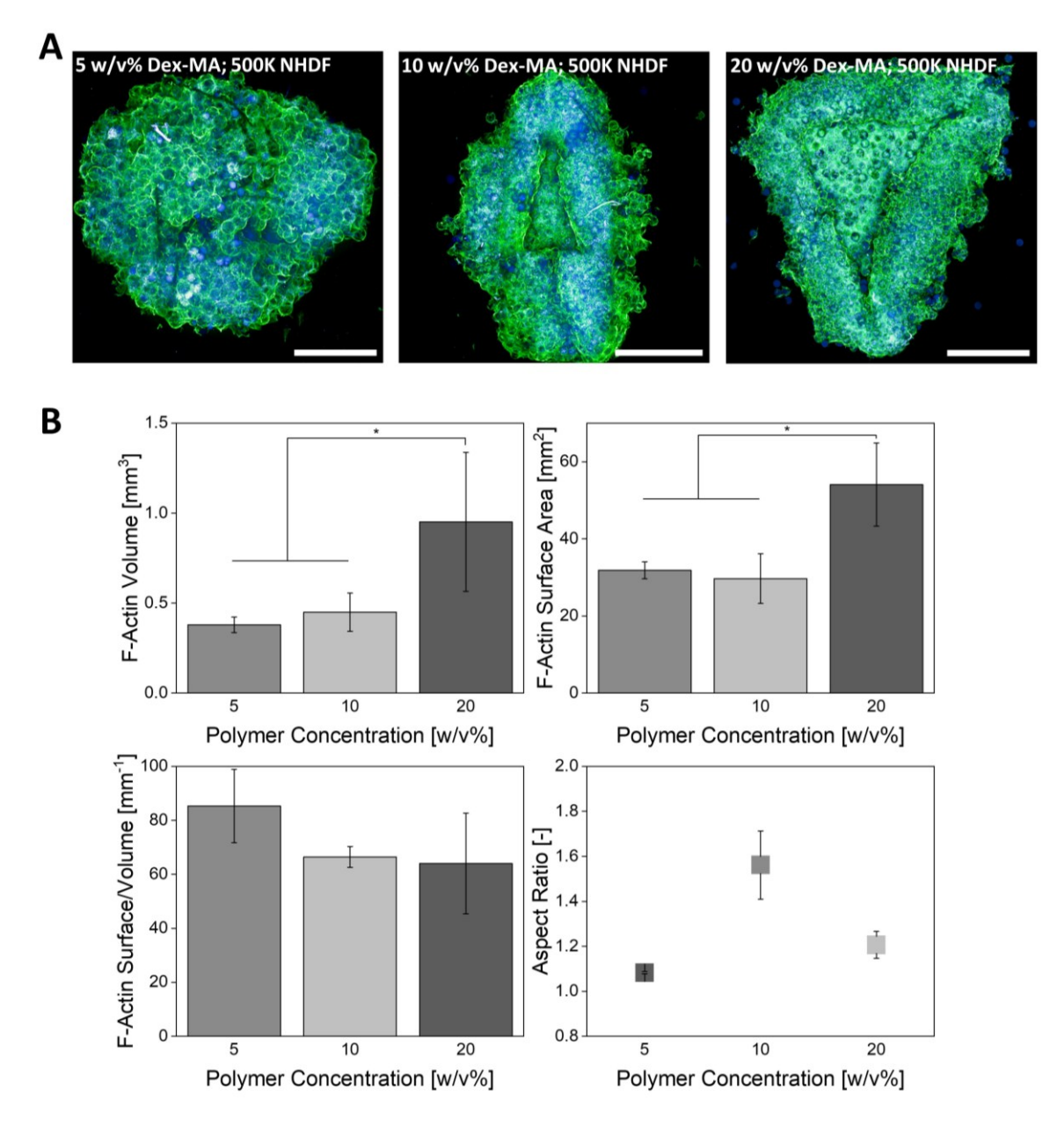


Figure 6.5: Mechanical characterization of MAP scaffolds. Microscopy images of MAP scaffolds formed with a fixed microgel concentration of 1.5 mg/mL and 500 000 NHDFs (A) as well as 200 000 NHDFs (B) on a glass slide in PBS. Scale bars: 1 mm. C) Rheological properties of MAP scaffolds with varying cell numbers and microgel stiffness. Microgel dispersions serve as control. Data is presented as mean \pm SD with n = 3 per conditions. P values are calculated using one-way ANOVA with post-hoc Tukey test, *p < 0.05, **p < 0.01, ***p < 0.001.

Additionally, the viability of the cells within MAP scaffolds with different microgel stiffnesses is evaluated by live/dead staining. In all conditions, the cells remain viable over the monitored period of 7 days (**Figure 6.6 A**). This demonstrates that the incorporated microgels provide an open network that allows for the diffusion of oxygen and nutrients, avoiding necrotic core formation within mm-scale scaffolds. To further monitor the metabolic cell activity in MAP scaffolds, a resazurin-based

alamarBlueTM assay is performed after 3, 5, and 7 days, which reveals that the resazurin reduction and thereby the metabolic activity decreases over time for all tested conditions (**Figure 6.6 B**). As the formation of stable scaffolds takes about 3 days, measurements at earlier time points are not conducted to prevent scaffold destruction as a result of pipetting during the processing. The results suggest that the interstitial space between the microgels within the MAP scaffolds is completely filled with cells and extracellular matrix (ECM) after 3 days. Thus, the high cell density could lead to contact inhibition of proliferation, resulting in reduced metabolic activity, which is characteristic for noncancerous cells.²³⁷ The reduction of the metabolic activity is also less pronounced in scaffolds made form softer microgels (5 and 10 w/v% dex-MA). While softer microgels could allow for better oxygen and nutrient diffusion to support cell growth, the contact inhibition affecting cell proliferation is potentially less significant as cells seem to form fewer cell-cell contacts in these constructs.

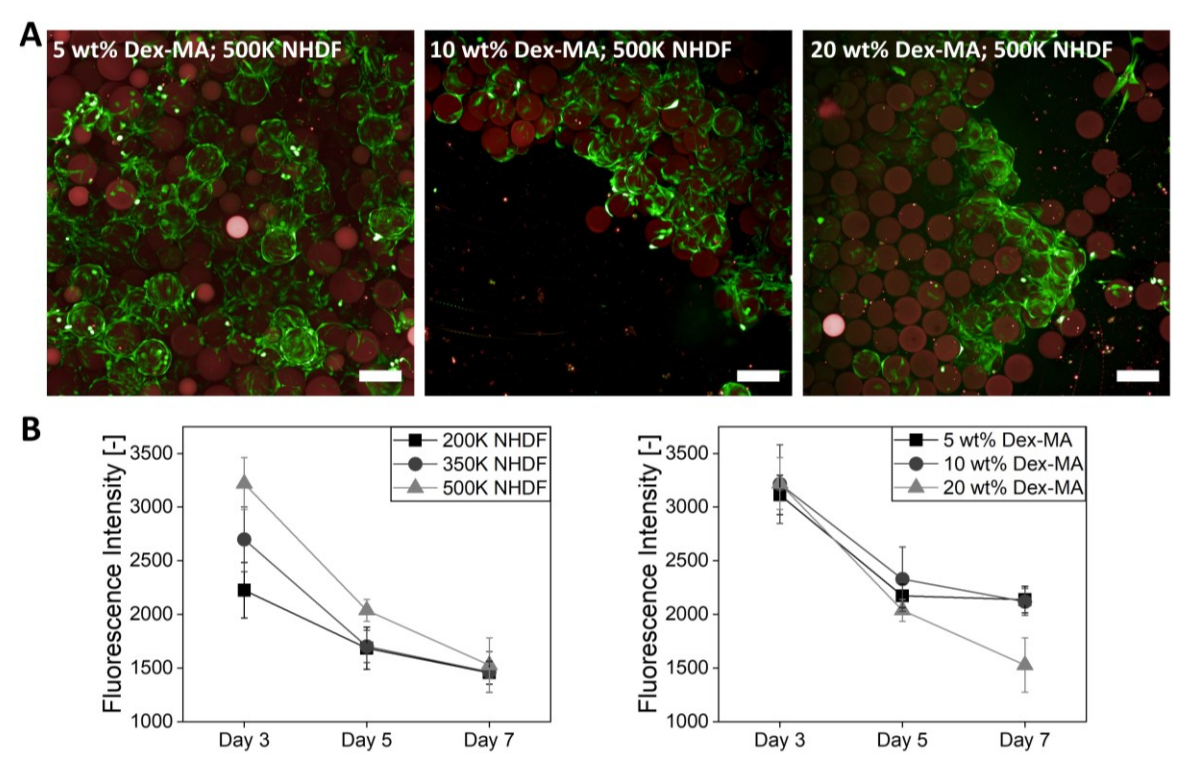


Figure 6.6: Viability and metabolic activity of cells in cell-induced interlinked MAP scaffolds. A) Live/Dead staining of MAP scaffolds formed with a fixed microgel concentration of 1.5 mg/mL with varying dex-MA concentrations of 5, 10 and 20 w/v% and 500 000 NHDFs after 7 days of culture. Live cells are shown in green, while red signal indicates dead cells and microgels. Scale bars: 200 μ m. B) Metabolic cell activity in MAP scaffolds with a fixed microgel concentration of 1.5 mg/mL and varying cell numbers of 200 000, 350 000 and 500 000 and 20 w/v% dex-MA as well as varying dex-MA concentration of 5, 10 and 20 w/v% and 500 000 NHDFs, monitored over a period of 7 days. Resazurin-based alamarBlueTM assay is performed on day 3, 5 and 7 of culture. Data is presented as mean \pm SD with n = 3 per condition.

6.2.2.3 Mechanical Properties of MAP Scaffolds

The cell-induced interlinking of microgels results in a mechanically stable MAP scaffold, which is able to withstand a significant amount of mechanical stress. Evaluation of the mechanical robustness of the fabricated scaffold under dynamic stress conditions demonstrated that the scaffold maintains structural integrity when subjected to repetitive mechanical forces, that is, the vertical shear stresses encountered during pipetting (not shown) and the transfer onto a glass surface for microscopy analysis (**Figure 6.7 A, B**).

To further understand how the microgel stiffness as well as the cell number influence the mechanical properties of the resulting MAP scaffolds, the rheological properties of the MAP scaffolds are characterized by oscillation rheometer measurements (Figure 6.7 C). The highest storage modulus of 608 ± 39 Pa is measured for the MAP scaffolds formed with 500 000 NHDFs and 1.5 mg/mL microgels containing 20 w/v% dex-MA. This is likely associated with the higher number of initial cells. MAP scaffolds formed with 350 000 and 200 000 NHDFs display similar storage moduli of 153 ± 48 Pa and 155 ± 467 Pa, respectively. A control experiment representing the initial state before scaffold formation (1.5 mg/mL microgel dispersion, 20 w/v% dex-MA) demonstrates a storage modulus of 21 ± 3 Pa, indicating that the rheological characteristics shift to higher storage moduli as a result of cell-induced interlinking of microgels into MAP scaffolds and likely cellular production of ECM. Additionally, the influence of the microgel stiffness on the mechanical integrity of the MAP scaffolds is investigated. The storage moduli of MAP scaffolds gradually increase with higher dex-MA concentration in the microgels. MAP scaffolds formed with 5 w/v% dex-MA exhibit a storage modulus of 26 ± 4 Pa and are significantly softer than MAP scaffolds formed with 10 and 20 w/v% Dex-MA, which are characterized by storage moduli of 79 ± 49 Pa and 608 ± 39 Pa. This demonstrates that, besides the scaffold geometries, the mechanical scaffold properties can be varied by changing the cell/microgel ratio and/or microgel stiffness.

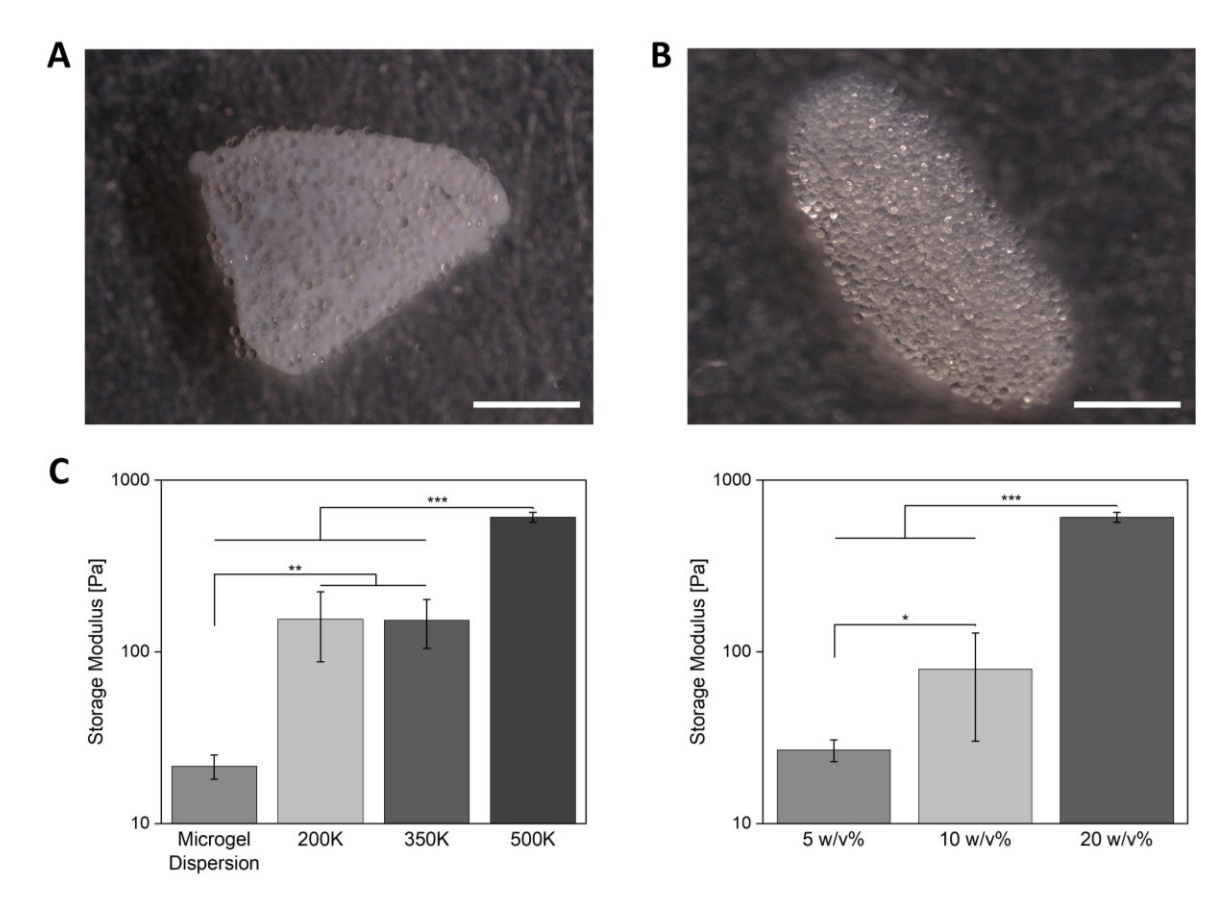
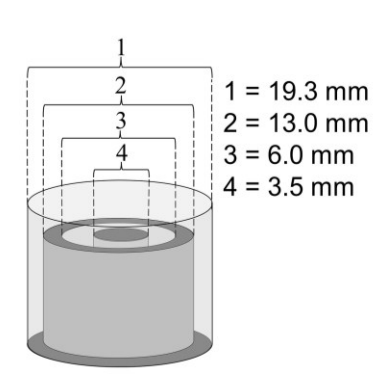
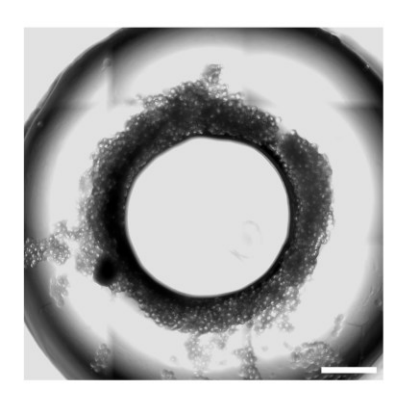


Figure 6.7: Influence of MAP scaffold composition on its mechanical properties. Microscopy images of MAP scaffolds formed with a fixed microgel concentration of 1.5 mg/mL and 500 000 NHDFs (A) as well as 200 000 NHDFs (B) on a glass slide in PBS. Scale bars: 1 mm. C) Rheological properties of MAP scaffolds with varying cell numbers and microgel stiffness. Microgel dispersions serve as control. Data is presented as mean \pm SD with n = 3 per conditions. P values are calculated using one-way ANOVA with post-hoc Tukey test, *p < 0.05, **p < 0.01, ***p < 0.001.

6.2.2.4 Geometry-Guided MAP Scaffold Formation

To design further advanced scaffold shapes, the influence of geometrical cues on scaffold formation is investigated. Here, a well of a 24-well plate is exemplary modified with a PDMS ring and cylinder (**Figure 6.8**). 500 000 NHDFs are cultured with 1.5 mg/mL microgels and a dex-MA concentration of 20 w/v% in the resulting interstitial space between the PDMS ring and cylinder, which matched the total surface area of the previous experiments. This way, ring-shaped MAP scaffolds are formed within 7 days of culture. As previously shown, cells induce the interlinking of the microgels and subsequently fold inwards during the process of scaffold formation. Due to the geometrical set-up of this experiment, the inward migration process is restricted by the inner PDMS cylinder and results in the formation of a ring-shaped MAP scaffold.





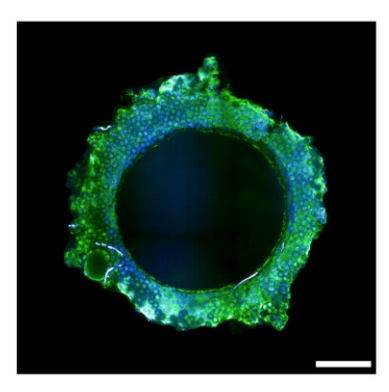


Figure 6.8: Geometry-guided scaffold formation. A PDMS ring (2-3) and cylinder (4) are placed into a well (1) of a 24-well plate. Brightfield and confocal images of 500 000 NHDFs that are co-cultured with 1.5 mg/mL microgels with 20 w/v% dex-MA in the interstitial space between the PDMS ring and cylinder, are recorded after 7 days. The samples are stained for F-actin (green) and nuclei (blue). Scale bars: 1 mm.

6.3 Conclusion

In this study, cell-induced interlinked MAP scaffolds are developed using dextranbased microgels of different dimensions and stiffnesses to investigate the dynamic formation of the resulting cellular constructs. Compared to previously reported MAP scaffolds, generated by the chemical interlinking of microgels and subsequent infiltration by cells, the scaffolds designed in this work overcome the limitations to achieve homogeneous cell infiltration into the scaffold and eliminate the need for engineering voids in-between the microgels. In addition to the mesoporous nature of dex-MA microgels, the macroporous structure of scaffolds in our approach is generated by cells themselves and does not require man-made constraint networks, which contradict the natural dynamics of cells. The shape and volume of the MAP scaffolds can be further varied from spherical to oval to triangular by adjusting the cell/microgel ratio and microgel stiffness. The resulting shape is shown to be highly dependent on the cell number relative to the number of microgels and the microgel stiffness since a higher number of cells is able to integrate more microgels into the scaffold. Thereby, stiffer microgels seem to increase both cell-material and cell-cell interactions. This is in agreement with the fact that the microgels need to present RGD on their surface to enable cell-microgel interactions, which generate the required forces needed for the cells to move the microgels and build their house. Stiffer microgels can also enhance cell proliferation, leading to more cell-cell contacts. Additionally, the desired shape of the resulting constructs can be pre-defined by the use of templates without

interference of the natural scaffold formation process. This demonstrates that the intrinsic cellular self-organization can be complemented by external guiding cues to control cell-driven scaffold formation and might ultimately provide a platform to build more advanced, organoid-like *in vitro* model systems by controlling stem cell self-organization in a reproducible manner. As the microgels enable the diffusion of nutrients and oxygen, millimeter-sized tissue constructs can be produced.

6.4 Materials and Methods

6.4.1 Microfluidic Synthesis of dex-MA Microgels

Dex-MA microgels are synthesized by Selin Bulut, Michelle Bund and Christina Haats as described in our publication, which is adapted from previously reported methods. $^{233, 238}$ Briefly, water in oil droplets are obtained with a self-made microfluidic device with a channel height of 80 µm. Different amounts of dex-MA (50, 100 and 200 g/L) are dissolved in water with 10 g/L LAP and used as the aqueous phase, which is filled into a glass syringe (Hamilton 1000 GASTIGHT). The syringes are mounted on syringe pumps (11 Elite Microfluidic Programmable Syringe Pump, Harvard Apparatus), which controls the flow rates. The flow rates for the aqueous phase and the continuous phase (FluoSurf) are 200 and 600 µL/h, respectively. The microgels are collected in Eppendorf tubes with a concentration set to 1.5 g/L. Microgels are purified by exchanging the supernatant of the microgel suspension with fluorinated oil (3×), followed by hexane (1×), water (3×) and PBS (5×).

6.4.2 Functionalization of dex-MA Microgels

The supernatant of the microgel suspension is discarded and the microgels are resuspended in a solution of 96.2 μ L DMEM and 3.8 μ L of an aqueous GRGDSPC solution (CPC Scientific, 25 mg/mL). The suspension is stored overnight at 4 °C to allow for thiol-Michael addition between the cysteine groups of GRGDPSC and the remaining acrylate groups of the microgels. An analogous procedure is performed for microgel functionalization with L-cysteine as a control experiment.

6.4.3 Cell Culture

Normal human dermal fibroblasts (NHDFs, Promocell) are cultured in tissue culture flasks with Dulbecco's modified Eagle medium (DMEM, Gibco) supplemented with 10% fetal calf serum (FCS, Biowest) and 1% ABM up to passage 8. Cell-induced interlinked MAP scaffolds are formed by mixing 100 µL of dex-MA microgels (1.5 mg/mL) and 100 µL cell suspension with concentrations ranging from 200 000-500 000 NHDFs/0.1 mL in 96-well plates. To prevent cell attachment to the well surface, the wells are coated with PDMS and cured by heating at 60 °C for 4 h prior to scaffolds formation. The medium is exchanged every 2-3 days.

6.4.4 Metabolic Cell Activity Assay

To assess the metabolic cell activity in MAP scaffolds, a resazurin-based alamarBlue[™] (Invitrogen) assay is performed after 3, 5 and 7 days of culture. The MAP scaffolds are incubated for 2 h at 37 °C and 5% CO₂ with the reagent that is 1:10 diluted in DMEM supplemented with 10% FCS and 1% ABM. The fluorescence intensity is measured using a BioTek Synergy HT plate reader with an excitation wavelength of 530 nm and an emission wavelength of 590 nm.

6.4.5 Live/Dead Staining of MAP Scaffolds

To assess the viability of cells in MAP scaffolds, live/dead staining is performed after 7 days of culture using a LIVE/DEAD Cell Imaging Kit (Invitrogen). MAP scaffolds are incubated with live (488/515 nm)/dead (570/602 nm) reagent, diluted in DMEM supplemented with 10% FCS and 1% ABM to create a 1x working solution, for 15 min at RT.

6.4.6 Immunofluorescence Staining

After 7 days of culture, the culture medium is removed from the samples, followed by washing with PBS for 10 min and fixation with 4% paraformaldehyde solution (PFA, AppliChem) for 30 min at RT. After washing twice with PBS, the samples are incubated with 0.1% Triton X-100 (Sigma-Aldrich) solution in PBS for 10 min for cell membrane permeabilization, followed by washing with PBS for 10 min. Afterwards, the cells are blocked by incubation with 4% bovine serum albumin (BSA, SEQENS) in PBS for 2 h. For F-actin staining, the samples are incubated with Phalloidin-iFluor 488 (abcam, 1:1000) in PBS for 1 h at RT and subsequently washed twice with PBS to remove the remaining staining reagent. Additionally, the samples are incubated with DAPI (1:200) in PBS for 20 min at RT to stain the nuclei and the microgels. After washing twice with PBS, the samples are stored in PBS at 4 °C prior to confocal imaging.

6.4.7 Confocal Imaging and Image Analysis

The scaffold are imaged using a PerkinElmer Opera Phenix Plus with a 10×/NA 0.3 air objective or a 20×/NA 1.0 water immersion objective. Z-stacks with a z-gap of 7.4 µm (10× objective) or 0.8 µm (20× objective) are recorded of each sample. For quantification, the obtained z-stacks are converted to imaris file format using the Imaris File Converter 9.91 and subsequently stitched together with the Imaris Stitcher. The resulting images are analyzed with the Imaris 10.0 software (Oxford instruments) by creating 3D volume renderings of the F-actin stained structures as well as DAPI stained microgels, using the surface rendering module with individually selected thresholds (**Figure 6.9**). To exclude DAPI stained nuclei, structures with a voxel number of < 1000 are not counted. To investigate the influence of cell/microgel ratios and the microgel stiffness on the resulting scaffold, the scaffold area, volume and bounding box OO length are determined and compared. The cell volume fraction is quantified as the F-actin (cell) volume fraction of the total construct volume, which is the sum of microgel and cell volume.

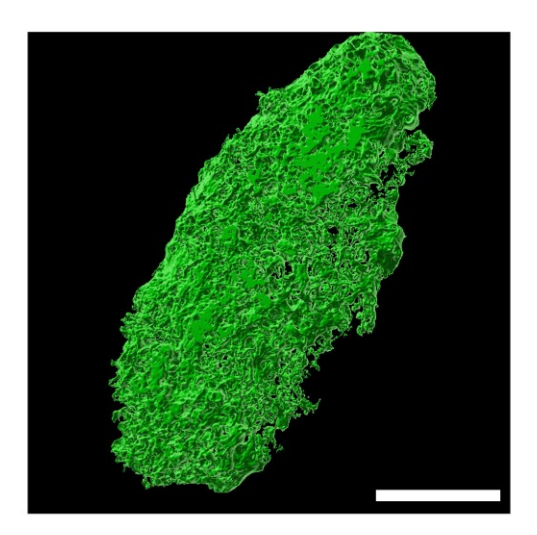


Figure 6.9: 3D volume rendered structure of the F-actin signal in Imaris based on z-stack confocal microscopy images. Scale bar: 1 mm.

6.4.8 Rheological Characterization of MAP Scaffolds

For rheological measurements, a Discovery HR-3 hybrid rheometer with a flat 20 mm Peltier plate is used. The cell-induced interlinked MAP scaffolds are placed on the rheometer plate and 74 μ L Milli-Q water are added. Time-dependent measurements are performed for 5 min at a frequency of 0.5 Hz, an oscillation strain of 2%, and a gap size of 100 μ m with triplicates per condition.

6.4.9 Statistical Analysis

Each experiment is performed with $n \ge 3$. Statistical analysis of the data is conducted in OriginPro 2022 using a one-way ANOVA. Pair comparisons are performed using Tukey's method, where p-values below 0.05 are considered as significant differences (*p < 0.05; **p < 0.01; ***p < 0.001).

7 References

1. Nordham, K. D.; Ninokawa, S., The history of organ transplantation. *Baylor University Medical Center Proceedings* **2022**, *35* (1), 124-128.

- 2. Pilch, N. A.; Bowman, L. J.; Taber, D. J., Immunosuppression trends in solid organ transplantation: The future of individualization, monitoring, and management. *Pharmacotherapy: The Journal of Human Pharmacology and Drug Therapy* **2021**, *41* (1), 119-131.
- 3. Abouna, G. M., Organ Shortage Crisis: Problems and Possible Solutions. *Transplantation Proceedings* **2008**, *40* (1), 34-38.
- 4. Lancet, T., Organ donation: lessons from the Spanish model. *The Lancet* **2024**, *404* (10459), 1171.
- 5. Lewis, A.; Koukoura, A.; Tsianos, G.-I.; Gargavanis, A. A.; Nielsen, A. A.; Vassiliadis, E., Organ donation in the US and Europe: The supply vs demand imbalance. *Transplantation Reviews* **2021**, *35* (2), 100585.
- 6. Brouillette, M., Can designer pigs solve the organ shortage? *Lab Animal* **2024,** *5*3 (10), 259-262.
- 7. Vacanti, J. P., Beyond Transplantation: Third Annual Samuel Jason Mixter Lecture. *Archives of Surgery* **1988**, *123* (5), 545-549.
- 8. Langer, R.; Vacanti, J. P., Tissue Engineering. *Science* **1993**, *260* (5110), 920-926.
- 9. Peneda Pacheco, D.; Suárez Vargas, N.; Visentin, S.; Petrini, P., From tissue engineering to engineering tissues: the role and application of in vitro models. *Biomaterials Science* **2021**, *9* (1), 70-83.
- 10. Sun, D.; Gao, W.; Hu, H.; Zhou, S., Why 90% of clinical drug development fails and how to improve it? *Acta Pharmaceutica Sinica B* **2022**, *12* (7), 3049-3062.
- 11. Owens, R. M., Advanced tissue engineering for in vitro drug safety testing. *MRS Communications* **2023**, *13* (5), 685-694.
- 12. Fong, E. L. S.; Toh, T. B.; Yu, H.; Chow, E. K., 3D Culture as a Clinically Relevant Model for Personalized Medicine. *SLAS Technol* **2017**, *22* (3), 245-253.
- 13. Afewerki, S.; Stocco, T. D.; Rosa da Silva, A. D.; Aguiar Furtado, A. S.; Fernandes de Sousa, G.; Ruiz-Esparza, G. U.; Webster, T. J.; Marciano,

F. R.; Strømme, M.; Zhang, Y. S.; Lobo, A. O., In vitro high-content tissue models to address precision medicine challenges. *Molecular Aspects of Medicine* **2023**, *91*, 101108.

- 14. Rawe, J., What Will Be the 10 Hottest Jobs? *Time Magazine* 2000.
- Cao, Y.; Vacanti, J. P.; Paige, K. T.; Upton, J.; Vacanti, C. A., Transplantation of Chondrocytes Utilizing a Polymer-Cell Construct to Produce Tissue-Engineered Cartilage in the Shape of a Human Ear. *Plastic* and Reconstructive Surgery 1997, 100 (2), 297-302.
- 16. Eaglstein, W. H.; Iriondo, M.; Laszlo, K., A Composite Skin Substitute (Graftskin) for Surgical Wounds: A Clinical Experience. *Dermatologic Surgery* **1995**, *21* (10), 839-843.
- 17. Trent, J.; Kirsner, R., Tissue Engineered Skin: Apligraf, A Bi-Layered Living Skin Equivalent. *International Journal of Clinical Practice* **1998,** *52* (6), 408-413.
- Oerlemans, A. J. M.; van Hoek, M. E. C.; van Leeuwen, E.; Dekkers, W. J. M., Hype and Expectations in Tissue Engineering. *Regenerative Medicine* 2014, 9 (1), 113-122.
- 19. Berthiaume, F.; Maguire, T. J.; Yarmush, M. L., Tissue Engineering and Regenerative Medicine: History, Progress, and Challenges. *Annual Review of Chemical and Biomolecular Engineering* **2011**, *2* (Volume 2, 2011), 403-430.
- 20. Ikada, Y., Challenges in tissue engineering. *Journal of The Royal Society Interface* **2006**, *3* (10), 589-601.
- 21. Devillard, C. D.; Marquette, C. A., Vascular Tissue Engineering: Challenges and Requirements for an Ideal Large Scale Blood Vessel. *Frontiers in Bioengineering and Biotechnology* **2021**, *9*.
- 22. Tsang, M.; Gantchev, J.; Ghazawi, F. M.; Litvinov, I. V., Protocol for Adhesion and Immunostaining of Lymphocytes and Other Non-Adherent Cells in Culture. *BioTechniques* **2017**, *63* (5), 230-233.
- 23. Lerman, M. J.; Lembong, J.; Muramoto, S.; Gillen, G.; Fisher, J. P., The Evolution of Polystyrene as a Cell Culture Material. *Tissue Engineering Part B: Reviews* **2018**, *24* (5), 359-372.
- 24. Segeritz, C.-P.; Vallier, L., Chapter 9 Cell Culture: Growing Cells as Model Systems In Vitro. In *Basic Science Methods for Clinical Researchers*, Jalali,

M.; Saldanha, F. Y. L.; Jalali, M., Eds. Academic Press: Boston, 2017; pp 151-172.

- 25. Leopold, B.; Strutz, J.; Weiß, E.; Gindlhuber, J.; Birner-Gruenberger, R.; Hackl, H.; Appel, H. M.; Cvitic, S.; Hiden, U., Outgrowth, proliferation, viability, angiogenesis and phenotype of primary human endothelial cells in different purchasable endothelial culture media: feed wisely. *Histochemistry and Cell Biology* 2019, 152 (5), 377-390.
- 26. Antoni, D.; Burckel, H.; Josset, E.; Noel, G., Three-dimensional cell culture: a breakthrough in vivo. *Int J Mol Sci* **2015**, *16* (3), 5517-27.
- Cardoso, B. D.; Castanheira, E. M. S.; Lanceros-Méndez, S.; Cardoso, V. F., Recent Advances on Cell Culture Platforms for In Vitro Drug Screening and Cell Therapies: From Conventional to Microfluidic Strategies. *Advanced Healthcare Materials* 2023, 12 (18), 2202936.
- 28. Bouchalova, P.; Bouchal, P., Current methods for studying metastatic potential of tumor cells. *Cancer Cell International* **2022**, *22* (1), 394.
- 29. Jensen, C.; Teng, Y., Is It Time to Start Transitioning From 2D to 3D Cell Culture? *Frontiers in Molecular Biosciences* **2020**, *7* (33), 33.
- 30. Hutchinson, L.; Kirk, R., High drug attrition rates—where are we going wrong? *Nature Reviews Clinical Oncology* **2011**, *8* (4), 189-190.
- Costa, E. C.; Moreira, A. F.; de Melo-Diogo, D.; Gaspar, V. M.; Carvalho, M. P.; Correia, I. J., 3D tumor spheroids: an overview on the tools and techniques used for their analysis. *Biotechnology Advances* 2016, 34 (8), 1427-1441.
- 32. Białkowska, K.; Komorowski, P.; Bryszewska, M.; Miłowska, K., Spheroids as a Type of Three-Dimensional Cell Cultures—Examples of Methods of Preparation and the Most Important Application. *International Journal of Molecular Sciences* **2020**, *21* (17), 6225.
- 33. Di Caprio, N.; Burdick, J. A., Engineered biomaterials to guide spheroid formation, function, and fabrication into 3D tissue constructs. *Acta Biomaterialia* **2023**, *165*, 4-18.
- 34. Cui, X.; Hartanto, Y.; Zhang, H., Advances in multicellular spheroids formation. *Journal of The Royal Society Interface* **2017**, *14* (127), 20160877.

35. Kim, S.-j.; Kim, E. M.; Yamamoto, M.; Park, H.; Shin, H., Engineering Multi-Cellular Spheroids for Tissue Engineering and Regenerative Medicine. *Advanced Healthcare Materials* **2020**, *9* (23), 2000608.

- 36. Jeong, Y.; Tin, A.; Irudayaraj, J., Flipped Well-Plate Hanging-Drop Technique for Growing Three-Dimensional Tumors. *Frontiers in Bioengineering and Biotechnology* **2022**, *10*.
- 37. Bornstein, S.; Shapiro, I.; Malyukov, M.; Züllig, R.; Luca, E.; Gelfgat, E.; Beuschlein, F.; Nölting, S.; Berruti, A.; Sigala, S.; Peitzsch, M.; Steenblock, C.; Ludwig, B.; Kugelmeier, P.; Hantel, C., Innovative multidimensional models in a high-throughput-format for different cell types of endocrine origin. *Cell Death & Disease* **2022**, *13* (7), 648.
- 38. Zanoni, M.; Piccinini, F.; Arienti, C.; Zamagni, A.; Santi, S.; Polico, R.; Bevilacqua, A.; Tesei, A., 3D tumor spheroid models for in vitro therapeutic screening: a systematic approach to enhance the biological relevance of data obtained. *Scientific Reports* **2016**, *6* (1), 19103.
- Ascione, F.; Ferraro, R.; Dogra, P.; Cristini, V.; Guido, S.; Caserta, S., Gradient-induced instability in tumour spheroids unveils the impact of microenvironmental nutrient changes. *Scientific Reports* 2024, 14 (1), 20837.
- Langan, L. M.; Dodd, N. J. F.; Owen, S. F.; Purcell, W. M.; Jackson, S. K.; Jha, A. N., Direct Measurements of Oxygen Gradients in Spheroid Culture System Using Electron Parametric Resonance Oximetry. *PLOS ONE* 2016, 11 (2), e0149492.
- 41. Kirsh, S. M.; Pascetta, S. A.; Uniacke, J., Spheroids as a 3D Model of the Hypoxic Tumor Microenvironment. In *The Tumor Microenvironment: Methods and Protocols*, Ursini-Siegel, J., Ed. Springer US: New York, NY, 2023; pp 273-285.
- 42. Frantz, C.; Stewart, K. M.; Weaver, V. M., The extracellular matrix at a glance. *Journal of Cell Science* **2010**, *123* (24), 4195-4200.
- 43. Järveläinen, H.; Sainio, A.; Koulu, M.; Wight, T. N.; Penttinen, R., Extracellular Matrix Molecules: Potential Targets in Pharmacotherapy. *Pharmacological Reviews* **2009**, *61* (2), 198-223.
- 44. Naba, A., Mechanisms of assembly and remodelling of the extracellular matrix. *Nature Reviews Molecular Cell Biology* **2024**, *25* (11), 865-885.

45. Bandzerewicz, A.; Gadomska-Gajadhur, A., Into the Tissues: Extracellular Matrix and Its Artificial Substitutes: Cell Signalling Mechanisms. *Cells* **2022**, *11* (5), 914.

- 46. Jayadev, R.; Sherwood, D. R., Basement membranes. *Current Biology* **2017**, *27* (6), R207-R211.
- 47. Hallmann, R.; Hannocks, M.-J.; Song, J.; Zhang, X.; Di Russo, J.; Luik, A.-L.; Burmeister, M.; Gerwien, H.; Sorokin, L., The role of basement membrane laminins in vascular function. *The International Journal of Biochemistry & Cell Biology* **2020**, *127*, 105823.
- 48. Leclech, C.; Natale, C. F.; Barakat, A. I., The basement membrane as a structured surface role in vascular health and disease. *Journal of Cell Science* **2020**, *133* (18).
- 49. Ruoslahti, E.; Pierschbacher, M. D., New Perspectives in Cell Adhesion: RGD and Integrins. *Science* **1987**, *238* (4826), 491-497.
- 50. Ludwig, B. S.; Kessler, H.; Kossatz, S.; Reuning, U., RGD-Binding Integrins Revisited: How Recently Discovered Functions and Novel Synthetic Ligands (Re-)Shape an Ever-Evolving Field. *Cancers* **2021**, *13* (7), 1711.
- 51. Yamada, K. M.; Sixt, M., Mechanisms of 3D cell migration. *Nature Reviews Molecular Cell Biology* **2019**, *20* (12), 738-752.
- 52. Pally, D.; Naba, A., Extracellular matrix dynamics: A key regulator of cell migration across length-scales and systems. *Current Opinion in Cell Biology* **2024**, *86*, 102309.
- 53. Bonnans, C.; Chou, J.; Werb, Z., Remodelling the extracellular matrix in development and disease. *Nature Reviews Molecular Cell Biology* **2014**, *15* (12), 786-801.
- Knight, E.; Przyborski, S., Advances in 3D cell culture technologies enabling tissue-like structures to be created in vitro. *Journal of Anatomy* 2015, 227 (6), 746-756.
- 55. Park, Y.; Huh, K. M.; Kang, S. W., Applications of Biomaterials in 3D Cell Culture and Contributions of 3D Cell Culture to Drug Development and Basic Biomedical Research. *Int J Mol Sci* **2021**, *22* (5).
- 56. Carletti, E.; Motta, A.; Migliaresi, C., Scaffolds for Tissue Engineering and 3D Cell Culture. In *3D Cell Culture: Methods and Protocols*, Haycock, J. W., Ed. Humana Press: Totowa, NJ, 2011; pp 17-39.

57. Jun, I.; Han, H.-S.; Edwards, J. R.; Jeon, H., Electrospun Fibrous Scaffolds for Tissue Engineering: Viewpoints on Architecture and Fabrication.

International Journal of Molecular Sciences 2018, 19 (3), 745.

- 58. Lutzweiler, G.; Ndreu Halili, A.; Engin Vrana, N., The Overview of Porous, Bioactive Scaffolds as Instructive Biomaterials for Tissue Regeneration and Their Clinical Translation. *Pharmaceutics* **2020**, *12* (7), 602.
- 59. Zauchner, D.; Müller, M. Z.; Horrer, M.; Bissig, L.; Zhao, F.; Fisch, P.; Lee, S. S.; Zenobi-Wong, M.; Müller, R.; Qin, X.-H., Synthetic biodegradable microporous hydrogels for in vitro 3D culture of functional human bone cell networks. *Nature Communications* 2024, 15 (1), 5027.
- 60. Caliari, S. R.; Burdick, J. A., A practical guide to hydrogels for cell culture.

 Nature Methods **2016**, *13* (5), 405-414.
- 61. Tibbitt, M. W.; Anseth, K. S., Hydrogels as extracellular matrix mimics for 3D cell culture. *Biotechnology and Bioengineering* **2009**, *103* (4), 655-663.
- 62. Cao, H.; Duan, L.; Zhang, Y.; Cao, J.; Zhang, K., Current hydrogel advances in physicochemical and biological response-driven biomedical application diversity. *Signal Transduction and Targeted Therapy* **2021**, 6 (1), 426.
- 63. Gyles, D. A.; Castro, L. D.; Silva, J. O. C.; Ribeiro-Costa, R. M., A review of the designs and prominent biomedical advances of natural and synthetic hydrogel formulations. *European Polymer Journal* **2017**, *88*, 373-392.
- 64. Zhang, X.; Chen, X.; Hong, H.; Hu, R.; Liu, J.; Liu, C., Decellularized extracellular matrix scaffolds: Recent trends and emerging strategies in tissue engineering. *Bioactive Materials* **2022**, *10*, 15-31.
- 65. Zhao, L.; Zhou, Y.; Zhang, J.; Liang, H.; Chen, X.; Tan, H., Natural Polymer-Based Hydrogels: From Polymer to Biomedical Applications. *Pharmaceutics* **2023**, *15* (10), 2514.
- 66. Chaudhuri, O., Viscoelastic hydrogels for 3D cell culture. *Biomaterials Science* **2017**, *5* (8), 1480-1490.
- 67. Lee, K. Z.; Jeon, J.; Jiang, B.; Subramani, S. V.; Li, J.; Zhang, F., Protein-Based Hydrogels and Their Biomedical Applications. *Molecules* **2023**, *28* (13), 4988.

68. Ho, T.-C.; Chang, C.-C.; Chan, H.-P.; Chung, T.-W.; Shu, C.-W.; Chuang, K.-P.; Duh, T.-H.; Yang, M.-H.; Tyan, Y.-C., Hydrogels: Properties and Applications in Biomedicine. *Molecules* **2022**, *27* (9), 2902.

- 69. Xu, K. L.; Mauck, R. L.; Burdick, J. A., Modeling development using hydrogels. *Development* **2023**, *150* (13).
- 70. Soliman, B. G.; Nguyen, A. K.; Gooding, J. J.; Kilian, K. A., Advancing Synthetic Hydrogels through Nature-Inspired Materials Chemistry. *Advanced Materials* **2024**, *36* (42), 2404235.
- 71. Duarte, A. C.; Costa, E. C.; Filipe, H. A. L.; Saraiva, S. M.; Jacinto, T.; Miguel, S. P.; Ribeiro, M. P.; Coutinho, P., Animal-derived products in science and current alternatives. *Biomaterials Advances* **2023**, *151*, 213428.
- 72. Hosseinzadeh, B.; Ahmadi, M., Degradable hydrogels: Design mechanisms and versatile applications. *Materials Today Sustainability* **2023**, 23, 100468.
- 73. Unal, A. Z.; West, J. L., Synthetic ECM: Bioactive Synthetic Hydrogels for 3D Tissue Engineering. *Bioconjugate Chemistry* **2020**, *31* (10), 2253-2271.
- 74. Felgueiras, H. P.; Evans, M. D. M.; Migonney, V., Contribution of fibronectin and vitronectin to the adhesion and morphology of MC3T3-E1 osteoblastic cells to poly(NaSS) grafted Ti6Al4V. *Acta Biomaterialia* **2015**, *28*, 225-233.
- 75. Salinas, C. N.; Anseth, K. S., The influence of the RGD peptide motif and its contextual presentation in PEG gels on human mesenchymal stem cell viability. *Journal of Tissue Engineering and Regenerative Medicine* **2008**, 2 (5), 296-304.
- 76. Pan, Z.; Brassart, L., Constitutive modelling of hydrolytic degradation in hydrogels. *Journal of the Mechanics and Physics of Solids* **2022**, *167*, 105016.
- 77. Lutolf, M. P.; Lauer-Fields, J. L.; Schmoekel, H. G.; Metters, A. T.; Weber, F. E.; Fields, G. B.; Hubbell, J. A., Synthetic matrix metalloproteinase-sensitive hydrogels for the conduction of tissue regeneration: Engineering cell-invasion characteristics. *Proceedings of the National Academy of Sciences* **2003**, *100* (9), 5413-5418.
- 78. Chrisnandy, A.; Blondel, D.; Rezakhani, S.; Broguiere, N.; Lutolf, M. P., Synthetic dynamic hydrogels promote degradation-independent in vitro organogenesis. *Nature Materials* **2022**, *21* (4), 479-487.

79. Paneer Selvam, S.; Ayyappan, S.; I Jamir, S.; Sellappan, L. K.; Manoharan, S., Recent advancements of hydroxyapatite and polyethylene glycol (PEG) composites for tissue engineering applications – A comprehensive review. *European Polymer Journal* **2024**, *215*, 113226.

- 80. Zhu, J., Bioactive modification of poly(ethylene glycol) hydrogels for tissue engineering. *Biomaterials* **2010**, *31* (17), 4639-56.
- 81. Padín-González, E.; Lancaster, P.; Bottini, M.; Gasco, P.; Tran, L.; Fadeel, B.; Wilkins, T.; Monopoli, M. P., Understanding the Role and Impact of Poly (Ethylene Glycol) (PEG) on Nanoparticle Formulation: Implications for COVID-19 Vaccines. *Frontiers in Bioengineering and Biotechnology* **2022**, *10*.
- 82. Lin, C.-C.; Anseth, K. S., PEG Hydrogels for the Controlled Release of Biomolecules in Regenerative Medicine. *Pharmaceutical Research* **2009**, 26 (3), 631-643.
- 83. Stanciu, L.; Diaz-Amaya, S., Chapter 5 Polymeric biomaterials. In *Introductory Biomaterials*, Stanciu, L.; Diaz-Amaya, S., Eds. Academic Press: Boston, 2022; pp 77-123.
- 84. Elbert, D. L.; Hubbell, J. A., Conjugate Addition Reactions Combined with Free-Radical Cross-Linking for the Design of Materials for Tissue Engineering. *Biomacromolecules* **2001**, *2* (2), 430-441.
- 85. Sabnis, A.; Rahimi, M.; Chapman, C.; Nguyen, K. T., Cytocompatibility studies of an in situ photopolymerized thermoresponsive hydrogel nanoparticle system using human aortic smooth muscle cells. *Journal of Biomedical Materials Research Part A* **2009**, *91A* (1), 52-59.
- 86. Nair, D. P.; Podgórski, M.; Chatani, S.; Gong, T.; Xi, W.; Fenoli, C. R.; Bowman, C. N., The Thiol-Michael Addition Click Reaction: A Powerful and Widely Used Tool in Materials Chemistry. *Chemistry of Materials* **2014**, *26* (1), 724-744.
- 87. Lowe, A. B., Thiol-ene "click" reactions and recent applications in polymer and materials synthesis. *Polymer Chemistry* **2010**, *1* (1), 17-36.
- 88. Gennari, A.; Wedgwood, J.; Lallana, E.; Francini, N.; Tirelli, N., Thiolbased michael-type addition. A systematic evaluation of its controlling factors. *Tetrahedron* **2020**, *76* (47), 131637.

89. Laidler, K. J., The development of the Arrhenius equation. *Journal of Chemical Education* **1984**, *61* (6), 494.

- 90. Gillette, B. M.; Rossen, N. S.; Das, N.; Leong, D.; Wang, M.; Dugar, A.; Sia, S. K., Engineering extracellular matrix structure in 3D multiphase tissues. *Biomaterials* **2011**, *32* (32), 8067-76.
- 91. Rose, J. C.; De Laporte, L., Hierarchical Design of Tissue Regenerative Constructs. *Advanced Healthcare Materials* **2018**, *7* (6), 1701067.
- 92. Gerardo-Nava, J. L.; Jansen, J.; Günther, D.; Klasen, L.; Thiebes, A. L.; Niessing, B.; Bergerbit, C.; Meyer, A. A.; Linkhorst, J.; Barth, M.; Akhyari, P.; Stingl, J.; Nagel, S.; Stiehl, T.; Lampert, A.; Leube, R.; Wessling, M.; Santoro, F.; Ingebrandt, S.; Jockenhoevel, S.; Herrmann, A.; Fischer, H.; Wagner, W.; Schmitt, R. H.; Kiessling, F.; Kramann, R.; De Laporte, L., Transformative Materials to Create 3D Functional Human Tissue Models In Vitro in a Reproducible Manner. Advanced Healthcare Materials 2023, 12 (20), 2301030.
- Suhail, S.; Sardashti, N.; Jaiswal, D.; Rudraiah, S.; Misra, M.; Kumbar, S.
 G., Engineered Skin Tissue Equivalents for Product Evaluation and Therapeutic Applications. *Biotechnology Journal* 2019, 14 (7), 1900022.
- 94. Rose, J. C.; Cámara-Torres, M.; Rahimi, K.; Köhler, J.; Möller, M.; De Laporte, L., Nerve Cells Decide to Orient inside an Injectable Hydrogel with Minimal Structural Guidance. *Nano Letters* **2017**, *17* (6), 3782-3791.
- 95. Valls-Margarit, M.; Iglesias-García, O.; Di Guglielmo, C.; Sarlabous, L.; Tadevosyan, K.; Paoli, R.; Comelles, J.; Blanco-Almazán, D.; Jiménez-Delgado, S.; Castillo-Fernández, O.; Samitier, J.; Jané, R.; Martínez, E.; Raya, Á., Engineered Macroscale Cardiac Constructs Elicit Human Myocardial Tissue-like Functionality. Stem Cell Reports 2019, 13 (1), 207-220.
- 96. Brassard, J. A.; Nikolaev, M.; Hübscher, T.; Hofer, M.; Lutolf, M. P., Recapitulating macro-scale tissue self-organization through organoid bioprinting. *Nature Materials* **2021**, *20* (1), 22-29.
- 97. Groll, J.; Boland, T.; Blunk, T.; Burdick, J. A.; Cho, D.-W.; Dalton, P. D.; Derby, B.; Forgacs, G.; Li, Q.; Mironov, V. A.; Moroni, L.; Nakamura, M.; Shu, W.; Takeuchi, S.; Vozzi, G.; Woodfield, T. B. F.; Xu, T.; Yoo, J. J.;

Malda, J., Biofabrication: reappraising the definition of an evolving field. *Biofabrication* **2016**, *8* (1), 013001.

- 98. Moroni, L.; Boland, T.; Burdick, J. A.; De Maria, C.; Derby, B.; Forgacs, G.; Groll, J.; Li, Q.; Malda, J.; Mironov, V. A.; Mota, C.; Nakamura, M.; Shu, W.; Takeuchi, S.; Woodfield, T. B. F.; Xu, T.; Yoo, J. J.; Vozzi, G., Biofabrication: A Guide to Technology and Terminology. *Trends in Biotechnology* **2018**, *36* (4), 384-402.
- 99. Moroni, L.; Burdick, J. A.; Highley, C.; Lee, S. J.; Morimoto, Y.; Takeuchi, S.; Yoo, J. J., Biofabrication strategies for 3D in vitro models and regenerative medicine. *Nature Reviews Materials* **2018**, *3* (5), 21-37.
- 100. Lee, K. Y.; Mooney, D. J., Hydrogels for Tissue Engineering. *Chemical Reviews* **2001**, *101* (7), 1869-1880.
- 101. Ohya, Y., 2.3 Injectable Hydrogels. In *Biomaterials Nanoarchitectonics*, Ebara, M., Ed. William Andrew Publishing: 2016; pp 41-57.
- 102. Ouyang, L.; Armstrong, J. P. K.; Chen, Q.; Lin, Y.; Stevens, M. M., Void-Free 3D Bioprinting for In Situ Endothelialization and Microfluidic Perfusion.
 Advanced Functional Materials 2020, 30 (1), 1908349.
- Malda, J.; Visser, J.; Melchels, F. P.; Jüngst, T.; Hennink, W. E.; Dhert,
 W. J. A.; Groll, J.; Hutmacher, D. W., 25th Anniversary Article: Engineering
 Hydrogels for Biofabrication. *Advanced Materials* 2013, 25 (36), 5011-5028.
- 104. Godau, B.; Stefanek, E.; Gharaie, S. S.; Amereh, M.; Pagan, E.; Marvdashti, Z.; Libert-Scott, E.; Ahadian, S.; Akbari, M., Non-destructive mechanical assessment for optimization of 3D bioprinted soft tissue scaffolds. *iScience* **2022**, *25* (5), 104251.
- 105. Skylar-Scott, M. A.; Uzel, S. G. M.; Nam, L. L.; Ahrens, J. H.; Truby, R. L.; Damaraju, S.; Lewis, J. A., Biomanufacturing of organ-specific tissues with high cellular density and embedded vascular channels. *Science Advances* 2019, 5 (9), eaaw2459.
- 106. Jain, R. K.; Au, P.; Tam, J.; Duda, D. G.; Fukumura, D., Engineering vascularized tissue. *Nature Biotechnology* **2005**, *23* (7), 821-823.
- 107. Vascular cells of blood vessels and organs across the human body. *Nature Medicine* **2024**, *30* (12), 3431-3432.
- 108. Marziano, C.; Genet, G.; Hirschi, K. K., Vascular endothelial cell specification in health and disease. *Angiogenesis* **2021**, *24* (2), 213-236.

109. Kovacic, J. C.; Boehm, M., Resident vascular progenitor cells: An emerging role for non-terminally differentiated vessel-resident cells in vascular biology. *Stem Cell Research* **2009**, *2* (1), 2-15.

- 110. Risau, W.; Flamme, I., Vasculogenesis. *Annual Review of Cell and Developmental Biology* **1995**, *11* (Volume 11, 1995), 73-91.
- 111. Goldie, L. C.; Nix, M. K.; Hirschi, K. K., Embryonic vasculogenesis and hematopoietic specification. *Organogenesis* **2008**, *4* (4), 257-263.
- 112. Carmeliet, P., Mechanisms of angiogenesis and arteriogenesis. *Nature Medicine* **2000**, *6* (4), 389-395.
- 113. Clapp, C.; Thebault, S.; Jeziorski, M. C.; Martínez De La Escalera, G., Peptide Hormone Regulation of Angiogenesis. *Physiological Reviews* 2009, 89 (4), 1177-1215.
- 114. Carmeliet, P.; Jain, R. K., Molecular mechanisms and clinical applications of angiogenesis. *Nature* **2011**, *473* (7347), 298-307.
- 115. Levenberg, S.; Rouwkema, J.; Macdonald, M.; Garfein, E. S.; Kohane, D. S.; Darland, D. C.; Marini, R.; van Blitterswijk, C. A.; Mulligan, R. C.; D'Amore, P. A.; Langer, R., Engineering vascularized skeletal muscle tissue. *Nature Biotechnology* 2005, 23 (7), 879-884.
- 116. Brown, A.; He, H.; Trumper, E.; Valdez, J.; Hammond, P.; Griffith, L. G., Engineering PEG-based hydrogels to foster efficient endothelial network formation in free-swelling and confined microenvironments. *Biomaterials* **2020**, *243*, 119921.
- 117. Hoch, E.; Tovar, G. E. M.; Borchers, K., Bioprinting of artificial blood vessels: current approaches towards a demanding goal. *European Journal of Cardio-Thoracic Surgery* **2014**, *46* (5), 767-778.
- 118. Elefteriades, J. A.; Ziganshin, B. A.; Rizzo, J. A.; Fang, H.; Tranquilli, M.; Paruchuri, V.; Kuzmik, G.; Gubernikoff, G.; Dumfarth, J.; Charilaou, P.; Theodoropoulos, P., Indications and imaging for aortic surgery: Size and other matters. *The Journal of Thoracic and Cardiovascular Surgery* **2015**, *149* (2, Supplement), S10-S13.
- 119. Aird, W. C., Spatial and temporal dynamics of the endothelium. *Journal of Thrombosis and Haemostasis* **2005**, 3 (7), 1392-1406.

120. Claesson-Welsh, L.; Dejana, E.; McDonald, D. M., Permeability of the Endothelial Barrier: Identifying and Reconciling Controversies. *Trends in Molecular Medicine* **2021**, *27* (4), 314-331.

- 121. Qu, J.; Wang, L.; Li, Y.; Li, X., Liver sinusoidal endothelial cell: An important yet often overlooked player in the liver fibrosis. *Clin Mol Hepatol* **2024**, *30* (3), 303-325.
- 122. Witter, K.; Tonar, Z.; Schöpper, H., How many Layers has the Adventitia?
 Structure of the Arterial Tunica Externa Revisited. *Anatomia, Histologia, Embryologia* 2017, 46 (2), 110-120.
- 123. Halper, J., Chapter Four Basic Components of Vascular Connective Tissue and Extracellular Matrix. In *Advances in Pharmacology*, Khalil, R. A., Ed. Academic Press: 2018; Vol. 81, pp 95-127.
- 124. Echeverria Molina, M. I.; Malollari, K. G.; Komvopoulos, K., Design Challenges in Polymeric Scaffolds for Tissue Engineering. *Frontiers in Bioengineering and Biotechnology* **2021**, 9.
- 125. Kämmerling, L.; Fisher, L. E.; Antmen, E.; Simsek, G. M.; Rostam, H. M.; Vrana, N. E.; Ghaemmaghami, A. M., Mitigating the foreign body response through 'immune-instructive' biomaterials. *Journal of Immunology and Regenerative Medicine* **2021**, *12*, 100040.
- 126. Wolf, M. T.; Dearth, C. L.; Ranallo, C. A.; LoPresti, S. T.; Carey, L. E.; Daly, K. A.; Brown, B. N.; Badylak, S. F., Macrophage polarization in response to ECM coated polypropylene mesh. *Biomaterials* 2014, 35 (25), 6838-6849.
- 127. Labow, R. S.; Meek, E.; Santerre, J. P., Hydrolytic degradation of poly(carbonate)-urethanes by monocyte-derived macrophages. *Biomaterials* **2001**, *22* (22), 3025-3033.
- 128. Carnicer-Lombarte, A.; Chen, S.-T.; Malliaras, G. G.; Barone, D. G., Foreign Body Reaction to Implanted Biomaterials and Its Impact in Nerve Neuroprosthetics. *Frontiers in Bioengineering and Biotechnology* **2021**, 9.
- 129. Tripathi, A. S.; Zaki, M. E. A.; Al-Hussain, S. A.; Dubey, B. K.; Singh, P.; Rind, L.; Yadav, R. K., Material matters: exploring the interplay between natural biomaterials and host immune system. *Frontiers in Immunology* **2023**, *14*.

130. Food and Drug Administration, Medical Devices Containing Materials

Derived from Animal Sources (Except for In Vitro Diagnostic Devices). In

FDA-2013-D-1574, Health, Ed. 2019.

- 131. Mazio, C.; Casale, C.; Imparato, G.; Urciuolo, F.; Attanasio, C.; De Gregorio, M.; Rescigno, F.; Netti, P. A., Pre-vascularized dermis model for fast and functional anastomosis with host vasculature. *Biomaterials* **2019**, *192*, 159-170.
- 132. Quizon, M. J.; Deppen, J. N.; Barber, G. F.; Kalelkar, P. P.; Coronel, M. M.; Levit, R. D.; Garcia, A. J., VEGF-delivering PEG hydrogels promote vascularization in the porcine subcutaneous space. *Journal of Biomedical Materials Research Part A* 2024, 112 (6), 866-880.
- 133. Mndlovu, H.; Kumar, P.; du Toit, L. C.; Choonara, Y. E., A review of biomaterial degradation assessment approaches employed in the biomedical field. *npj Materials Degradation* **2024**, *8* (1), 66.
- 134. Holloway, J. L.; Ma, H.; Rai, R.; Burdick, J. A., Modulating hydrogel crosslink density and degradation to control bone morphogenetic protein delivery and in vivo bone formation. *Journal of Controlled Release* **2014**, *191*, 63-70.
- 135. Berkovitch, Y.; Seliktar, D., Semi-synthetic hydrogel composition and stiffness regulate neuronal morphogenesis. *International Journal of Pharmaceutics* **2017**, *523* (2), 545-555.
- 136. Pérez-Neri, I.; González-Aguilar, A.; Sandoval, H.; Pineda, C.; Ríos, C., Potential Goals, Challenges, and Safety of Focused Ultrasound Application for Central Nervous System Disorders. *Curr Neuropharmacol* 2022, 20 (10), 1807-1810.
- 137. Arulpragasam, A. R.; van 't Wout-Frank, M.; Barredo, J.; Faucher, C. R.; Greenberg, B. D.; Philip, N. S., Low Intensity Focused Ultrasound for Non-invasive and Reversible Deep Brain Neuromodulation—A Paradigm Shift in Psychiatric Research. *Frontiers in Psychiatry* **2022**, *13*.
- 138. Shi, Z.; Wu, J.; Song, Q.; Göstl, R.; Herrmann, A., Toward Drug Release Using Polymer Mechanochemical Disulfide Scission. *Journal of the American Chemical Society* **2020**, *142* (34), 14725-14732.
- 139. Zhang, X.; Li, Y.; He, D.; Ma, Z.; Liu, K.; Xue, K.; Li, H., An effective strategy for preparing macroporous and self-healing bioactive hydrogels for

cell delivery and wound healing. *Chemical Engineering Journal* **2021,** *425*, 130677.

- 140. Li, Z.; Yang, B.; Yang, Z.; Xie, X.; Guo, Z.; Zhao, J.; Wang, R.; Fu, H.; Zhao, P.; Zhao, X.; Chen, G.; Li, G.; Wei, F.; Bian, L., Supramolecular Hydrogel with Ultra-Rapid Cell-Mediated Network Adaptation for Enhancing Cellular Metabolic Energetics and Tissue Regeneration. *Advanced Materials* 2024, 36 (15), 2307176.
- 141. Handler, K.; Bach, K.; Borrelli, C.; Piscuoglio, S.; Ficht, X.; Acar, I. E.; Moor, A. E., Fragment-sequencing unveils local tissue microenvironments at single-cell resolution. *Nature Communications* **2023**, *14* (1), 7775.
- 142. Gehlen, D. B.; Jürgens, N.; Omidinia-Anarkoli, A.; Haraszti, T.; George, J.; Walther, A.; Ye, H.; De Laporte, L., Granular Cellulose Nanofibril Hydrogel Scaffolds for 3D Cell Cultivation. *Macromolecular Rapid Communications* 2020, 41 (18), 2000191.
- 143. Griffin, D. R.; Weaver, W. M.; Scumpia, P. O.; Di Carlo, D.; Segura, T., Accelerated wound healing by injectable microporous gel scaffolds assembled from annealed building blocks. *Nature Materials* **2015**, *14* (7), 737-744.
- 144. Karsenti, E., Self-organization in cell biology: a brief history. *Nature Reviews Molecular Cell Biology* **2008**, 9 (3), 255-262.
- Marsee, A.; Roos, F. J. M.; Verstegen, M. M. A.; Marsee, A.; Roos, F.; Verstegen, M.; Clevers, H.; Vallier, L.; Takebe, T.; Huch, M.; Peng, W. C.; Forbes, S.; Lemaigre, F.; de Koning, E.; Gehart, H.; van der Laan, L.; Spee, B.; Boj, S.; Baptista, P.; Schneeberger, K.; Soroka, C.; Heim, M.; Nuciforo, S.; Zaret, K.; Saito, Y.; Lutolf, M.; Cardinale, V.; Simons, B.; van Ijzendoorn, S.; Kamiya, A.; Chikada, H.; Wang, S.; Mun, S. J.; Son, M. J.; Onder, T. T.; Boyer, J.; Sato, T.; Georgakopoulos, N.; Meneses, A.; Broutier, L.; Boulter, L.; Grün, D.; Ijzermans, J.; Artegiani, B.; van Boxtel, R.; Kuijk, E.; Carpino, G.; Peltz, G.; Banales, J.; Man, N.; Aloia, L.; LaRusso, N.; George, G.; Rimland, C.; Yeoh, G.; Grappin-Botton, A.; Stange, D.; Prior, N.; Tirnitz-Parker, J. E. E.; Andersson, E.; Braconi, C.; Hannan, N.; Lu, W.-Y.; Strom, S.; Sancho-Bru, P.; Ogawa, S.; Corbo, V.; Lancaster, M.; Hu, H.; Fuchs, S.; Hendriks, D.; Gehart, H.; de Koning, E.; Lemaigre, F.; Forbes, S. J.; Peng, W. C.; Huch, M.; Takebe, T.;

Vallier, L.; Clevers, H.; van der Laan, L. J. W.; Spee, B., Building consensus on definition and nomenclature of hepatic, pancreatic, and biliary organoids. *Cell Stem Cell* **2021**, *28* (5), 816-832.

- Jensen, K. B.; Little, M. H., Organoids are not organs: Sources of variation and misinformation in **a0; organoid biology. Stem Cell Reports 2023, 18 (6), 1255-1270.
- 147. Zustiak, S. P.; Leach, J. B., Hydrolytically Degradable Poly(Ethylene Glycol) Hydrogel Scaffolds with Tunable Degradation and Mechanical Properties. Biomacromolecules 2010, 11 (5), 1348-1357.
- 148. Neumann, A. J.; Quinn, T.; Bryant, S. J., Nondestructive evaluation of a new hydrolytically degradable and photo-clickable PEG hydrogel for cartilage tissue engineering. *Acta Biomaterialia* **2016**, *39*, 1-11.
- 149. Gjorevski, N.; Sachs, N.; Manfrin, A.; Giger, S.; Bragina, M. E.; Ordóñez-Morán, P.; Clevers, H.; Lutolf, M. P., Designer matrices for intestinal stem cell and organoid culture. *Nature* **2016**, *539* (7630), 560-564.
- 150. Patterson, J.; Hubbell, J. A., Enhanced proteolytic degradation of molecularly engineered PEG hydrogels in response to MMP-1 and MMP-2. *Biomaterials* **2010**, *31* (30), 7836-7845.
- Licht, C.; Rose, J. C.; Anarkoli, A. O.; Blondel, D.; Roccio, M.; Haraszti,
 T.; Gehlen, D. B.; Hubbell, J. A.; Lutolf, M. P.; De Laporte, L., Synthetic
 3D PEG-Anisogel Tailored with Fibronectin Fragments Induce Aligned
 Nerve Extension. *Biomacromolecules* 2019, 20 (11), 4075-4087.
- 152. Babu, S.; Chen, I.; Vedaraman, S.; Gerardo-Nava, J.; Licht, C.; Kittel, Y.; Haraszti, T.; Di Russo, J.; De Laporte, L., How do the Local Physical, Biochemical, and Mechanical Properties of an Injectable Synthetic Anisotropic Hydrogel Affect Oriented Nerve Growth? *Advanced Functional Materials* 2022, 32 (50), 2202468.
- 153. Zhang, K.; Zhou, Y.; Zhang, J.; Liu, Q.; Hanenberg, C.; Mourran, A.; Wang, X.; Gao, X.; Cao, Y.; Herrmann, A.; Zheng, L., Shape morphing of hydrogels by harnessing enzyme enabled mechanoresponse. *Nature Communications* 2024, 15 (1), 249.
- 154. Narayan, O. P.; Dong, J.; Huang, M.; Chen, L.; Liu, L.; Nguyen, V.; Dozic, A. V.; Liu, X.; Wang, H.; Yin, Q.; Tang, X.; Guan, J., Reversible light-

responsive protein hydrogel for on-demand cell encapsulation and release. *Acta Biomaterialia* **2025**.

- 155. Madl, C. M.; Wang, Y. X.; Holbrook, C. A.; Su, S.; Shi, X.; Byfield, F. J.; Wicki, G.; Flaig, I. A.; Blau, H. M., Hydrogel biomaterials that stiffen and soften on demand reveal that skeletal muscle stem cells harbor a mechanical memory. *Proceedings of the National Academy of Sciences* 2024, 121 (35), e2406787121.
- 156. Riley, L.; Wei, G.; Bao, Y.; Cheng, P.; Wilson, K. L.; Liu, Y.; Gong, Y.; Segura, T., Void Volume Fraction of Granular Scaffolds. *Small* **2023**, *19* (40), 2303466.
- 157. Qazi, T. H.; Wu, J.; Muir, V. G.; Weintraub, S.; Gullbrand, S. E.; Lee, D.; Issadore, D.; Burdick, J. A., Anisotropic Rod-Shaped Particles Influence Injectable Granular Hydrogel Properties and Cell Invasion. *Advanced Materials* 2022, 34 (12), 2109194.
- 158. Rommel, D.; Mork, M.; Vedaraman, S.; Bastard, C.; Guerzoni, L. P. B.; Kittel, Y.; Vinokur, R.; Born, N.; Haraszti, T.; De Laporte, L., Functionalized Microgel Rods Interlinked into Soft Macroporous Structures for 3D Cell Culture. *Advanced Science* 2022, 9 (10), 2103554.
- 159. Suturin, A. C.; Krüger, A. J. D.; Neidig, K.; Klos, N.; Dolfen, N.; Bund, M.; Gronemann, T.; Sebers, R.; Manukanc, A.; Yazdani, G.; Kittel, Y.; Rommel, D.; Haraszti, T.; Köhler, J.; De Laporte, L., Annealing High Aspect Ratio Microgels into Macroporous 3D Scaffolds Allows for Higher Porosities and Effective Cell Migration. *Advanced Healthcare Materials* 2022, 11 (24), 2200989.
- 160. Kniebs, C.; Kreimendahl, F.; Köpf, M.; Fischer, H.; Jockenhoevel, S.; Thiebes, A. L., Influence of Different Cell Types and Sources on Pre-Vascularisation in Fibrin and Agarose–Collagen Gels. *Organogenesis* 2020, 16 (1), 14-26.
- 161. Bastard, C.; Günther, D.; Gerardo-Nava, J.; Dewerchin, M.; Sprycha, P.; Licht, C.; Lüken, A.; Wessling, M.; De Laporte, L., How Does Temporal and Sequential Delivery of Multiple Growth Factors Affect Vascularization Inside 3D Hydrogels? *Advanced Therapeutics* 2024, 7 (1), 2300091.
- 162. Ben-Shaul, S.; Landau, S.; Merdler, U.; Levenberg, S., Mature vessel networks in engineered tissue promote graft–host anastomosis and prevent

graft thrombosis. *Proceedings of the National Academy of Sciences* **2019**, *116* (8), 2955-2960.

- 163. Gentile, C.; Fleming, P. A.; Mironov, V.; Argraves, K. M.; Argraves, W. S.; Drake, C. J., VEGF-mediated fusion in the generation of uniluminal vascular spheroids. *Developmental Dynamics* 2008, 237 (10), 2918-2925.
- 164. Fleming, P. A.; Argraves, W. S.; Gentile, C.; Neagu, A.; Forgacs, G.; Drake, C. J., Fusion of uniluminal vascular spheroids: A model for assembly of blood vessels. *Developmental Dynamics* **2010**, *239* (2), 398-406.
- 165. De Moor, L.; Merovci, I.; Baetens, S.; Verstraeten, J.; Kowalska, P.; Krysko, D. V.; De Vos, W. H.; Declercq, H., High-throughput fabrication of vascularized spheroids for bioprinting. *Biofabrication* **2018**, *10* (3), 035009.
- 166. De Moor, L.; Smet, J.; Plovyt, M.; Bekaert, B.; Vercruysse, C.; Asadian, M.; De Geyter, N.; Van Vlierberghe, S.; Dubruel, P.; Declercq, H., Engineering microvasculature by 3D bioprinting of prevascularized spheroids in photo-crosslinkable gelatin. *Biofabrication* 2021, 13 (4), 045021.
- 167. De Lorenzi, F.; Hansen, N.; Theek, B.; Daware, R.; Motta, A.; Breuel, S.; Nasehi, R.; Baumeister, J.; Schöneberg, J.; Stojanović, N.; von Stillfried, S.; Vogt, M.; Müller-Newen, G.; Maurer, J.; Sofias, A. M.; Lammers, T.; Fischer, H.; Kiessling, F., Engineering Mesoscopic 3D Tumor Models with a Self-Organizing Vascularized Matrix. *Advanced Materials* 2024, 36 (5), 2303196.
- 168. Li, X.; Liu, B.; Pei, B.; Chen, J.; Zhou, D.; Peng, J.; Zhang, X.; Jia, W.; Xu, T., Inkjet Bioprinting of Biomaterials. *Chemical Reviews* **2020**, *120* (19), 10793-10833.
- 169. Daly, A. C.; Kelly, D. J., Biofabrication of spatially organised tissues by directing the growth of cellular spheroids within 3D printed polymeric microchambers. *Biomaterials* 2019, 197, 194-206.
- 170. Antoshin, A.; Minaeva, E.; Koteneva, P.; Peshkova, M.; Bikmulina, P.; Kosheleva, N.; Efremov, Y.; Shpichka, A.; Yusupov, V.; Minaev, N.; Timashev, P., LIFT of cell spheroids: Proof of concept. *Bioprinting* 2023, 34, e00297.

171. Chang, J.; Sun, X., Laser-induced forward transfer based laser bioprinting in biomedical applications. *Frontiers in Bioengineering and Biotechnology* **2023**, *11*.

- 172. Hall, G. N.; Fan, Y.; Viellerobe, B.; Iazzolino, A.; Dimopoulos, A.; Poiron, C.; Clapies, A.; Luyten, F. P.; Guillemot, F.; Papantoniou, I., Laser-assisted bioprinting of targeted cartilaginous spheroids for high density bottom-up tissue engineering. *Biofabrication* 2024, 16 (4), 045029.
- 173. Ahrens, J. H.; Uzel, S. G. M.; Skylar-Scott, M.; Mata, M. M.; Lu, A.; Kroll, K. T.; Lewis, J. A., Programming Cellular Alignment in Engineered Cardiac Tissue via Bioprinting Anisotropic Organ Building Blocks. *Advanced Materials* 2022, 34 (26), 2200217.
- 174. Paternoster, J. L.; Vranckx, J. J., State of the Art of Clinical Applications of Tissue Engineering in 2021. *Tissue Eng Part B Rev* **2022**, *28* (3), 592-612.
- 175. Daly, A. C.; Prendergast, M. E.; Hughes, A. J.; Burdick, J. A., Bioprinting for the Biologist. *Cell* **2021**, *184* (1), 18-32.
- 176. Bernal, P. N.; Bouwmeester, M.; Madrid-Wolff, J.; Falandt, M.; Florczak, S.; Rodriguez, N. G.; Li, Y.; Größbacher, G.; Samsom, R.-A.; van Wolferen, M.; van der Laan, L. J. W.; Delrot, P.; Loterie, D.; Malda, J.; Moser, C.; Spee, B.; Levato, R., Volumetric Bioprinting of Organoids and Optically Tuned Hydrogels to Build Liver-Like Metabolic Biofactories. *Advanced Materials* **2022**, *34* (15), 2110054.
- 177. Kilty, S. J.; Al-Hajry, M.; Al-Mutairi, D.; Bonaparte, J. P.; Duval, M.; Hwang, E.; Tse, D., Prospective clinical trial of gelatin-thrombin matrix as first line treatment of posterior epistaxis. *Laryngoscope* **2014**, *124* (1), 38-42.
- 178. Morimoto, N.; Kakudo, N.; Matsui, M.; Ogura, T.; Hara, T.; Suzuki, K.; Yamamoto, M.; Tabata, Y.; Kusumoto, K., Exploratory clinical trial of combination wound therapy with a gelatin sheet and platelet-rich plasma in patients with chronic skin ulcers: study protocol. *BMJ Open* **2015**, *5* (5), e007733.
- Klotz, B. J.; Gawlitta, D.; Rosenberg, A. J. W. P.; Malda, J.; Melchels, F.
 P. W., Gelatin-Methacryloyl Hydrogels: Towards Biofabrication-Based
 Tissue Repair. *Trends in Biotechnology* 2016, 34 (5), 394-407.

180. Hasan, M. M.; Ahmad, A.; Akter, M. Z.; Choi, Y.-J.; Yi, H.-G., Bioinks for bioprinting using plant-derived biomaterials. *Biofabrication* **2024**, *16* (4), 042004.

- 181. Kwon, H.; Lee, S.; Byun, H.; Huh, S. J.; Lee, E.; Kim, E.; Lee, J.; Shin, H., Engineering pre-vascularized 3D tissue and rapid vascular integration with host blood vessels via co-cultured spheroids-laden hydrogel. *Biofabrication* **2024**, *16* (2), 025029.
- 182. Khoeini, R.; Nosrati, H.; Akbarzadeh, A.; Eftekhari, A.; Kavetskyy, T.; Khalilov, R.; Ahmadian, E.; Nasibova, A.; Datta, P.; Roshangar, L.; Deluca, D. C.; Davaran, S.; Cucchiarini, M.; Ozbolat, I. T., Natural and Synthetic Bioinks for 3D Bioprinting. *Advanced NanoBiomed Research* **2021**, *1* (8), 2000097.
- 183. Hockaday, L. A.; Kang, K. H.; Colangelo, N. W.; Cheung, P. Y. C.; Duan, B.; Malone, E.; Wu, J.; Girardi, L. N.; Bonassar, L. J.; Lipson, H.; Chu, C. C.; Butcher, J. T., Rapid 3D printing of anatomically accurate and mechanically heterogeneous aortic valve hydrogel scaffolds. *Biofabrication* 2012, 4 (3), 035005.
- 184. Piluso, S.; Skvortsov, G. A.; Altunbek, M.; Afghah, F.; Khani, N.; Koç, B.; Patterson, J., 3D bioprinting of molecularly engineered PEG-based hydrogels utilizing gelatin fragments. *Biofabrication* **2021**, *13* (4), 045008.
- 185. Gao, G.; Schilling, A. F.; Hubbell, K.; Yonezawa, T.; Truong, D.; Hong, Y.; Dai, G.; Cui, X., Improved properties of bone and cartilage tissue from 3D inkjet-bioprinted human mesenchymal stem cells by simultaneous deposition and photocrosslinking in PEG-GelMA. *Biotechnology Letters* **2015**, *37* (11), 2349-2355.
- 186. Peak, C. W.; Singh, K. A.; Adlouni, M. a.; Chen, J.; Gaharwar, A. K., Printing Therapeutic Proteins in 3D using Nanoengineered Bioink to Control and Direct Cell Migration. *Advanced Healthcare Materials* **2019**, *8* (11), 1801553.
- 187. Ouyang, L.; Highley, C. B.; Sun, W.; Burdick, J. A., A Generalizable Strategy for the 3D Bioprinting of Hydrogels from Nonviscous Photocrosslinkable Inks. *Advanced Materials* 2017, 29 (8), 1604983.

188. Wang, Z.; Abdulla, R.; Parker, B.; Samanipour, R.; Ghosh, S.; Kim, K., A simple and high-resolution stereolithography-based 3D bioprinting system using visible light crosslinkable bioinks. *Biofabrication* **2015**, *7* (4), 045009.

- 189. Schwab, A.; Levato, R.; D'Este, M.; Piluso, S.; Eglin, D.; Malda, J., Printability and Shape Fidelity of Bioinks in 3D Bioprinting. *Chemical Reviews* **2020**, *120* (19), 11028-11055.
- 190. Ouyang, L.; Armstrong, J. P. K.; Lin, Y.; Wojciechowski, J. P.; Lee-Reeves, C.; Hachim, D.; Zhou, K.; Burdick, J. A.; Stevens, M. M., Expanding and optimizing 3D bioprinting capabilities using complementary network bioinks. *Science Advances* **2020**, *6* (38), eabc5529.
- Mosiewicz, K. A.; Kolb, L.; van der Vlies, A. J.; Martino, M. M.; Lienemann,
 P. S.; Hubbell, J. A.; Ehrbar, M.; Lutolf, M. P., In situ cell manipulation through enzymatic hydrogel photopatterning. *Nature Materials* 2013, 12 (11), 1072-1078.
- 192. Geevarghese, A.; Herman, I. M., Pericyte-endothelial crosstalk: implications and opportunities for advanced cellular therapies. *Translational Research* **2014**, *163* (4), 296-306.
- 193. Trappmann, B.; Baker, B. M.; Polacheck, W. J.; Choi, C. K.; Burdick, J. A.; Chen, C. S., Matrix degradability controls multicellularity of 3D cell migration. *Nature Communications* 2017, 8 (1), 371.
- 194. Mierke, C. T.; Zitterbart, D. P.; Kollmannsberger, P.; Raupach, C.; Schlötzer-Schrehardt, U.; Goecke, T. W.; Behrens, J.; Fabry, B., Breakdown of the Endothelial Barrier Function in Tumor Cell Transmigration. *Biophysical Journal* 2008, 94 (7), 2832-2846.
- 195. Modak, R. V.; Zaiss, D. M., Isolation and Culture of Murine Hepatic Stellate Cells. *Bio-protocol* **2019**, *9* (21), e3422.
- 196. Graham, J. M., Isolation of Nuclei and Nuclear Membranes From Animal Tissues. *Current Protocols in Cell Biology* **2001**, *12* (1), 3.10.1-3.10.19.
- 197. Allazetta, S.; Kolb, L.; Zerbib, S.; Bardy, J. a.; Lutolf, M. P., Cell-Instructive Microgels with Tailor-Made Physicochemical Properties. *Small* **2015**, *11* (42), 5647-5656.
- 198. Truong, V. X.; Tsang, K. M.; Forsythe, J. S., Nonswelling Click-Cross-Linked Gelatin and PEG Hydrogels with Tunable Properties Using Pluronic Linkers. *Biomacromolecules* **2017**, *18* (3), 757-766.

199. Liu, J.; Long, H.; Zeuschner, D.; Räder, A. F. B.; Polacheck, W. J.; Kessler, H.; Sorokin, L.; Trappmann, B., Synthetic extracellular matrices with tailored adhesiveness and degradability support lumen formation during angiogenic sprouting. *Nature Communications* **2021**, *12* (1), 3402.

- 200. Buffa, F. M.; West, C.; Byrne, K.; Moore, J. V.; Nahum, A. E., Radiation response and cure rate of human colon adenocarcinoma spheroids of different size: the significance of hypoxia on tumor control modelling. *International Journal of Radiation Oncology*Biology*Physics* 2001, 49 (4), 1109-1118.
- 201. Gunay, G.; Kirit, H. A.; Kamatar, A.; Baghdasaryan, O.; Hamsici, S.; Acar, H., The effects of size and shape of the ovarian cancer spheroids on the drug resistance and migration. *Gynecologic Oncology* 2020, 159 (2), 563-572.
- 202. Pugh, C. W.; Ratcliffe, P. J., Regulation of angiogenesis by hypoxia: role of the HIF system. *Nature Medicine* **2003**, 9 (6), 677-684.
- 203. Kim, S.-j.; Byun, H.; Lee, S.; Kim, E.; Lee, G. M.; Huh, S. J.; Joo, J.; Shin, H., Spatially arranged encapsulation of stem cell spheroids within hydrogels for the regulation of spheroid fusion and cell migration. *Acta Biomaterialia* **2022**, *142*, 60-72.
- 204. Ma, Y.; Zhao, F., Nonlinear oscillation and acoustic scattering of bubbles. *Ultrasonics Sonochemistry* **2021**, *74*, 105573.
- 205. Yamada, K. M.; Collins, J. W.; Cruz Walma, D. A.; Doyle, A. D.; Morales, S. G.; Lu, J.; Matsumoto, K.; Nazari, S. S.; Sekiguchi, R.; Shinsato, Y.; Wang, S., Extracellular matrix dynamics in cell migration, invasion and tissue morphogenesis. *International Journal of Experimental Pathology* 2019, 100 (3), 144-152.
- 206. Sternlicht, M. D.; Werb, Z., How Matrix Metalloproteinases Regulate Cell Behavior. *Annual Review of Cell and Developmental Biology* **2001**, *17*, 463-516.
- 207. Mott, J. D.; Werb, Z., Regulation of matrix biology by matrix metalloproteinases. *Current Opinion in Cell Biology* **2004,** *16* (5), 558-564.
- 208. Löffek, S.; Schilling, O.; Franzke, C.-W., Biological role of matrix metalloproteinases: a critical balance. *European Respiratory Journal* **2010**, 38 (1), 191-208.

209. Kremastiotis, G.; Handa, I.; Jackson, C.; George, S.; Johnson, J., Disparate effects of MMP and TIMP modulation on coronary atherosclerosis and associated myocardial fibrosis. *Scientific Reports* **2021**, *11* (1), 23081.

- 210. Arpino, V.; Brock, M.; Gill, S. E., The role of TIMPs in regulation of extracellular matrix proteolysis. *Matrix Biology* **2015**, *44-46*, 247-254.
- 211. Madl, C. M.; LeSavage, B. L.; Dewi, R. E.; Dinh, C. B.; Stowers, R. S.; Khariton, M.; Lampe, K. J.; Nguyen, D.; Chaudhuri, O.; Enejder, A.; Heilshorn, S. C., Maintenance of neural progenitor cell stemness in 3D hydrogels requires matrix remodelling. *Nature Materials* 2017, 16 (12), 1233-1242.
- 212. Jones, J. A.; McNally, A. K.; Chang, D. T.; Qin, L. A.; Meyerson, H.; Colton, E.; Kwon, I. L. K.; Matsuda, T.; Anderson, J. M., Matrix metalloproteinases and their inhibitors in the foreign body reaction on biomaterials. *Journal of Biomedical Materials Research Part A* 2008, 84A (1), 158-166.
- 213. Cui, N.; Hu, M.; Khalil, R. A., Chapter One Biochemical and Biological Attributes of Matrix Metalloproteinases. In *Progress in Molecular Biology and Translational Science*, Khalil, R. A., Ed. Academic Press: 2017; Vol. 147, pp 1-73.
- 214. Lindner, D.; Zietsch, C.; Becher, P. M.; Schulze, K.; Schultheiss, H.-P.; Tschöpe, C.; Westermann, D., Differential Expression of Matrix Metalloproteases in Human Fibroblasts with Different Origins. *Biochemistry Research International* 2012, 2012 (1), 875742.
- 215. Griffin, D. R.; Archang, M. M.; Kuan, C.-H.; Weaver, W. M.; Weinstein, J. S.; Feng, A. C.; Ruccia, A.; Sideris, E.; Ragkousis, V.; Koh, J.; Plikus, M. V.; Di Carlo, D.; Segura, T.; Scumpia, P. O., Activating an adaptive immune response from a hydrogel scaffold imparts regenerative wound healing. *Nature Materials* 2021, 20 (4), 560-569.
- 216. Amer, L. D.; Bryant, S. J., The In Vitro and In Vivo Response to MMP-Sensitive Poly(Ethylene Glycol) Hydrogels. *Annals of Biomedical Engineering* **2016**, *44* (6), 1959-1969.
- 217. Hsieh, Z.-H.; Fan, C.-H.; Ho, Y.-J.; Li, M.-L.; Yeh, C.-K., Improvement of light penetration in biological tissue using an ultrasound-induced heating tunnel. *Scientific Reports* **2020**, *10* (1), 17406.

218. Huo, S.; Zhao, P.; Shi, Z.; Zou, M.; Yang, X.; Warszawik, E.; Loznik, M.; Göstl, R.; Herrmann, A., Mechanochemical bond scission for the activation of drugs. *Nature Chemistry* **2021**, *13* (2), 131-139.

- 219. Zou, M.; Zhao, P.; Fan, J.; Göstl, R.; Herrmann, A., Microgels as drug carriers for sonopharmacology. *Journal of Polymer Science* **2022**, *60* (12), 1864-1870.
- 220. Lutolf, M. P.; Tirelli, N.; Cerritelli, S.; Cavalli, L.; Hubbell, J. A., Systematic Modulation of Michael-Type Reactivity of Thiols through the Use of Charged Amino Acids. *Bioconjugate Chemistry* **2001**, *12* (6), 1051-1056.
- 221. Ahmad, R.; Knafo, L.; Xu, J.; Sindhu, S. T. A. K.; Menezes, J.; Ahmad, A., Thrombin induces apoptosis in human tumor cells. *International Journal of Cancer* **2000**, *87* (5), 707-715.
- 222. Park, M. J.; Won, J. H.; Kim, D. K., Thrombin Induced Apoptosis through Calcium-Mediated Activation of Cytosolic Phospholipase A₂ in Intestinal Myofibroblasts. *Biomolecules & Therapeutics* **2023**, *31* (1), 59-67.
- 223. Rabiet, M.-J.; Plantier, J.-L.; Rival, Y.; Genoux, Y.; Lampugnani, M.-G.; Dejana, E., Thrombin-Induced Increase in Endothelial Permeability Is Associated With Changes in Cell-to-Cell Junction Organization.

 *Arteriosclerosis, Thrombosis, and Vascular Biology 1996, 16 (3), 488-496.
- 224. Chambers, R. C.; Leoni, P.; Blanc-Brude, O. P.; Wembridge, D. E.; Laurent, G. J., Thrombin Is a Potent Inducer of Connective Tissue Growth Factor Production via Proteolytic Activation of Protease-activated Receptor-1*. *Journal of Biological Chemistry* 2000, 275 (45), 35584-35591.
- 225. Sun, G.; Mao, J. J., Engineering Dextran-Based Scaffolds for Drug Delivery and Tissue Repair. *Nanomedicine* **2012**, *7* (11), 1771-1784.
- 226. Jansen, J.; Reimer, K. C.; et al., SARS-CoV-2 infects the human kidney and drives fibrosis in kidney organoids. *Cell Stem Cell* **2022**, *29* (2), 217-231.e8.
- 227. Schneeberger, K.; Sánchez-Romero, N.; Ye, S.; van Steenbeek, F. G.; Oosterhoff, L. A.; Pla Palacin, I.; Chen, C.; van Wolferen, M. E.; van Tienderen, G.; Lieshout, R.; Colemonts-Vroninks, H.; Schene, I.; Hoekstra, R.; Verstegen, M. M. A.; van der Laan, L. J. W.; Penning, L. C.; Fuchs, S. A.; Clevers, H.; De Kock, J.; Baptista, P. M.; Spee, B., Large-

Scale Production of LGR5-Positive Bipotential Human Liver Stem Cells. *Hepatology* **2020,** *72* (1), 257-270.

- 228. Rossi, G.; Broguiere, N.; Miyamoto, M.; Boni, A.; Guiet, R.; Girgin, M.; Kelly, R. G.; Kwon, C.; Lutolf, M. P., Capturing Cardiogenesis in Gastruloids. *Cell Stem Cell* **2021**, *28* (2), 230-240.e6.
- 229. Eichmüller, O. L.; Knoblich, J. A., Human cerebral organoids a new tool for clinical neurology research. *Nature Reviews Neurology* **2022**, *18* (11), 661-680.
- 230. Rossi, G.; Manfrin, A.; Lutolf, M. P., Progress and potential in organoid research. *Nature Reviews Genetics* **2018**, *19* (11), 671-687.
- 231. Nikolaev, M.; Mitrofanova, O.; Broguiere, N.; Geraldo, S.; Dutta, D.; Tabata, Y.; Elci, B.; Brandenberg, N.; Kolotuev, I.; Gjorevski, N.; Clevers, H.; Lutolf, M. P., Homeostatic mini-intestines through scaffold-guided organoid morphogenesis. *Nature* 2020, 585 (7826), 574-578.
- 232. Leferink, A.; Schipper, D.; Arts, E.; Vrij, E.; Rivron, N.; Karperien, M.; Mittmann, K.; van Blitterswijk, C.; Moroni, L.; Truckenmüller, R., Engineered Micro-Objects as Scaffolding Elements in Cellular Building Blocks for Bottom-Up Tissue Engineering Approaches. *Advanced Materials* 2014, 26 (16), 2592-2599.
- 233. Bulut, S.; Jung, S.-H.; Bissing, T.; Schmitt, F.; Bund, M.; Braun, S.; Pich, A., Tuning the Porosity of Dextran Microgels with Supramacromolecular Nanogels as Soft Sacrificial Templates. *Small* 2023, 19 (45), 2303783.
- 234. Ryu, N. E.; Lee, S. H.; Park, H., Spheroid Culture System Methods and Applications for Mesenchymal Stem Cells. *Cells* **2019**, *8* (12).
- 235. Atcha, H.; Choi, Y. S.; Chaudhuri, O.; Engler, A. J., Getting physical: Material mechanics is an intrinsic cell cue. *Cell Stem Cell* **2023**, *30* (6), 750-765.
- 236. Chaudhuri, O.; Gu, L.; Darnell, M.; Klumpers, D.; Bencherif, S. A.; Weaver, J. C.; Huebsch, N.; Mooney, D. J., Substrate stress relaxation regulates cell spreading. *Nature Communications* **2015**, *6* (1), 6365.
- 237. Pavel, M.; Renna, M.; Park, S. J.; Menzies, F. M.; Ricketts, T.; Füllgrabe, J.; Ashkenazi, A.; Frake, R. A.; Lombarte, A. C.; Bento, C. F.; Franze, K.; Rubinsztein, D. C., Contact inhibition controls cell survival and proliferation via YAP/TAZ-autophagy axis. *Nature Communications* **2018**, *9* (1), 2961.

238. Bulut, S.; Günther, D.; Bund, M.; Haats, C.; Bissing, T.; Bastard, C.; Wessling, M.; De Laporte, L.; Pich, A., Cellular Architects at Work: Cells Building their Own Microgel Houses. Advanced Healthcare Materials 2024, 13 (25), 2302957.

List of Abbreviations 155

8 List of Abbreviations

2D Two-dimensional

3D Three-dimensional

ABM Antibiotic-Antimycotic

Ang-1 Angiopoietin-1

Ang-2 Angiopoietin-2

ANOVA Analysis of Variance

aOBB Anisotropic Organ Building Block

BATE Bioprinting-Assisted Tissue Emergence

bFGF Basal Fibroblast Growth Factor

BSA Bovine Serum Albumin

CD31 Cluster of Differentiation 31

DAPI 4',6-diamidino-2-phenylindole

Dex-MA Dextran Methacrylate

DMEM Dulbecco's Modified Eagle Medium

ECM Extracellular Matrix

EGF Epidermal Growth Factor

EGM-2 Endothelial Cell Growth Medium 2

EMA European Medical Agency

EWG Electron-Withdrawing Group

FCS Fetal Calf Serum

FDA Food and Drug Administration

156 List of Abbreviations

FRP Free Radical Polymerization

G' Storage Modulus

GelMA Gelatin Methacrylate

HLA Human Leukocyte Antigen

HS-Esters-SH Ester-Functionalized Di-Thiol Crosslinker

HS-MMPsens-SH MMP-Sensitive Peptide Crosslinker

HS-TCP-SH Thrombin-Cleavable Peptide Crosslinker

HUVEC Human Umbilical Vein Endothelial Cell

IGF Insulin-Like Growth Factor

LAP Lithium Phenyl-2,4,6-Trimethylbenzoylphosphinate

LIFT Laser-Induced Forward Transfer

LIFU Low Intensity Focused Ultrasound

MAP Microporous Annealed Particle Scaffold

MMP Matrix Metalloproteinase

MSC Mesenchymal Stem Cell

NA Numerical Aperture

NHDF Normal Human Dermal Fibroblasts

PDGF Platelet-Derived Growth Factor

PDMS Polydimethylsiloxane

PECAM-1 Platelet Endothelial Cell Adhesion Molecule 1

PEG Polyethylene Glycol

PEG-VS PEG-Vinyl Sulfone

PFA Paraformaldehyde

List of Abbreviations 157

PLGA Polylactic Glycolic Acid

PLLA Poly-L-Lactic Acid

RGD Arginine-Glycine-Aspartate

RT Room Temperature

SD Standard Deviation

SEM Scanning Electron Microscopy

SH Thiol

t Time point

TIMP Tissue Inhibitor of Metalloproteinases

UV Ultraviolet

VEGF Vascular Endothelial Growth Factor

VS Vinyl Sulfone

YAP Yes-Associated Protein

158 Acknowledgments

9 Acknowledgments

Although I have worked towards this moment of writing the final pages of my dissertation for multiple years, I somehow never expected it to become a reality... While this thesis marks the end of my PhD journey, the influences of all the amazing people I met along the way have taught me invaluable lessons that shaped me for life. Getting the opportunity to join the research group of **Prof. Dr.**-**Ing. Laura De Laporte** is one of the best things that ever happened to me. From the moment when I read the article "eng verbunden" about her in the Leibniz magazine, her level of dedication and commitment towards her goals was inspiring and I knew I had to join her research group. This is why I will never forget the moment on February 23, 2021 when I received her email saying "I would now like to offer you the position in our group if you are still interested of course." - It was the starting point to the best four years of my life. Four years that I will always be deeply grateful for and keep in the best memory forever. Laura, your support over these years has meant more to me than I can put into words. You believed in me even in moments when I did not and gave me the freedom to explore my own ideas while providing guidance whenever needed. All this time, I have wondered how you manage to balance all of this – the research, lecturing, mentoring students, an agenda more packed than most could imagine, your family, and life. But I came to the realization that this is simply who you are: Someone who gives their absolute best to everything they do. And I am sure that, should we ever have a minimallyinvasive therapy for spinal cord injury, your name will be associated with it.

I would further like to thank **Prof. Stefan Jockenhövel** for being my second supervisor. More than that, he was also the second supervisor of my master thesis, which I completed in his institute under the guidance of **PD Dr. Anja Lena Thiebes** and **Dr. Caroline Kniebs**. Here, I worked for the first time in the field of tissue engineering and developed a strong desire to continue to work in this field. Ultimately, it was Caro's suggestion to apply to Laura's research group, which connected the pieces of the puzzle and marked the starting point of my PhD.

I truly enjoyed to work at DWI not just for our amazing research but mainly for the great colleagues and friends to share the work with. I do not know what I would have done in my first PhD year without **Sitara**. Thank you for your guidance and

Acknowledgments 159

mentorship – I have learned so much from you! Next to Sitara, **Cédric** was one of my first contacts at DWI and more than that my OrganTrans partner-in-science. Together, we spent hours in the car driving to Utrecht and even more hours printing until late night, but the free hot chocolate made up for all of this. Thank you for answering all my chemistry questions and proving that interdisciplinary research leads to great outcomes. Within our research group, **Céline** and I both worked so extensively on vascularization, we should have started our own subgroup! Besides sharing materials and resources, I knew that I could always count on her expertise and help throughout this journey and I am so grateful for it. I could not be prouder to have been part of the **De Laporte research group** for so long. Thank you **Alisa**, Anna, Bernhard, Carolina, Catarina, Corinna, Dirk, Ekin, Fred, Greta, Iris, José, Julia, Laura, Matthias, Misael, Nina, Ninon, Oscar, Piet, Susan, Tanja, Till, Tom, Veronica, and Yonca for all the scientific discussions. You made being in the lab something I genuinely looked forward to every day. This work would not have been the same without the contributions of my students Hannah, Michelle, Christina, Vanessa and Si-Ting. It was a pleasure to work with you. Apart from our research group, I would like to thank all collaboration partners, namely Ary Marsee, Alba Pueyo Moliner, Dr. Mieke Dewerchin, Prof. Peter Carmeliet, Dr. Bart Spee and Dr. Kerstin Schneeberger for the collaboration within the OrganTrans project, Johannes Hahn and Prof. Dr.-Ing. Horst Fischer for the work on acoustic spheroid alignment, Kuan Zhang and Prof. Andreas Herrmann for the project on on-demand hydrogel degradation and Selin Bulut and Prof. **Andrij Pich** for the development of cell-induced interlinked MAP scaffolds.

I am incredibly grateful to my family, whose unwavering love and support have been the foundation of everything I have achieved. Their encouragement and sacrifices made this journey possible. This thesis is as much theirs as it is mine. I would further like to thank **Jan** and **Jonas** who never fail to put a smile on my face.

The final sentences belong to the most important person in my life, **Karin**. I wrote almost every page of this thesis with you by my side and your presence, love, and support were my constant source of strength and inspiration. While I have always been passionate about my work, you have shown me that life is about so much more and gave me a sense of belonging I never knew I was missing. *Te iubesc din toată inima și abia aștept să descoperim împreună ce înseamnă cu adevărat viața*.